CRANFIELD UNIVERSITY

BING XIA

INVESTIGATION OF NOVEL MULTI-LAYER SPOKE-TYPE FERRITE INTERIOR PERMANENT MAGNET MACHINES

SCHOOL OF WATER, ENERGY AND ENVIRONMENT
Energy Engineering

PhD
Academic Year: 2012 - 2017

Supervisor: PROFESSOR PATRICK LUK
March 2017

CRANFIELD UNIVERSITY

SCHOOL OF WATER, ENERGY AND ENVIRONMENT
Power Engineering

PhD

Academic Year 2012 - 2017

BING XIA

INVESTIGATION OF NOVEL MULTI-LAYER SPOKE-TYPE FERRITE INTERIOR PERMANENT MAGNET MACHINES

Supervisor: PROFESSOR PATRICK CHI-KWONG LUK
March 2017

This thesis is submitted in partial fulfilment of the requirements for the degree of DOCTOR OF PHILOSOPHY

© Cranfield University 2017. All rights reserved. No part of this publication may be reproduced without the written permission of the copyright owner.

ABSTRACT

The permanent magnet synchronous machines have been attracting more and more attention due to the advantages of high torque density, outstanding efficiency and maturing technologies. Under the urges of mandatory energy efficiency requirements, they are considered as the most potential candidates to replace the comparatively low-efficient induction machines which dominate the industrial market. However, most of the high performance permanent magnet machines are based on high cost rare-earth materials. Thus, there will be huge demands for low-cost high-performance permanent magnet machines.

Ferrite magnet is inexpensive and abundant in supply, and is considered as the most promising alternative to achieve the goal of low cost and high performance. In consideration of the low magnetic energy, this thesis explored the recent developments and possible ideas of ferrite machines, and proposed a novel multi-layer spoke-type interior permanent magnet configuration combining the advantages of flux focusing technique and multi-layer structure. With comparable material cost to induction machines, the proposed ferrite magnet design could deliver 27% higher power with 2-4% higher efficiency with exactly the same frame size. Based on the data base of International Energy Agency (IEA), electricity consumed by electric machines reached 7.1PWh in 2006 [1]. Considering that induction machines take up 90% of the overall industrial installation, the potential energy savings is enormous.

This thesis contributes in five key aspects towards the investigation and design of low-cost high-performance ferrite permanent magnet machines. Firstly, accurate analytical models for the multi-layer configurations were developed with the consideration of spatial harmonics, and provided effective yet simple way for preliminary design. Secondly, the influence of key design parameters on performance of the multi-layer ferrite machines were comprehensively investigated, and optimal design could be carried out based on the insightful knowledge revealed. Thirdly, systematic investigation of the demagnetization mechanism was carried out, focusing on the three key factors: armature MMF, intrinsic coercivity and working temperature. Anti-demagnetization designs were

presented accordingly to reduce the risk of performance degradation and guarantee the safe operation under various loading conditions. Then, comparative study was carried out with a commercial induction machine for verification of the superior performance of the proposed ferrite machine. Without loss of generality, the two machines had identical stator cores, same rotor diameter and stacking length. Under the operating condition of same stator copper loss, the results confirmed the superior performance of the ferrite machine in terms of torque density, power factor and efficiency. Lastly, mechanical design was discussed to reduce the cost of mass production, and the experimental effort on the prototype machine validates the advantageous performance as well as the analytical and FEA predictions.

Keywords:

Ferrite, spoke-type, multi-layer, analytical model, demagnetization, induction machine, low cost, high efficiency.

ACKNOWLEDGEMENTS

I would like to acknowledge everyone who has knowingly and unknowingly helped me and wished me the best in successfully accomplishing this research.

I would like to express particular thanks to my supervisor, Professor Patrick Chi-kwong Luk. His supportive encouragement and supervision over the whole study have been extremely helpful and essential.

I would like to thank Dr Weizhong Fei and Mr Wenyi Liang for the valuable helps and discussions during the research. I would also like to thank Mr Chen Yuan from Wujiang Nanyuan Electrical Co., Ltd, China for his professional advices on the prototype design as well as prompt and excellent prototype manufacture services.

I would like to thank the Engineering and Physical Sciences Research Council (EPSRC) for their sponsorship of this research (VESI project, reference: EP/I038543/1).

I would like to give my special thanks to my parents and my sister for their unconditional support and care. I owe every step forward in my life to them.

TABLE OF CONTENTS

LIST OF FIGURES

LIST OF TABLES

LIST OF EQUATIONS

LIST OF ABBREVIATIONS

AC	Alternating Current
AFPM	Axial Flux Permanent Magnet
AMM	Amorphous Magnetic Material
BLDC	Brushless Direct Current
CPSR	Constant Power Speed Range
DC	Direct Current
DEA	Differential Evolution Algorithms
DOE	Design of Experiments
EIA	US Energy Information Administration
EMF	Electromotive Force
EU	European Union
FEA	Finite Element Analysis
FSPM	Flux Switching Permanent Magnet
IM	Induction Motor
IPM	Interior Permanent Magnet
MMF	Magnetomotive Force
MTPA	Maximum Torque-per-Ampere
NdFeB	Neodymium-Iron-Boron
PM	Permanent Magnet
PMASynRM	Permanent Magnet Assisted Synchronous Reluctance Machine
PMSM	Permanent Magnet Synchronous Motor
PVPM	Permanent Magnet Vernier Machine
RSM	Response Surface Method
p.u.	Per Unit
SDM	Steepest Decent Method
SMC	Soft Magnetic Composite
SPM	Surface-mounted Permanent Magnet
SynRM	Synchronous Reluctance Machine
UK	United Kingdom
US	United States
2D	Two Dimension
3D	Three Dimension

NOMENCLATURE

B_{adv}	Flux Distribution Due to the d-axis the vth MMF
B_{admv}	Magnitude of Flux Density Excited by the vth MMF
B_{aqv}	Flux Distribution Due to the q-axis the vth MMF
B_{fv}	Amplitude of vth Flux Harmonic in the Airgap
B_g	Flux Density in the Airgap for the One-layer Structure
B_{g1}	Flux Density in the Airgap of Core Area ①
B_{g2}	Flux Density in the Airgap of Core Area ②
B_{gd1uv}	Airgap Flux Density Contributed by the Flux in the Core Area
B_{gd2uv}	Airgap Flux Density Contributed by the Flux in the PM Slot Area
B_{gdv}	Amplitude of the vth Airgap Flux Distribution by d-axis Current
B_{gduv}	Amplitude of the vth Component Decomposed from B_{gdu}
B_{gquv}	Amplitude of the vth Component Decomposed from B_{gqu}
B_{gqv}	Amplitude of the vth Airgap Flux Distribution by q-axis Current
B_i	Intrinsic Magnetization
B_m	Flux Density of the PM
B_r	Nominal Residual Flux Density
B_{r20}	Residual Flux Density at the Temperature of 20°C
B_{rn}'	Degraded Remanence after Partial Demagnetization
B_{rT}	Residual Flux Density at the Temperature of T_c
B_s	Flux Density in the PM Slot Opening
b_0	Stator Slot Opening
D_m	Location of the Secondary Pole
D_{m3}	Location of the Third Pole
D_{ro}	Rotor Outer Diameter
D_{so}	Stator Outer Diameter
E_{mf}	Back EMF
F_{ad}	d-axis MMF
F_{adv}	Amplitude of the vth d-axis MMF
F_{aq}	q-axis MMF
F_{aqv}	Amplitude of the vth q-axis MMF
F_m	Stator Synthetic MMF
F_{rs}	Rotor MMF Distribution

F_{rsv}	Amplitude of the vth Rotor MMF Distribution
f	Operation Frequency
g	Actual Airgap Length
g_c	Equivalent Airgap Length
H_{aqv}	Flux Intensity Excited by the vth q-axis MMF
H_g	Flux Intensity in the Airgap for One-layer Structure
H_{g1}	Flux Intensity in the Airgap of Core Area ①
H_{g2}	Flux Intensity in the Airgap of Core Area ②
H_{gd}	Flux Intensity in the Airgap Due to the d-axis MMF
H_{lam}	Flux Intensity in the Lamination Cores
H_m	Flux Intensity of the PM for One-layer Structure
H_{m1}	Flux Intensity of the Main PM
H_{m2}	Flux Intensity of the Secondary PM
H_{m1d}	Flux Intensity Inside the Main PM slots by d-axis MMF
H_{m2d}	Flux Intensity Inside the Secondary PM slots by d-axis MMF
H_{md}	Flux Intensity Inside the PM Slot by d-axis MMF for One-layer Structure
H_s	Flux Intensity in the PM Slot Opening for the One-layer Structure
H_{s1}	Flux Intensity in the Main PM Slot Opening
H_{s2}	Flux Intensity in the Secondary PM Slot Opening
I_m	Amplitude of Armature Current
I_{rated}	Rated Current
i_a	Current of Phase a
i_b	Current of Phase b
i_c	Current of Phase c
i_{cd1}	Critical Current for the Main PMs
i_{cd2}	Critical Current for the Secondary PMs
i_d	d-axis Current
i_q	q-axis Current
k_{br}	PM Temperature Coefficient
k_c	Carter's Coefficient
k_{rpac}	Increment factor of Proximity Effect
k_{rs1}	Rotor Main PM Slot Coefficient
k_{rs2}	Rotor Secondary PM Slot Coefficient

k_{wv}	Winding Factor for the vth Harmonic Component
k_{wv}	Winding Factor for the υth Harmonic Component
L_1	Length of the Main PM Pole
L_2	Length of the Secondary PM Pole
L_3	Length of the Third PM Pole
L_{lam}	Length of Lamination Core in the Flux Loop
L_{md}	d-axis Magnetizing Inductance
L_{mdv}	d-axis Magnetizing Inductance by the vth flux Component
L_{md}	q-axis Magnetizing Inductance
L_{mqv}	q-axis Magnetizing Inductance by the vth flux Component
L_{s1}	Depth of the Main PM Slot Opening
L_{s2}	Depth of the Secondary PM Slot Opening
l_{ef}	Stack Length
M	PM Magnetization
m	Number of Phases
N_{fa}	Winding Function of Phase a
N_{fb}	Winding Function of Phase b
N_{fc}	Winding Function of Phase c
N_a	Number of Turns in Series Per Phase
N_t	Number of Stator Teeth
p	Number of Poles
q	Number of Stator Slots
R_a	Phase AC Resistance of Armature Winding
R_{dc}	Phase DC Resistance of Armature Winding
R_{ro}	Rotor Outer Radius
R_{si}	Stator Inner Radius
S_{en}	Area of Element n
S_{PM}	Total Area of All PMs
T_c	Operational Temperature of PM
T_{em}	Electromagnetic Torque
T_{pm}	PM Torque Component
T_{pmm}	Maximum PM Torque
T_r	Reluctance Torque Component

T_{rm}	Maximum Reluctance Torque
W_1	With of the Main PM Pole
W_2	With of the Secondary PM Pole
W_3	With of the Third PM Pole
W_{s1}	With of the Main PM Slot Opening
W_{s2}	With of the Secondary PM Slot Opening
W_{s3}	With of the Third PM Slot Opening
α_1	Mechanical Radians of Core Area ①
α_2	Mechanical Radians of Core Area ②
β_1	Mechanical Radians of Half of the Main PM Slot Opening
β_2	Mechanical Radians of the Secondary PM Slot Opening
γ	Euler–Mascheroni Constant
δ	Skin Depth of Skin Effect
Θ	Mechanical Position in the Stator Frame
λ_d	Demagnetization Index
μ_0	Permeability of Vacuum
μ_m	Relative Permeability of PM
μ_r	Relative Permeability of Conductors
ξ	Demagnetization Ratio
π	The Ratio of a Circle's Circumference to the Diameter
ρ_c	Conductor Resistivity
τ_s	Stator Tooth Pitch
τ_p	Pole Pitch
Ψ_f	Open-circuit PM flux linkage
Ψ_{md}	d-axis Flux Linkage Due to d-axis Excitation
Ψ_{mq}	q-axis Flux Linkage Due to d-axis Excitation
ϕ_{bri}	Flux through the Saturation Bridge
ϕ_g	Flux through the Airgap Due to PM Excitation
ϕ_{g1}	Flux through Core Area ①
ϕ_{g2}	Flux through Core Area ②
ϕ_{gd}	Flux through the Airgap Due to d-axis MMF
ϕ_{m1}	Flux through the Main PM
ϕ_{m2}	Flux through the Secondary PM

ϕ_{md}	Flux through the PM Slot Due to d-axis MMF
ϕ_{ml1}	Flux through the Main PM Slot
ϕ_{ml2}	Flux through the Secondary PM Slot
ω	Electric Angular Velocity

1 INTRODUCTION

1.1 Background

Due to the concerns of energy crisis and adverse environmental impact, particular attentions have been paid to the energy saving in any energy transformation. As one of the most important types of loads in both household and industry, electric machines consume 35-40% of the electricity generated worldwide. Especially in the industrial sector, electric motor systems account for 70% of all industrial electric energy [2]. Electric machines with higher efficiency can not only cut down energy bills but also reduce greenhouse gas emissions. Because of the tremendous advantages for the ambient, researchers from both academia and industry are seeking for viable solution of electrical drives with high power density and efficiency. Studies showed that potentially 25-30% of energy saving could be achieved in electric machines if higher efficiency motors were used in the past decade [3]. As mandatory efficiency standards are put into effect in US and European countries, there are more critical needs of improving motor efficiency. As well known, induction machines (IMs) are the most widely used machine type in various industrial applications such as pumps, fans, mills, traction motors and so on, owing to the merits of the mature manufacturing technology, robustness, high reliability, low material costs and maintenance requirements. However, IMs have the disadvantages of low power factor and low efficiency. Since the excitation field in IMs is established by the magnetizing component of stator armature current, the power factor is inevitably lower than PM machines. What's more, due to existence of considerable copper loss in the rotor cage, the efficiency of IMs is usually inferior to their PM counterparts, which put them in a disadvantageous position to meet the higher power saving requirements [4]. Researches have shown that the total loss can be reduced by 15-20% and the efficiency can be improved by 1-2% by using die-cast copper rotors for IMs [5,6]. But the melting point of copper is much higher aluminium, and the copper die-casting process is not yet mature and quite costly. Thus the copper die-casted IMs usually have shortened lifetime and much higher manufacturing costs, especially for the small and medium

scale IMs [7]. Manufacturers of electric machines and advocates of energy efficiency indicated that the efficiency improvements of IMs had reached the point of diminishing returns [8]. In other words, the benefit gained from efficiency improvement of IM is not worth the increased cost of manufacture and material. Currently mandatory efficiency requirement standards have been enacted in many countries including US, EU, China and Brazil. The efficiency regulations cast the burden of designing more efficient electric machines on the manufacturers. It is of significant importance to improve the efficiency, not only for business purpose but also for the mandatory requirements [2,9,10].

With the development of machine design technologies and high energy permanent (PM) materials, permanent magnet synchronous machines (PMSMs) are becoming more and more attractive in various applications with advantages of high power density, high efficiency and controllability. Since excitation current is not required using pre-magnetized PMs as field excitation, the overall loss can be reduced and thus higher power factor and efficiency is possible. Statistical data shows that a vast amount of energy can be saved by replacing old low efficient induction machines [11]. Compared to IMs, 3-4% improvement in efficiency could be achieved for the PM machines, and the cost difference due to the PM materials could be paid back through operating cost savings in less than 2.5 years at 50% percent duty cycle [12]. According to [1], electric machines consumed 7.1PWh electricity in 2006, and most of the machines were IMs, which taking up to 90% of the overall industrial installation. With 3-4% of efficiency improvement, the energy savings would be enormous by replacing the widely installed IMs with PMSMs. What's more, with the development of high energy PM materials, torque density can be improved, and smaller and lighter electric motor is possible. Thus, PM machines with high energy rare-earth materials such as neodymium-iron-boron magnet (NdFeB) have been an appealing contender for various high performance applications since its discovery, owing to the outstanding features in terms of efficiency and power density [13–17]. However, the supply chain and prices of rare-earth materials are unstable and highly rely on China's export. As depicted in Figure 1-1, the price of rare-earth metal neodymium soared into a sky-high level by a factor of

over 20 in 2011 as China declared to restrict rare-earth supply. The unexpected increase in the price of neodymium was a heavy blow to those companies that relied heavily on high strength rare-earth magnets. As a result, there have been a surge of interests in seeking alternative solutions for non-rare-earth PM based electric machines in industry considering the high material cost and supply uncertainty of rare-earth materials. Consequently, it is of strategic importance to develop alternative electric machines with less or even none rare-earth PM materials for high performance with low cost [18–20].

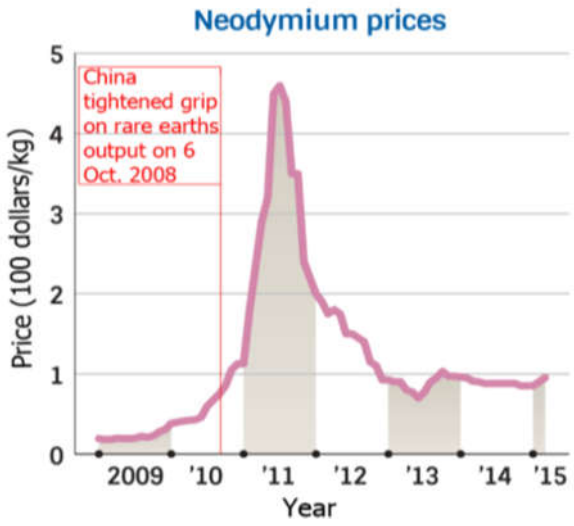

Figure 1-1 The price trends of rare-earth material in recent years.

Ferrite magnets, on the other hand, are abundant in supply and much cheaper than rare-earth. As one of the commonly used PM materials, ferrite PMs are considered as a most potential alternative for high-performance low-cost applications. However, the residual flux density of ferrite magnets is only one third of NdFeB magnet, which raises a challenge for ferrite PM machines to achieve required torque density. Thus, new geometric configurations need to be developed for ferrite PMSMs to achieve comparable performance to that of rare-earth machines.

1.2 Motivation

Nowadays, fossil fuels still dominate the energy market. According to the World Energy Council, 86% of all the primary energy consumption worldwide came

from fossil fuels in 2015. With concerns over the fuel depletion and environmental impact, energy efficiency has been given high priority in order to reduce greenhouse gas emissions. Thus stricter efficiency mandatory standards are being introduced in China, US and EU countries. As one of the most important loads in both domestic and industrial applications, electric machines are facing challenges to meet the efficiency requirements since the majority of them are induction machines. PMSMs are showing remarkable performance for delivering high torque density and efficiency comparing to the IMs, which are the most promising way to improve the efficiency and fulfil the mandatory requirements. However, the high performance PM machines are too reliant on expensive rare-earth materials at the moment. As the future supply of rare-earth materials is likely to be restricted because of the strategical nature, the price of rare-earth materials is prohibitive and highly unstable in the global market. As a result, the development of PMSM is hindered due to the concern over the volatility of rare-earth material market and IMs are still particularly attractive owing to the advantage of much lower material costs. Considering the potential benefit could be achieved by energy saving, there is an urge for high-efficiency, low-cost and sustainable machines from both academia and industry.

With the advantages of low price and abundant supply, ferrite magnets are the most potential candidates for non-rare-earth PMSMs to replace the IMs with similar material cost but higher efficiency. Despite of the low residual flux density, ideas of flux focusing technology and reluctance torque harnessing provide inspiring thoughts on the ferrite machine design. According to [21], the annual sales volume of electric machines reached 330 million in 2006, and there is a vast prospect in developing high efficient ferrite PM machines for the replacement of low efficient IMs in the market.

1.3 Aims and Objectives

This research project aims to investigate and develop novel machine structure suitable for low-cost ferrite PMSM to fulfil the requirements of high efficiency and high torque density, in order to provide a viable alternative solution with

improved performances and competitive cost to the widely used IMs. The objectives of this thesis can be summarized and listed as follows:

1. Extensive review on the developments and current state of ferrite PM machines, evaluation of the pros and cons of different ferrite machine structures and identification of potential low-cost high-efficient solutions for the research project.
2. Development of effective analytical models for the preliminary designs and optimizations of the proposed multi-layer spoke-type ferrite IPM machines.
3. Investigation of the influence of key design parameters on the machine performance such as PM size, location and configuration, so as to implement optimal designs of multi-layer ferrite IPM machines.
4. Systematic investigation of demagnetization mechanism for the ferrite machines, comprehensive analysis of the demagnetization performance of multi-layer ferrite machines under various working conditions, and proposal of anti-demagnetization designs for the safety operation of ferrite machine.
5. Performance comparison between the two-layer ferrite PMSM and a commercial IM with the same frame;
6. Manufacture of the prototype machine based on the electromagnetic and mechanical design and experimental validations of the performance of novel two-layer ferrite IPM machine.

1.4 Outline

The thesis is organized as follows:

Chapter 2 reviews the previous work and current state of the ferrite PM machines, and the most potential solution for the research project is noted for the proposed of novel spoke-type multi-layer configurations.

Chapter 3 proposes the development of analytical models for one-layer and two-layer spoke-type IPM machines and reveals the influence of key design parameters over the machine performances.

Chapter 4 presents the design and optimization of multi-layer ferrite IPM machines, compares the performances of different rotor configurations, and determine the electromagnetic design solution for the project.

Chapter 5 investigates the demagnetization performances of the proposed multi-layer IPMs under various operating conditions, and anti-demagnetization designs are also proposed.

Chapter 6 discusses some practical issues on mechanical design and rotor assembly, compares the performances of the two-layer ferrite machine and a commercial induction machine, and confirms the advantages of the proposed ferrite design by testing the prototype machine under various operating conditions.

Chapter 7 summarizes the outcomes of the thesis and discusses possible future work.

1.5 Main Contributions

The contribution of this research project can be summarized as follows:

- A novel multi-layer structure for low-energy ferrite PM machines is proposed and developed. With excellent flux focusing effect and improved rotor saliency, higher torque density and efficiency is achieved with low-cost design ferrite magnet.
- Simple and effective analytical methods for the proposed multi-layer configurations are developed with high accuracy and provide more efficient way for the preliminary designs.
- Systematic design process is presented and the influence of the key design parameters over the machine performance is revealed.
- Comprehensive investigations on demagnetization are carried out, and the impact of armature current, material property and temperature are analysed to reveal the demagnetization mechanism on the proposed machine.
- Effective anti-demagnetization designs are proposed to reduce the risk of degradation.

- A prototype machine with two-layer configuration is developed and tested under various operating conditions, and the advantageous performance is validated.

1.6 Publications

1.6.1 Papers Based on the Thesis

1. Bing Xia, Weizhong Fei, P. C. K. Luk, Demin Wu, "Design of a Multi-Layer Interior Ferrite Permanent Magnet Synchronous Machine for Traction Applications," *7th IET International Conference on Power Electronics, Machines and Drives (PEMD 2014)*, pp.1-6, April 2014.
2. Bing Xia, Weizhong Fei and P. Luk, "Analysis and design of V-spoke ferrite interior permanent magnet machine for traction applications," *6th International Conference on Power Electronics Systems and Applications (PESA)*, Hong Kong, 2015, pp. 1-6. **(Awarded for a Third Place Prize)**
3. B. Xia and P. C. Luk, “Analytical Model of Open-Circuit Characteristics of Two-Layer Spoke Type Ferrite Interior Permanent Magnet Machines.” *IEEE Electric Machines & Drives Conference (IEMDC) 2017*.
4. B. Xia and P. C. Luk, “Analytical Model for Inductance Calculation of Two-Layer Spoke-Type Ferrite Interior Permanent Magnet Machines.” *IEEE Electric Machines & Drives Conference (IEMDC) 2017*.

1.6.2 Further Contributed Work

1. Weizhong Fei, P.C.K. Luk, Bing Xia, D. Wu, "Design improvement of outer-rotor permanent magnet flux switching machine for direct-drive urban electric vehicle propulsion," *39th Annual Conference of Industrial Electronics Society (IECON)*, pp.7319-7324, Nov. 2013.
2. Weizhong Fei, P.C.K. Luk, D. Wu, Bing Xia, "Approximate three-dimensional finite element analysis of large permanent magnet synchronous generators with stator radial ventilating ducts," *39th Annual Conference of Industrial Electronics Society (IECON)*, pp.7313-7318, Nov. 2013.

3. Bing Xia, Weizhong Fei, P.C.K. Luk, Lixiang Yu, "Particle Swarm Optimization of Air-cored Axial Flux Permanent Magnet Generator for Small-Scale Wind Power Systems," *7th IET International Conference on Power Electronics, Machines and Drives (PEMD 2014),* pp.1-6, April 2014.
4. Demin Wu, Weizhong Fei, P.C.-K. Luk, Bing Xia, "Design Considerations of Outer-Rotor Permanent Magnet Synchronous Machines for In-Wheel Electric Drivetrain Using Particle Swarm Optimization," *7th IET International Conference on Power Electronics, Machines and Drives (PEMD 2014),* pp.1-6, April 2014.
5. B. Xia, J. X. Shen, P. C. K. Luk and W. Fei, "Comparative Study of Air-Cored Axial-Flux Permanent-Magnet Machines With Different Stator Winding Configurations," *IEEE Transactions on Industrial Electronics*, vol. 62, no. 2, pp. 846-856, Feb. 2015.

2 LITERATURE REVIEW ON FERRITE PM MACHINES

2.1 Background Introduction

With the development of power electronics, magnetic materials and electric machine design technologies, PMSMs are becoming one of the most promising solutions for various application, with the remarkable features of high torque density, excellent controllability and good efficiency [22]. During the past decade, most of the high performance PMSMs have been using high-energy rare-earth magnets to deliver high power density and efficiency. However, the soaring price and uncertainty in the supply chain of the rare-earth materials have been a major concern for developers and researchers, which would definitely hinder further developments. After the difficult struggle in 2011 when the price of rare-earth material hiked over 20 times, PM machine manufacturers started the search of alternative solutions to substitute rare-earth for the PM machines.

As one important type of PM materials in the market, ferrite magnet is drawing people's attentions for the design of high performance PM motors. In fact, ferrite PMs were first commercialized in the 1960s, and are still the most widely used magnets today on the basis of the consumption mass. However, the residual flux density and energy product of ferrite PMs are the much lower compared with its rare-earth counterpart, as illustrated in Figure 2-1. The typical remanence of ferrite magnets is in the vicinity of 0.4T, which is only one third that of NdFeB. Thus, the machine characteristics would be greatly reduced simply by replacing rare-earth with ferrite PM or even increasing the amount of ferrite PM in the original design based on conventional PM machine configurations. Nevertheless, with merits of abundant raw material resources, low price, stability to corrosion and temperature, and very high electrical resistivity, ferrite magnets are considered as a most potential candidate for low-cost high-performance PM machines [23–25]. To fulfil the design requirements of high efficiency, large power density and wide speed range, suitable design needs to be investigated to maximize the torque capability of ferrite PM machines.

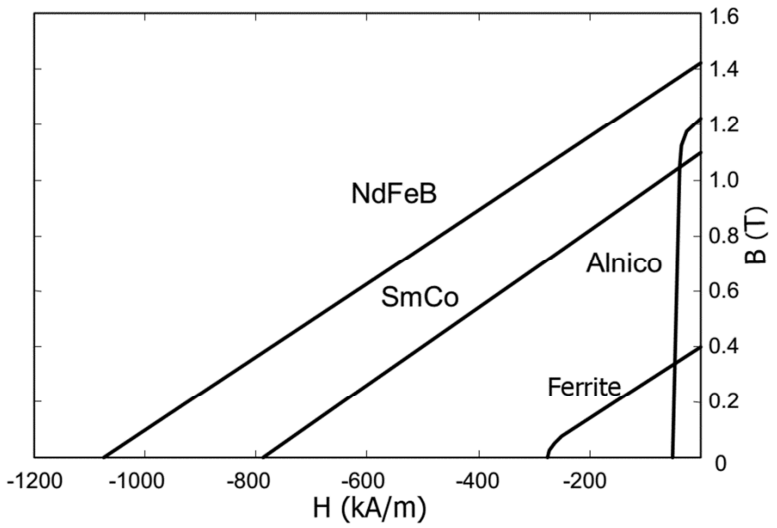

Figure 2-1 Comparison of BH curves among different PM materials.

There are normally two types of electromagnetic torques induced in PMSMs: the PM torque arising from the interactions between the PM field and the armature windings, and the reluctance torque produced by the winding inductance variation with the rotor position due to the rotor saliency. It is obvious that ferrite PM machines would suffer lower PM torque component as a result of much lower PM strength. To compensate the lower PM torque, special attention should be paid to the machine configurations with higher reluctance torque component.

Ferrite PM materials have long been used in the design of PM machines very soon after their commercialization [26–31], and various machine configurations with different PM materials were investigated and compared in [18,32–34]. Based on the existing literature, ferrite machine solutions can be divided into four categories:

- Conventional PM machines, which are of similar structure as the rare-earth machine with larger amount of ferrite PM;
- PM assisted synchronous reluctance machines (PMASynRMs), whose structures originate from synchronous reluctance machines (SynRMs) with PMs in the flux barriers;

- Spoke-type PM machines, using flux focusing techniques to achieve similar airgap flux density and torque density as rare-earth machines;
- Other types, which are not widely studied or not practical for mass production at the moment.

2.2 Conventional PM Machines with Ferrite Materials

Conventional PM machines adopted similar configurations as rare-earth ones by using ferrite instead of rare-earth PM. Due to the low residual flux density of ferrite magnets, larger amount of PM was usually used to increase the flux density. Even so, the power density of ferrite machines is still very low comparing to its rare-earth counterparts. As a result, ferrite machines with conventional structures were mostly used in low-cost and low-power applications such as electric assisted bicycles [35], pumps [36] and fans [37]. According the location of PM poles, they could be further divided into surface-mounted PM (SPM) and Interior PM (IPM) machines.

S. Pal in [38] studied the different performances of SPM machines with exactly the same machine geometry but different PM materials of ferrite, SmCo and NdFeB respectively. The ferrite machine can only achieve 36% torque of SmCo and 31% that of NdFeB, because of the low residual flux density of ferrite. P. Sekerak in [39] optimized ferrite SPM design and obtained a final design with slightly larger size but only 60% torque of rare-earth one. To increase the airgap flux density for SPM ferrite machines, one method was to increase the size of the machine to accommodate larger amount of PMs. But larger size would increase the volume and weight of the machines. A.M. Mihai et al. in [40] and S. Laurit et al. in [41] all considered rare-earth PMs as the best solutions for wind power generator, in terms of overall weight , size, and most importantly cost, as the extra cost would be paid on the larger housing and foundation structure for ferrite machines. But for small power machines, lower energy PMs can be competitive with machines adopting rare-earth PMs, if the machine designs were optimized specially for each PM material [42,43]. Nevertheless, the drawback of much larger volume restricted the usage of ferrite PM generators.

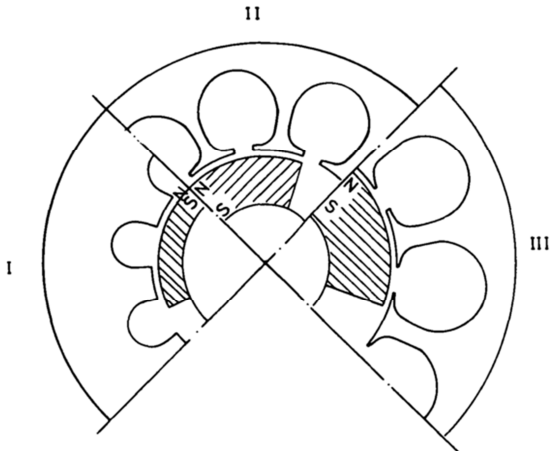

Figure 2-2 Design consideration with more PM material, thinner stator yoke and larger size [30]**.**

In spite of larger amount of ferrite being using in SPM machine, the airgap flux density still couldn't achieve that of rare-earth ones [40]. Thus, the stator yoke thickness can be reduced and larger diameters were necessary in order to place more armature conductors to increase electric load and power output [30], as shown in Figure 2-2. In this case, the copper loss would be increased and over 10% lower efficiency was observed under the same current density. K. Kim et al. in [44] compared rare-earth and ferrite SPM machines with the same frame size, and the ferrite model had over 5 times higher copper loss due to larger amount of copper used. In [45], copper loss of ferrite generator was almost 3 times as that of NdFeB machines with the same outer diameter, and thus ferrite machine suffered 7% lower efficiency. And with 30% larger diameter, the efficiency of ferrite motor was still 1% lower compared with NdFeB motor in [46]. R. Gupta et al. in [37] proposed a ferrite SPM machine with radial- and Halbach-magnetized magnets to increase the flux density and improve the efficiency, but extra cost was brought in due to the Halbach-magnetization.

D. Woo et al. and H. Kim et al. in [47,48] proposed another way to increase the flux density and PM flux linkage by applying the structure of longer rotor than stator, which is called rotor overhang configuration. With this structure, the leakage flux loss would be offset at the end of the lamination cores, and thus the performance of the machine can be improved. With 3mm overhang, up to 6.8% of increase in load torque can be achieved at the expense of more PM

material and larger mass. Moreover, the overhang structure required 3D analysis for accurate predictions in the design period, which would increase the calculation time.

By using anisotropic ferrite bonded cores, the rotor core was no longer necessary and thus removed for low inertia and low manufacturing cost. This design was usually used in brushless direct current (BLDC) machines. The magnetization distribution of anisotropic bonded ferrite is depicted in Figure 2-3. By adopting this polar anisotropic PMs, the fundamental component could be greatly increase and other harmonic components would be suppressed. Results showed that 29% increase could be obtained in the airgap flux density, and together with overhang design, the performance was improved by 39% compared with radial-magnetized ferrite PMs [49–51].

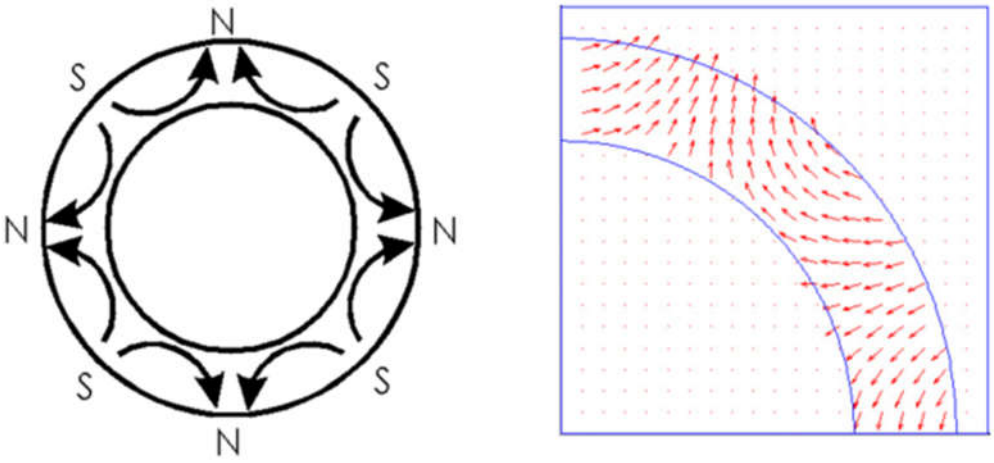

Figure 2-3 Magnetization distribution of anisotropic bonded ferrite [36]**.**

Outer-rotor structure, with a larger airgap diameter, was able to increase the torque, and thus can improve the performance of the machine. I. Petrov and J. Pyrhonen in [52,53] presented outer-rotor low cost ferrite SPM machines of 4.7 kW and 50 kW for automotive applications. Although high efficiency of 93.4% was achieved, the torque density is relatively low. A dual-rotor SPM machine with toroidal windings was proposed by R. Qu and T.A, Lipo in [54] to increase torque density and reduce end-windings. But the flux density in the airgap was still too low to achieved acceptable power density. Also, the uncommon dual rotor structure would increase the cost of manufacturing. Since it is hard to

achieve high flux density in the airgap only with ferrite magnets, hybrid excitation with both ferrite and NdFeB designs were developed in [55,56]. Though the usage of rare-earth could be reduced, it would bring in new issues on assembly without demagnetizing the ferrite PM by strong rare-earth PM.

With PMs buried inside the rotor, the magnetic airgap length could be reduced and higher flux density would be achieved for IPM machines. H. Kim et al. in [57] concentrated on the magnet pole shape optimization to increase airgap flux density and reduce the cogging torque. Y. Im in [58] focused on the rotor rib shape optimization using response surface methodology (RSM) to improve performance of ferrite IPM. However, the improvements are still far from the requirement for high torque density. B.N. Chaudhari et al. in [59,60] presented an IPM design using combined circumferentially and radially magnetized PMs to increase the flux density and rotor saliency, as shown in Figure 2-4. However, since the magnet poles were not sinusoidal distributed in the rotor, there would be high content of harmonics in the airgap flux density, which would affect the overall performance of the machine. Although the power density also could be improved by using more PMs, the amount of PMs was restrained by the available space inside the rotor, and it was almost impossible to accomplish the design goal for high power density owing to the sizing constraints [61]. To deliver similar torque with rare-earth machines, the ferrite designs required 47% higher volume to accommodate enough PM material [62].

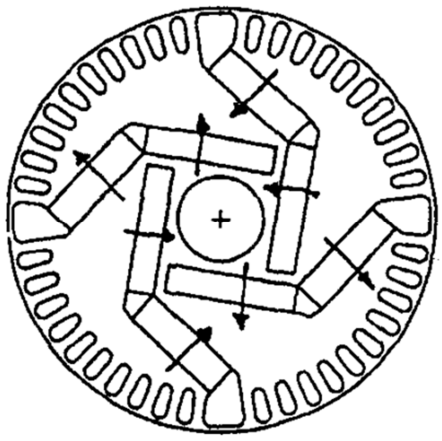

Figure 2-4 IPM with combined circumferentially and radially magnetized PMs [59]**.**

To conclude, due to the low residual flux density of ferrite materials and the large magnetic airgap length, SPM machines are not able to achieve the required torque density and efficiency. Despite that the airgap flux density can be improved by IPM structures, it is unlikely for conventional IPMs fulfil the requirements of high torque density and efficiency simply by increasing the amount of PM as the available space inside the rotor to accommodate PMs is limited.

2.3 PM-Assisted Synchronous Reluctance Machines

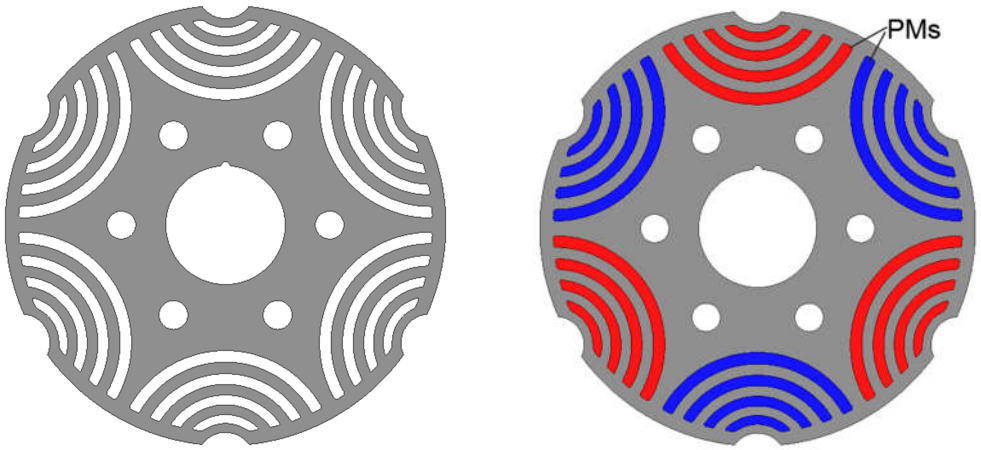

Figure 2-5 Configurations of SynRM and PMASynRM rotor.

PMASynRMs are derived directly from SynRMs, as illustrated in Figure 2-5. By adding proper amount of PM materials into the flux barriers in the SynRM rotor lamination, the torque density, power factor and efficiency of the PMASynRM can be improved, which makes it a potential solution for the ferrite IPM design [63–65].

E. Armando in [66] pointed out that with even a small amount of PM, not only the torque output but also the constant power speed range could be improved greatly compared with SynRM design for washing machines. And with more ferrite PM added to the original SynRM lamination, higher power factor as well as efficiency could be achieved [67,68]. However it is not always the case that more PM results in higher torque. The main component of the torque for PMASynRMs is reluctance torque, and the rotor with too much PM would affect the thickness of barrier ribs and thus rotor saliency. D. Prieto et al. in [69]

investigated the influence of the thickness of inserted PM poles, and suggested more PM material could improve power factor, but also may cause significate decrease in torque output. M. Barcaro and N. Bianchi in [70] optimized the length and thickness of PMs and indicated with similar rotor structure, reduced PM thickness can still attain similar torque capability, but slightly lower power factor.

The shape of the PMs and flux barriers also showed great importance to the PMASynRM design. S. Musuroi et al. in [71] presented a ferrite PMASynRM design with two V-shaped flux barriers, since it has simple flux barriers and rectangular PM poles. K. Hayakawa et al. investigated the influence of flat, V-shaped and circular arc flux barriers, as shown in Figure 2-6 (a)-(c). And results revealed that circular arc structure could substantially improve the maximum torque and power output with three flux barriers [72]. It should be noted that ferrite PM was brittle especially when large thin arc shape was used. Y. Matsumoto et al. in [73] proposed a barrier structure that the third flux barrier was divided into three parts by 0.5mm ribs, so as to reduce the mechanical stress on the PMs. But the ribs provided extra path for the PM flux leakage and the torque output was reduced. When taken massive production in consideration, long arc shape PMs were more expensive to produce and difficult to assemble. Thus, rectangular segmented PMs were proposed in place of arc shaped magnets for easy manufacturing and assembly [74,75], as shown in Figure 2-6(d). Although there was about 4% decrease in the torque output, both the amount of ferrite and manufacturing cost was reduced.

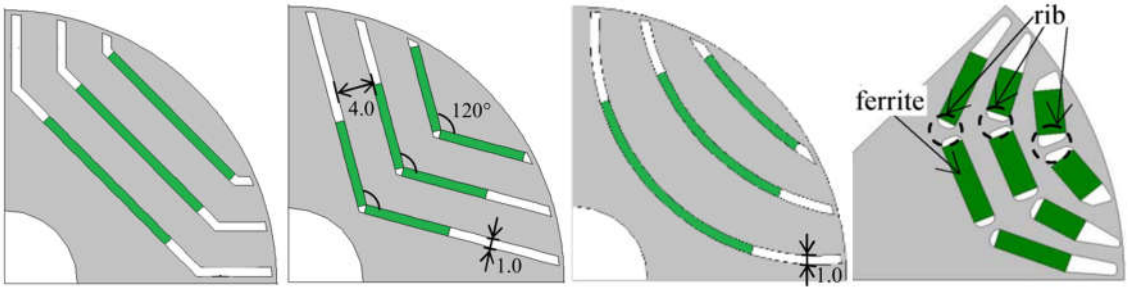

(a) Flat; (b) V-shaped; (c) Circular arc; (d) Segmented;

Figure 2-6 Rotor with different shapes flux barriers and PMs [72,74]**.**

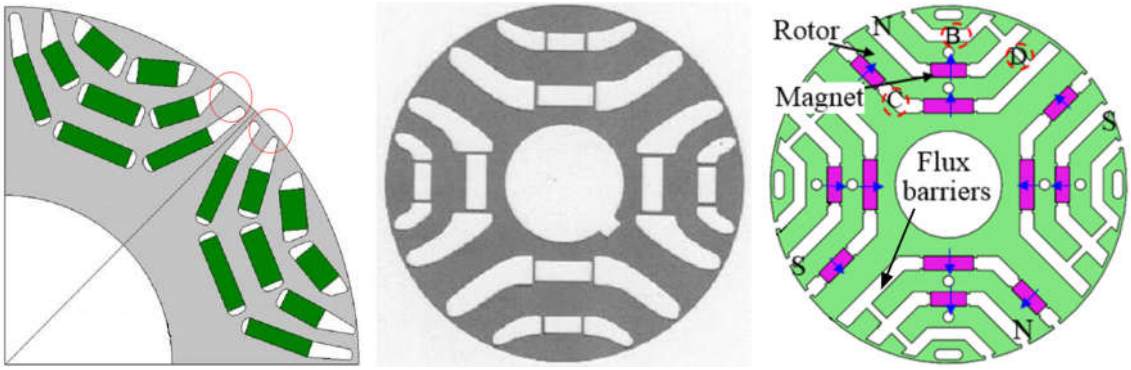

(a) Barrier angle [74]; (b) Barrier pitch [76]; (c) Barriers and PMs [77];

Figure 2-7 Asymmetrical rotor structures for PMASynRM.

PMASynRMs with three flux barriers were the most common configurations for the rotor design, with a compromise between complexity and saliency. However designs with higher number of flux barrier were also adopted in some research works. M. Paradkar et al. in [78] presented a design with 4 flux barriers, and Y. Jeong et al. in [79] proposed a design with 5 flux barriers to gain a higher saliency. But the structures became too complicated. With the thickness of the PMs reduced, designs with more flux barriers made the PMs more fragile against mechanic stress and armature demagnetizing field. Researchers also found the thickness of saturation bridges, pitch and angle of flux barriers could affect the machine performance. Since the saturation bridges provided flux path for PM flux leakage and d-axis flux, both PM torque and reluctance torque could be reduced. H. Cai et al. proposed a design with all the bridges removed and yielded 8% increase of overall torque [80]. However, the lamination rib layers would be completely detached from one another, and the assembly of the rotor was not discussed, which would seriously affect robustness of the rotor especially during high speed operation.

Descending from reluctance machine, PMASynRMs had the drawback of large torque ripple. N. Bianchi optimized the pitch and angle of flux barriers to reduce the torque ripple while keeping the same average torque [76]. H. Cai et al. minimized torque ripple by 35% by adjusting width of flux barrier opening [80]. To further reduce the torque ripple, asymmetric flux barrier structures were proposed. M. Obata et al. presented a rotor structure with different flux barrier

angles for the two neighbouring poles [74], as depicted in Figure 2-7(a). N. Bianchi developed a model with flux barriers of different pitches for the adjacent poles [76], as illustrated in Figure 2-7(b). Furthermore, W. Zhao et al. in [77] proposed a model with both asymmetrical PMs and flux barriers arrangement to make the PM and reluctance torques to reach maximum values at nearly the same current phase angles, so that the overall torque was augmented, as demonstrated in Figure 2-7(c). However, these asymmetrical designs would bring in higher harmonic contents, which would have negative effect on the machine losses and torque ripple.

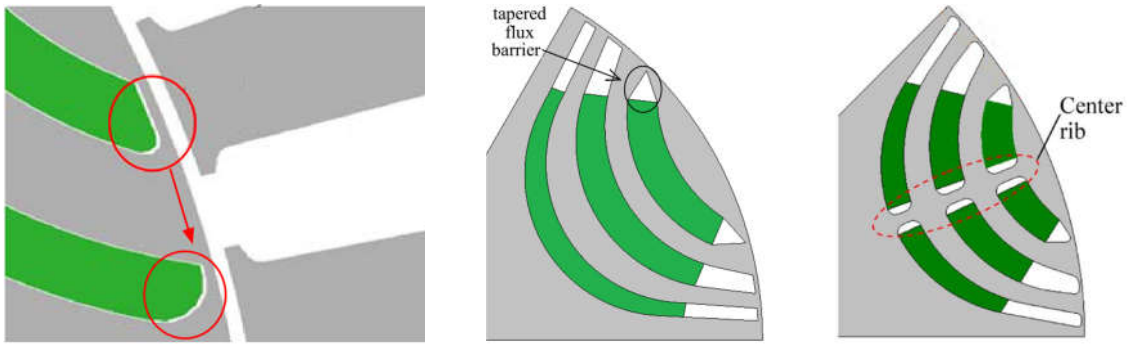

(a) Fillet smoothing; **(b) Tapered flux barrier;** **(c) Center rib;**

Figure 2-8 Rotor design to reduce demagnetization of PMASynRM [81–83].

Ferrite PM has higher temperature stability than rare-earth and can operate at 250 ^{0}C. However, the residual flux density is much lower comparing to rare-earth, which makes ferrite PMs quite fragile if exposed directly to the armature reactive field. Some recent papers have put in evidence that the electric loading must be limited, and the flux barriers must be shaped properly to avoid de-magnetization. T. Tokuda et al. in [84] suggested that the outer layer was more prone to demagnetization than the inner layers as the armature reactive field was stronger. Thus the thickness of difference flux barriers was rearranged, and the outer layer would be thicker to resist demagnetization while the inner layers can be thinner maintaining constant flux path width. By using fillet smoothing the magnet edge and tapered flux barriers as shown in Figure 2-8(a) and (b), noticeable decrease in demagnetization could be achieved [81,82]. With center ribs added as shown in Figure 2-8(c), demagnetization ratio was reduced with

better mechanical stress. The works on demagnetization mentioned above presented some useful methods on the design to avoid demagnetization, but no systematic approach was proposed and theoretical guidance was provided.

To conclude, PMASynRM machines are descendent from SynRM and mainly rely on the reluctance torque component. Due to the inherent limitations of reluctance machines, PMASynRMs have inferior performances in terms of torque ripple, power factor and efficiency. Higher number of flux barriers is able to increase the rotor saliency and thus the power density, but it also complicates the rotor structure.

2.4 Spoke-Type IPM Machines

The spoke-type configuration, also known as flux-squeezing configuration, has long PMs magnetized in the circumferential directions as shown in Figure 2-9. This structure concentrates the fluxes from the PMs to lamination poles, and is able to achieve approximately the same air-gap flux density as the rare-earth machine. Thus the spoke-type structure is also considered as one of the most potential solutions for high performance ferrite PM machines.

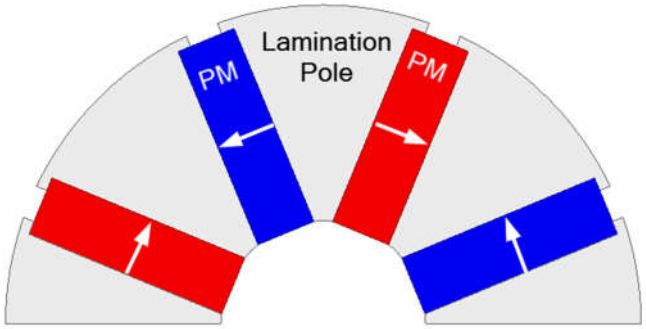

Figure 2-9 Rotor configuration of a typical spoke-type machine.

A. Isfanuti et al. in [85] compared surface NdFeB and spoke-type ferrite machines within the power range of 100-2000W, and results showed that same torque can be achieved with low-cost ferrite magnets, but higher mass and torque ripple. Eriksson and Bernhoff in [86] evaluated the spoke-type wind generators of the same power range with ferrite and NdFeB PMs, and revealed that ferrite generators would be 50% heavier but with only 30% of PM cost. E.

D.G. Dorrell in [87] presented a spoke-type design benchmarked with Prius rare-earth IPM, and the amount of ferrite PM was almost maximized while only 2/3 torque was obtained even though larger machine diameter was adopted. Design, optimization and assembly of ferrite spoke-type machines were presented and promising results were verified by the prototype machines in [88,89]. Although the torque density was much lower than rare-earth machines, they were still considered to be viable alternative solution in the sense of cost. To increase the torque density, an outer-rotor spoke-type design was proposed in [90]. In order to achieve the same performance with rare-earth design, much larger amount of PM was used with 26 % larger outer diameter. To compensate the low residual flux of ferrite and reduce the consumption of rare-earth, hybrid PM arrangements with both ferrite and rare-earth PMs were presented in [89]. Though the PM amount was reduced, rare-earth PM was still necessary for the design. Another issue which should be paid special attention to was the cross-demagnetization between strong rare-earth and weak ferrite PMs.

To achieve similar airgap flux density as rare-earth machines, various designs are proposed to use more PM to enhance the PM excited field. K. Kim et al. in [91] proposed a ferrite spoke-type design with large axial overhang and the air-gap flux density was increased by 33%. I.C. Chabu et al. obtained a 55% increase in the airgap flux density by applying 68% longer rotor stacking than the stator [92]. W. Kakihara et al. in [93] also applied 6mm rotor overhang and 6mm PM overhang, the torque output was improved and PM demagnetization rate was reduced. Large rotor overhang would certainly increase the amount of PM and rotor lamination, but the overhang PMs were not actually fully utilised since considerable part of the flux didn't go through the airgap directly but became flux leakage and wasted. A more effective way to increase flux density was presented in [94,95] by adding axially magnetized PMs at each side of the rotor to enhance the flux focusing effect, as illustrated in Figure 2-10(a). However, the amount of ferrite used usually doubled or even tripled to add axially magnetized PM poles. Moreover, due to the existence of axial flux, soft magnetic composite (SMC) cores were necessary because of the 3-dimentional (3D) flux distribution, which would increase the material cost.

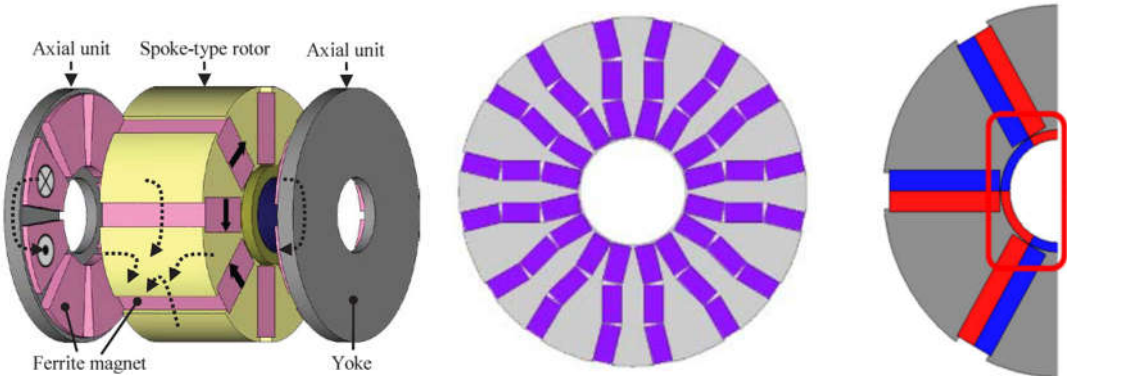

(a) With axial PMs [94]; (b) Segmented poles [96]; (c) Spoke plus ring [97];

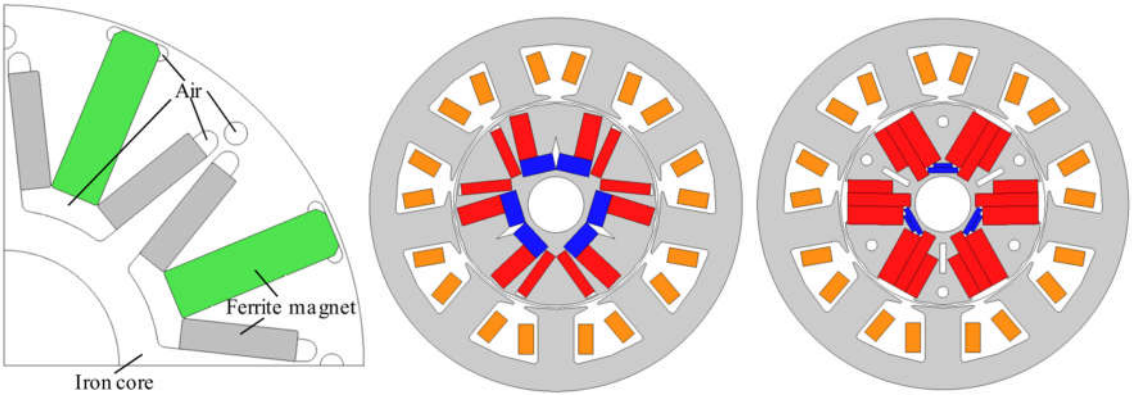

(d) W-shaped PMs [98]; (e) Wing-type [99]; (f) Wing-shaped [100];

Figure 2-10 Spoke-type IPMs of more PM designs.

For more cost-effective way of increase PM excited field, more ferrite was inserted by making full use of the space inside the rotor. I. Seo et al. presented a segmented spoke-type PM structure with certain angles between different PM segments [96], which allowed larger amount of PM inserted inside the rotor, as demonstrated in Figure 2-10(b). What's more, by adjusting the angles of the segmented PMs, cogging torque could be reduced. However, this asymmetrical PM distribution would bring in unwanted harmonics. H. Kim et al. in [97,101] presented a ring-type assistant pole in the inner rotor part to intensify PM flux and the overall torque was increased 3.8%. Sub-magnets were added in between the spoke-type PMs in the inner part of the rotor to increase PM flux, as depicted in Figure 2-10(c). A W-shaped spoke-type pole arrangement was presented in [98], and the magnet volume and surface were maximized by folding the PM poles as shown Figure 2-10(d).

To further increase the amount of PM, wing-type and wing-shaped spoke-type rotor configurations were developed in [99,100] and more and more space inside the rotor were used to accommodate PMs, as demonstrated in Figure 2-10 (e) and (f). Compared to original spoke-type structure, the airgap flux density could be enhanced by up to 25%. [99,100] even reported that slightly higher airgap flux density and torque output were achieved compared to the rare-earth IPM counterparts. However, the designs utilised most of the space in the rotor to place PMs, and less space was left for the steel laminations. Thus, issues would be raised concerning about the rotor assembly and mechanical robustness. Most of the attention was paid on PM excited field and PM torque. As another important part for the PMSM torque output, reluctance torque was not considered at all during the designs. In view of the poor saliency of the rotor configuration, low reluctance torque could be presumed. Although the wing-shaped spoke-type machine maximized the PM excitation and thus the PM torque component for ferrite machine, these structures were not very practical for industrial mass production in the sense of huge amount of ferrite required and difficulty for the rotor manufacturing.

Other than PM torque, reluctance torque is also a very important component in the total torque production for IPM machines. It would be more cost-effective to improve the overall torque production by increasing rotor saliency rather than adding more PMs. W. Kakihara et al. in [93] proposed a 50kW ferrite machine with triangular cut-outs on the rotor outer surface and triangular cavities inside the rotor to increase the salient pole ratio, and 7.7% maximum torque output was achieved due to the increase of reluctance torque, as demonstrated in Figure 2-11(a). Auxiliary radial magnetized poles were applied in between two spoke-type main poles to increase flux density as well as reluctance torque in [94,102] as depicted in Figure 2-11(b). A improved spoke-type design was proposed by splitting the each of the conventional spoke-type pole into two parts [103,104]. In such way, a flux path for q-axis reactive field emerged in between the split poles through rotor yoke, and q-axis inductance and saliency were increased. Therefore, the overall torque could benefit from the increased reluctance torque despite that the PM flux stayed more or less the same, as

shown in Figure 2-11 (c). However, rotor inner yoke took up relatively large area of rotor where longer spoke-type PMs could be place to increase the PM flux field, and the overall torque was only marginally improved. It is a very good idea to improve reluctance torque since it is too difficult for ferrite machine to achieve the same PM torque as rare-earth one. More effort could be done to increase the rotor saliency without losing too much PM excitation.

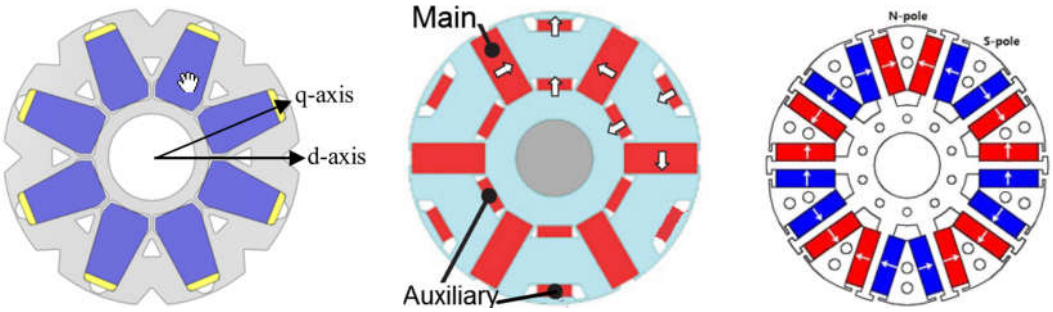

(a) Cut-outs and cavities [93]; (b) auxiliary poles [94]; (c) Divided main poles [104] ;

Figure 2-11 Spoke-type IPM designs to increase saliency.

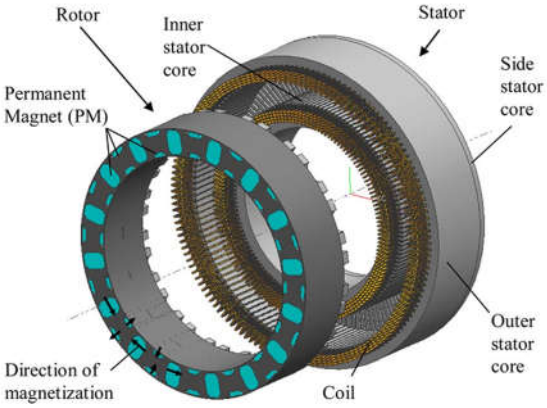

Figure 2-12 Double-stator spoke-type machine with 3D trench airgap [102]**.**

To fully utilise the machine space and gain higher torque density, a model with 3D trench airgap configuration was proposed in [102] to increase airgap area for torque generation. The proposed machine consisted of double stators and a spoke-type rotor with side rotor poles sandwiched in between, as depicted in Figure 2-12. Comparable torque density with rare-earth machines could be achieved. However, double-stator structures required larger amount of copper

to increase the power density, which resulted in relatively low efficiency level (similar to IMs). Moreover, the complicated structure would increase the manufacturing cost and would not be suitable for massive production at the moment.

Compared with PMASynRM, spoke-type suffers higher risks of irreversible demagnetization [33], and the investigation of irreversible demagnetization is critical for the electromagnetic robustness of ferrite machines. Demagnetization occurred in many of the papers reviewed above [25,94,98,105], but no solution was presented. Wider and thicker PM poles were used to enhance PM MMF [89], but this would affected the whole electromagnetic design of the machine, especially for those harnessing reluctance torque. B. Lee et al. in [106] proposed flux barriers in between the adjacent spoke-type poles to reduce the demagnetizing armature field, but PM flux would also be reduced. It was indicated in [103] that divided main pole structure had lower risk of demagnetization than conventional one. Since the part of PMs near the airgap was facing strong armature field, the PM edges closer to the stator suffered higher risk of local demagnetization. Thus, chamfered PM edges were applied in [102], and deeper burying of PMs were presented in [87,93,107]. Although PM flux field was weakened, local demagnetization on the PM edges could be greatly reduced. After all, demagnetization was discussed during the design for certain cases, but no systematic research was published for ferrite PM machines yet.

Since the optimization of the design is a very complicated work considering the flux distribution, torque generation, efficiency and so on, various multi-objective optimization algorithms were used to accomplish optimal design. K. Hwang et al. applied steepest decent method (SDM) to minimize the cogging torque and RSM to reduce harmonics in airgap flux distribution and cogging torque in [108] and [109] respectively. P. Zhang et al. in [110] used a combined design of experiments (DOE) and differential evolution algorithms (DEA) to optimize three key objective of loss, cost and torque ripple. Although good results were achieved, the optimizations still required finite element analysis (FEA) to

evaluate each design. Also, no clear relation between the performance and sizing parameters were derived, and provided weak guidance on the design. For more useful theoretical guidance during the preliminary design period, analytical methods were required for fast calculation. Approximate open-circuit flux density was obtained in [92,111,112] for conventional spoke-type configurations. PM flux distribution equations were derived for spoke-type machines with auxiliary ring poles [113,114], wing-type [99], and wing-shaped [100]. However, the overall torque profiles, especially the reluctance torque component, could not be expressed only by PM flux field, and thus the analytical were not complete. PM flux together with dq-axis inductance were derived for the spoke-type configuration in [115,116], showing the influence of different design parameters on the performances. But only the fundamental flux was considered, which could bring in relatively larger error.

To conclude, spoke-type ferrite PM machines have the potential of achieving high torque density, power factor and efficiency with flux focusing structures. But the reluctance torque is relatively low and further improvement needs to be explored. What's more, the rotor structures of spoke-type motors needs to be design very carefully due to the higher risks of irreversible demagnetizations.

2.5 Other Types of Ferrite Machines

There are many other works proposing ferrite PM machines for various applications with different motor configuration, such as flux switching, axial flux machines, claw-pole, and vernier-type.

2.5.1 Flux Switching PM machines

Flux switching permanent magnet (FSPM) machines have both armature windings and magnet located in the stator, and only simple laminations are necessary for the salient rotors. A ferrite FSPM design was presented in [117], and ferrite and rare-earth FSPM machines were compared in [118]. The ferrite FSPM required much larger amount of PM and higher electric loading to achieved the same torque density compared to the rare-earth design. Therefore, loss would be increased, resulting in much lower efficiency for ferrite

FSPM machines. Since the stator needed to accommodate both windings and PMs, the space was quite limited for wider PMs. M. Al-Ani et al. in [119] proposed a stator design with radial magnetized PMs situated around the stator yoke and a lamination ring frame surrounding the whole machine. In this way, the PM flux field and torque can be increase for the FSPM, but large machine diameter was required for the radially-magnetized PMs and extra ring frame. D. Kim et al. proposed a double-stator FSPM configuration in [120], and torque density could be greatly improved. But more copper was needed and the structure was significantly complicated with the double-stator configuration, which would increase the cost of manufacturing. Ferrite FSPM machines with field excitations were presented in [121–124], and higher torque density and better flux weakening ability were achieved. However, extra direct current (DC) field excitation windings led to higher copper loss in field winding, much more complicated structure and control system. In all, the FSPM was a highly magnet-consuming structure because of large flux leakage. The low-energy ferrite PM apparently is not very suitable for the FSPM configurations. Due to the limited space in the stator for PMs, the highly PM torque dependent machine would not be able to achieve high torque density. What's more, it also should be noted that the risk of demagnetization for ferrite FSPMs are very high because the low magnetic energy PM would face directly to reactive field from the armature installed together in stators [32].

2.5.2 Axial Flux Machines

Axial flux permanent magnet (AFPM) machines are expect to have high torque density and compact structure, and are considered as a candidate for high performance applications. Dual-stator AFPM generators with spoke-type PMs in the rotor were proposed in [125,126]. But the assembly of the spoke-type rotor was difficult since the rotor was divided into a number of modular parts by PM poles. Double-rotor inner coreless stator structure was presented in [127] for micro-wind turbines. But slotless configurations had large magnetic airgap length, and were inherently not suitable for low energy ferrite materials. Z. Wang et al. in [128] presented a AFPM ferrite machine with amorphous metal

cores. Each of the stator teeth was a modular part piled up using amorphous magnetic materials (AMMs) cut sheets to reduce iron loss. Since the sheets in one stator tooth were of different width, it would be difficult for massive production.

K. Chiba and K. Sone et al. in [129,130] proposed double-stator single-rotor ferrite AFPM machine, and the PM shape were optimized to reduce torque ripple. K. Sone in [131,132] indicated that the rotor core in the double-stator single-rotor AFPM machines would aggravate demagnetization in PMs. Thus, the rotor back iron was removed and thicker PMs were introduced to suppress irreversible demagnetization. In order to increase the reluctance torque of this machine design, S. Chino et al. in [131] proposed a SMC cores assembled in between adjacent PM poles to increase the rotor salient ratio. In all, SMC cores are usually necessary due to the existence of 3D flux path for the construction of AFPM machine cores. It surely would increase the material cost comparing to steel laminations. Moreover, the manufacturing and assembly of axial machines flux are also more complicated than their radial counterparts.

2.5.3 Claw Pole Machines

Claw pole ferrite PM machines with field coils were investigated in [133,134]. The hybrid-excited configuration compensated the lower flux density of ferrite compared with rare-earth. High torque output was achieved but the efficiency of 85% was relatively low due to high copper loss. In [135,136] segmented rotors with claw poles were proposed for easy power scaling up with existing designs.

2.5.4 Vernier Machines

Permanent magnet Vernier machines (PMVMs) can deliver large torque at low speed and multipolarize in fewer slots than conventionally designed machines. Therefore, they are considered for in-wheel machines for EV applications. R. Hosoya and K. Sato et al. in [137] and [138] presented a ferrite PMVM to accomplish high torque density design goals. A V-shaped PM outer-rotor configuration was applied and 58% of higher flux density was achieved in the

airgap. Due to the intrinsic property of Vernier machines, they are mostly used in low speed large torque applications.

2.6 Comparisons

Ferrite PMs were invented in the 1950s, and has been commonly used in small-power low-cost applications where volume and mass were not concerned, such as DC motor for electric toys and fans [139]. To increase the power density, there were three commonly used solutions: more PM material, more copper and larger size. However, due to the low residual flux density of ferrite PM, conventional designs are very unlikely to realize the required efficiency and torque density for the low-cost high-performance requirements in various industrial applications.

According to the existing literature, PMASynRM and spoke-type IPMs are most attractive solutions with relatively mature technology to achieve the aim of rare-earth-free high efficient machine designs. PMASynRM configurations descend from SynRMs with PM inserted inside the flux barriers to increase the torque production and power factor. Since the PMASynRM originates from reluctance machines, it has high saliency ratio and depends largely on reluctance torque. Also, it can operate at wider speed range with better flux weakening ability. On the other hand, spoke-type IPMs can potentially achieve approximately similar open-circuit flux distribution with rare-earth machines using flux focusing structures. As a result, high PM torque and power factor can be obtained. Additional, reluctance torque can also be harnessed for high torque density. And attempts have been made to increase rotor saliency such as introducing auxiliary poles and splitting main poles to further increase in torque density. Since the length of PM poles to pole pitch ratio is very critical to the flux focusing effect, relative high pole number structure is more preferred for spoke-type machines. Compared with PMASynRMs, spoke-type configurations show poorer flux weakening capability and thus smaller constant power speed range (CPSR), but in terms of overall efficiency, power factor and torque density, PMASynRMs are inferior to spoke-type IPM machines.

Other types of machines provide some insight for possible future developments for ferrite PM machines, and are not practical for wide applications in industry at the moment. FSPMs rely highly on strong PM excitation to obtain high torque density and are not quite suitable with low energy ferrite PM. Surface-mounted AFPMs won't be able to achieve relatively high PM field and hence sufficient torque density, while the technology of interior AFPMs are still immature concerning the manufacture and assembly for massive production. AFPM and claw pole machines have 3D flux distributions, and usually need to use SMC materials, which will increase the material cost. As for Vernier machines, they are mostly restrained in low speed high torque applications.

Considering that most of the low efficient IMs used in domestic and industrial applications are medium speed machines, the spoke-type IPM machine with advantages of high torque density, power factor and efficiency show higher potential to fulfil the high-performance requirements. To take full advantages of the reluctance torque of IPM machines, multiple layer concept of PMASynRM can be introduced into the spoke-type design to further increase the torque density. Due to the relatively weak magnetization of ferrite materials, demagnetization should be paid special attention to so that the durability can be insured without degradation.

2.7 Conclusion

The demand for high efficient electric machine is ever increasing as both energy consumption and CO_2 emission can be greatly reduced. The widely installed IMs are not able to fulfil the efficiency requirements, and PMSMs with low-cost ferrite magnets are considered to be the most attractive solution. In this chapter, extensive review on the current development of ferrite PM machines were made searching for low-cost high-efficiency candidates, and the focus was concentrated on torque density and efficiency. The reviewed papers were divided into four categories, namely conventional SPM/IPM machines, PMASynRMs, spoke-type machines and machines with other special structures or topologies. According the existing literature, ferrite spoke-type and PMASynRM machines are the most promising candidates to replace currently

widely used low efficient IMs. PMASynRMs rely mainly on reluctance torque and thus have better high speed performances. Spoke-type machines adapt the flux-squeeze structure for flux concentration to compensate the low residual flux density of ferrite material, and exhibit higher torque density, power factor and efficiency. Considering the operating conditions and requirements of various industrial applications, the spoke-type IPM shows better overall performance. Meanwhile the multi-flux-barrier concept of PMASynRMs can be introduced to spoke-type machine design to increase the salient pole ratio for higher reluctance torque. There is still potential to improve the saliency of the spoke-type configuration with multi-layer structure.

3 ANALYTICAL MODELS OF MULTI-LAYER SPOKE-TYPE MACHINES

3.1 Introduction

Although commercial finite element analysis (FEA) software is widely used nowadays, it is still time-consuming comparing to analytical methods. There is always a need for simple and effective analytical models with good accuracy for preliminary designs. Moreover, by developing analytical models, the influence of design parameters on the performance can be clearly presented and better understanding between certain parameters and electromagnetic behaviour of the machine can be obtained. A general way of developing analytical methods is based on Maxwell's equations by solving Laplace's or Poisson's equations [99,140,141]. Since IPM machines have their PM poles buried inside the rotor, the boundary conditions would be too complicated to solve the equations, especially for the armature reactive field. The open-circuit flux distribution and back EMF are derived by Laplace's equation in [99], but the armature inductance is not included. Since the inductance plays an important role in IPM machines, PM excited field and back EMF are not enough to determine the performance. Hence, this method is more popular with surface-mounted or surface-inset PM machines whose structures are much simpler [140–142]. Meanwhile, the equivalent magnetic circuit models were also widely used because of simplicity and fair accuracy [143]. The lumped parameter models based on magnetic circuit can handle with the saturation and nonlinear B-H curve by using FEA coefficients [144] or iterative calculations [145] for higher accuracy. However, FEA models are still necessary to extract saturation coefficients, which vary due to different saturation level under various load conditions. The saturation coefficients also could be different when some key design parameters change. Thus, considerable amount of simulations are still necessary from FEA software. On the other hand, significant simplification can be made by neglecting saturation, and clear relational understanding could be achieved by the analytical model. Although error could be caused by making the assumptions, the analytical model should be fairly acceptable to provide

theoretical guidance for preliminary designs and optimizations. Then further modifications can be carried out based on the preliminary designs and significant amount of time and effort could be saved.

In this chapter, analytical models based on the d-q frame are developed for spoke-type multi-layer machine configurations. In addition to fundamental components, higher order components are also considered for more accuracy prediction of the machine performances.

3.2 Development of Analytical Models

3.2.1 General Assumptions

The aim of an analytical method is to develop an effective yet simple way for preliminary design. As a result, some assumptions and simplifications have been made during the derivation of analytical models.

Since the relative permeability of steel lamination is thousands of times higher than air, the magnetomotive force (MMF) drop in the lamination is negligible compared with the air regions. Thus, the steel is assumed to have infinite permeability. Under this circumstance, all flux lines go radially in the airgap and purely tangential to the edge of lamination cores.

As the stator slot is usually very small, the stator is assumed to be smooth with Carter's coefficient to present the equivalent airgap length to account for the influence of stator slot openings. According to [116], Carter's coefficient k_c for the stator slots is obtained by

$$k_c = \frac{\tau_s}{\tau_s + (b_0^{\,2} / (b_0 + 5g))} \tag{3-1}$$

$$\tau_s = \frac{2\pi R_{si}}{N_t} \tag{3-2}$$

where τ_s is the stator tooth pitch, b_0 is the stator slot opening, g is the airgap length, N_t is the number of teeth and R_{si} is the stator inner radius. Then equivalent airgap length can be obtained by

$$g_c = k_c \cdot g \tag{3-3}$$

One the other hand, the rotor PM slot opening is usually much larger comparing to that of the stator slots, and the flux distribution would be severely distorted. For more accurate solutions, the rotor slotting effect should be taken into consideration. According to [146], the flux lines goes through the airgap radially and reaches the slot edge tangentially in the rotor PM slot, as demonstrated in Figure 3-1(a). The flux lines will be arcs whose centres locate at the crossover point of airgap edge and slot edge. Thus the flux line distance within the slot area at x becomes (g_c+$\pi x/2$). Consequently, the permeance along the airgap at different position can be displayed in Figure 3-1(b). According to equivalent magnetic circuit theory, if the excitation is kept constant, the flux density is proportional to permeance. Therefore, the flux density decreases significantly in the PM slot area of the airgap, and can even be negligible if simpler models are preferred with lower accuracy requirements.

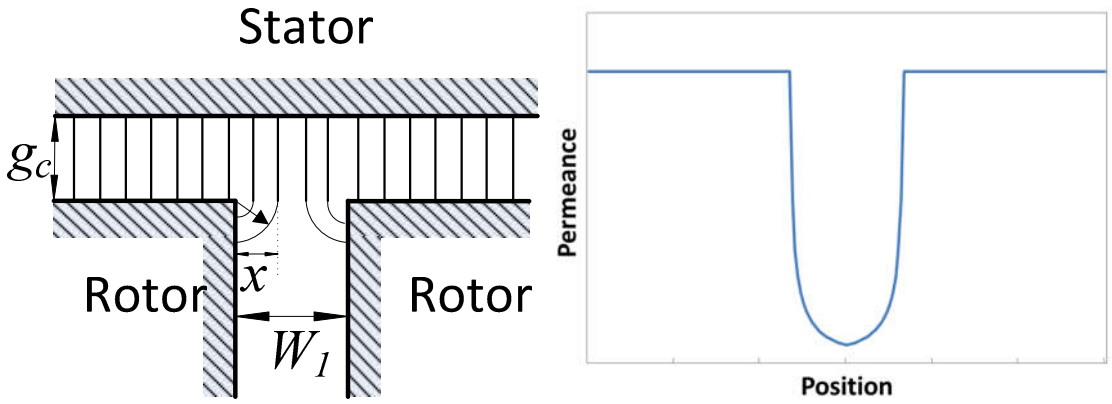

(a) Flux lines; (b) Permeance distribution;

Figure 3-1 Flux lines and the permeance distribution in the airgap.

The stator MMF is generated by the current in the armature windings. To calculate the armature reaction, armature current and windings distributions are the two essentials. The armature current is considered as purely sinusoidal with only the fundamental component, as it is the ultimate aim of control. Assuming that the initial phase angle is zero for winding a, the armature current in a balanced three phase system can be written as

$$\begin{cases} i_a(t) = I_m \cos(\omega t) \\ i_b(t) = I_m \cos(\omega t - 2\pi/3) \\ i_c(t) = I_m \cos(\omega t + 2\pi/3) \end{cases} \quad \textbf{(3-4)}$$

where I_m is magnitude of the armature current, ω is the electric angular velocity.

According to [147], the winding function is defined to describe any actual winding configurations. As the three phase windings are evenly distributed with a displacement of $2\pi/3$ radians among one another, the winding function for three phase windings can be expressed in Fourier series:

$$\begin{cases} N_{fa}(\Theta) = \sum_{\upsilon} \frac{2}{\pi\upsilon} N_a k_{w\upsilon} \cos\upsilon(\Theta) \\ N_{fb}(\Theta) = \sum_{\upsilon} \frac{2}{\pi\upsilon} N_a k_{w\upsilon} \cos\upsilon\left(\Theta - \frac{2}{3}\pi\right) \\ N_{fc}(\Theta) = \sum_{\upsilon} \frac{2}{\pi\upsilon} N_a k_{w\upsilon} \cos\upsilon\left(\Theta + \frac{2}{3}\pi\right) \end{cases} \quad \textbf{(3-5)}$$

where Θ is the mechanical position of the stator, N_a is the number of turns in series per phase, $k_{w\upsilon}$ is winding factor for the υth MMF space harmonic component, and υ=1, 2, 3….

And the synthetic MMF produced by the armature windings is expressed by

$$\begin{aligned} F_m &= N_{fa}(\Theta) i_a(t) + N_{fb}(\Theta) i_b(t) + N_{fc}(\Theta) i_c(t) \\ &= \sum_{\upsilon \neq mk} \frac{m}{\pi\upsilon} N_a I_m k_{w\upsilon} \cos(\upsilon\Theta \mp \omega t) \end{aligned} \quad \textbf{(3-6)}$$

where m is the number of phases, and k=1, 2, 3, …

Generally, the synchronous component is considered as the fundamental, and electric position is more convenient for the analysis of electric machine. In a machine with p poles, there are p/2 electric cycles. Thus, the spatial harmonic order v defined in a multi-pole machine and the relation between the mechanical position and electric position are described by

$$\begin{cases} \nu = 2\upsilon / p \\ \Theta = 2\theta / p \end{cases} \tag{3-7}$$

As the triplen of spatial harmonics synthesized by armature windings are equal to zero in the three phase machines, Equation (3-6) can be written as

$$F_m = \sum_{v=\frac{6k-4}{p}} \frac{2m}{\pi v p} N_a I_m k_{wv} \cos\left(v\theta - \omega t\right) + \sum_{v=\frac{6k-2}{p}} \frac{2m}{\pi v p} N_a I_m k_{wv} \cos\left(v\theta + \omega t\right) \tag{3-8}$$

To verify the analytical method, FEA models are necessary to evaluate the accuracy of the developed models. Hence, examples are chosen for the convenience of building FEA models. The general sizing parameters are given in Table 3-1.

Table 3-1 Common dimensional properties and specifications

Parameters	Value	Unit
Stator Outer Diameter (D_{so})	160	mm
Rotor Outer Diameter (D_{ro})	94.5	mm
Airgap Length (g)	0.25	mm
Stack Length (l_{ef})	90	mm
Base Rotating Speed	1500	rpm
Number of Poles (p)	8	
Number of Slots (q)	48	
PM Material	Y40	

3.2.2 One-Layer Configuration

The typical structure of a conventional spoke-type machine is demonstrated in Figure 3-2(a), and the simplified analytical model and its dimensional definitions are illustrated in Figure 3-2(b). For the one-layer configuration, R_{ro} is the outer diameter of the rotor, g_c is the length of the airgap, W_1 and L_1 is width and length of the PM poles, W_{s1} and L_{s1} is the width and depth of the PM slot opening, and β_1 is the mechanical radians of half of the PM slot opening, which is calculated by:

$$\beta_1 = \arcsin\frac{W_1}{2R_{ro}} \tag{3-9}$$

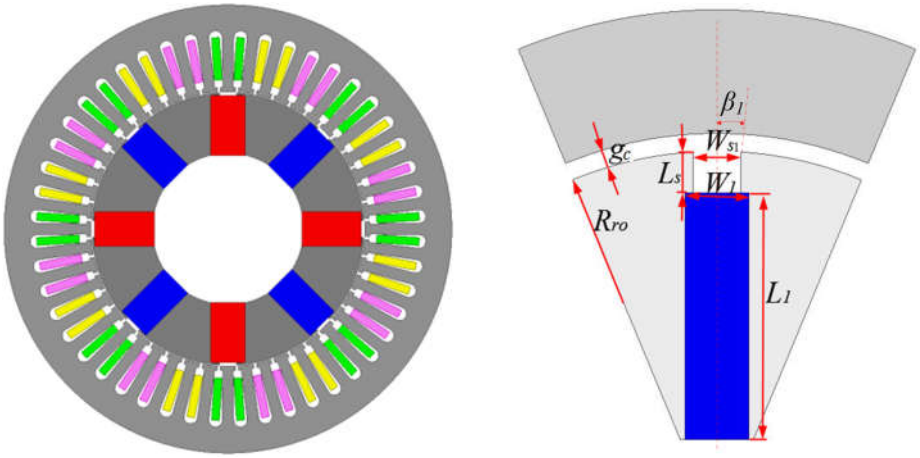

(a) Machine model (b) Dimensional parameters

Figure 3-2 Model and the dimensional parameters of the one-layer machine.

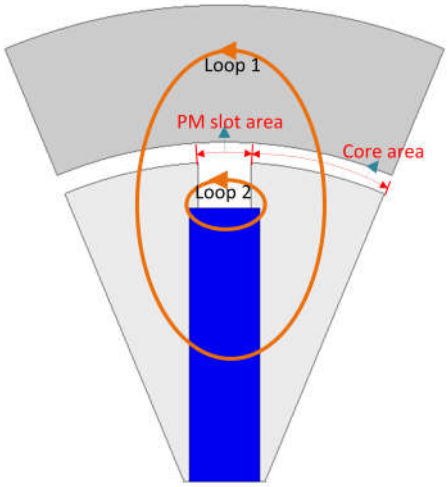

Figure 3-3 Flux path excited by PM in a one-layer machine.

3.2.2.1 Open-circuit flux and airgap flux distribution

To reduce model complexity and calculation, only minimum solution area is necessary for the whole model based on the periodic and symmetric conditions in electric machines. A model with p poles or p/2 pole pairs has p/2 identical electromagnetic periods in the circumferential direction. Hence, only 1/p of the model is able to represent the whole solution area. Moreover, the flux distribution in one electrical period is symmetric between the north (positive) and south (negative) half-cycles and the minimum solution area can be further reduced to half accordingly. In this case, the examples of 8-pole machines are

used for verification, and thus only 1/8 of the whole machine is sufficient for modeling to save time and effort.

The flux loops of open-circuit flux in a one-layer structure are demonstrated in Figure 3-3, and the open-circuit PM flux can be divided into two parts. A major part of the flux generates flux linkage in the armature windings by going through the airgap to the stator from the north pole and returning to south pole crossing over the airgap again, designated as Loop 1. The other part goes through the PM slot instead of the airgap. Since it does not participate in the energy conversion, it is called rotor slot flux leakage. Due to the huge differences in flux distributions, the airgap can be divided into two areas in the circumferential direction, namely core and PM slot areas. According to Ampere's law, the followings are obtained:

$$\begin{cases} H_m \cdot W_1 + 2 \cdot H_g \cdot g_c = 0 \\ H_m \cdot W_1 + H_s \cdot W_{s1} = 0 \end{cases} \tag{3-10}$$

And based on the flux conversion law, flux equations are given by

$$\begin{cases} \phi_m = \phi_g + \phi_s \\ \phi_m = B_m \cdot L_1 \cdot l_{ef} \\ \phi_s = B_s \cdot L_{s1} \cdot l_{ef} \\ \phi_g = l_{ef} \cdot \dfrac{2}{p} \int_0^{\frac{\pi}{2}} B_g(\theta) R_{ro} d\theta = \left(\dfrac{\pi}{p} - \beta_1 \right) B_{g1} R_{ro} l_{ef} \end{cases} \tag{3-11}$$

According to different material magnetic properties, the relations between magnetic flux density and magnetic field intensity are expressed as

$$\begin{cases} B_g = \mu_0 H_g \\ B_s = \mu_0 H_s \\ B_m = B_r + \mu_0 \mu_m H_m \end{cases} \tag{3-12}$$

where H_m, H_g and H_s are the flux intensity of the PM, the airgap and the PM slot respectively, l_{ef} is the effective stacking length, B_m, B_g and B_s are the flux density of the PM, the airgap and the PM slot respectively, μ_0 is the vacuum permeability, and μ_m is relative permeability of the PM material. As the

permeance drops dramatically in the PM slot area, the reluctance in the PM slot area can be assumed to be infinite to simplify the model. Then there is no flux passing through the airgap within the PM slot area, and the flux density in the core of the airgap is calculated by:

$$B_g = \frac{L_1 \cdot B_r}{\frac{2g_c}{W_{s1}} \cdot L_{s1} + R_{ro} \cdot \left(\frac{\pi}{p} - \beta_1\right) + \mu_m \frac{2g_c}{W_1} L_1} \tag{3-13}$$

To calculate the PM flux linkage in the armature winding, Fourier transform is used to decompose the flux distribution waveform to gain the content of different harmonic components. Due to the special nature of magnetic field in electric machines, the flux distribution waveform can be divided into infinite sum of sines or cosines of different order components. The magnitude for each order can be calculated by

$$B_{fgv} = \frac{1}{\pi}\int_0^{2\pi} B_{fg}(\theta)\cos v\theta d\theta = \frac{4B_r}{\pi v} \frac{\sin(v\frac{\pi - p\beta_1}{2})}{\frac{2g_c}{W_{s1}} \cdot \frac{L_{s1}}{L_1} + \frac{R_{ro}}{L_1} \cdot \left(\frac{\pi}{p} - \beta_1\right) + \mu_m \frac{2g_c}{W_1}} \tag{3-14}$$

Although the flux density in the PM slot area is much smaller than that of core area, there is still flux going through this area. The flux in the PM slot area may be negligible for the fundamental, but it may not be ignored when compared with higher order harmonics. To improve the accuracy of the analytical model, this part of flux should be counted into the main flux. Based on the assumption demonstrated in Figure 3-1, the total airgap flux in Equation (3-11) should be written as

$$\begin{aligned} \phi_g &= \left(\frac{\pi}{p} - \beta_1\right) B_g R_{ro} l_{ef} + \frac{2l_{ef}}{p} B_g R_{ro} \int_{\frac{\pi - p\beta_1}{2}}^{\frac{\pi}{2}} \frac{g_c}{g_c + \frac{\pi}{2} \cdot R_{ro} \cdot (\frac{2\theta}{p} - \frac{\pi}{p} + \beta_1)} d\theta \\ &= \left[\left(\frac{\pi}{p} - \beta_1\right) + \frac{2g_c}{\pi R_{ro}} \ln\left(1 + \frac{\pi}{2} \cdot \frac{R_{ro}}{g_c} \beta_1\right)\right] B_g R_{ro} l_{ef} \end{aligned} \tag{3-15}$$

Then the flux density in the airgap can be derived by

$$B_g = \frac{L_1 \cdot B_r}{\frac{2g_c}{W_{s1}} \cdot L_{s1} + R_{ro} \cdot \left(\frac{\pi}{p} - \beta_1\right) + \mu_m \frac{2g_c}{W_1} L_1 + \frac{2g_c}{\pi} \cdot \ln(1 + \frac{\pi R_{ro}}{2g_c} \beta_1)} \quad \textbf{(3-16)}$$

And the flux in the PM slot area is obtained

$$B_{fg}(\theta) = \begin{cases} B_g & 0 < \theta \le \frac{\pi - p\beta_1}{2} \\ \frac{B_g}{1 + \frac{\pi R_{ro}}{2g_c}(\frac{2\theta}{p} - \frac{\pi}{p} + \beta_1)} & \frac{\pi - p\beta_1}{2} < \theta < \frac{\pi}{2} \end{cases} \quad \textbf{(3-17)}$$

The magnitude of harmonic components for the improved analytical model can be calculated:

$$\begin{aligned} B_{fgv} &= \frac{4}{v\pi} B_g \sin(v\frac{\pi - p\beta_1}{2}) \\ &+ \frac{4}{\pi}\frac{pg_c}{\pi R_{ro}} B_g \cos v\left(\frac{\pi}{2} - \frac{pg_c}{\pi R_{ro}} - \frac{p\beta_1}{2}\right)\left\{\mathrm{Ci}\left[v\left(\frac{pg_c}{\pi R_{ro}} + \frac{p\beta_1}{2}\right)\right] - \mathrm{Ci}\left[v\left(\frac{pg_c}{\pi R_{ro}}\right)\right]\right\} \\ &- \frac{4}{\pi}\frac{pg_c}{\pi R_{ro}} B_g \sin v\left(\frac{\pi}{2} - \frac{pg_c}{\pi R_{ro}} - \frac{p\beta_1}{2}\right)\left\{\mathrm{Si}\left[v\left(\frac{pg_c}{\pi R_{ro}} + \frac{p\beta_1}{2}\right)\right] - \mathrm{Si}\left[v\left(\frac{pg_c}{\pi R_{ro}}\right)\right]\right\} \end{aligned} \quad \textbf{(3-18)}$$

where

$$\mathrm{Si}(x) = \int_0^x \frac{\sin t}{t} dt = \sum_{k=1}^{\infty} (-1)^{k-1} \frac{x^{2k-1}}{(2k-1)(2k-1)!} \quad \textbf{(3-19)}$$

$$\mathrm{Ci}(x) = -\int_x^{\infty} \frac{\cos t}{t} dt = \gamma + \ln x + \sum_{k=1}^{\infty} \frac{(-x^2)^k}{(2k)(2k)!} \quad \textbf{(3-20)}$$

and γ is Euler–Mascheroni constant.

Figure 3-4 depicts the airgap flux distribution waveforms and spectra of a typical spoke-type machine by both the analytical methods and FEA model. For better comparison between the PM slotting effect in the simplified and improved analytical methods, ideal smooth stator is applied for the FEA model as well. In terms of the flux distribution waveform shapes, the analytical models show good

agreement with the FEA result. Since flux conservation law is applied, the total amount of PM flux is the same for all the analytical and FEA models. With the presumption that flux travels in the core areas only, the actual flux through the PM slot area is counted into core area for the simplified analytical model, and thus the flux density in the core area is slightly higher than FEA. Meanwhile, high accuracy is accomplished by the improved analytical method as good approximation of PM slotting effect is implemented. Due to the higher core area flux density predicted by the simplified model, the fundamental is 2.8% higher than FEA. Besides, the simplification incurs greater impact on higher order harmonics. For example, larger percentage of error for harmonic orders such as 5^{th} and 7^{th} is observed in Figure 3-4(b). On the other hand, the improved model achieves high accuracy in both fundamental and harmonic contents.

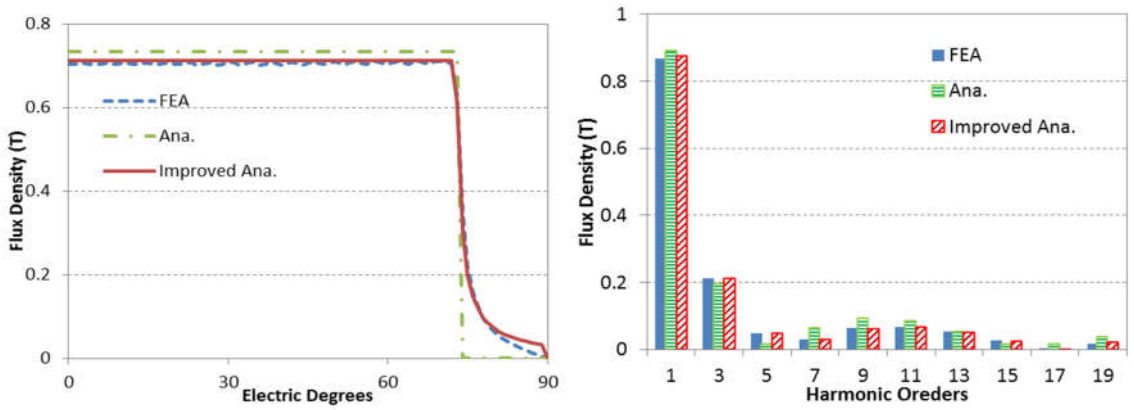

(a) Waveform; (b) Spectra;

Figure 3-4 Open-circuit airgap flux distribution with W_i=7mm and L_i=31mm.

Similarly, the stator slotting effect can also be considered by the same approximation method illustrated in Figure 3-1 and further improvement is achieved. As demonstrated in Figure 3-5 (a)-(c), while a good capture of the flux distribution waveforms can be observed with smooth stator and Carter's coefficient, almost identical flux waveforms to FEA are achieved with the stator slotting effect included in the analytical model. The spectra of flux distributions are depicted in Figure 3-5 (d)-(e), and the result indicates that considerable deviations appear only in tooth harmonics with ideal stator cores, e.g. the 11^{th} and 13^{th} harmonics. Although highly accurate predictions can be achieved with the consideration of actual stator slotting effect, the analytical model would be

greatly complicated with only minor improvements. Comparing to the rotor PM slots, stator winding slots have much smaller slot openings, and thus much smaller influence on the flux distribution. What's more, the mathematical expressions would be slightly different for machines with different number of stator slot per pole per phase. With the simplification of ideal smooth stator, the expressions for the analytical models are more universal since the stator winding configurations can be easy defined by winding functions. The relative positions of stator slots and PM slots are irrelevant to the model, and the investigation can be better focused on the rotor design.

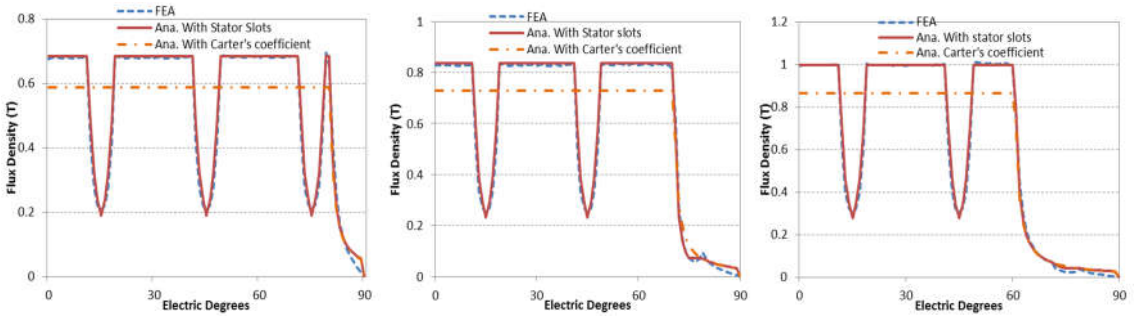

(a) W_1=4mm waveform; (b) W_1=8mm waveform; (c) W_1=12mm waveform;

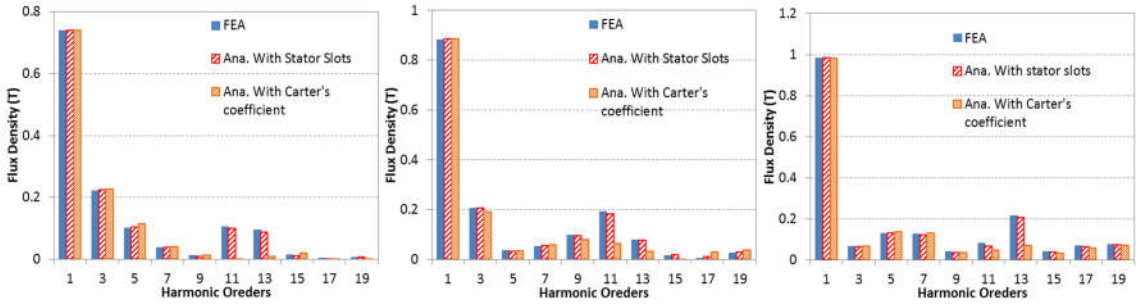

(d) W_1=4mm spectra; (e) W_1=8mm spectra; (f) W_1=12mm spectra;

Figure 3-5 Comparison of Flux distribution by FEA, improved analytical models considering stator slots and Carter's coefficient for stator.

The influence of width and length of the PMs on the airgap flux distributions is demonstrated in Figure 3-6 and Figure 3-7 respectively. It can be seen that the width of the PMs plays a more active role for the rotor design, which affects not only the magnitude of fundamental flux, but also the harmonic content. Although wider PMs can enhance the fundamental component, harmonic contents will

also change accordingly. As the increase of PM width, the enhancement becomes less effective, which is not very practical concerning the cost of material. And by choosing proper parameter of the PM length, certain harmonics can be reduced according to Equation (3-18). The length of the PMs affects only the flux density but shows no influence on the percentage of harmonic contents. According to Equations (3-17) and (3-18), the PM length is proportional to the airgap flux density and has no impact on the shape of distribution waveform. Thus, longer PMs are preferred for the spoke-type machine owing to the effective flux enhancement, while the width should be chosen with balanced consideration between good flux density and low harmonic contents and material cost.

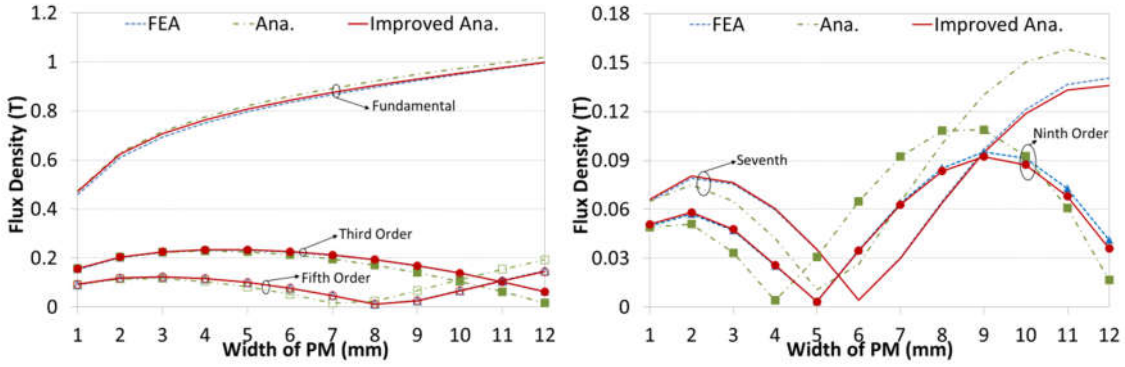

(a) Fundamental to 5th; (b) 7th and 9th;

Figure 3-6 Magnitude of main harmonic orders of airgap flux distribution with different PM width (L_I=31mm).

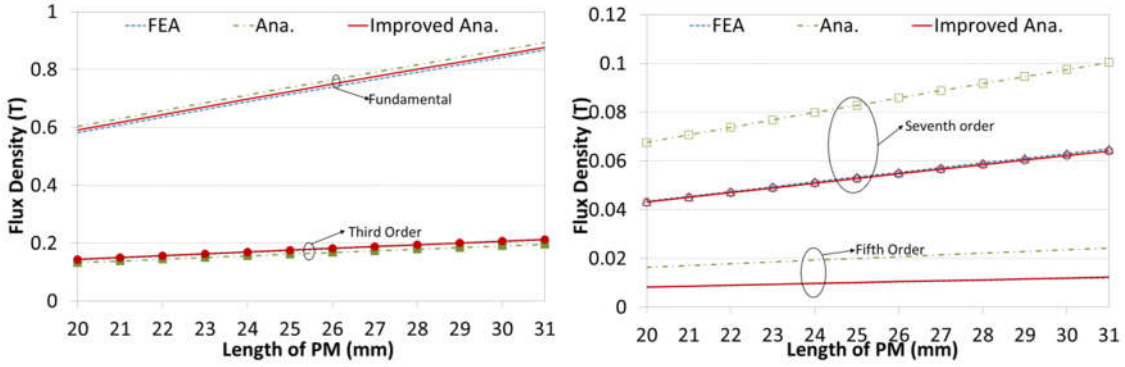

(a) Fundamental and 3rd; (b) 5th and 7th;

Figure 3-7 Magnitude of main harmonic orders of airgap flux distribution with different PM length (W_I=8mm).

It should also be noted that the accurate result can be achieved even by the simplified analytical methods when the PM width is very small and the slotting effect is negligible. But the error between FEA and analytical result increases with the increase of the PM width, because more severe distortion of flux distribution is caused by large PM slot. Additionally, the magnitude decays for higher harmonic orders, and larger deviation appears for the analytical model. However, the variation trend of the harmonic contents against the key design parameters can still be roughly predicted. By taking the flux through the PM slot areas into consideration, the improved analytical method is able to achieve very low error percentage even with very wide range of parameter variations, which offers helpful and accurate insight for preliminary designs.

To maintain relative high airgap flux density, wide and long PMs are usually used for the design of ferrite spoke-type IPMs, and the following conditions are satisfied:

$$\begin{cases} L_1 >> L_{s1} \\ W_1 >> g_c \end{cases} \tag{3-21}$$

Then the working point of the PM is very close to its remanence flux density. With the ignorance of the flux leakage and PM slot flux, the magnitude of the vth airgap harmonic flux can be roughly calculated by

$$B_{fgv} \approx \frac{4}{\pi v} B_r \frac{L_1}{\left(\frac{\pi}{p} - \beta_1\right) R_{ro}} \sin(v\frac{\pi - p\beta_1}{2}) = 2B_r \frac{pL_1}{\pi R_{ro}} \frac{\sin(v\frac{\pi - p\beta_1}{2})}{v\left(\frac{\pi - p\beta_1}{2}\right)} \tag{3-22}$$

And approximate relations between the airgap flux distribution and key design parameters can be obtained. The magnitude of the vth harmonic decays by a factor of v, which means higher order harmonics decreases dramatically in general. The denominator $(\pi/p\text{-}\beta_1)R_{ro}$ in Equation (3-22) denotes the arc length of half a core area. It is obvious that the flux density is in proportion to PM length and inversely proportional to core area length. The ratio between L_1 and $(\pi/p\text{-}\beta_1)R_{ro}$ is the flux focusing factor, which represents the flux focusing effect.

This explains the reason why longer PM poles are usually preferred for spoke-type machines to achieve higher airgap flux density so long as there is enough space in the rotor.

As for the width of the PM, the influence is more complicated. Firstly, wider PMs should certainly increase the PM work point. Since the PM width is much larger than airgap length, the influence becomes ignorable. Secondly, it affects the length of core area. On one hand, the length of the core area is reduced with wider PMs, which intensifies the airgap flux density. On the other, the shape of the flux waveform will be changed, which influences the harmonic contents. Due to the multiplier of v inside the sine function in Equation (3-22), the magnitudes of different harmonic orders varies differently. For example, the fundamental increases with W_1 (or β_1) monotonically, and the 5th order reaches its minimum when W_1 equals 8mm. As the PM width can affect the shape of flux waveform, certain harmonic order can be effectively reduced by carefully chosen PM width. For example, the 5th and 7th harmonic components are greatly reduced with 7mm of PM width, which is also indicated in Figure 3-6.

Base on the analytical models developed, the PM flux linkage and PM torque can be derived accordingly. Since the harmonic flux components with triplen orders in a three phase machine are with the same phase angle in a balanced machine, it will not develop flux linkage in the d-q frame. Then the PM flux linkage and PM torque can be expressed as:

$$\Psi_f = \frac{4R_{ro}l_{ef}N_a}{p}\sum_{v=1,5,7...}^{6k\pm1}(-1)^{\frac{v-1}{2}}\frac{k_{wv}}{v}B_{fgv} \qquad \textbf{(3-23)}$$

$$T_{pm} = \frac{mp}{4}\Psi_f i_q = mR_{ro}l_{ef}N_a i_q\sum_{v=1,5,7...}^{6k\pm1}(-1)^{\frac{v-1}{2}}\frac{k_{wv}}{v}B_{fgv} \qquad \textbf{(3-24)}$$

where i_q is q-axis current. Apparently, the magnitudes of higher order harmonic flux distributions are much lower than the fundamental. What's more, the contribution of the vth harmonic to the total flux linkage is multiplied by winding factor k_{wv} and divided by harmonic order v, which means the flux linkage generated by higher harmonic orders is dramatically reduced. And as the

increase of the harmonic order, the flux linkage generated is becoming negligible. As listed in Table 3-2, the fundamental contributes up to 99% of the total PM flux linkage, and the flux linkage generated by an individual harmonic will be less than 2%. Since there is considerable inaccuracy in the prediction of harmonic flux by the simplified analytical model, error might be accumulated for flux linkage calculation. But as the flux linkage due to the harmonics is quite subtle, the error is well within 2%. Since the fundamental is the predominant contribution, the PM flux linkage can be estimated by counting only the flux linkage of the fundamental component. Despite that slightly higher deviation from FEA model is exhibited, much simpler and fast calculation can be carried out if accuracy is not too critical during preliminary design period.

Figure 3-8 depicts the overall PM flux linkage and torque with different PM width and length. As the predominant of PM flux linkage is generated by fundamental and PM torque is proportional to flux linkage, the variation trends are almost the same with fundamental flux amplitude. The estimations using only fundamental component are also illustrated in Figure 3-8 as a simpler alternative. Since flux linkage produced by harmonics could be positive or negative to armature windings, the error of prediction by fundamental only varies with different PM widths. As for the PM length, the error ratio is approximately the same if the width of PMs is fixed.

Table 3-2 PM flux linkage (Wb·Turns) generated by different flux harmonics with various PM length

W_1 / v	8mm		12mm	
	Ana.	**Ana. Improved**	**Ana.**	**Ana. Improved**
1	0.743	0.725	0.820	0.809
5	$5.42\text{x}10^{-4}$	$1.79\text{x}10^{-3}$	$-6.80\text{x}10^{-3}$	$-5.69\text{x}10^{-3}$
7	$2.01\text{x}10^{-3}$	$1.43\text{x}10^{-3}$	$4.98\text{x}10^{-3}$	$3.86\text{x}10^{-3}$
11	$4.98\text{x}10^{-3}$	$1.44\text{x}10^{-2}$	$-3.10\text{x}10^{-3}$	$6.23\text{x}10^{-3}$
13	$2.01\text{x}10^{-3}$	$-4.88\text{x}10^{-3}$	$-5.30\text{x}10^{-3}$	$-1.38\text{x}10^{-2}$
17	$-4.10\text{x}10^{-4}$	$-1.10\text{x}10^{-4}$	$6.75\text{x}10^{-5}$	$7.44\text{x}10^{-4}$
19	$4.62\ \text{x}10^{-4}$	$2.18\ \text{x}10^{-4}$	$-5.78\text{x}10^{-4}$	$-9.50\text{x}10^{-4}$
23	$5.55\text{x}10^{-4}$	$-1.61\text{x}10^{-3}$	$-4.5\text{x}10^{-4}$	$4.38\text{x}10^{-3}$
Ana. all	**0.752**	**0.737**	**0.812**	**0.801**
FEA all	**0.739**		**0.803**	

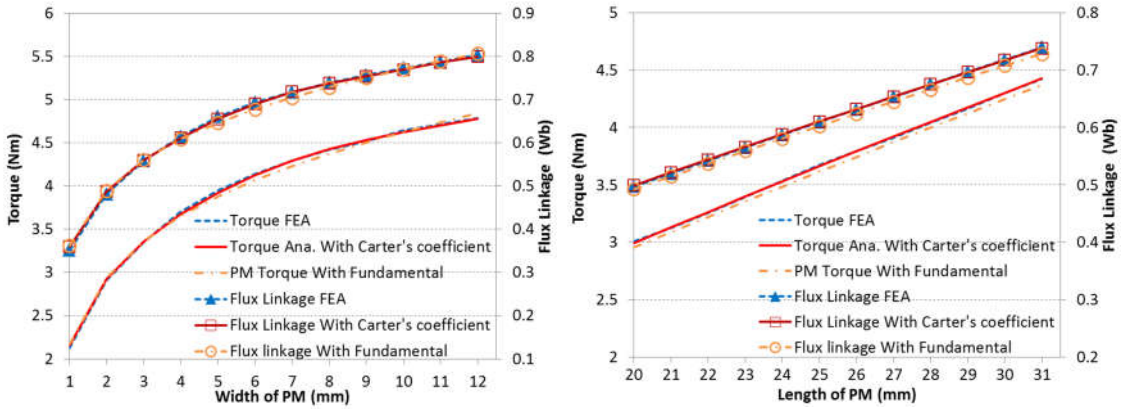

(a) With different W_1 when L_1=31mm; (b) With different L_1 when W_1=8mm;

Figure 3-8 Comparison of PM flux linkage and PM torque with difference PM width and length.

3.2.2.2 D-Axis Magnetizing Inductance

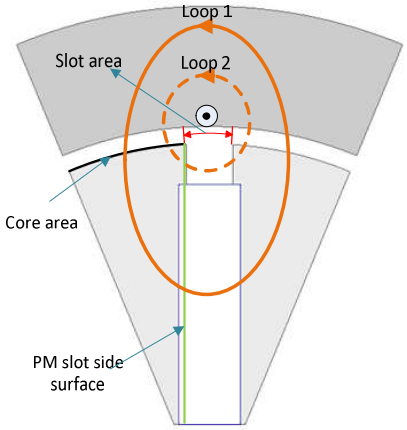

Figure 3-9 Flux line loops for d-axis current

The paths of flux loops excited by d-axis current are illustrated in Figure 3-9. With d-axis current flowing out of conductors and the flux paths are depicted as Loop 1 and Loop 2. Since saturation is ignored for the analytical model, the superposition principle is applicable. Therefore, the armature reaction can be estimated separately and the magnet poles are removed from the model. Because the height of slot opening is very small compared with PM length, the flux in Loop 2 is subtle. What's more, wide slot opening is usually applied to reduce flux leakage, approximation of $W_{s1} \approx W_1$ can be made and then Loop 1

and Loop 2 can be combined as one loop. The MMF generated by d-axis armature current in a balanced three phase sinusoidal machine is obtained by

$$F_{ad}(\theta) = \sum F_{adv} \cos(v\theta) \tag{3-25}$$

where

$$F_{adv} = \begin{cases} \dfrac{2m}{vp\pi} k_{wv} N_a i_d & v \neq 3k \\ 0 & v = 3k \end{cases} \tag{3-26}$$

Based on the Ampere's and Gauss's law, the following can be obtained

$$\begin{cases} H_{md} \cdot W_1 + 2 \cdot H_{gd}(\theta) \cdot g_c = 2F_{ad}(\theta) \\ \phi_{md} = \phi_{gd} \end{cases} \tag{3-27}$$

where H_{md} is the flux intensity inside the PM slot, $H_{gd}(\theta)$ is flux intensity in the airgap, ϕ_{md} is the flux through PM slot side surface (green line shown in Figure 3-9) and ϕ_{gd} is the flux through the core area of half pole pitch (dark line shown in Figure 3-9). Since the width of the PM slots along the radial direction is constant, H_{md} is assumed constant with the boundary effect ignored. Then the following is derived by solving Equation (3-27):

$$H_{md} = \frac{\sum_{v \neq mk} F_{adv} \dfrac{4}{vp} \sin v\left(\dfrac{\pi}{2} - \dfrac{p\beta_1}{2}\right)}{W_1(\pi / p - \beta_1) + 2g_c(L_1 + L_s)/R_{ro}} = \frac{\sum_{v \neq mk} \dfrac{8m}{v^2 p^2 \pi} i_d k_{wv} N_a \sin v\left(\dfrac{\pi}{2} - \dfrac{p\beta_1}{2}\right)}{W_1(\pi / p - \beta_1) + 2g_c(L_1 + L_s)/R_{ro}} \tag{3-28}$$

Equation (3-28) indicates that a summation of all d-axis MMF is required for the calculation of the PM slot flux intensity (H_{md}). Since the vth term in the summation is inversely proportional to space harmonic order squared, its value decreases dramatically with v. By using short-pitch or distributed winding connections, there may be further reduction for higher order harmonics. Thus, the terms of the summation decrease exponentially as the growth of harmonic orders, and there is no need to perform the infinite summation. The number of terms can be chosen according to the accuracy required. Generally, it is not necessary to consider the terms with harmonic order higher than 20.

In Equation (3-27) d-axis MMF (F_{ad}) is expressed in Fourier series and is a function of angular position, while PM slot flux intensity (H_{md}) is constant and seems irrelevant to the angular position. But because all the d-axis flux travels through the PM slot, there is constant MMF drop inside the rotor, which is called rotor MMF. Considering that the direction of flux is reversed in the neighboring PM slot and the period is the same with airgap flux distribution, the rotor MMF can be described as a square wave with maximum value of H_{md} and minimum value of $-H_{md}$, and the length of PM slots is linked with angular position by the flux lines. To maintain the unity of the expression for the analytical models, H_{md} is expanded into Fourier series:

$$H_{mdv}(\theta) = \frac{4}{v\pi} H_{md} \sin\left(\frac{v\pi}{2}\right)\cos(v\theta) \tag{3-29}$$

Applying Equation (3-29) to (3-27), the flux density distribution excited by the vth MMF in the core area is calculated by:

$$B_{adv}(\theta) = \begin{cases} B_{admv}\cos(v\theta), & 0 \le \theta \le \dfrac{\pi - p\beta_1}{2} \\ \dfrac{B_{admv}\cos(v\theta)}{\dfrac{\pi R_{ro}}{pg_c}\left(\theta - \dfrac{\pi}{2} + \dfrac{p\beta_1}{2}\right)+1}, & \dfrac{\pi - p\beta_1}{2} < \theta < \dfrac{\pi}{2} \end{cases} \tag{3-30}$$

where B_{admv} is the magnitude flux density excited by the vth MMF in the airgap, and it can be expressed as:

$$B_{admv} = \begin{cases} \dfrac{2\mu_0 m}{v\pi p g_c} k_{wv} N_a i_d - \dfrac{16\mu_0 m N_a i_d \sum\limits_{j\neq mk}\left[\dfrac{k_{wj}}{j^2}\sin j\left(\dfrac{\pi}{2} - \dfrac{p\beta_1}{2}\right)\right]}{vp^2\pi^2\left[g_c\left(\dfrac{\pi}{p} - \beta_1\right) + 2{g_c}^2\dfrac{L_1 + L_{s1}}{R_{ro}W_1}\right]}\sin\left(\dfrac{v\pi}{2}\right) & v \neq 3k \\ -\dfrac{16\mu_0 m N_a i_d \sum\limits_{j\neq mk}\left[\dfrac{k_{wv}}{j^2}\sin j\left(\dfrac{\pi}{2} - \dfrac{p\beta_1}{2}\right)\right]}{vp^2\pi^2\left[g_c\left(\dfrac{\pi}{p} - \beta_1\right) + 2{g_c}^2\dfrac{L_1 + L_{s1}}{R_{ro}W_1}\right]}\sin\left(\dfrac{v\pi}{2}\right) & v = 3k \end{cases} \tag{3-31}$$

And airgap flux distribution can be obtained by adding up all the terms:

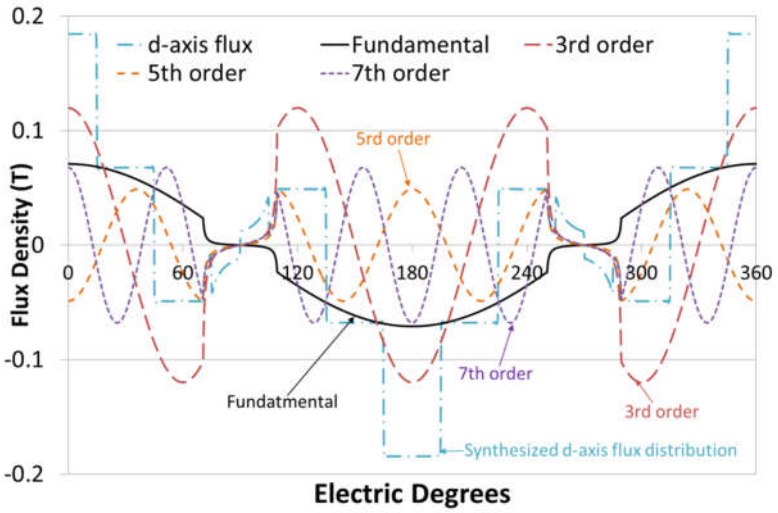

Figure 3-10 Flux density excited by 1st, 3rd, 5th and 7th MMF in the airgap.

$$B_{gd}(\theta)=\sum_{v=1}^{2k+1}B_{adv}(\theta) \tag{3-32}$$

The flux waveforms excited by corresponding orders of *d*-axis armature MMF are illustrated in Figure 3-10, and the actual flux distribution in the airgap is synthesized by adding all the flux waveforms together according to Equation (3-32), which is also depicted in Figure 3-10. With more terms in taken in to account, the more accurate the analytical models becomes comparing to FEA results. Because all the flux travels through the large PM slots in the rotor and generates rotor MMF with square waveform, large amount of harmonics are brought in, resulting in high harmonic contents in the airgap flux.

It should also be noted that the airgap flux waveform due to each harmonic MMF is further distorted by the large PM slot openings, which incurs even higher harmonics. Since the flux density decays dramatically in the slot area for all harmonics derived by Equation (3-30), the vth flux distribution $B_{adv}(\theta)$ generated by corresponding MMF component is no longer sinusoidal, and B_{admv} is not the real magnitude for vth flux distribution in the airgap. In fact, $B_{adv}(\theta)$ can be further decomposed as a sum of Fourier series, and the actual vth order harmonic content of the flux distribution is a summation of all the vth components decomposed from the flux field excited by different order armature MMF, which can be expressed as:

$$B_{gdv}=\sum_{u=1}^{2k+1}\left[\frac{1}{\pi}\int_0^{2\pi}B_{adu}(\theta)\cos(v\theta)\,d\theta\right]=\sum_{u=1}^{2k+1}B_{gduv} \tag{3-33}$$

$$B_{gduv}=\frac{4}{\pi}\left[\begin{array}{l}\displaystyle\int_0^{\frac{\pi-p\beta_1}{2}}B_{adu}\cos(u\theta)\cos(v\theta)\,d\theta \\ \displaystyle+\int_{\frac{\pi-p\beta_1}{2}}^{\frac{\pi}{2}}B_{adu}\frac{\cos(u\theta)\cos(v\theta)}{\frac{\pi R_{ro}}{pg_c}\left(\theta-\frac{\pi}{2}+\frac{p\beta_1}{2}+\frac{pg_c}{\pi R_{ro}}\right)}d\theta\end{array}\right]=B_{gd1uv}+B_{gd2uv} \tag{3-34}$$

where B_{gdv} is the amplitude of the vth flux distribution in the airgap, $B_{gdu}(\theta)$ denotes flux distribution due to the uth MMF component, and B_{gduv} represents the amplitude of the vth order component decomposed from $B_{gdu}(\theta)$. The calculation of the harmonic components can be divided into two parts. The first part (B_{gd1uv}) is contributed by the flux in the core area and is the predominant portion, while the second part (B_{gd2uv}) is due to the flux through PM slot area. Since the flux density in the PM slot area is very low, the second part usually has minor effect. If the flux in the PM slot area is ignored, only the first term in Equation (3-34) is necessary for calculation. Then the following can be derived:

$$B_{gduv}=B_{gd1uv}=\begin{cases}(-1)^{\frac{u+v-2}{2}}\dfrac{2}{\pi}B_{admu}\left[\dfrac{\sin\frac{(u+v)p\beta_1}{2}}{u+v}-\dfrac{\sin\frac{(u-v)p\beta_1}{2}}{u-v}\right] & (u\neq v)\\ B_{admv}\left(1-\dfrac{p\beta_1}{\pi}+\dfrac{\sin v(\pi-p\beta_1)}{v\pi}\right) & (u=v)\end{cases} \tag{3-35}$$

If the flux in the PM slot area should be taken into consideration, the second term in Equation (3-34) is derived if u=v:

$$\begin{aligned}B_{gd2vv}=&\frac{2pg_c}{\pi^2R_{ro}}B_{admv}\cdot\\ &\left\{\begin{array}{l}\cos\left[2v\left(\frac{\pi}{2}-\frac{pg_c}{\pi R_{ro}}-\frac{p\beta_1}{2}\right)\right]\left\{\mathrm{Ci}\left[2v\left(\frac{pg_c}{\pi R_{ro}}+\frac{p\beta_1}{2}\right)\right]-\mathrm{Ci}\left[2v\left(\frac{pg_c}{\pi R_{ro}}\right)\right]\right\}\\ -\sin\left[2v\left(\frac{\pi}{2}-\frac{pg_c}{\pi R_{ro}}-\frac{p\beta_1}{2}\right)\right]\left\{\mathrm{Si}\left[2v\left(\frac{pg_c}{\pi R_{ro}}+\frac{p\beta_1}{2}\right)\right]-\mathrm{Si}\left[2v\left(\frac{pg_c}{\pi R_{ro}}\right)\right]\right\}\\ +\ln\left(1+\frac{\pi R_{ro}\beta_1}{2g_c}\right)\end{array}\right\}\end{aligned} \tag{3-36}$$

If $u \neq v$, then

$$B_{gd2uv} = \frac{2pg_c}{\pi^2 R_{ro}} B_{admu} \cdot$$

$$\begin{Bmatrix} \cos\left[(u+v)\left(\frac{\pi}{2}-\frac{pg_c}{\pi R_{ro}}-\frac{p\beta_1}{2}\right)\right]\left\{\mathrm{Ci}\left[(u+v)\left(\frac{pg_c}{\pi R_{ro}}+\frac{p\beta_1}{2}\right)\right]-\mathrm{Ci}\left[(u+v)\frac{pg_c}{\pi R_{ro}}\right]\right\} \\ -\sin\left[(u+v)\left(\frac{\pi}{2}-\frac{pg_c}{\pi R_{ro}}-\frac{p\beta_1}{2}\right)\right]\left\{\mathrm{Si}\left[(u+v)\left(\frac{pg_c}{\pi R_{ro}}+\frac{p\beta_1}{2}\right)\right]-\mathrm{Si}\left[(u+v)\frac{pg_c}{\pi R_{ro}}\right]\right\} \\ +\cos\left[(u-v)\left(\frac{\pi}{2}-\frac{pg_c}{\pi R_{ro}}-\frac{p\beta_1}{2}\right)\right]\left\{\mathrm{Ci}\left[(u-v)\left(\frac{pg_c}{\pi R_{ro}}+\frac{p\beta_1}{2}\right)\right]-\mathrm{Ci}\left[(u-v)\frac{pg_c}{\pi R_{ro}}\right]\right\} \\ -\sin\left[(u-v)\left(\frac{\pi}{2}-\frac{pg_c}{\pi R_{ro}}-\frac{p\beta_1}{2}\right)\right]\left\{\mathrm{Si}\left[(u-v)\left(\frac{pg_c}{\pi R_{ro}}+\frac{p\beta_1}{2}\right)\right]-\mathrm{Si}\left[(u-v)\frac{pg_c}{\pi R_{ro}}\right]\right\} \end{Bmatrix} \quad \textbf{(3-37)}$$

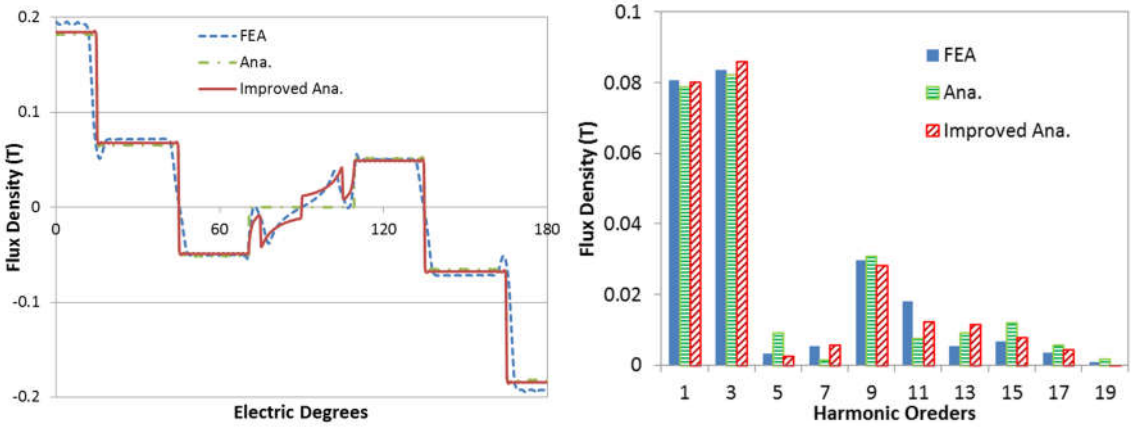

(a) Waveform; (b) Spectra;

Figure 3-11 Airgap flux distribution between analytical and FEA methods.

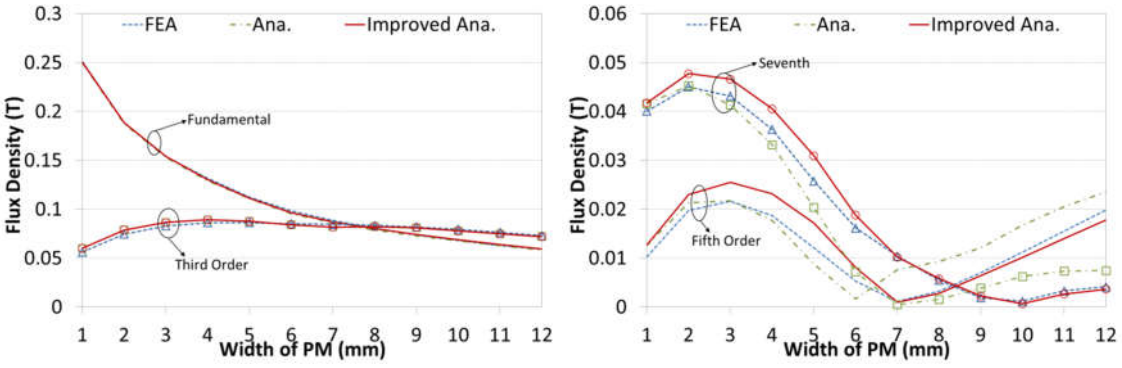

(a) Fundamental and third; (b) Fifth and Seventh;

Figure 3-12 Magnitude of main harmonic orders of airgap flux distribution with different PM width (L_1=31mm).

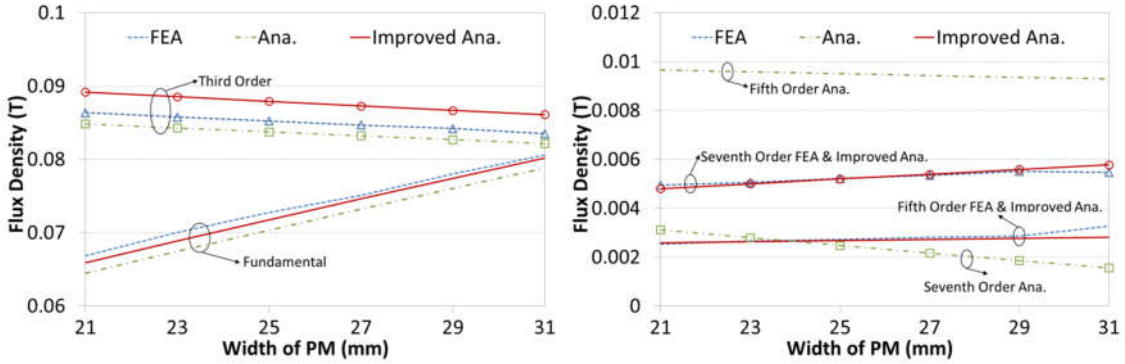

(a) Fundamental and third; (b) Fifth and Seventh;

Figure 3-13 Magnitude of main harmonic orders of airgap flux distribution with different PM width (W_1=8mm).

It is obvious that the calculation becomes much more complicated if the flux in the slot area is counted. Similar to the PM excited field, it is not necessary to calculate the flux of all the harmonics as the amplitude decreases dramatically to the harmonic order. A typical flux distribution waveform and spectra excited by the d-axis current are illustrated in Figure 3-11 and good agreement is obtained by analytical methods. The spectra analysis indicates accurate prediction of the harmonics by improved analytical method, except minor different for the tooth harmonics. Since the major harmonics are brought in by the equivalent square wave rotor MMF, no significant error is seen even when the PM slot flux is assumed to be zero.

Since the PM slots incur large amount of harmonic contents, the slot size have great influence on the d-axis current excited flux distribution. Figure 3-12 demonstrates the magnitudes of the fundamental and key harmonic components (up to 7th order) against the PM slot width. Because the main flux generated by d-axis current needs to go through the PM slots, the reluctance of the flux loop increases with wider PM slots. As a result, the overall airgap flux density and thus the fundamental decreases significantly as the increase of PM width. The 3rd order harmonic is caused by the rotor MMF since synthesized three phase armature MMF doesn't contain triplen components. Hence the 3rd harmonic increases with PM width due to the higher rotor MMF. On the other side, the flux density reduces dramatically in the PM slot area in the airgap.

When the reduction effect is dominating, it will cause the decrease of the 3rd harmonic. For higher order harmonics, the PM width could be larger than their wavelength, and the integrals in (3-34) will not be monotonic functions any more. And thus attenuated waveform is gained as shown in Figure 3-12(b), which indicates ways of reducing certain order harmonics with suitable PM slot width.

As depicted in Figure 3-13, the length of the PM slots has a minor influence on the flux distribution. The area of the PM slot side surface increases with the length, which increases the PM slot permeance and reduces rotor MMF. As a result, the fundamental and non-triplen harmonics increase while the triplen harmonics decrease. But the impact is subtle comparing to that of PM width.

In all, good accuracy is achieved for the analytical methods. Despite that the accuracy decreases with harmonic order due to the ignorance of the flux in the PM slot area, the trend of the influence by PM slot size can be roughly predicted. To account for the flux in the slot area, the improved analytical method achieves higher accuracy for both the fundamental and harmonics. With the derived flux distribution, the d-axis magnetizing inductance is obtained by:

$$L_{md} = \frac{\Psi_{md}}{i_d} = \frac{4N_a R_{ro} l_{ef}}{p \cdot i_d} \sum_{v \neq m \cdot k} \frac{k_{wv}}{v} B_{gdv} = \sum_{v \neq m \cdot k} L_{mdv} \qquad \textbf{(3-38)}$$

Table 3-3 D-axis magnetizing inductance of one-layer configuration due to different flux harmonics (mH).

	Analytical			**Improved Analytical**		
v \ W_1	**4mm**	**8mm**	**12mm**	**4mm**	**8mm**	**12mm**
L_{md1}	105.9	64.8	47.8	107.8	66.9	48.7
L_{md5}	-0.78	0.41	1.04	-1.02	0.12	0.78
L_{md7}	1.05	0.05	-0.23	1.28	0.18	-0.11
L_{md11}	2.35	0.57	1.46	3.04	0.93	1.45
L_{md13}	1.23	0.59	1.16	1.81	0.74	1.19
L_{md17}	-0.14	0.08	-0.02	-0.04	0.06	0.01
L_{md19}	0.26	-0.02	0.08	0.19	0.01	0.07
L_{md23}	-0.28	-0.06	-0.04	-0.96	-0.23	-0.20
L_{md25}	0.205	0.07	0.01	0.77	-0.22	-0.11
L_{md}	109.9	66.3	51.3	112.2	68.9	52.1
FEA L_{md}	114.1	69.3	52.7	114.1	69.3	52.7

where L_{mdv} is the magnetizing inductance contributed to L_{md} by the vth flux component in the airgap. All spatial harmonic components will generate flux linkage and thus contribute to d-axis inductance except triplen orders in the d-q frame.

The contributions of different flux harmonic orders as well as the overall magnetizing inductance in d-axis are listed in Table 3-3. The major contribution to L_{md} comes from the fundamental flux, which accounts for over 90% to the overall magnetizing inductance. Due to the high amount of harmonic content, harmonics cannot be ignored completely. Tooth harmonics show higher impact than the others. That is because they have the same winding factors with the fundamental, and their contents in armature MMF and their contributions to flux linkage will not be reduced by the winding configurations. As for the other higher order harmonics, their impact reduces exponentially to v, and would be further reduced by short-pitch windings. Thus, those harmonics with v higher than 20 could be ignored.

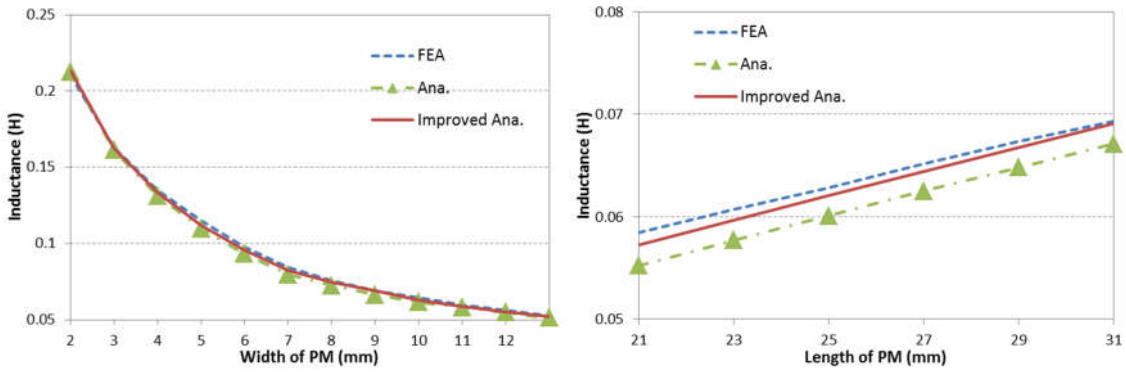

(a) Against PM width (L_1=31mm); (b) Against PM length (W_1=8mm);

Figure 3-14 Comparison of d-axis magnetizing inductance L_{md}.

The d-axis magnetizing inductance derived from FEA and analytical methods are illustrated and compared in Figure 3-14. The magnetizing inductance exhibits the same variation trend with fundamental flux density which contributes over 90% of armature flux linkage. The improved analytical method shows very good agreement with FEA result, and the error is less than 2%. With the assumption of infinite reluctance in the PM slot area, calculation of Equation

(3-37) and (3-36) can be avoided, which dramatically simplifies the model. Still, the result can also follow the FEA well enough, with less than 5% of error. It is noteworthy that the flux leakage in the inner rotor side is ignored to reduce complexity of the model. With shorter PMs, the inner diameter of rotor lamination increases and the area of inner rotor lamination surface is enlarged, which results in higher flux leaks through the inner rotor area instead of going by the PM slot. Therefore, the decrease of PM length brings about higher error for the model. However, large PM length is usually preferred for higher flux focusing effect, and it won't be necessary to count this part of flux leakage. The inductance reduces significantly with PM width, which indicates worse flux weakening abilities for the one-layer spoke-type configurations.

3.2.2.3 Q-Axis Magnetizing Inductance

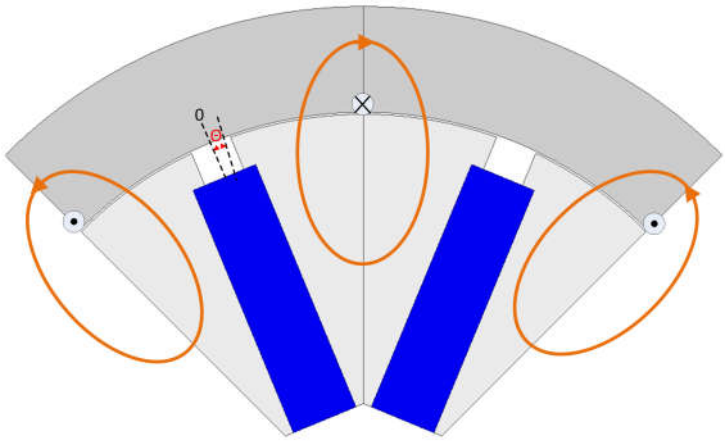

Figure 3-15 Flux loop generated by q-axis current.

Figure 3-15 depicts the flux path under q-axis current. In this circumstance, the armature excited magnetic field goes through rotor lamination rather than push the flux going through the PM poles. As a result, the PM slots only have a minor influence, affecting the active length of core area. According to Ampere's law, the following equation needs to be fulfilled in the lamination pole area:

$$H_{aqv}(\theta)\cdot g_c = F_{aqv}(\theta) \tag{3-39}$$

Similarly, to approximate the flux distribution in the PM slot area, the flux distribution due to the vth MMF can be express as:

$$B_{aqv}(\theta)=\begin{cases}\dfrac{2\mu_0 mN_a k_{wv}}{\pi vpg_c}i_q\cos(v\theta) & 0<\theta<\dfrac{p\beta_1}{2}\\ \dfrac{2\mu_0 mN_a k_{wv}}{\pi vpg_c}i_q\dfrac{1}{1+\dfrac{\pi R_{ro}}{pg_c}(\dfrac{p\beta_1}{2}-\theta)}\cos(v\theta) & \dfrac{p\beta_1}{2}\le\theta\le\dfrac{\pi}{2}\end{cases} \quad \textbf{(3-40)}$$

where $H_{aqv}(\theta)$ and $B_{aqv}(\theta)$ is the flux intensity and flux density distribution in the airgap excited by the vth q-axis MMF respectively. Obviously the waveform excited by each armature MMF order is seriously distorted by the PM slot openings, and they could not represent the actual vth harmonic component. Thus, Fourier transformation needs to be performed to decompose the each order flux distribution waveform derived by Equation (3-40):

$$B_{gqv}=\sum_{u=1}^{2k+1}\left[\frac{1}{\pi}\int_0^{2\pi}B_{aqu}(\theta)\cos(v\theta)\,d\theta\right]=\sum_{u=1}^{2k+1}B_{gquv} \quad \textbf{(3-41)}$$

where B_{gquv} is the magnitude of vth flux harmonic in the airgap excited by the uth order q-axis MMF. If the flux through the PM slot area is ignored, then B_{gquv} can be obtained by:

$$B_{gquv}=\begin{cases}\dfrac{2\mu_0 m}{\pi vpg_c}\cdot N_a k_{wv}i_q\left(1-\dfrac{p\beta_1}{\pi}-\dfrac{\sin(vp\beta_1)}{v\pi}\right) & u=v\\ -\dfrac{4\mu_0 m}{\pi^2 upg_c}\cdot N_a k_{wv}i_q\left\{\dfrac{\sin[(u+v)p\beta_1/2]}{u+v}+\dfrac{\sin[(u-v)p\beta_1/2]}{u-v}\right\} & u\ne v\end{cases} \quad \textbf{(3-42)}$$

If the flux in the PM slot area should be considered, B_{gquv} could be expressed when $u = v$:

$$B_{gquv}=\frac{2\mu_0 m}{\pi vpg_c}\cdot N_a k_{wv}i_q\left(1-\frac{p\beta_1}{\pi}-\frac{\sin(vp\beta_1)}{v\pi}\right)+\frac{4\mu_0 m}{v\pi^3 R_{ro}}N_a k_{wv}i_q\cdot$$
$$\left\{\begin{aligned}&\cos\left[2v\left(\frac{pg_c}{\pi R_{ro}}+\frac{p\beta_1}{2}\right)\right]\left\{\mathrm{Ci}\left[2v\left(\frac{pg_c}{\pi R_{ro}}+\frac{p\beta_1}{2}\right)\right]-\mathrm{Ci}\left[2v\left(\frac{pg_c}{\pi R_{ro}}\right)\right]\right\}\\ &+\sin\left[2v\left(\frac{pg_c}{\pi R_{ro}}+\frac{p\beta_1}{2}\right)\right]\left\{\mathrm{Si}\left[2v\left(\frac{pg_c}{\pi R_{ro}}+\frac{p\beta_1}{2}\right)\right]-\mathrm{Si}\left[2v\left(\frac{pg_c}{\pi R_{ro}}\right)\right]\right\}+\ln\left(1+\frac{\pi R_{ro}\beta_1}{2g_c}\right)\end{aligned}\right\} \quad \textbf{(3-43)}$$

And when $u \ne v$, B_{gquv} is calculated by:

$$B_{gquv} = -\frac{4\mu_0 m}{\pi^2 upg_c} \cdot N_a k_{wv} i_q \left\{ \frac{\sin\left[(u+v)\, p\beta_1 / 2\right]}{u+v} + \frac{\sin\left[(u-v)\, p\beta_1 / 2\right]}{u-v} \right\} + \frac{4\mu_0 m}{u\pi^3 R_{ro}} N_a k_{wv} i_q$$

$$\cdot \left\{ \begin{array}{l} \cos\left[(u+v)\left(\frac{pg_c}{\pi R_{ro}} + \frac{p\beta_1}{2}\right)\right] \left\{ \mathrm{Ci}\left[(u+v)\left(\frac{p\beta_1}{2} + \frac{pg_c}{\pi R_{ro}}\right)\right] - \mathrm{Ci}\left[(u+v)\left(\frac{pg_c}{\pi R_{ro}}\right)\right] \right\} \\ + \sin\left[(u+v)\left(\frac{pg_c}{\pi R_{ro}} + \frac{p\beta_1}{2}\right)\right] \left\{ \mathrm{Si}\left[(u+v)\left(\frac{p\beta_1}{2} + \frac{pg_c}{\pi R_{ro}}\right)\right] - \mathrm{Si}\left[(u+v)\left(\frac{pg_c}{\pi R_{ro}}\right)\right] \right\} \\ + \cos\left[(u-v)\left(\frac{pg_c}{\pi R_{ro}} + \frac{p\beta_1}{2}\right)\right] \left\{ \mathrm{Ci}\left[(u-v)\left(\frac{p\beta_1}{2} + \frac{pg_c}{\pi R_{ro}}\right)\right] - \mathrm{Ci}\left[(u-v)\left(\frac{pg_c}{\pi R_{ro}}\right)\right] \right\} \\ + \sin\left[(u-v)\left(\frac{pg_c}{\pi R_{ro}} + \frac{p\beta_1}{2}\right)\right] \left\{ \mathrm{Si}\left[(u-v)\left(\frac{p\beta_1}{2} + \frac{pg_c}{\pi R_{ro}}\right)\right] - \mathrm{Si}\left[(u-v)\left(\frac{pg_c}{\pi R_{ro}}\right)\right] \right\} \end{array} \right\} \quad \textbf{(3-44)}$$

The flux distribution and spectra by q-axis current are illustrated in Figure 3-16. As the flux density in q-axis is decided only by the permeance of the airgap, the difference of airgap flux distribution waveform is only observed in the slot area for analytical and improved analytical models. The assumption of infinite reluctance in the PM slot area would certainly increase the equivalent airgap length, which results in lower flux density for the analytical model. Additionally, because the maximum value of q-axis current MMF happens to appear at the PM slot area, neglecting the flux in this area will bring about much larger errors than the d-axis flux model. As shown in Figure 3-16(b), the magnitude of the fundamental flux appears to be 10% lower than FEA, and noticeable error is caused without counting the flux in the slot area. Thus, it is necessary to approximate the flux distribution in the slot area and great improvement is achieved by improved analytical model.

In q-axis analytical models, the PM length is irrelevant to the flux path, and thus only the width of the PMs is discussed for the influence over flux distribution. Figure 3-17(a) illustrates the magnitudes of fundamental, 3rd and 5th harmonics with different PM width, and the variation trends can be well predicted by both analytical methods. Due to the ignoring of the flux in the PM slot area, there is noticeable error for the simplified model. And the error ratio grows as the widening of the PM slot opening, because larger amount of flux is excluded. The error ratio reaches 12% with 12mm of PM slot openings. On the other hand,

the error can be compensated with improved analytical model, and high accuracy is obtained.

Because the flux density attenuates dramatically in the PM slot area, the fundamental flux component decreases with the increase of PM width. But the descent rate of q-axis flux against PM width is not as significant as that of the d-axis flux.

Similarly, based on the airgap flux distribution derived, the q-axis magnetizing inductance can be obtained by

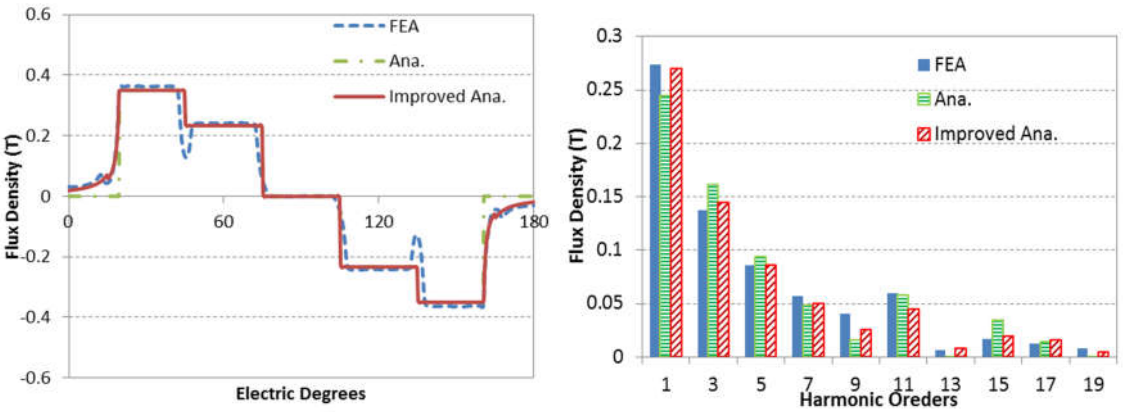

(a) Flux distribution; (b) Spectra;

Figure 3-16 Comparison of airgap flux distribution excited by q-axis current between analytical and FEA methods.

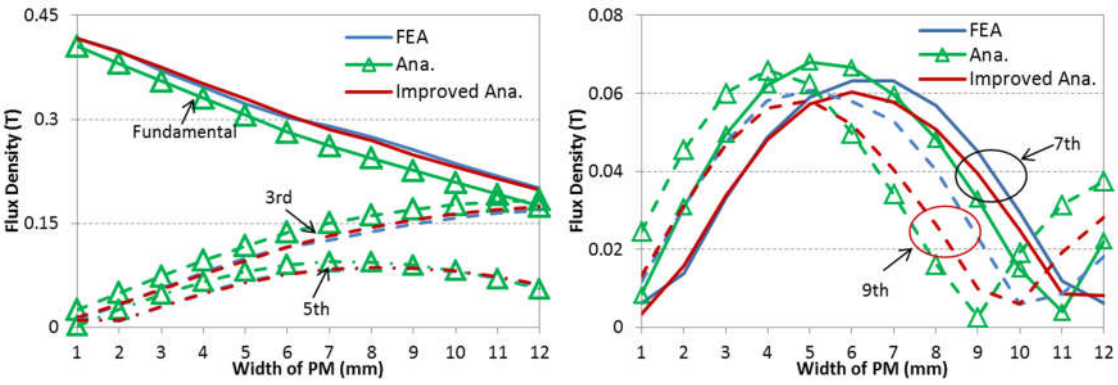

(a) Fundamental, 3rd and 5th harmonics; (b) 7th and 9th harmonics;

Figure 3-17 Comparison of the fundamental, and 3rd to 9th harmonic flux distribution by analytical and improved analytical methods.

$$L_{mq} = \frac{\Psi_{mq}}{i_q} = \frac{4N_a R_{ro} l_{ef}}{p \cdot i_q} \sum_{v \neq m \cdot k} \frac{k_{wv}}{v} B_{gqv} = \sum_{v=6k\pm1} L_{mqv} \quad \textbf{(3-45)}$$

where Ψ_{mq} is the *q*-axis flux linkage, L_{mqv} is the magnetizing inductance induced by the vth airgap flux harmonic component. To reveal the influence of flux distributions of different harmonic orders, their contributions to the q-axis magnetizing inductance are listed in Table 3-4. Since q-axis airgap flux distribution contains lower harmonic content than the d-axis flux, the fundamental flux component is responsible for over 97% of the magnetizing inductance. In view of that the contribution of harmonics decreases exponentially with harmonic order, only the contribution of the fundamental derived from the improved analytical model is of acceptable accuracy for preliminary predictions.

Table 3-4 Q-axis magnetizing inductance of one-layer configuration due to different flux harmonics (mH).

	Analytical			Improved Analytical		
W_1 / v	4mm	8mm	12mm	4mm	8mm	12mm
L_{mq1}	271.4	200.3	143.6	285.4	221.3	163.5
L_{mq5}	-2.90	-4.14	-2.45	-2.37	-3.77	-2.61
L_{mq7}	-1.96	-1.52	0.70	-1.64	-1.79	0.20
L_{mq11}	-0.94	4.34	4.57	2.13	4.47	5.94
L_{mq13}	4.43	-0.16	2.62	2.16	-0.40	1.19
L_{mq17}	0.21	-0.19	0.21	0.31	-0.16	0.33
L_{mq19}	0.04	0.03	-0.08	0.17	-0.09	0.00
L_{mq23}	0.05	1.30	0.09	1.63	1.42	0.39
L_{mq25}	1.26	0.04	0.42	-0.32	-0.42	0.20
L_{mq}	274.1	202.1	151.4	291.2	221.5	168.8
FEA L_{mq}	289.9	225.3	170.8	289.9	225.3	170.8

Figure 3-18 demonstrates the result of magnetizing inductance obtained by FEA and analytical methods with different PM width, and the trend is very similar to that of fundamental flux. Due to the considerable error caused by the flux in the PM slot area, the simplified analytical model is unlikely to achieve acceptable accuracy. But the improved model is apparently much more complicated to calculate the sine and cosine integral functions in Equations (3-44) and (3-43).

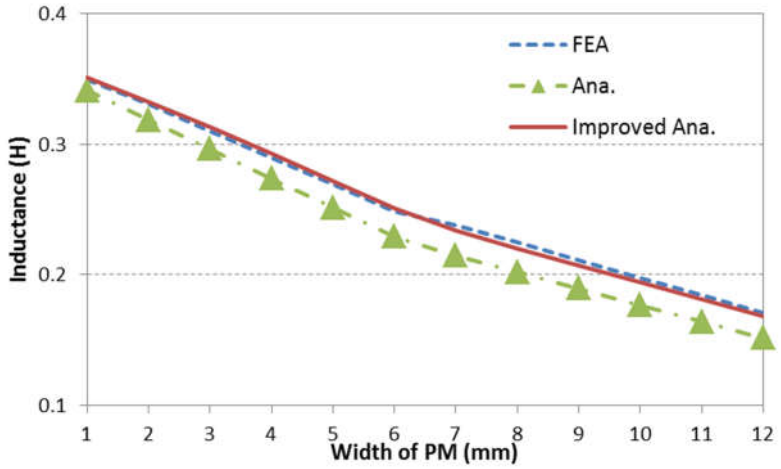

Figure 3-18 Q-axis magnetizing inductance L_{mq} against PM width by FEA and analytical models.

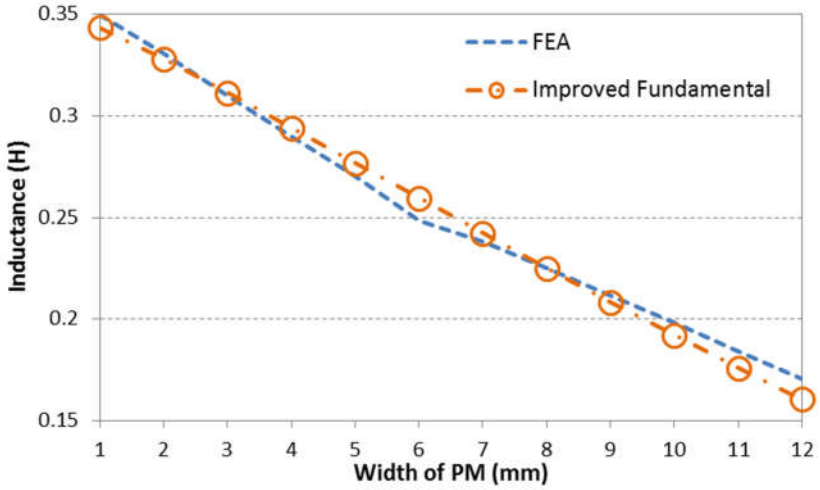

Figure 3-19 Q-axis magnetizing inductance L_{mq} against PM width by FEA and analytical model with only fundamental flux component.

Considering that good accuracy can be accomplished by the fundamental component, Equation (3-43) is calculated when u=v=1. Generally, β_1 is quite small due to the rotor geometric limits, and the q-axis magnetizing inductance due to the fundamental can be approximated as:

$$L_{mq} \approx L_{mq1} = \frac{8\mu_0 m N_a{}^2 R_{ro} l_{ef} k_{w1}{}^2}{\pi p^2 g_c} \left\{ \begin{array}{l} \left(1 - \frac{p\beta_1}{\pi} - \frac{\sin p\beta_1}{\pi}\right) \\ + \frac{4pg_c}{\pi^2 R_{ro}} \left[\left(1 - \frac{p^2\beta_1^2}{4}\right) \ln\left(1 + \frac{\pi R_{ro}\beta_1}{2g_c}\right) \right] \end{array} \right\} \quad \textbf{(3-46)}$$

where k_{w1} is the winding factor for the fundamental component. As shown in Figure 3-19, fair agreement for *q*-axis magnetizing inductance is obtained by only fundamental component. The accuracy is greatly improved comparing to simplified model and very clear relations between the q-axis magnetizing inductance and size of the PM is achieved. Despite of slightly lower accuracy than the complete model, the error by Equation (3-46) is within 5%, achieving a compromise between accuracy and simplicity.

3.2.2.4 Performance Based on Analytical Method

Based on the analytical models built, back electromotive force (EMF) can be obtained by

$$E_{mf}(t) = \frac{d\Psi_f}{dt} = \frac{4N_a R_{ro} l_{ef} \omega}{p} \sum_{v=2k-1} B_{fgv} k_{wv} \sin(v\omega t) \quad \textbf{(3-47)}$$

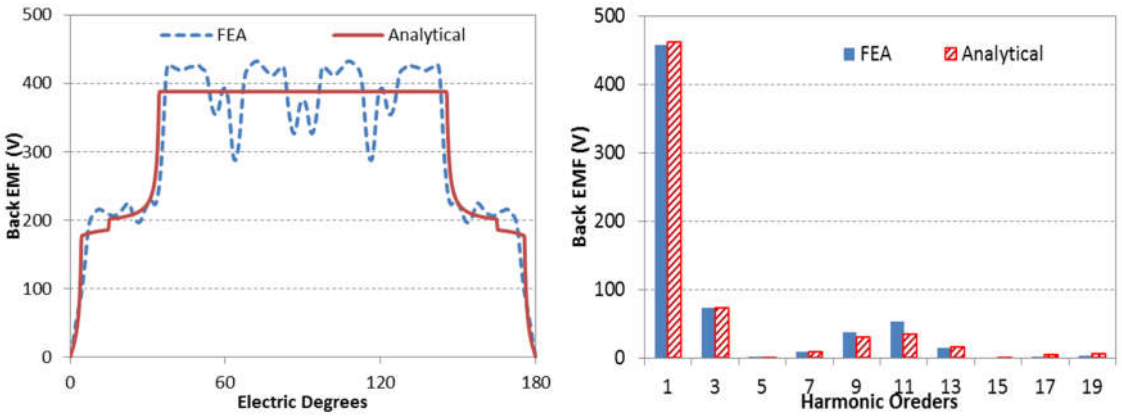

(a) Flux distribution; (b) Spectra;

Figure 3-20 Phase back EMF and spectra with W_1=8mm, L_1=31mm.

Figure 3-20(a) demonstrates the back EMF waveforms of FEA and analytical models with PM dimension of 8x31mm. Analytical method has a good capture of the actual back EMF, though some deviation is observed owing to the spatial harmonics caused by stator slots. As shown in Figure 3-20(b), the spectra of back EMF indicate quite accurate result of analytical model even for harmonic components, with less than 1% error for the fundamental. The variation trend of the back EMF against PM size is almost the same with the impact over PM flux distribution, as demonstrated in Figure 3-21. Harmonic contents are further

reduced by short-pitched windings except the tooth harmonics, and lower total harmonic distortion is seen in back EMF.

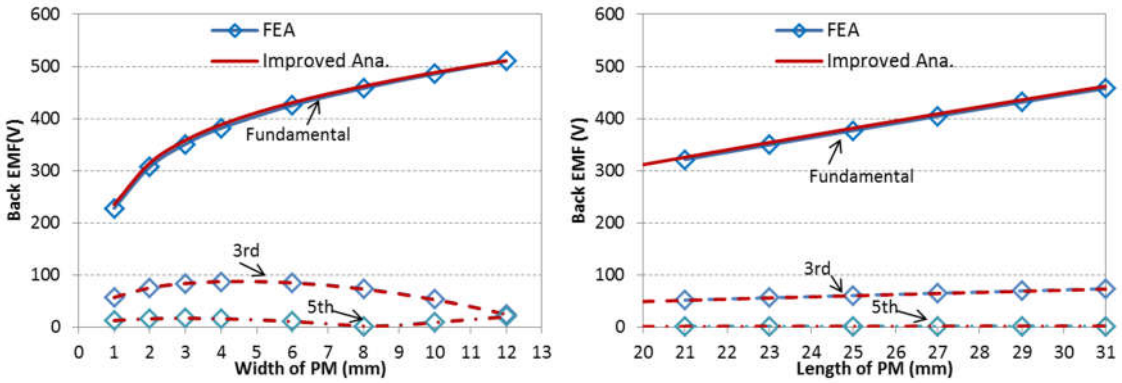

(a) Against W_1; (b) Against L_1;

Figure 3-21 Fundamental, 3rd and 5th components of Back EMF with different PM width and length.

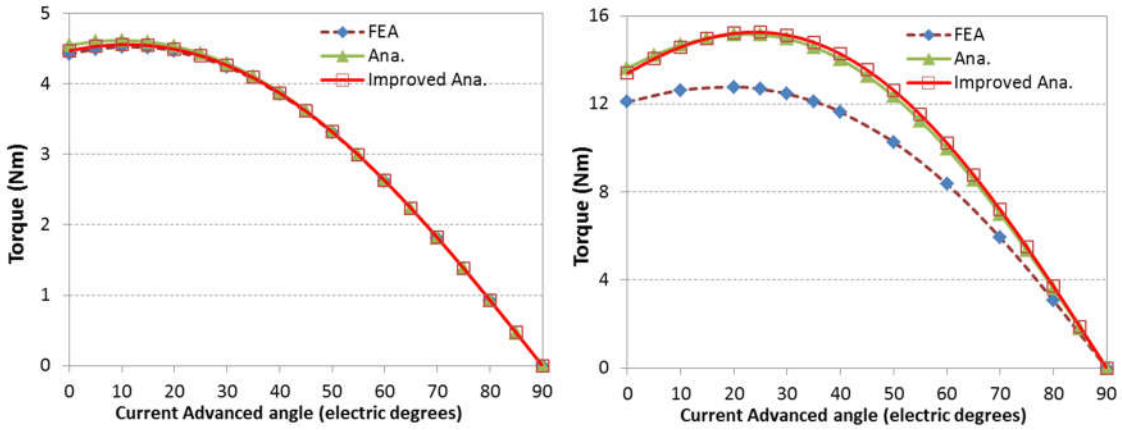

(a) Under 1/3 of rated current; (b) Under rated current;

Figure 3-22 Torque output of FEA and analytical models W_1=10mm, L_1=31mm.

According to [147], the total electromagnetic torque can be computed by:

$$T_{em} = \frac{mp}{4}\left[\Psi_f i_q + (L_d - L_q) i_d i_q\right] \quad \textbf{(3-48)}$$

where i_d and i_q is the d-axis and q-axis current respectively.

The torque profiles against current angle from both analytical and FEA with different PM width and length are illustrated in Figure 3-22. Under light current

loading conditions where the saturation in the machine is negligible, the result of the improved analytical model almost coincides with FEA and verifies the accuracy. The difference between the analytical and FEA methods increases under rated load condition when considerable saturation is occurring in the lamination cores. Since the reluctance of motor cores cannot be neglected, the corresponding PM excited field and armature reactive field would be weakened. Therefore, the actual torque would be lower than ideal model. In this case, the maximum torque output of analytical method is 19% higher than that of FEA in this case. But the trend of torque output against current angle can be followed and the optimal angle can be well predicted. As for the analytical model with the flux through PM slot ignored, slightly higher error is observed because more simplifications are made. And with slightly higher open-circuit flux density and lower dq-axis inductance derived, the analytical model shows higher torque at low current angle and lower torque at high current angle.

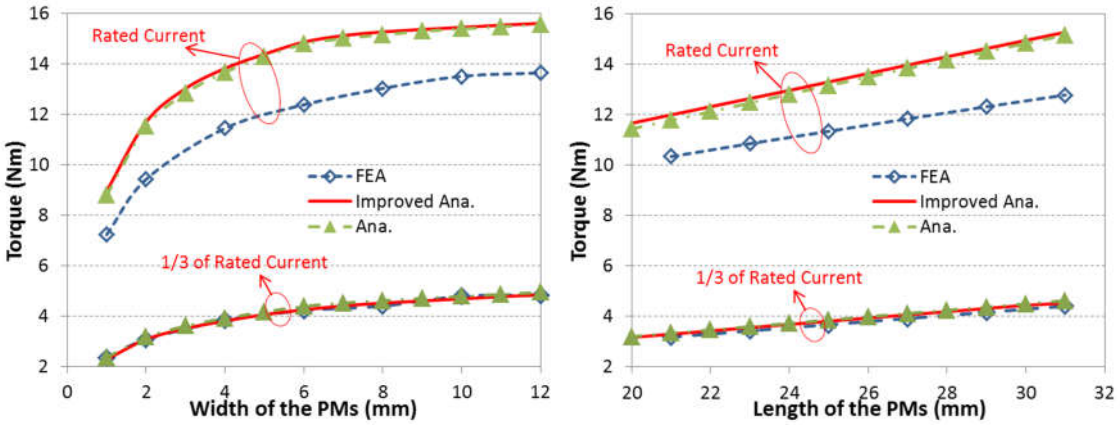

(a) With different PM width; (b) With different PM length;

Figure 3-23 Torque output with different PM width and length under light and rated load conditions.

Figure 3-23 demonstrates the influence of PM width and length over the maximum torque output. As expected, the analytical models agree with the FEA quite well under light load conditions. Despite that considerable error exists under heavy load conditions, the influence of the key design parameters can be predicted by the analytical models. The error ratio tends to rise with wider and longer PMs as a result of stronger PM field and thus higher saturation level in

the laminations. The results also show that larger amount of PM material enhances the overall torque output, because this can intensify PM flux and thus increase PM torque component. Although the armature reactive field and winding inductances will be reduced, it seems to have minor effect on the torque. That is because the PM torque component dominates the overall torque production for the one-layer spoke-type configuration, and thus larger amount of PM exhibits better effect for torque enhancement. When the PM width is small, it is effective to increase the torque output by using wider PMs, as the working point of the PM will be remarkably increased. But when the PM width is much larger than the airgap length, the improvement of torque is quite limited because of little increment in the PM working point but considerably increased reluctance in the PM slot area. On the other hand, longer PMs are more effective to increase the PM torque and thus the overall torque output, yet little impact was imposed on the rotor saliency.

3.2.3 Two-Layer Configuration

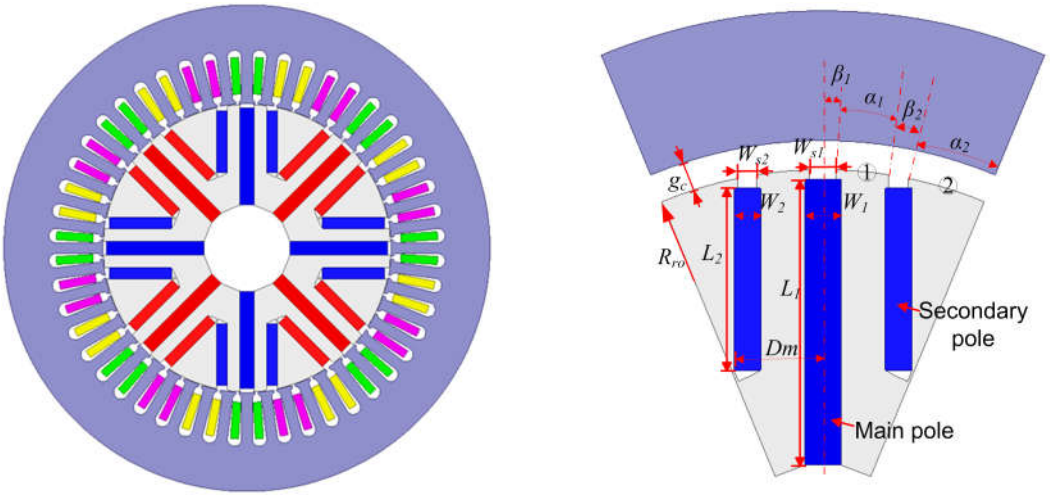

(a) Machine cross-section model; (b) Dimensional definitions;

Figure 3-24 Dimensions of two-layer machine model.

The cross-section of the two-layer spoke-type machine and the dimensional definitions for the analytical models are demonstrated in Figure 3-24. Each rotor pole consists of three magnets, which are the main PM with circumferential magnetization located in the middle, and two secondary magnets on both sides

of the main PM with the same magnetization direction. The neighbouring V-shaped poles are magnetized in opposite directions to form a flux focusing structure to increase the airgap flux density. Because secondary PM layers are introduced to the conventional spoke-type structure, the airgap region in half a pole-pitch area is divided into two portions, as illustrated in Figure 3-24(b). Area ① represents for the rotor lamination area in between main pole and one of its neighbouring secondary poles, while area ② denotes the region between two adjacent V-shaped PMs. R_{ro} is the outer radius of the rotor, g_c is the equivalent length of the airgap, W_1 and L_1 are width and length of the main PM poles, W_2 and L_2 are width and length of the secondary PM poles, W_{s1}, L_{s1}, W_{s2} and L_{s2} are the width and depth of the main and secondary PM slot opening respectively, D_m is the location of the secondary pole, β_1 is the mechanical radians of half of the main PM slot openings, and β_2, α_1 and α_2 are the mechanical radians of the secondary PM slot openings, area ① and ② respectively. Compared to the spoke-type, the two-layer rotor structure is more complicated. Because the rotor lamination area has been divided into two areas apart from the PM slot areas, more flux loops will be created. By proposing this novel rotor structure, more sinusoidal back-EMF waveform and higher rotor salient ratio is expected to improve the performance of ferrite PM machines.

3.2.3.1 Open-circuit flux and airgap flux distribution

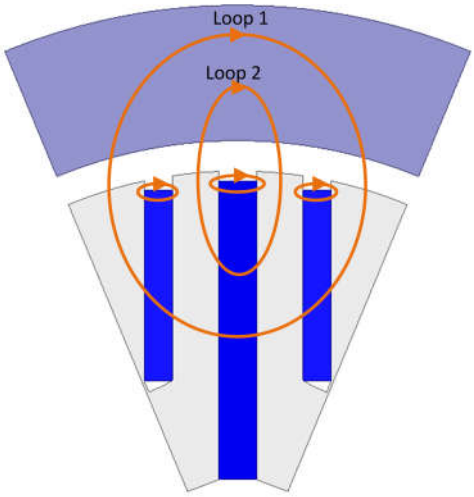

Figure 3-25 Flux loops excited by PMs of two-layer configurations.

The flux loops excited by PMs are depicted in Figure 3-25. Because all the flux goes through the main pole except the flux leakage of the secondary PMs, the main poles should have the major impact on the flux distributions. According to Ampere's law and flux conversion law, the flux of the main and leakage loops must fulfil the following equations:

$$\begin{cases} H_{m1}\cdot W_1 + 2\cdot H_{g1}\cdot g_c = 0 \\ H_{m1}\cdot W_1 + H_{s1}\cdot W_{s1} = 0 \\ H_{m1}\cdot W_1 + 2H_{m2}\cdot W_2 + 2H_{g2}\cdot g_c = 0 \\ H_{m2}\cdot W_2 + H_{s2}\cdot W_{s2} = 0 \end{cases} \tag{3-49}$$

$$\begin{cases} \phi_{m1} = \phi_{g1} + \phi_{g2} + \phi_{ml1} \\ \phi_{m2} = \phi_{g2} + \phi_{ml2} + \phi_{bri} \end{cases} \tag{3-50}$$

where H_{m1} and H_{m2} are the flux intensity of the main and secondary PMs, H_{g1} and H_{g2} are the flux intensity in the airgap area ① and ②, H_{s1} and H_{s2} are the flux intensity inside the main and secondary PM slots, and ϕ_{m1}, ϕ_{m2} ,ϕ_{g1}, ϕ_{g2}, ϕ_{ml1}, ϕ_{ml2} and ϕ_{bri} are the flux through the main PM, secondary PM, area ①, area ②, main PM slot, secondary PM slot and the saturation bridge respectively. Considering that W_1=W_{s1} and W_2=W_{s2}, the flux density of area ① and ② in the airgap can be derived:

$$B_{g1} = \frac{B_r\left[L_1\left(\mu_m L_2 + L_{s2}\right)W_1 g_c + L_1 W_1 W_2 R_{ro}\alpha_2 - L_2 W_1 W_2 R_{ro}\alpha_2\right]}{\left(\mu_m L_2 + L_{s2}\right)W_1 g_c R_{ro}\alpha_2 + \left[\left(\mu_m L_2 + L_{s2}\right)g_c + W_2 R_{ro}\alpha_2\right]\left[2\left(\mu_m L_1 + L_{s1}\right)g_c + W_1 R_{ro}\alpha_1\right]} \tag{3-51}$$

$$B_{g2} = \frac{B_r\cdot\left[L_1\left(\mu_m L_2 + L_{s2}\right)W_1 g_c + 2\left(\mu_m L_1 + L_{s1}\right)L_2 W_2 g_c + L_2 W_1 W_2 R_{ro}\alpha_1\right]}{\left(\mu_m L_2 + L_{s2}\right)W_1 g_c R_{ro}\alpha_2 + \left[\left(\mu_m L_2 + L_{s2}\right)g_c + W_2 R_{ro}\alpha_2\right]\left[2\left(\mu_m L_1 + L_{s1}\right)g_c + W_1 R_{ro}\alpha_1\right]} \tag{3-52}$$

If the flux in the PM slot areas should be taken into consideration, Equation (3-51) and (3-52) can be written as

$$B_{g1} = \frac{B_r L_1 W_1\left(\mu_m L_2 g_c + 2L_{s2}g_c + W_2 R_{ro}k_{rs2}\alpha_2\right) - B_r L_2 W_1 W_2 R_{ro}k_{rs2}\alpha_2}{\mu_m L_2 W_1 g_c R_{ro}k_{rs2}\alpha_2 + \left(\mu_m g_c L_2 + g_c L_{s2} + W_2 R_{ro}k_{rs2}\alpha_2\right)\left(2\mu_m L_1 g_c + 2L_{s1}g_c + W_1 R_{ro}k_{rs1}\alpha_1\right)} \tag{3-53}$$

$$B_{g2} = \frac{B_r\cdot\left[\mu_m L_1 L_2 W_1 g_c + L_2 W_2\left(2\mu_m g_c L_1 + 2g_c L_{s1} + W_1 R_{ro}k_{rs1}\alpha_1\right)\right]}{\mu_m L_2 W_1 g_c R_{ro}k_{rs2}\alpha_2 + \left(\mu_m L_2 g_c + L_{s2}g_c + W_2 R_{ro}k_{rs2}\alpha_2\right)\left(2\mu_m L_1 g_c + 2L_{s1}g_c + W_1 R_{ro}k_{rs1}\alpha_1\right)} \tag{3-54}$$

where k_{rs1} and k_{rs2} are the slot coefficients for the main and secondary PM slot openings, and they can be expressed by

$$k_{rs1} = 1 + \frac{2g}{\pi R_{ro}\alpha_1}\ln\left(1 + \frac{\pi \cdot R_{ro}\beta_1}{2g}\right) + \frac{2g}{\pi R_{ro}\alpha_1}\ln\left(1 + \frac{\pi \cdot R_{ro}\beta_2}{4g}\right) \quad \textbf{(3-55)}$$

$$k_{rs2} = 1 + \frac{4g}{\pi R_{ro}\alpha_2}\ln\left(1 + \frac{\pi \cdot R_{ro}\beta_2}{4g}\right) \quad \textbf{(3-56)}$$

$$\begin{cases} \beta_1 = \arcsin\dfrac{W_{s1}}{2R_{ro}}, \quad \beta_2 = \arcsin\dfrac{D_m}{R_{ro}} - \arcsin\dfrac{D_m - W_{s2}}{R_{ro}} \\ \alpha_1 = \arcsin\dfrac{D_m - W_{s2}}{R_{ro}} - \beta_1, \quad \alpha_2 = \dfrac{\pi}{p} - \arcsin\dfrac{D_m}{R_{ro}} \end{cases} \quad \textbf{(3-57)}$$

Based on the derived B_{g1} and B_{g2}, the waveform of the flux distribution in the airgap can be obtained. But it is more convenient to express the flux distribution in Fourier series to assess the fundamental component as well as higher order space harmonics. If infinite reluctance in the PM slot area is assumed, the magnitude of vth harmonic component is expressed by

$$B_{fgv} = \frac{4}{v\pi}B_{g2}\sin\left(v\frac{p\alpha_2}{2}\right) + \frac{4}{v\pi}B_{g1}\left[\sin\left(v\frac{\pi - p\beta_1}{2}\right) - \sin\left(vp\frac{\alpha_2 + \beta_2}{2}\right)\right] \quad \textbf{(3-58)}$$

With the consideration of the flux in the PM slot areas, the complete model for the vth flux component is included in

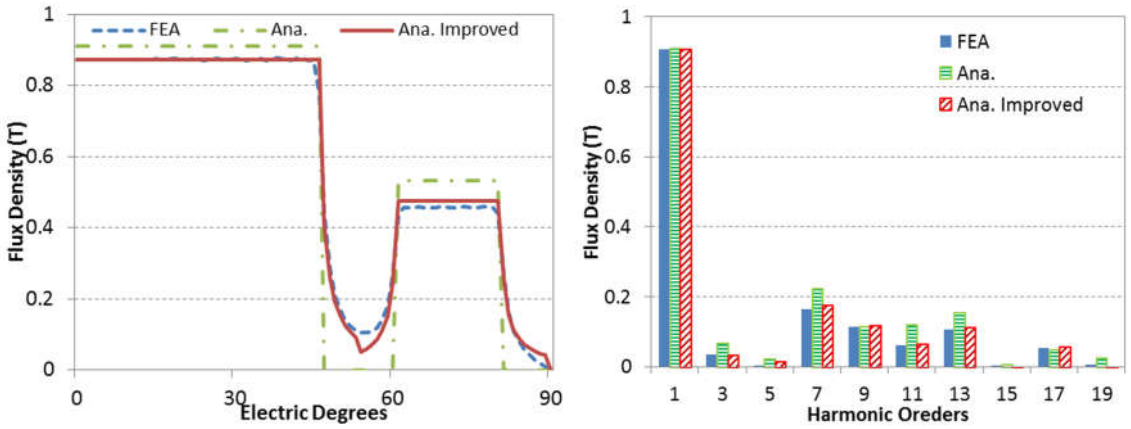

(a) Flux distribution; (b) Spectra;

Figure 3-26 of PM flux distribution and spectra in the airgap with smooth stator.

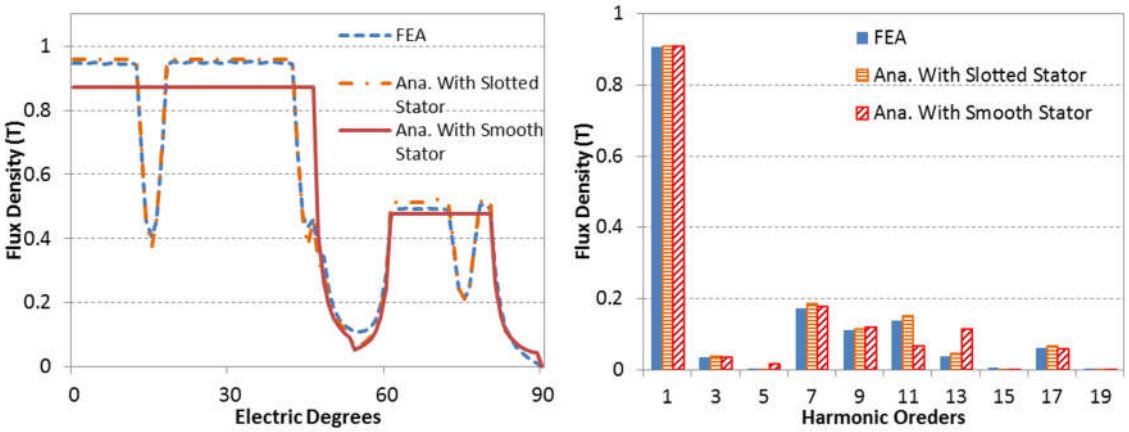

(a) Flux distribution; (b) Spectra;

Figure 3-27 Comparison of PM flux distribution and spectra in the airgap with slotted and smooth stator.

As there are more PM slots for the two-layer configurations, the analytical models are much more complicated than the one-layer ones. The flux distributions and spectra from analytical and FEA models are compared in Figure 3-26 with smooth stator for model verification. The flux density in the core area is slightly higher for the analytical model because all the main flux is assumed to go through this area. Compared with one-layer structure, the two-layer rotor has thinner PMs as more PM layers are applied within the same rotor diameter. Hence the slotting openings incur less harmonic content to the airgap flux distribution, and lower error ratio for the prediction is obtained. High accuracy for the fundamental is predicted with error less than 1% even though infinite reluctance in the PM slot areas is presumed. However, higher errors are observed for the harmonics as the flux in the PM slot area may not be negligible for them. On the other hand, with more complicated approximation of the flux distribution in the PM slot areas, higher accuracy can be achieved even for the harmonics by the improved analytical model.

Since stator slots are necessary to accommodate windings, their impact over flux distribution is also discussed. Figure 3-27 depicts the flux distributions with smooth and actual slotted stators. The flux distribution waveform can be further improved by considering the stator slots. Nevertheless, with the introduction stator slotting effect, noticeable improvements are only observed for the tooth

harmonics such as the 11th and 13th order in this case. In light of the complexity and minor improvement, the stator slotting effect is simplified with Carter's coefficient for the following discussions in this section.

Compared to the one-layer configuration, the two-layer machine contains lower harmonic contents because of the distinctive structure with two PM layers. Since the flux loops through the two core areas are different, two-stepped waveforms are created rather than the square-wave form of its one-layer counterparts. What's more, the flux waveform can be modified by adjusting the size and location of the secondary layers, and the two-layer configurations can potentially achieved more sinusoidal flux waveform with lower harmonic content. With the introduction of secondary layer, there are more parameters affecting the rotor design, and it is important to carry out investigations to understand the influence on the machine performance.

To get a clearer understanding of the relations of the key parameters and flux distribution, some approximation and simplification are made to obtain simpler equations. On the preconditions of much larger PM width than airgap length and zero flux in the PM slot area, Equation (3-58) can be simplified as:

$$B_{fgv} \approx \frac{4B_r}{v\pi}\left\{\frac{L_1 - L_2}{R_{ro}\alpha_1}\left[\sin\left(v\frac{\pi - p\beta_1}{2}\right) - \sin\left(vp\frac{\alpha_2 + \beta_2}{2}\right)\right] + \frac{L_2}{R_{ro}\alpha_2}\sin\left(v\frac{p\alpha_2}{2}\right)\right\} \quad \textbf{(3-59)}$$

Each flux component can be regarded as an addition of two parts, the flux distribution in core area ① and ②. The term $R_{ro}\alpha_2$ is the arc length of core area ②. Hence, B_{g2} can be regarded as proportional to secondary PM length which represents the secondary PM flux, and inversely proportional to area ② arc length which represents the area. Since the overall PM flux is decided by L_1 and the PM flux in area ② is decided by L_2, the flux in core area ① is proportional to (L_1-L_2). And B_{g1} is approximated by the flux difference between the main and secondary poles divided by the arc length of core area ①. That's the reason why the flux distribution can be adjusted by changing the length (or location) of the secondary poles, and two-stepped waveforms of the airgap flux distributions can be obtained with less harmonic content.

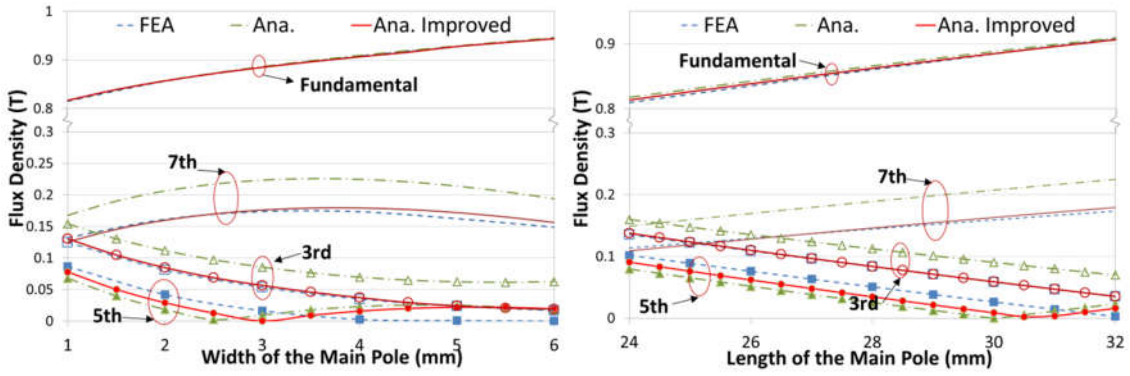

(a) Width of the main PM; (b) Length of the main PM;

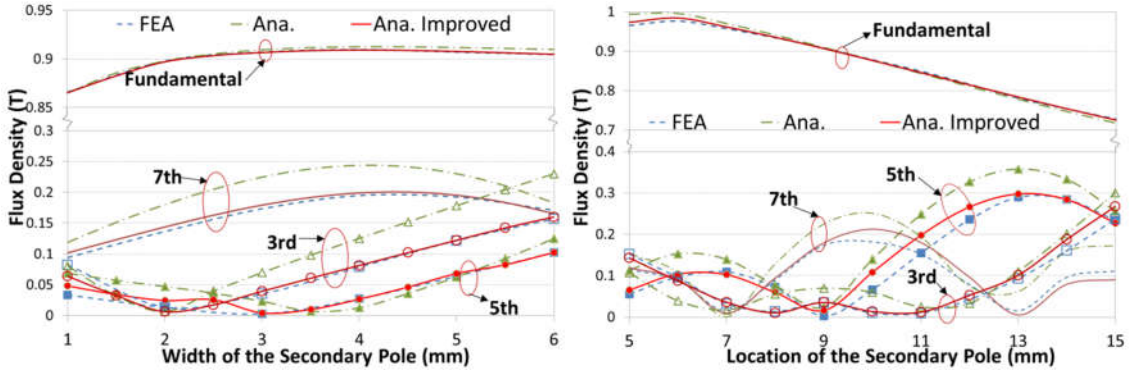

(c) Width of the secondary PM; (d) Location of the secondary PM;

Figure 3-28 Influence of the size and location of the main and secondary PMs on flux distribution.

The fundamental can be obtained by Equation (3-59) when ν=1. Since all the sine terms are positive, the fundamental always increases with width of the main PMs, as shown in Figure 3-28(a). That is because both the working points of the PMs and flux focus effect could be improved by thicker PM poles. But the effect of intensification decreases with thicker PMs as the PM working points get close to B_r. Therefore it is not as effective to increase the PM width to enhance PM flux field. More importantly, the PM width affects the PM slot opening and thus has considerable influence on the harmonics. The width of PMs should be chosen with the criteria of relatively high fundamental and low harmonic contents.

Equation (3-59) also indicates that the length of main PMs is proportional to the flux focusing effect and thus is able to increase airgap flux density effectively, as demonstrated in Figure 3-28(b). Since the two-layer configurations are

developed from the one-layer structures, the main PM poles have similar flux focusing effect. As the sine terms could be positive or negative for different order harmonics, their amplitudes may increase or decrease with main PM length. However, its impact on the harmonic content is quite small compared with other factors. Because the main PM length is the key factor to flux focusing effect, longer main PMs are preferred as long as there is enough space inside the rotor, and the harmonic content should be adjusted by modifying other sizing parameters.

The influence of the secondary PMs is quite different from the main PMs. The secondary poles play more active role in the flux allocation between the two core areas, as shown in Figure 3-28 (c). The width of the secondary PM doesn't have to be too thick, because its impact on intensify the fundamental is limited. The prime consideration should be on the harmonic content when choosing the width of secondary PMs.

The most active and complicated factor for the airgap flux distribution has been the location of secondary PMs. By changing the distance between the main and secondary poles, the arc length of the rotor lamination surface of area ① and ② together with the length of secondary poles are all changed. This will affect not only the amount of flux through area ② but also the shape of flux distribution waveforms. Therefore, both the fundamental and harmonics are greatly affected, as shown in Figure 3-28(d). As the secondary PM moves towards the main PM, D_m decreases and L_2 increases because the secondary pole can go deeper inside the rotor. Therefore, the total amount of PM increases and so does the arigap flux density. But when the secondary PM is very close to the main pole, the increment of L_2 and flux density becomes very small. And due to the increase of harmonic content, the fundamental flux may decline. In all, the fundamental flux distribution increases with smaller D_m. And when the secondary pole touches the main PM, the rotor becomes one-layer structure, which indicates that potentially higher flux density can be achieved for the one-layer configuration. Meanwhile, the harmonic contents are even more sensitive to the location of secondary PM. Owing to the re-allocation of the PM flux

between area ① and ②, the square flux waveform of the one-layer machine could be modified into two-stepped waveform for the two-layer structure with lower harmonic content. But if over adjusted, the flux distribution could be deteriorated with dramatically increased harmonics.

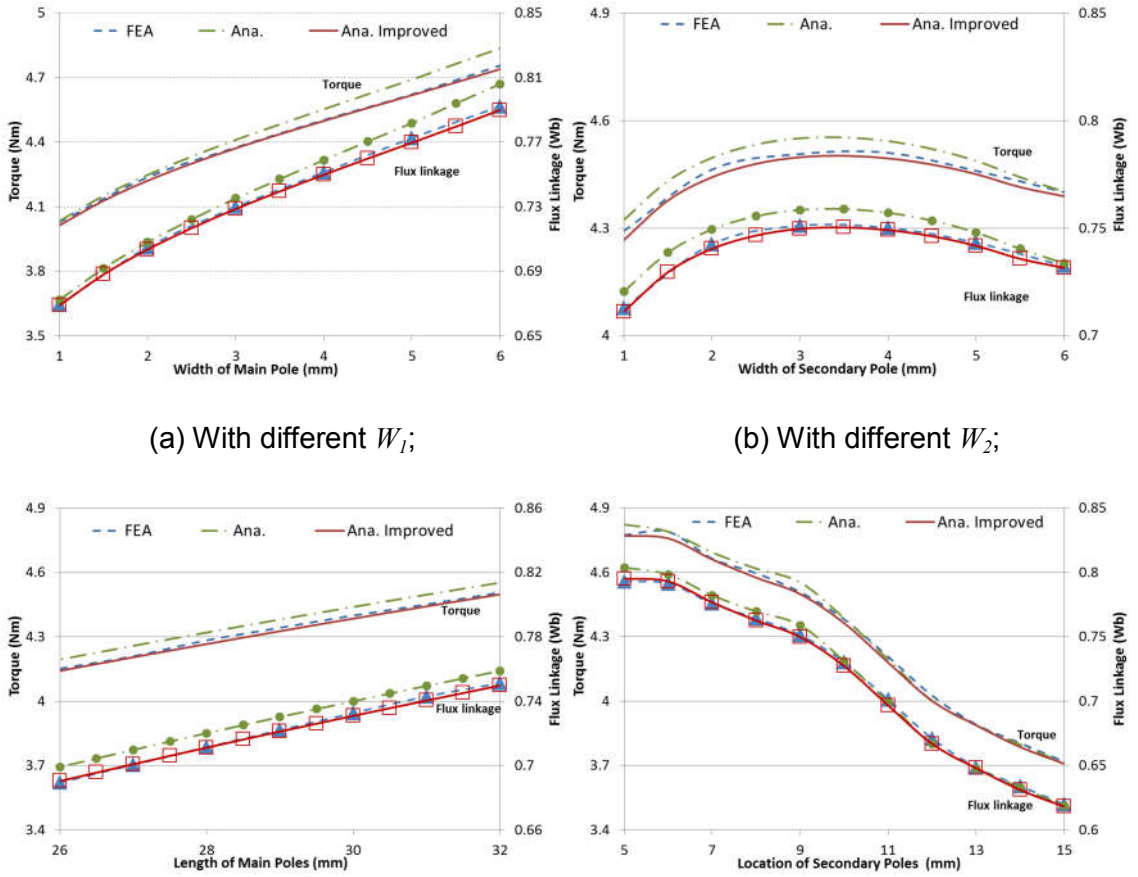

(a) With different W_1; (b) With different W_2;

(c) With different L_1; (d) With different D_m;

Figure 3-29 PM flux linkage and PM torque with difference PM poles.

Similarly, the PM flux linkage and PM torque can be obtained by Equation (3-23) and (3-24), and the influence of different parameters on the performance is demonstrated in Figure 3-29. Obviously, both the PM flux linkage and torque share the same trends over different parameters with the fundamental flux distribution, as normally over 97% of the flux linkage and torque are due to the fundamental flux. As expected, longer PMs can enhance the flux linkage and PM torque effectively and linear relation is observed between main PM length and PM flux linkage (torque). Thicker main PMs can also increase PM flux linkage and torque in terms of high working point and flux density, but not as

effectively as increasing PM length in terms of the amount of ferrite used. Since compositions of the fundamental and harmonic contents of the flux density are quite sensitive to the location of the secondary pole, PM flux linkage and torque are all affected greatly. In general smaller D_m can increase the secondary pole length, and thus higher PM flux and PM torque are achieved. This indicates that conventional spoke-type configuration is able to achieve higher PM torque. But the one-layer configuration contains larger harmonic contents, which would incur higher core loss and torque ripple. With carefully designed secondary PM layers, the flux distribution waveform in the airgap can be improved with less harmonic content whereas the fundamental can be kept approximately the same to conventional spoke-type structures. Furthermore, the location of the secondary PMs has prominent influence on the rotor salient ratio, which will affect the reluctance torque component greatly and will be discussed in the following sections.

3.2.3.2 D-Axis Magnetizing Inductance

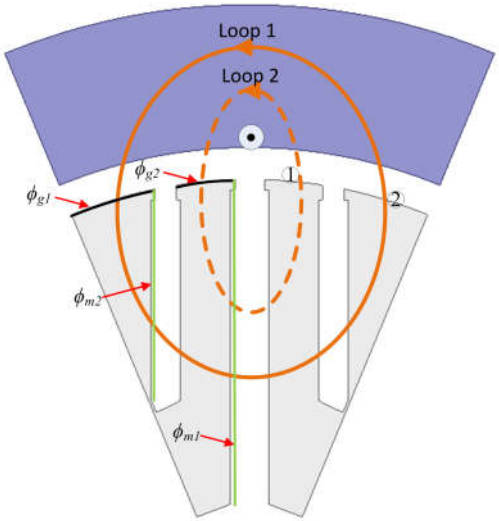

Figure 3-30 Flux loops for two-layer configuration under d-axis current.

The magnetic flux loops excited by d-axis armature current in one pole pitch area is depicted in Figure 3-30. The flux loops are similar to PM excited field except that there is no flux leakage in the rotor PM slots. By applying the Ampere's law and the flux conversion law, the d-axis MMF and flux through different areas should satisfy the following equations:

$$\begin{cases} 2F_{ad}(\theta) = H_{m1d}W_1 + 2H_{gd}(\theta)g_c & \dfrac{p\alpha_2 + p\beta_2}{2} \le \theta \le \dfrac{\pi}{2} - \dfrac{p\beta_1}{2} \\ 2F_{ad}(\theta) = H_{m1d}W_1 + 2H_{m2d}W_2 + 2H_{gd}(\theta)g_c & 0 \le \theta \le \dfrac{p\alpha_2}{2} \end{cases} \quad \textbf{(3-60)}$$

$$\begin{cases} \phi_{m1} = \phi_{g1} + \phi_{g2} \\ \phi_{m2} = \phi_{g2} \end{cases} \quad \textbf{(3-61)}$$

where H_{m1d} and H_{m2d} are the flux intensity inside the main and secondary PM slots, ϕ_{m1} and ϕ_{m2} are the flux going across the main and secondary PM slots, $H_{gd}(\theta)$ is flux intensity in the airgap, ϕ_{g1} and ϕ_{g2} is the flux through the rotor core area ① and ② in half a pole-pitch area, respectively. By solving Equation (3-60) and (3-61), the flux intensity inside the main and secondary PM slots can be derived by:

$$H_{m1d} = \frac{\dfrac{4}{p}\left\{\sum_{v\neq mk}\frac{F_{adv}}{v}\left[\sin v\left(\frac{\pi}{2} - \frac{p\beta_1}{2}\right) - \sin v\left(\frac{p\alpha_2 + p\beta_2}{2}\right)\right] + \frac{g_c(L_2 + L_{s2})}{W_2\alpha_2 R_{ro} + g_c(L_2 + L_{s2})}\sum_{v\neq mk}\frac{F_{adv}}{v}\left[\sin\left(v\frac{p\alpha_2}{2}\right)\right]\right\}}{W_1\alpha_1 + \dfrac{2g_c(L_1 + L_{s1})}{R_{ro}} + \dfrac{W_1 g_c(L_2 + L_{s2})\alpha_2}{W_2 R_{ro}\alpha_2 + g_c(L_2 + L_{s2})}} \quad \textbf{(3-62)}$$

$$H_{m2d} = \frac{\dfrac{4}{p}\sum\frac{F_{adv}}{v}\left[\sin\left(v\frac{p\alpha_2}{2}\right)\right] - B_{m1d}W_1\alpha_2}{2W_2\alpha_2 R_{ro} + 2g_c(L_2 + L_{s2})}R_{ro} \quad \textbf{(3-63)}$$

According to the flux loops demonstrated in Figure 3-30, all main flux travels across the main PM slot, and the flux of rotor core area ② passes through secondary PM slot. Thus, the two-stepped rotor MMF waveform is obtained by:

$$F_{rs}(\theta) = \begin{cases} H_{m1d}W_1 + 2H_{m2d}W_2 & 0 \le \theta \le \dfrac{p\alpha_2}{2} \\ H_{m1d}W_1 & \dfrac{p\alpha_2}{2} < \theta \le \dfrac{\pi}{2} \end{cases} \quad \textbf{(3-64)}$$

To maintain the unified format for the equations, the rotor MMF is decomposed into Fourier series, and the amplitude of the vth component is expressed by

$$F_{rsv} = \frac{4}{\pi v}\left[H_{m1d} W_1 \sin\left(v\frac{\pi}{2} \right) + 2H_{m2d} W_2 \sin\left(v\frac{p\alpha_2}{2} \right) \right] \tag{3-65}$$

Then the flux density distribution excited by the vth MMF in the lamination pole area is calculated by:

$$B_{adv}(\theta) = \frac{2\mu_0 F_{adv} - \mu_0 F_{rsv}}{2g_c} \cos(v\theta) \tag{3-66}$$

Since the d-axis flux travels across the PM slots inside the rotor, the flux distribution excited by each MMF component will be severely distorted. Together with further deformation caused by PM slot opening in the airgap, $B_{adv}(\theta)$ is not the actual vth harmonic order of the airgap flux. Therefore, Fourier transformation is applied to each armature MMF harmonic field, and the vth harmonic component for the flux distribution is obtained by:

$$B_{gdv} = \sum_{u=1}^{2k+1}\left[\frac{1}{\pi}\int_0^{2\pi} B_{adu} \cos(u\theta)\cos(v\theta)\, d\theta \right] = \sum_{u=1}^{2k+1} B_{gduv} \tag{3-67}$$

With the flux in the PM slot areas assumed to be zero, the following is derived:

$$\begin{aligned} B_{gduv} &= \frac{4}{\pi} B_{adu}\left[\int_0^{\frac{p\alpha_2}{2}} \cos(u\theta)\cos(v\theta)\, d\theta + \int_{\frac{p(\alpha_2+\beta_2)}{2}}^{\frac{\pi - p\beta_1}{2}} \cos(u\theta)\cos(v\theta)\, d\theta \right] \\ &= \begin{cases} B_{adu}\left[1 - \dfrac{p(\beta_1+\beta_2)}{\pi} + \dfrac{\sin v(\pi - p\beta_1) - \sin vp(\alpha_2+\beta_2) + \sin vp(\alpha_2)}{v\pi} \right] & (u = v) \\ \dfrac{2}{\pi} B_{adu}\left[\dfrac{\sin\dfrac{(u+v)p\alpha_2}{2} + \sin\dfrac{(u+v)(\pi - p\beta_1)}{2} - \sin\dfrac{(u+v)p(\alpha_2+\beta_2)}{2}}{u+v} + \right. & \\ \left. + \dfrac{\sin\dfrac{(u-v)p\alpha_2}{2} + \sin\dfrac{(u-v)(\pi - p\beta_1)}{2} - \sin\dfrac{(u-v)p(\alpha_2+\beta_2)}{2}}{u-v} \right] & (u \neq v) \end{cases} \end{aligned} \tag{3-68}$$

where B_{gdv} is the vth flux distribution in the airgap, $B_{adu}(\theta)$ denotes flux distribution due to the uth MMF component, and $B_{gduv}(\theta)$ represents the vth order component of $B_{gdu}(\theta)$. Because of more PM slots for the two-layer structure, the expression will be much more complicated by taking PM slot flux into consideration. The complete model is included in Appendix A.1.

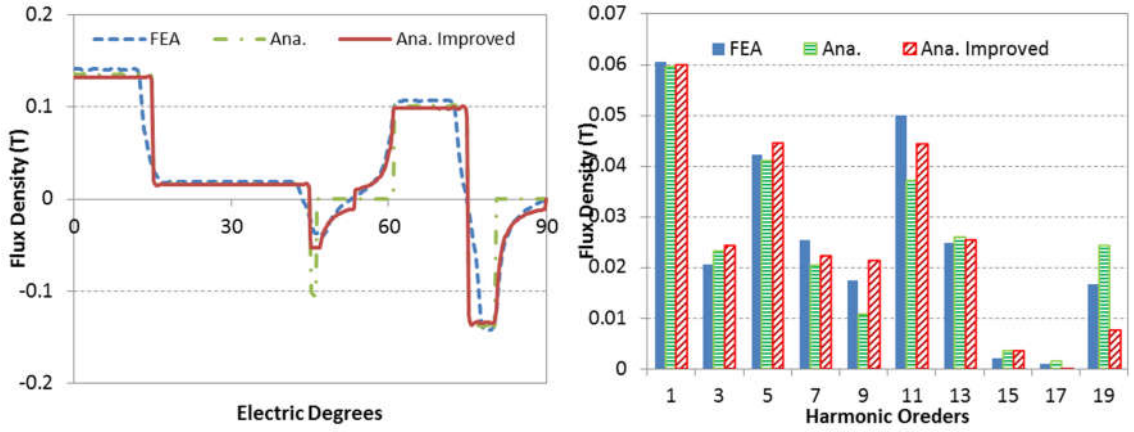

(a) Flux distribution; (b) Spectra

Figure 3-31 Flux distribution and spectra in the airgap excited by d-axis current.

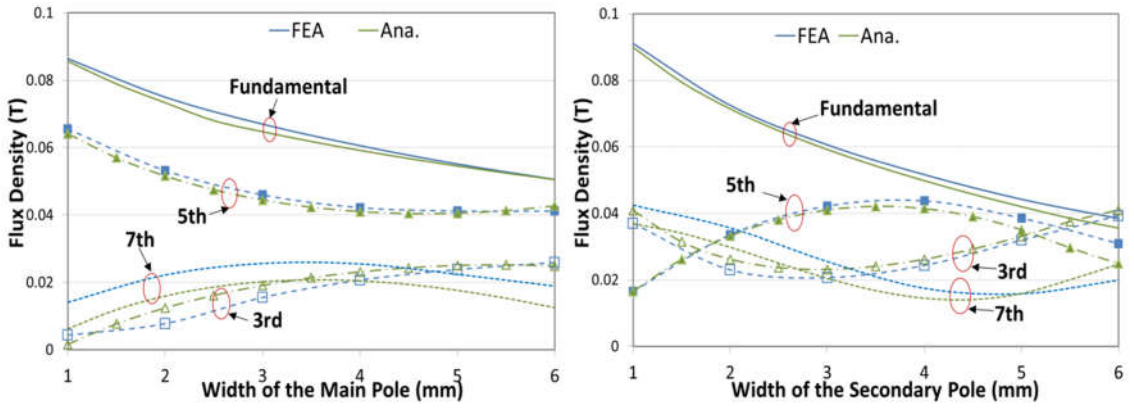

(a) With different W_1; (b) With different W_2;

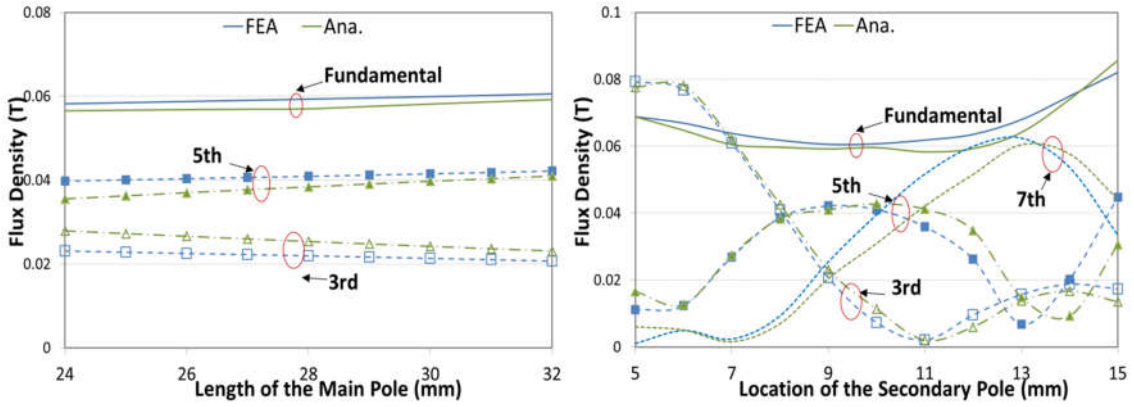

(c) With different L_1; (d) With different D_m;

Figure 3-32 Fundamental, 3rd and 5th component of flux distribution excited by d-axis current.

The flux distributions and their spectra are illustrated in Figure 3-31. Despite of zero flux in the PM slot areas are assumed, the analytical models show good agreement with FEA results. The improved analytical method exhibits slightly higher accuracy in the PM slot areas by considering the flux through them. But the model is too complicated because of the more intricate geometrical design of two-layer rotor. Usually the width of PM slot openings are much smaller than the one-layer configuration, the influence on the airgap flux distribution is much lower. As shown in Figure 3-31(b), the spectra analysis indicates that acceptable accuracy can be achieved by the analytical model even with the flux in the PM slots neglected.

Figure 3-32 depicts the fundamental as well as some main order harmonic components against the key design parameters. Since the main MMF drop in the flux loops is on the PM slots, larger PM slot width leads to significant decrease in fundamental flux. The width of the PMs also exhibits considerable impact on the harmonic contents due to the distortion of the PM slots. The width of the secondary PM shows higher influence than the main PM due to its more active role in the flux allocation between the two core areas. Since longer PMs would increase the permeance of the PM slots, subtle increment in flux density can be observed. However, since the reluctance of the PM slot is mainly decided by the width, the influence of the main PM slot length over the flux distribution can be ignored. And the most influential parameter on the flux distribution has been the location of the secondary pole. As the flux waveform will be serious shaped and the flux through area ① and ② is regulated, both the fundamental and the harmonic components are significantly affected.

With flux distribution solved, the d-axis magnetizing inductance of can be obtained by Equation (3-38), and the results of both FEA and analytical models are depicted and compared in Figure 3-33. As the fundamental flux contributes to the major part of the magnetizing flux linkage, similar influences are observed for the inductance. The d-axis magnetizing inductance decreases dramatically with larger PM width of the main and secondary PMs because of larger PM slot reluctance. The length of the main PM slot has subtle impact on the flux

distribution excited by armature MMF, and thus there is only marginal increment in the inductance with longer PM slots. In spite that the location of secondary poles has a high impact on the harmonic compositions of the flux distribution, no significant variation is seen for the inductance when D_m is not very large. As the secondary pole moves further away from the main pole, the arc length of area ② and the length of secondary PMs reduce dramatically. Consequently, most of the main flux goes by Loop 1 through area ②, and only needs to travel across the main PM slot. The reluctance of the flux loops decreases and the inductance increases significantly. It should be noted that the flux distribution due to the d-axis current contains high amount of harmonics, which also generates flux linkage in the windings and contributes to inductance. It should be of interest to investigate the contributions by harmonics to understand their influence on the flux linkage and inductance.

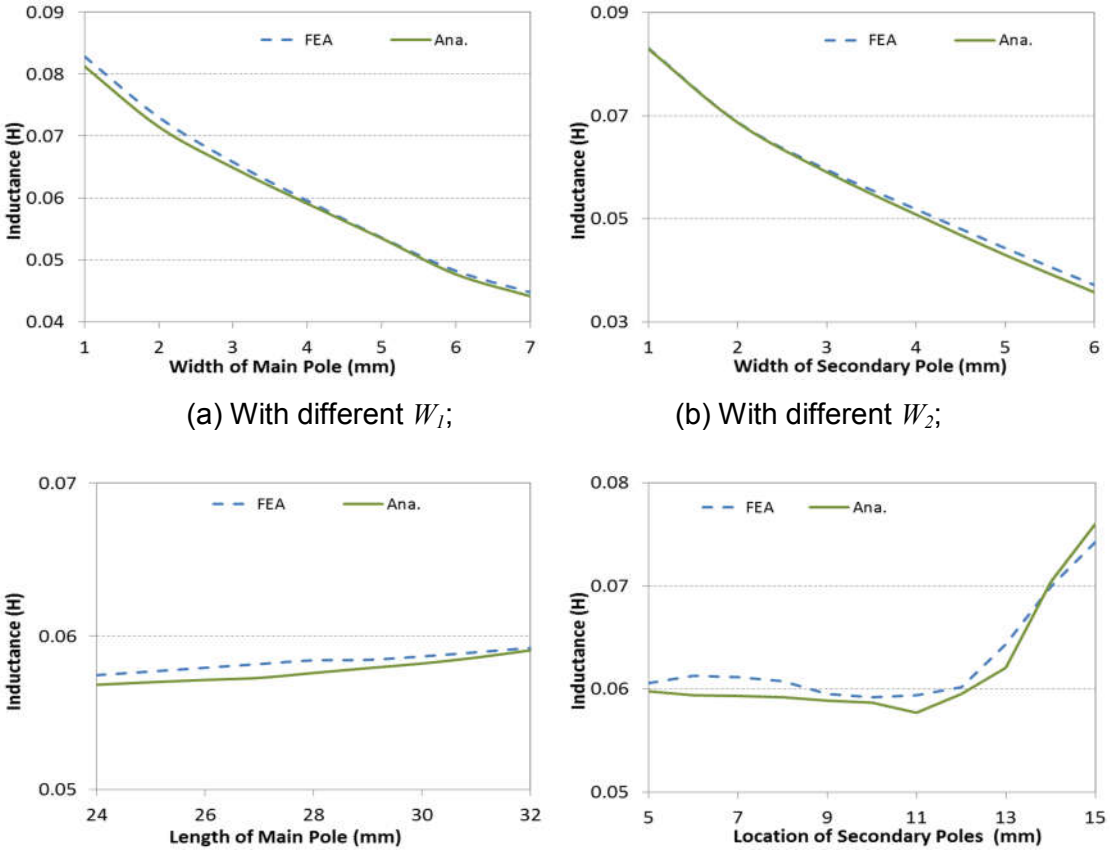

(a) With different W_1; (b) With different W_2;

(c) With different L_1; (d) With different D_m;

Figure 3-33 Comparison of d-axis magnetizing inductance against different rotor design paratmeters.

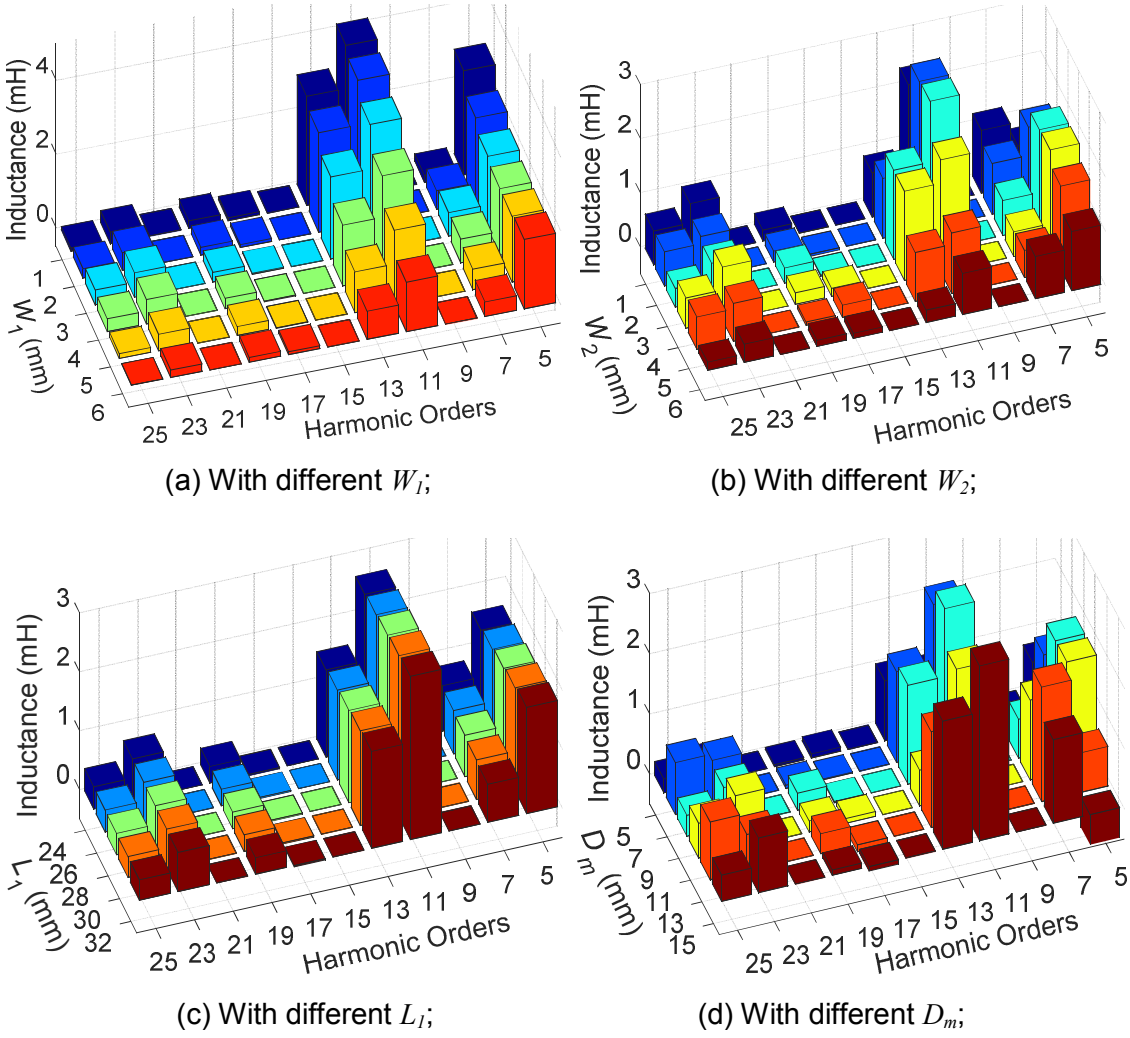

Figure 3-34 Contributions of flux harmonics to *d*-axis magnetizing inductance.

The contributions of flux harmonics to d-axis inductance against different PM parameters are illustrated in Figure 3-34. Due to the relatively large contents of 5th and 7th order harmonics, a considerable part of the magnetizing inductance is due the harmonic flux linkage. Up to 15% of L_{md} could be generated by harmonics, especially from 5th, 7th and tooth harmonic orders such as 11th and 13th. Since all the flux goes through the main PM slot, the harmonics also decreases with wider W_1. But little impact is seen from L_1. Because a large part of the flux needs to cross the secondary PM slots as well, harmonic contents reduced with W_2 in general. On the other hand, the location of secondary poles has huge effect on the harmonic content, and the inductance contribution of different harmonics varies enormously with D_m, which makes this parameter very important to regulate the harmonic contents of the flux distribution.

3.2.3.3 Q-Axis Magnetizing Inductance

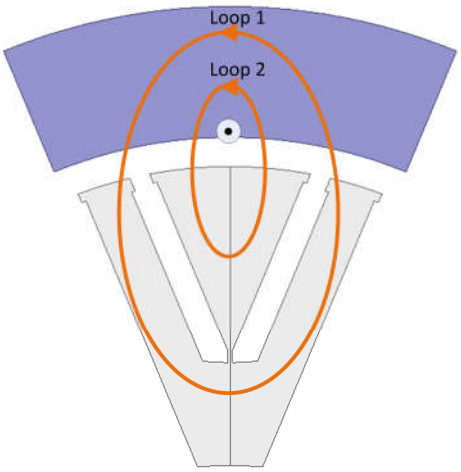

Figure 3-35 Flux loops for two-layer configuration under q-axis current

The flux loops excited by q-axis current are depicted in Figure 3-35. The main flux does not pass through the PM slot, and the MMF drop occurs only in the airgap. Although two flux loops are displayed in Figure 3-35, their equivalent magnetic circuit models are exactly the same. The two flux loops are actually one, and the flux distribution in the core areas due to the vth order MMF can be expressed by:

$$B_{aqv}(\theta)=\frac{\mu_0 F_{aqv}(\theta)}{g_c}=\frac{2\mu_0 m N_a k_{wv}}{\pi v p g_c} i_q \cos(v\theta) \tag{3-69}$$

With the flux in the PM slot area neglected, the amplitude of the vth harmonic can be derived by Fourier transformation:

$$B_{gdv}=\sum_{u=1}^{2k+1}\left[\frac{1}{\pi}\int_0^{2\pi} B_{adu}(\theta)\cos(v\theta)\,d\theta\right]=\sum_{u=1}^{2k+1} B_{gduv} \tag{3-70}$$

$$B_{gquv}=\begin{cases} B_{aqu}\left[1-\dfrac{p(\beta_1+\beta_2)}{\pi}+\dfrac{\sin vp(\alpha_1+\beta_1)-\sin(vp\beta_1)-\sin v(\pi-p\alpha_2)}{v\pi}\right] & (u=v) \\ \dfrac{2}{\pi}B_{aqu}\left[\dfrac{\sin\dfrac{(u+v)p(\alpha_1+\beta_1)}{2}-\sin\dfrac{(u+v)p\beta_1}{2}-\sin\dfrac{(u+v)(\pi-p\alpha_2)}{2}}{u+v}\right. & \\ \left.+\dfrac{\sin\dfrac{(u-v)p(\alpha_1+\beta_1)}{2}-\sin\dfrac{(u-v)p\beta_1}{2}-\sin\dfrac{(u-v)(\pi-p\alpha_2)}{2}}{u-v}\right] & (u\neq v) \end{cases} \tag{3-71}$$

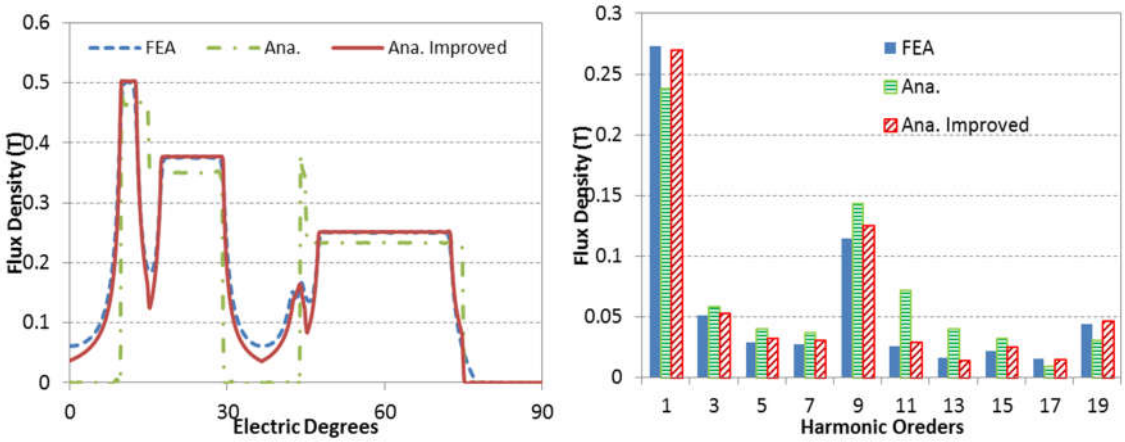

(a) Flux distribution; (b) Spectra;

Figure 3-36 Flux distribution and spectra in the airgap excited by q-axis current.

And if the slotting effect is to be considered, the flux distribution in the slot areas needs to be approximated as suggested in Figure 3-1, which would associate with complicated calculation of sine and cosine integral functions for the main and secondary PM slot openings. The complete analytical model with consideration of the PM slot flux is included in Appendix A.2.

The flux distribution and spectra in the airgap excited by q-axis current for a typical two-layer model are depicted in Figure 3-36. The flux waveform by FEA can be well followed by the analytical methods. But the spectra of the airgap flux distribution indicate that noticeable error on the fundamental is caused due to the ignored flux in the PM slot areas. Since the maximum value of armature MMF appears in the main PM slot area, the average flux density in the main slot area is still over 10% that of the maximum value in the core area and cannot be ignored completely. Additionally, this part of flux has higher contributions to the fundamental according to the definition of Fourier transform with electric position close to zero. As a result, fundamental component derived by the analytical method is over 10% lower. Because the fundamental is the major source of the armature flux linkage, the error would result in considerable inaccuracy for the prediction of flux linkage and inductance. On the other hand, fair agreement can be achieved by the analytical model when the harmonic order is lower than ten. With the improved analytical model, more accurate

result can be achieved for both the fundamental and harmonic components at the expense of much more complicated model.

Despite of the very high accuracy accomplished by the improved analytical model, the equations are too complicated and it is difficult to obtain clear relations between the machine performance and the key design parameters. In order to achieve acceptable accuracy for analytical method, the flux through PM slot areas has to be taken into account. Since the fundamental is extremely critical for the machine performance prediction and is not accurately estimated in the simplified analytical model, it is of great importance to find a simpler way to improve the accuracy without complicating the overall model too much.

The fundamental content of the airgap flux is derived by summation of the first order component decomposed from all the flux components excited by various armature MMF harmonics. However, the maximum flux density excited by the vth MMF is inversely proportional to v, and would be further reduced due to short pitch windings according to Equation (3-69). By performing Fourier transform, the decomposed fundamental from flux field excited by the vth MMF harmonic will be further reduced to at least $1/v$ according to Equation (3-71). Thus, the fundamental content due to higher order stator MMF excitation is very small, and the flux distribution induced by the fundamental MMF is of sufficient accuracy to be included for the analytical method. As the flux in the PM slots areas cannot be ignored, the flux excited by fundamental MMF in these regions should also be added as compensation to the fundamental. Considering that rotor radius is much larger than the width of the main and secondary PM slots, an approximation of the fundamental flux component for the analytical method can be revised as:

$$B_{gq1} \approx \frac{2\mu_0 m N_a k_{w1}}{\pi p g_c} i_q \left\{ \begin{array}{l} 1 - \dfrac{p(\beta_1+\beta_2)}{\pi} + \dfrac{\sin p(\alpha_1+\beta_1) - \sin(p\beta_1) - \sin(\pi - p\alpha_2)}{\pi} \\ + \dfrac{4pg_c}{\pi^2 R_{ro}} \left[\begin{array}{l} \left(1 - \dfrac{p^2\beta_1^2}{4}\right) \ln\left(1 + \dfrac{\pi R_{ro}\beta_1}{2g_c}\right) + \ln\left(1 + \dfrac{\pi R_{ro}\beta_2}{4g_c}\right) \\ + \cos\left(p\dfrac{2\alpha_1 + 2\beta_1 + \beta_2}{2}\right) \ln\left(1 + \dfrac{\pi R_{ro}\beta_2}{4g_c}\right) \end{array} \right] \end{array} \right\} \quad \textbf{(3-72)}$$

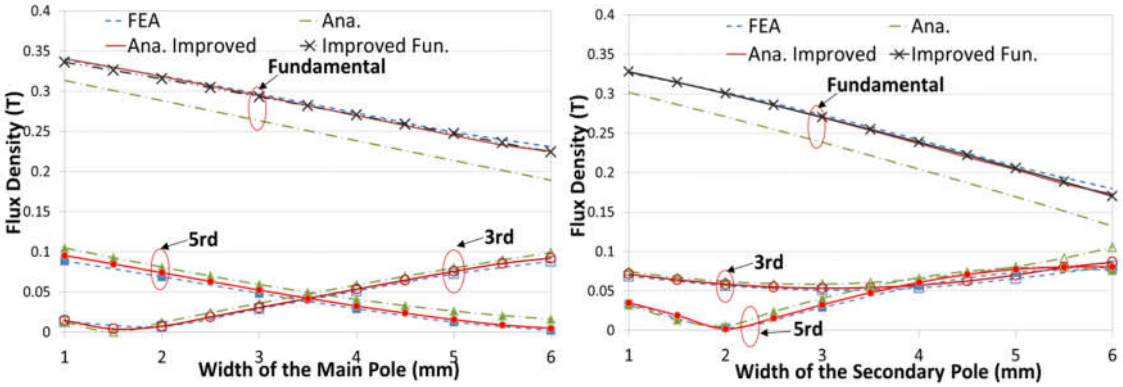

(a) With different W_1; (b) With different W_2;

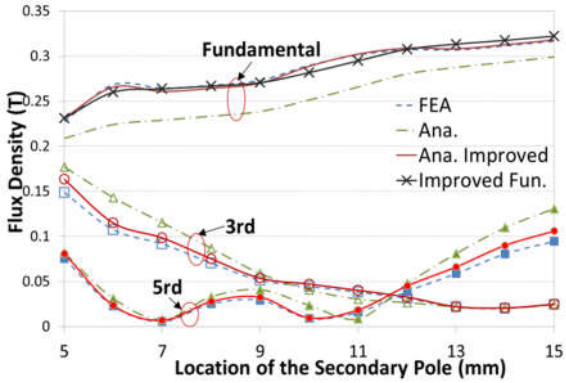

(c) With different D_m;

Figure 3-37 Fundamental, 3rd and 5th components of flux distribution excited by of q-axis armature current.

The results of the flux distribution by FEA and different analytical methods are demonstrated in Figure 3-37. With the compensation of the PM slot flux, great improvement is achieved for the fundamental with relatively simple model. The two-layer structure exhibits much lower harmonic contents compared with to the one-layer configurations. Since the higher order harmonics is not as critical and good agreement is accomplished, the simplified analytical model could be used for the prediction of the harmonic components.

As indicated in Equation (3-72), the fundamental flux decreases with the width of the main and secondary PM slots. That's because wider PM slots enlarge slot area and reduce the equivalent airgap permeance. On the other hand, the location of the secondary poles also has considerable influence on the fundamental. As secondary PM slots moving away from the main pole, the flux

density in the secondary PM slot area becomes weaker due to the lower q-axis stator MMF, while the flux field excited by the fundamental MMF is less affected. However, since the airgap flux distribution waveform can be flexibly modulated by changing the location of the secondary pole, the flux waveform as well as harmonic contents are significantly affected, which could be made full use of during the machine design process to obtain higher flux linkage and inductance. The length of main pole doesn't have any influence over the q-axis flux distribution in the theoretical model, and it is not discussed.

For the sake of simplicity, the magnetizing inductance is calculated using only the improved fundamental flux component, and the result is compared with FEA in Figure 3-38. The results show similar varying trend with the flux fundamental component, and sufficient accuracy is achieved. Due to the neglecting of the flux in the PM slot areas for the higher harmonics, the error would be slightly higher as PM slot width increases. Since the harmonic content is greatly affected by the secondary PM location, higher variation is observed as the location changes. In all, much simpler model and fairly good accuracy can be achieved by the approximated model, and the error ratio is within 3%. The contributions of various harmonics to the magnetizing inductance are demonstrated in Figure 3-39, and the higher order harmonics show very low impact on the inductance as a result of low harmonic contents. The fundamental flux contributes over 95% of the flux linkage and magnetizing inductance, and the highest contribution from a single harmonic component is less than 3%.

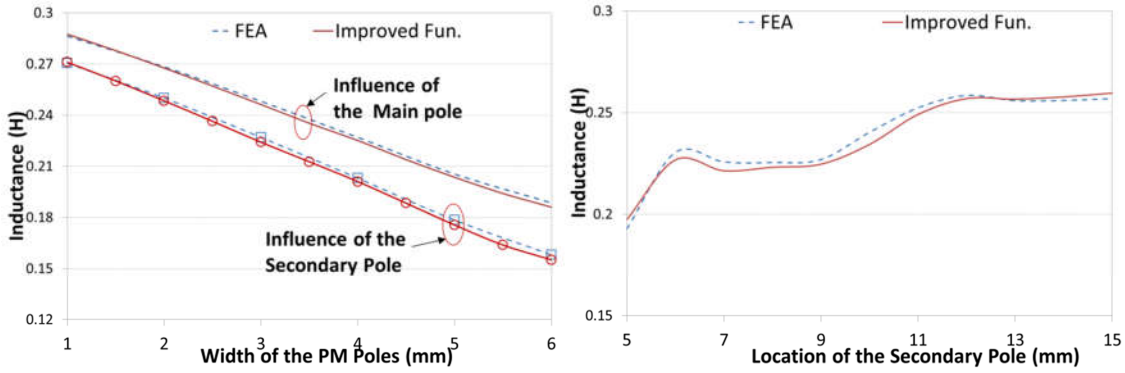

(a) With different PM width; (b) With different secondary pole location;

Figure 3-38 Comparison of q-axis magnetizing inductance by FEA model and analytical method with consideration of only fundamental component.

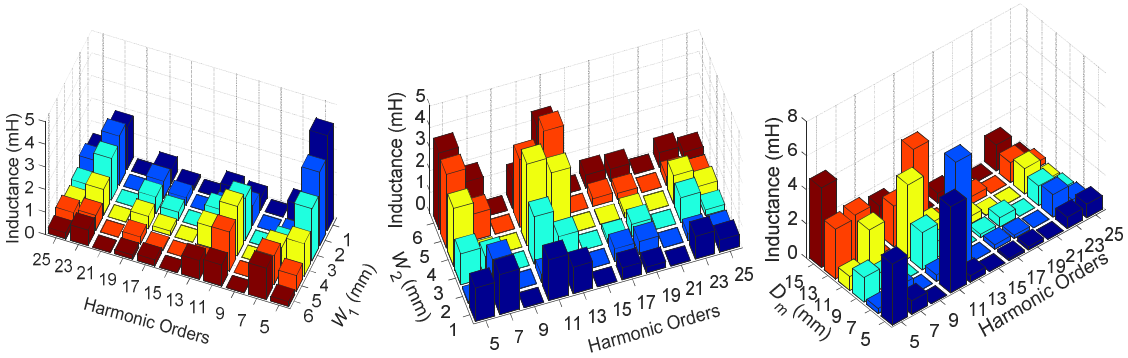

(a) With different W_1; (b) With different W_2; (c) With different D_m;

Figure 3-39 Contributions of flux harmonics to q-axis magnetizing inductance.

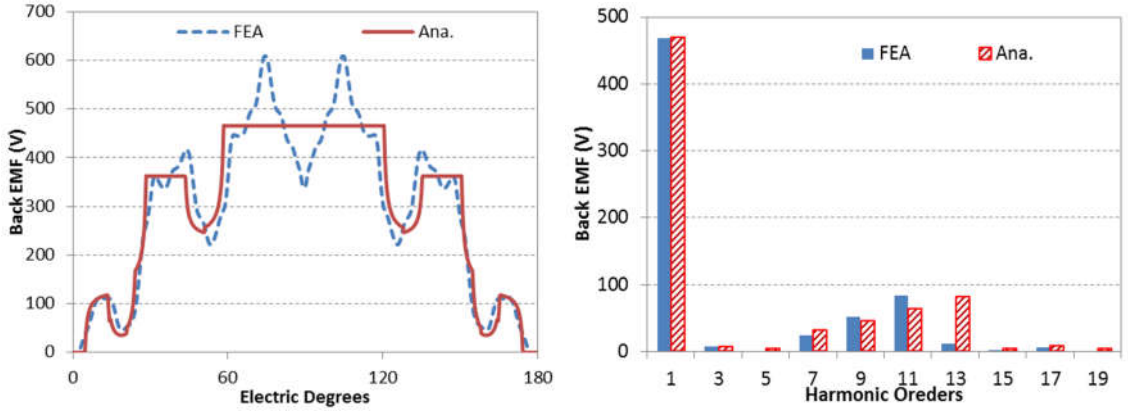

(a) Flux distribution; (b) Spectra;

Figure 3-40 Back EMF waveform and spectra of a typical two-layer structure.

3.2.3.4 Performance based on analytical method

The open-circuit back EMF can be calculated based on the PM excited flux field by Equation (3-47), and the waveforms and spectra are derived as illustrated in Figure 3-40. Good capture of the shape of the waveform is achieved, and the spectra analysis indicates good accuracy of the developed analytical method. However, the back EMF waveform of analytical method is not exactly the same with FEA and deviations are seen. The main reason is that the back EMF obtained by FEA is calculated with the rotor spinning, while the analytical model is based on static model under dq frame. Since the relative location of the stator and rotor slots changes when rotating, the tooth harmonics are slightly different from those at standstill.

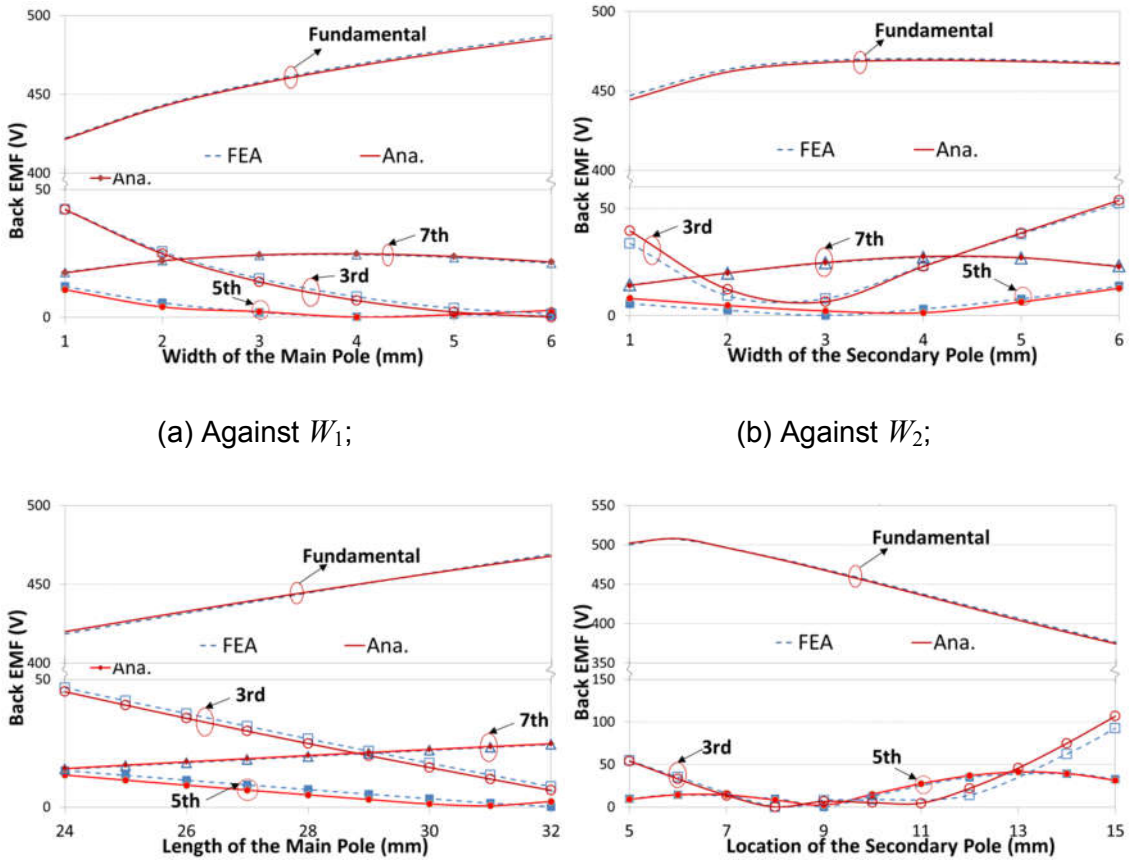

(a) Against W_1; (b) Against W_2;

(c) Against L_1; (d) Against D_m;

Figure 3-41 Fundamental, 3rd and 5th components of Back EMF with various rotor parameters.

Since the winding back EMF is induced by the flux field excited by the PMs, the influence of key design parameters is similar to that of open-circuit airgap flux distribution. The harmonic components which are not the tooth harmonics are reduced by short-pitched windings. Hence, the harmonic contents in the back EMF are much lower than the airgap flux distribution. As the major flux supplier, the size of the main PM has higher effect on the fundamental of back EMF, as shown in Figure 3-41(a) and (c). Since the working point of the PM increases with the width and the flux focusing effect is enhanced with length, wider and longer main PMs can intensify the PM flux density. Because the flux waveform is regulated by the secondary pole, both the fundamental and harmonics are greatly affected. With the flexible design of the secondary pole, low harmonic contents can be achieved, which could potentially reduce loss and torque ripple.

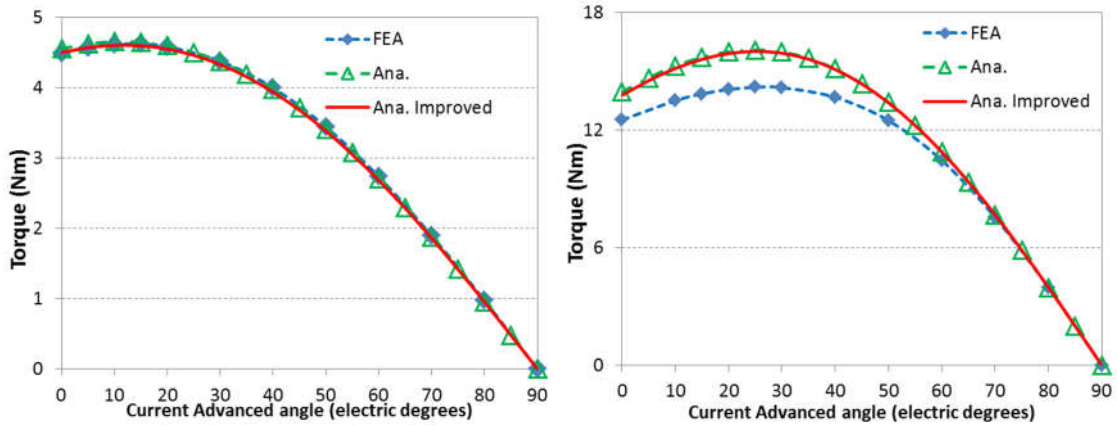

(a) Under 1/3 of rated current; (b) Under rated current;

Figure 3-42 Comparison of torque profiles by FEA and analytical models.

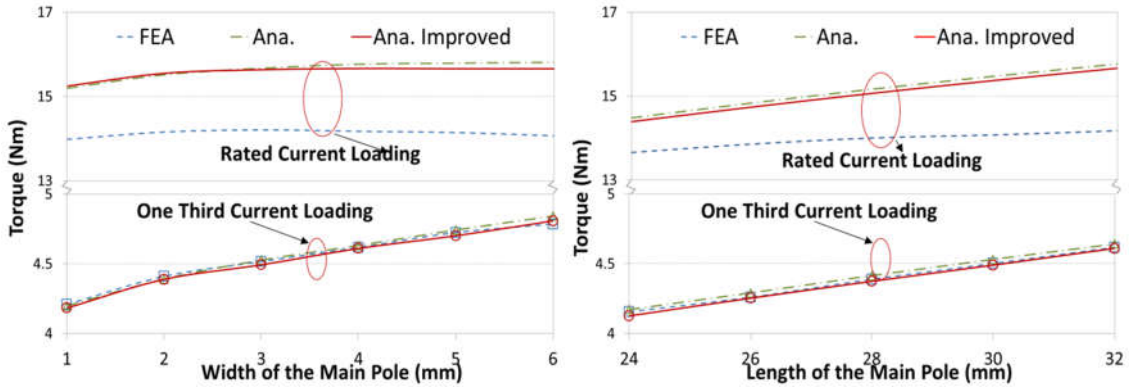

(a) Against W_1; (b) Against L_1;

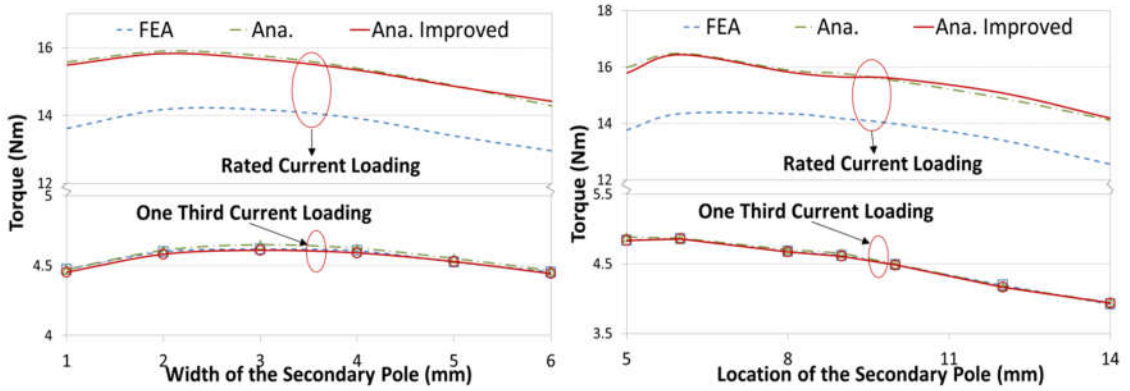

(c) Against W_2; (d) Against D_m;

Figure 3-43 Torque output with different PM parameters under light and rated load conditions.

The electromagnetic torque profiles of FEA and analytical methods are compared in Figure 3-42 under light load and rated load conditions. As no saturation occurs in the lamination cores when under light load conditions, the torque profile can be predicted with high accuracy by the analytical methods. With flux in the PM slots ignored, the analytical model shows slightly higher torque at low current angle because of slightly higher PM flux derived. But the PM slots are relatively small and the impact on the flux distribution is low, therefore very good agreement is achieved. On the other hand, the improved analytical method almost coincides with FEA result owing to more accurate approximation of PM slot flux distribution. With the increase of machine loading, the error will increase due to the occurrence of saturation. Under heavy load conditions, severe saturation appears in the machine, and error percentage can go up to 14% for the maximum torque output, as shown in Figure 3-42 (b). With higher current angle, larger demagnetizing current is injected and saturation is alleviated. Thus, the torque predicted by analytical models coincides with FEA again. Although the error percentage increases with saturation, the trend of torque profile and the optimal current angle can be well predicted, which can be very helpful for the preliminary design.

The maximum torque against different PM parameters under 1/3 and rated current are illustrated in Figure 3-43. Under light load conditions, the PM torque consists of the majority of the overall torque, and can be effectively enhanced by wider and longer main PMs. Therefore, the output torque increases with the main PM width and length. Under rated loading, reluctance torque consists of considerable part of the overall torque, and wider main PM doesn't always mean higher torque because it also leads to higher saturation and possible deterioration in rotor saliency. Consequently, the overall torque is increased very little by wider main PMs when W_1 is relatively small. And even decrease in the overall torque can be observed when W_1 is too large, as demonstrated in Figure 3-43(a). Thus, the optimal composition of PM and reluctance torque components should be compromised with suitable W_1 to achieve higher torque density. Although the length of the main PM has little impact on the armature inductance, the torque increases with L_1 due to the increased PM torque. That's

why longer main PMs are always preferred so long as there is enough space to accommodate the PMs.

As discussed previously, the width of the secondary pole has very small effect on enhancement of PM flux field but higher influence on the armature inductance. Proper W_2 can increase the PM torque slightly due to the higher PM working point and better rotor saliency. But as W_2 becomes wider, significant decrease in L_{mq} occurs without noticeable enhancement in PM flux, which leads to the decrease in reluctance torque and thus the overall torque. The impact is more complicated for D_m because both the PM flux and rotor saliency can be greatly affected. The length of secondary PM poles is increased as the decrease of D_m, which results in much higher PM field and thus PM torque. As a result, increase of maximum torque is observed when secondary poles are closer to the main poles at light current loading. Meanwhile, armature inductance reduces with the decrease of D_m, and highest difference between d- and q-axis inductances is achieved with an optimal value for D_m. And because of the improvement in reluctance torque, the overall torque increases D_m at first despite of smaller PM torque. As the secondary pole moves further away, both the PM and reluctance torques decrease, resulting in the decrease of overall torque.

3.3 Conclusion

The analytical methods for both the one-layer and two-layer spoke-type IPM machines are developed based on the equivalent magnetic circuit theory. And FEA models are built to verify the analytical method. Due to the large PM slots in the rotor, sudden variation of airgap reluctance occurs in the PM slot areas and causes serious distortion for both PM and armature reactive field. For the sake of simplicity, infinite reluctance can be assumed for the analytical model. But slightly higher error percentage is observed comparing to FEA results. With approximation of the flux distribution in the PM slot area, higher accuracy is obtained with more complicated model by the improved analytical methods. To obtain simple and accurate relations between the machine performance and design parameters, the fundamental compensation solutions are also

developed by using the analytical method with simplified PM slot flux compensation for the fundamental components, and a compromise between simplicity and accuracy is achieved. Since no saturation is considered in the analytical model, there would be noticeable difference under heavy load conditions. However, variation trends of torque profiles against the key design parameters and current angle can be well predicted, which can still provide very helpful insight into the design and optimization of multi-layer spoke-type machines. The analytical model for spoke-type machines with more PM layers can be developed by the same procedures proposed in the chapter.

Based on the analytical models derived, the influence of different design parameters is investigated to provide insight for the design of ferrite IPM machines. For the one-layer configuration, higher torque can be achieved with larger amount of PM material due to the high PM focusing effect and low rotor saliency. However, it is not cost-effective in practice and may cause problems concerning rotor assembly by adding more and more PMs. By introducing the secondary PM layer, the flux distribution can be improved with less harmonic contents, and the rotor saliency and reluctance torque can be greatly improved even with less PM.

4 DESIGN OF MULTI-LAYER SPOKE-TYPE MACHINES

4.1 Background Introduction

The multi-layer configurations, maximize the rotor saliency while retaining the flux focusing structure, and are able to synergize the torque output for compelling performances. The electromagnetic features of the machines are highly dependent on the key design parameters such as the number of PM layers, the size and location of the PMs. It would be of particular interest to reveal the impacts of these parameters over the PM and reluctance torque components, and provide insightful understanding of their influences on the overall electromagnetic torque generation. As relations of the key design parameters and machine performance are derived with mathematical equations in Chapter 3, the influence of key design parameters can be obtained and the optimization can be quite intuitive.

In this chapter, electromagnetic design and optimizations are carried out for the spoke-type multi-layer IPM machines with up to three PM layers. The inner and outer diameters of stator and rotor of the models are all kept the same, and the torque is maximized based on the developed analytical models and then verified by FEA simulations. The optimal design is based on the understanding of the mathematic model of the multi-layer configurations. Firstly, the influence of each design parameter is derived and discussed according to the analytical equations. Then the interactions of the parameters are also comprehensively investigated to provide helpful insight into the design of multi-layer IPM ferrite machines and optimal designs are obtained accordingly. FEA models are built to verify the analytical method. Because the saturation is ignored for the analytical methods, the optimal parameters might be slightly different from the actual case. But the variation trends can be well predicted by the analytical models, and minor modifications can be made with the FEA by parametric sweeping within a small range. In this way, loads of time and effort can be saved for the optimal design involving multiple parameters. Finally, the performances of the machines with different PM layers are compared and the one with best overall performance is chosen for the prototype machine.

4.2 General Optimisation Sizing Specifications

To avoid invidious comparisons, some of the main critical parameters under this study must keep identical so that the research could be of both theoretical and practical significance. Therefore, the diameters of the stator and rotor, stacking length and electrical loadings of different models are all kept the same. Table 4-1lists the common parameters for the design of ferrite IPM machines.

Table 4-1 Properties common dimensions and specifications

Parameters	Value	Unit
Stator Outer Diameter (D_{so})	160	mm
Rotor Outer Diameter (D_{ro})	94.5	mm
Rotor Inner Diameter (D_{ri})	27	mm
Airgap Length (g)	0.25	mm
Stack Length (l)	90	mm
Base Rotating Speed	1500	rpm
Lamination Material	50CS470	
PM Material	Ferrite Y30H	

4.3 One-Layer Machines

4.3.1 Airgap Flux Distribution

To obtain direct relations between flux distribution and the size of the PMs, simpler equations are preferred during preliminary design. According to Equation (3-13) and (3-22) under the preconditions that L_s<<L_1 and g_c<<W_1, the flux density in the core area and the fundamental of airgap flux distribution can be simplified as

$$B_g = \frac{B_r}{\frac{R_{ro}}{L_1}\cdot\left(\frac{\pi}{p}-\beta_1\right)+\mu_m\frac{2g_c}{W_1}} \approx B_r\frac{2L_1}{\tau_p - W_1} \qquad \textbf{(4-1)}$$

$$B_{gf1} \approx \frac{8B_r}{\pi}\frac{L_1}{\tau_p - W_1}\cos(\frac{p\beta_1}{2}) \qquad \textbf{(4-2)}$$

where τ_p is the pole pitch and $\tau_p=2\pi R_{ro}/p$. (τ_p-W_1) is the approximate arc length of rotor core area in one pole pitch. Since the ratio of L_1 over $(\tau_p-W_1)/2$ stands for the flux focusing factor, the flux density in the core area can be approximated by multiplying the magnet remanence by the flux focusing factor. Longer PMs are preferable to boost air flux density because of better flux focusing effect. Thicker PM can increase the flux focusing factor, but also enlarges zero flux area due to wider the openings. Thus the increase of PM width is not as effective to PM length in terms of the effect of enhancing flux distribution.

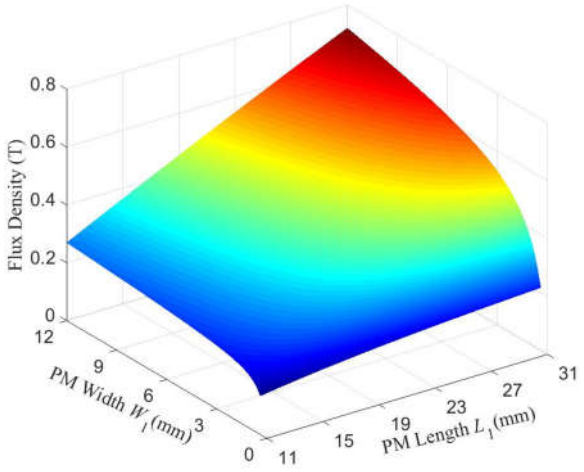

Figure 4-1 Influence of PM width and length on fundamental flux distribution

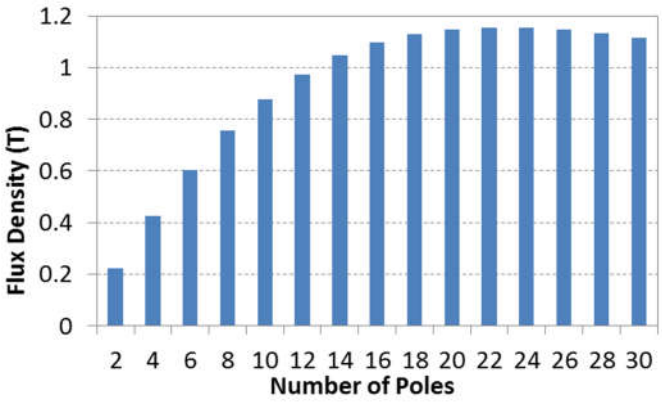

Figure 4-2 Influence of pole number on flux distribution.

Figure 4-1 depicts the influence of PM size on the fundamental flux in the airgap. As expected, proportional relation between the fundamental and PM length is obtained, and thus longer PM length is surely a better way to enhance flux density. On the other side, the flux field can be effectively enhanced by

thicker PMs when the PM width is small, since there would be considerable improvement in PM working point. But when the rotor is equipped with relatively wide PMs, the increment is quite limited and less cost-effective concerning the amount of ferrite magnet. Furthermore, certain amount of lamination core is indispensable to provide paths for the main flux and sufficient mechanical stress for rotor assembly, which also limits the total amount of magnets.

Equation (4-2) also suggests that the airgap flux density can be improved by higher number of poles. As the pole pitch is inversely proportion to the number of poles, the flux focusing factor can be greatly increased. Meanwhile, the width of the PMs also decreases since less space in one pole pitch is available to accommodate PMs, and PM working point drops accordingly. With the increase of the number of poles, the decline in PM working point will eventually surpass the increment in flux focusing factor and cause the decrease of the PM flux field, as illustrated in Figure 4-2. Besides, larger number of poles will incur issues of higher loss due to the higher operating frequency and manufacturing difficulties in terms of machining precision.

4.3.2 Magnetizing Inductance

Based on the analytical models developed in the in the previous chapter, the magnetizing inductances with different PM width and length are demonstrated in Figure 4-3 (a) and (b). As the fundamental is the major contribution to flux linkage, the change of inductance due to the size of PMs can be estimated by:

$$L_{md} \approx \frac{8\mu_0 m R_{ro} l_{ef} N_a{}^2 k_{w1}{}^2}{\pi p^2 g_c}\left[1-\frac{4}{\pi}\frac{\sin\left(\frac{\pi}{2}-\frac{p\beta_1}{2}\right)}{\left(\frac{\pi}{2}-\frac{p\beta_1}{2}+\frac{pg_c}{W_1 R_{ro}}L_1\right)}\right]\left[1-\frac{p\beta_1}{\pi}+\frac{\sin\left(\pi-p\beta_1\right)}{\pi}\right] \quad \textbf{(4-3)}$$

$$L_{mq} \approx \frac{8\mu_0 m N_a{}^2 R_{ro} l_{ef} k_{w1}{}^2}{\pi p^2 g_c}\left(1-\frac{p\beta_1}{\pi}-\frac{\sin p\beta_1}{\pi}\right) \quad \textbf{(4-4)}$$

The PM length shows little impact on the winding inductance. L_{md} is marginally increased by longer PMs as the reluctance of the PM slot is slightly reduced. The PM length is irrelevant to L_{mq} as the q-axis flux only travels through

laminations in the rotor. On the other hand, both L_{md} and L_{mq} are greatly affected by the PM width. But as the d-axis flux travels across PM slots, L_{md} decreases more significantly with larger W_1. Because of the different impact on L_{md} and L_{mq}, rotor saliency is created and can be exploited for torque enhancement. As illustrated in Figure 4-3 (c), L_{md} declines much faster with PM width than L_{mq} when the PM slots are not too wide, and rotor saliency is increased as larger d- and q-axis difference is obtained. But as the further increase of the PM slot width, L_{md} becomes negligible comparing to L_{mq} and the inductance difference decreases with L_{mq}.

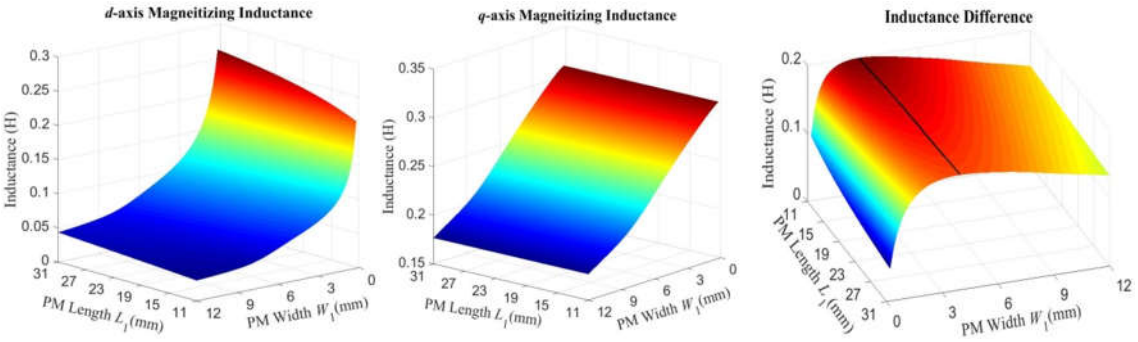

(a) L_{md}; (b) L_{mq}; (c) L_{mq} - L_{md};

Figure 4-3 Influence of PM size on d- and q-axis magnetizing inductance and their difference.

4.3.3 Torque

As indicated in Equation (3-48), the total electromagnetic torque in PMSMs can be segregated into two parts, which are the PM torque T_{pm} and the reluctance torque T_r. And they can be calculated by

$$\begin{cases} T_{pm} = \dfrac{mp}{4}\Psi_f i_q \\ T_r = \dfrac{mp}{4}(L_d - L_q) i_d i_q \end{cases} \quad \textbf{(4-5)}$$

The phasor diagram of a PMSM is demonstrated in Figure 4-4, and according to the relations of the current and voltage vectors, the two torque components as well as the total torque can be written as:

$$\begin{cases} T_{em} = T_{pmm}\cos\phi + T_{rm}\sin 2\phi \\ T_{pmm} = \dfrac{mp}{4}\Psi_f I_m \\ T_{rm} = \dfrac{mp}{8}(L_q - L_d)I_m{}^2 \end{cases} \quad \textbf{(4-6)}$$

where T_{em} is the total electromagnetic torque, ϕ is the electric angle of back EMF vector and armature current, or the advanced current angle, T_{pm} and T_r the PM and reluctance torque component, T_{pmm} and T_{rm} are the maximum PM torque and reluctance torque that can be achieved for a PMSM.

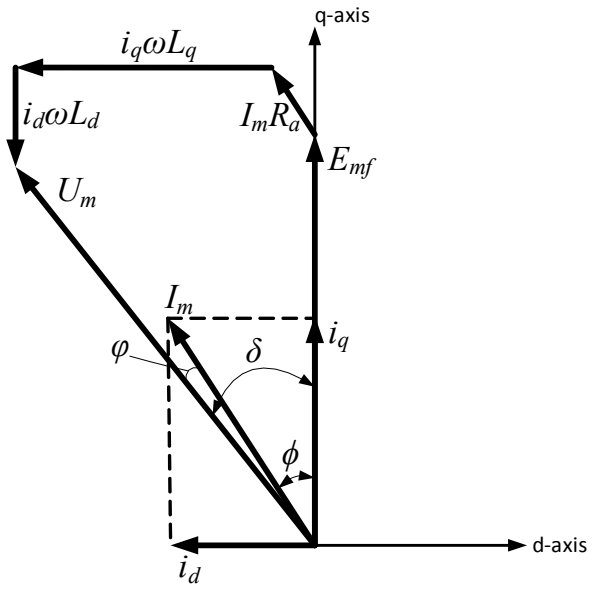

Figure 4-4 Phasor diagram of a PMSM

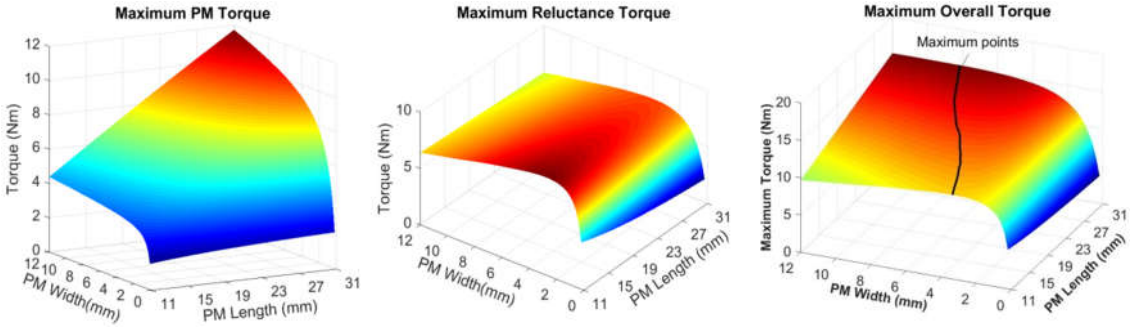

(a) Max. PM torque; (b) Max. reluctance torque; (c) Max. overall torque;

Figure 4-5 Maximum torque profiles against PM width and length.

The maximum PM and reluctance torque components with different PM size are depicted in Figure 4-5. T_{pmm} can be regarded as proportional to airgap flux distributions, and they share the same changing trend against PM size. T_{rm} increases linearly with the inductance difference (L_{mq}−L_{md}). Since PM torque is determined by PM length and reluctance torque is mainly affected by PM width, the maximum overall electromagnetic torque is the decided by the combination of the two factors, as demonstrated in Figure 4-5 (c). Apparently, longer PMs intensified the PM torque while having little impact on saliency, which are preferred to achieve higher PM torque. Width of the magnet can enhance the PM flux, but it may also deteriorate the saliency. Hence, compromise between the two torque components should be optimized for higher torque density. The black line in Figure 4-5(c) depicts the maximum torque points achieved at different PM length. The optimal width increased with PM length as the machine relies more heavily on the PM torque. It should be noted that the PM torque could account for up to 80% of the overall torque for one-layer configurations, and thus relatively large PM width is adopted the design.

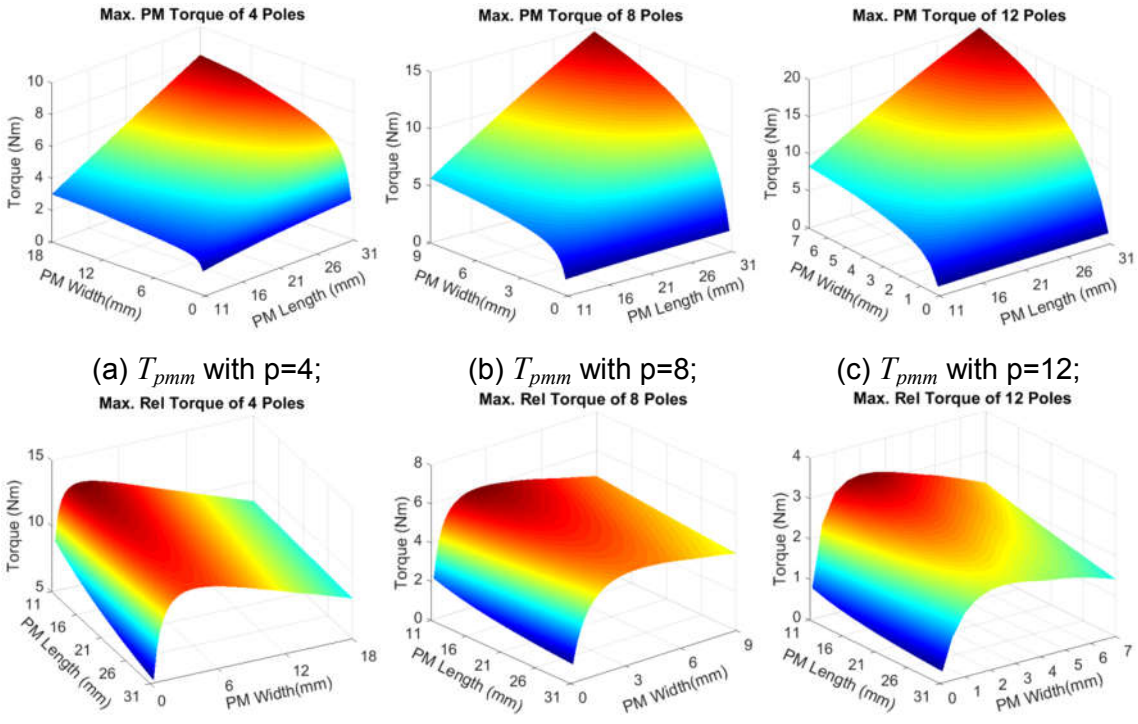

(a) T_{pmm} with p=4; (b) T_{pmm} with p=8; (c) T_{pmm} with p=12;

(d) T_{rm} with p=4; (e) T_{rm} with p=8; (f) T_{rm} with p=12;

Figure 4-6 Maximum PM and reluctance torque with different pole numbers.

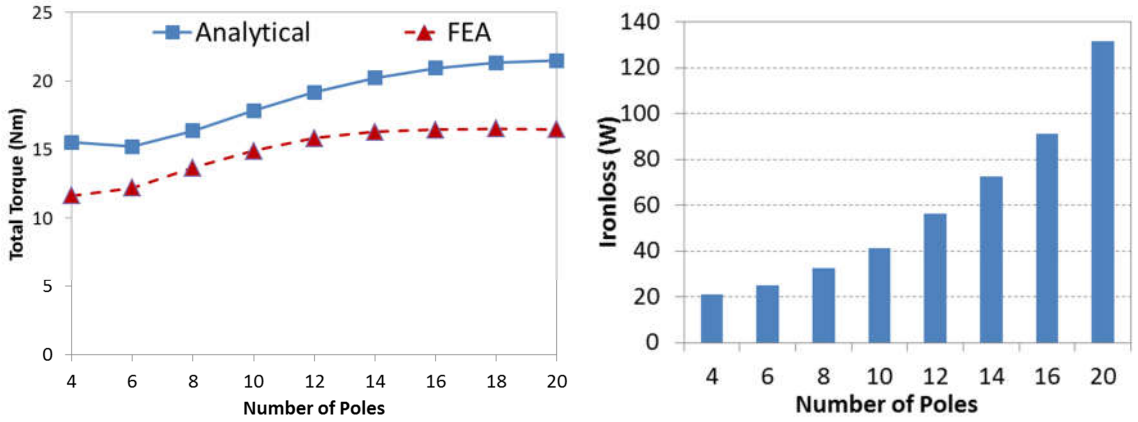

(a) Maximum torque output; (b) Iron loss;

Figure 4-7 Maximum overall torque and iron loss with different pole numbers.

Higher number of poles is able to boost the fundamental flux density and thus the PM torque, giving that the diametrical dimensions and electric loading of the models are kept the same. On the other hand, both the d- and q-axis inductances decline dramatically with the number of poles according to Equation (4-3) and (4-4). Hence, much lower reluctance torque is expected for the machines with higher number of poles. The maximum PM and reluctance torques of the models with different number of poles are illustrated in Figure 4-6. Due to the much better flux focusing effect, the maximum PM torque increases dramatically with the growth of number of poles, from 8.25Nm of the 4-pole model to 20.1Nm of the 12-pole model. In contrast, the maximum reluctance torque decreases from 12.88Nm of the 4-pole model to 3.26Nm of the 12-pole model. Owing to the poor saliency ratio of the conventional spoke-type machines, the increment in PM torque is higher than that of reluctance torque until p=18 when the overall torque begins to drop, as depicted in Figure 4-7(a). For machines with very low number of poles, reluctance torque accounts for larger part of the total torque, which makes the performance of the machine closer to reluctance machines. Without considering saturation in the lamination cores, the torque of analytical model increases when the number of poles reduces from 6 to 4, because higher increment in reluctance torque is possible theoretically. But in practical, the saturation in the stator yoke becomes more severe for lower number of poles, which degrades the overall torque output.

Hence, the FEA result shows that the overall torque of the 6-pole model is still higher than that of the 4-pole one.

In all, the overall torque declines in general as the decrease of the number of poles because the most distinctive advantage of flux focusing effect will be weakened. There are also disadvantages for high number of poles. Since operating frequency is proportional to the number of poles at the same rotating speed, iron loss increases exponentially as shown in Figure 4-7(b). This brings about problems of lower efficiency and overheating. Manufacture issues should also be taken into consideration. Machines with larger number of poles require thinner PM poles, which would cause difficulties in the machining and assembling of the brittle ferrite magnet pieces.

4.3.4 Preliminary Design for One-Layer Configuration

By compromising among torque density, iron loss and ease of manufacture, the model with 8-pole is chosen as final candidate for spoke-type. To leave enough space for the shaft, the maximum possible PM length for the design is 31mm. Because the saturation is not considered in the analytical models, the optimal value for PM width is might be different from FEA result. But the influence of these design variables can be predicted by the analytical method, which will narrow down the range of the key design parameters. Only final verification is necessary from FEA software, and a lot of time and effort can be saved. The optimal parameters for the preliminary design are shown in Table 4-2.

Table 4-2 Optimal parameters for the one-layer design by analytical and FEA methods

Parameters	Ana.	FEA	Unit
Number of Poles (p)	8	8	
Length of PMs (L_1)	31	31	mm
Width of PMs (W_1)	9	9	mm
Length of PM Slots (W_s)	1	1	mm
Volume of Ferrite	200	200	cm^3

4.4 Two-Layer Machines

The two-layer configuration is developed based on the conventional spoke-type structure. Thus, the feature of the two-layer configuration shares certain similarities with the one-layer structures.

4.4.1 Airgap Flux Distribution

In a two-layer machine, all the open-circuit main flux starts from the main PM poles and the size of the main poles have direct impact on the average flux density in the airgap. On the other hand, the secondary poles regulate the flux between the core area ① and ②, and mainly affect the shape of the airgap flux distribution. According to Equation (3-59), the open-circuit fundamental flux component can be very roughly estimated by

$$B_{fg1} \approx \frac{4B_r}{\pi}\left\{\frac{L_1 - L_2}{R_{ro}\alpha_1}\cdot\left[\sin\left(p\frac{\alpha_1+\alpha_2+\beta_2}{2}\right)-\sin\left(p\frac{\alpha_2+\beta_2}{2}\right)\right]+\frac{L_2}{R_{ro}\alpha_2}\cdot\sin\left(\frac{p\alpha_2}{2}\right)\right\} \quad \textbf{(4-7)}$$

Figure 4-8 depicts the influence of the size of main and secondary PM poles on fundamental flux density in the airgap. The result indicates that the length of the PM poles has higher impact on the flux density. By contrast, the width of PMs shows smaller influence because the PM working point and the flux focusing ratio can be slightly improved. The length of PMs is able to boost the flux focusing effect, and similar to the one-layer struture, the longer they are, the higher the flux density will be. For the main pole, longer PMs are preferred to maximize the flux focusing effect since L_1 is proportional to the overall PM flux. The length of the secondary poles can also increase the fundamental flux since more PM is used and the flux density in area ② is intensified. It should be noted that the length of secondary PMs increases as they move towards to the main pole. And when the maximum length is reached, the model becomes a conventional spoke-type machine. In other words, higher open-circuit flux density can be achieved by the spoke-type configuration. Nevertheless, the waveform of airgap flux distribution can be improved by the secondary PM layers, and more sinusoidal flux distribution can be achieved with lower

harmonic contents. And more importantly, the rotor salient ratio is expected to be improved by proper design of the second PM layers.

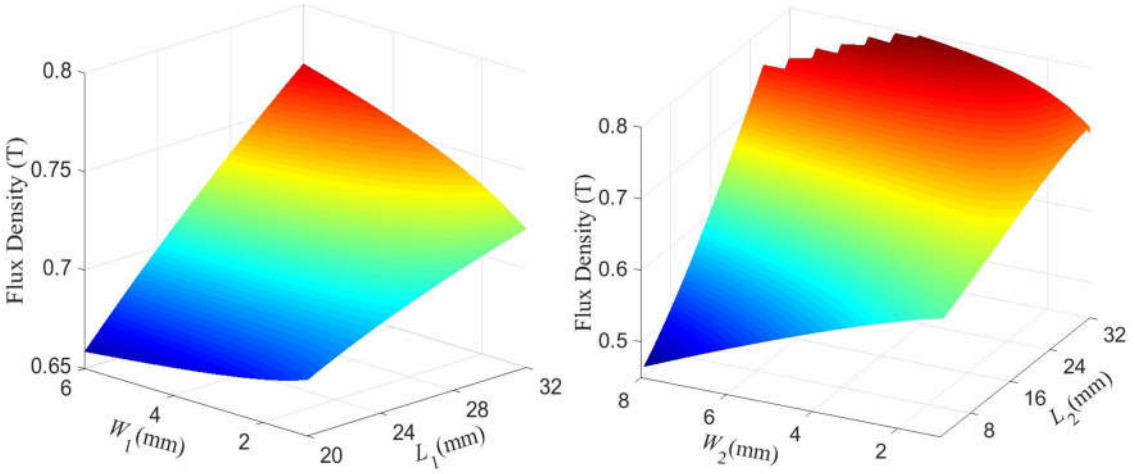

(a) Main PMs; (b) Secondary PMs;

Figure 4-8 Magnitude of fundamental flux density against PM size

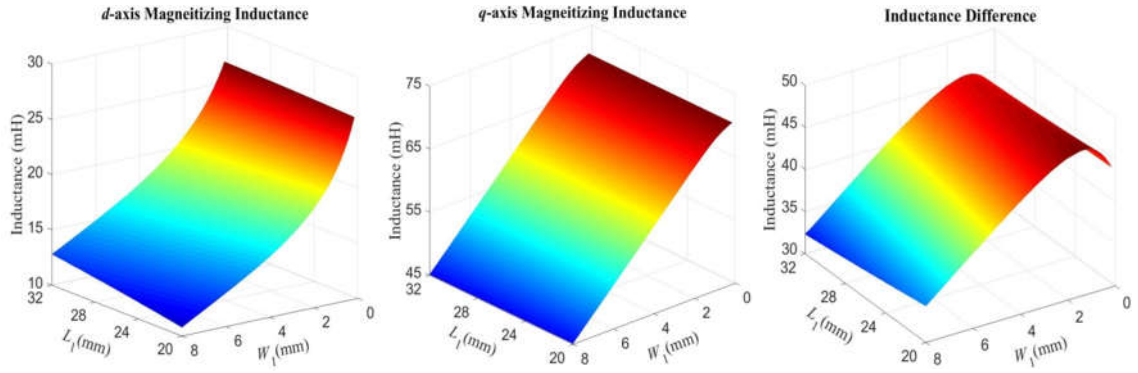

(a) L_{md}; (b) L_{mq}; (c) L_{mq}-L_{md};

Figure 4-9 Influence of the main PM size on magnetizing inductance

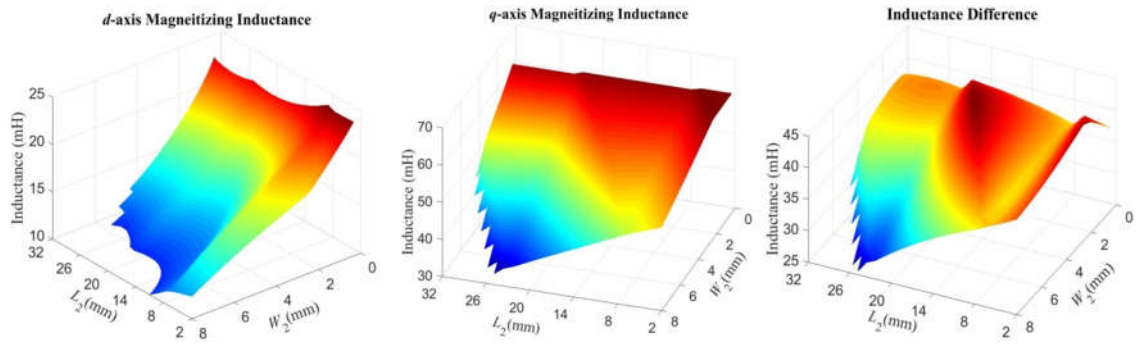

(a) L_{md}; (b) L_{mq}; (c) L_{mq}-L_{md};

Figure 4-10 Influence of the secondary PMs on magnetizing inductance.

4.4.2 Magnetizing Inductance

The d- and q-axis inductance together with their inductance difference against the width and length of the main PM are demonstrated in Figure 4-9. Since the main PM poles function similarly to the spoke-type poles of the one-layer structure, the influences are more or less the same. Both the d- and q-axis inductances decrease dramatically with the main PM width as the reluctance of the magnetic equivalent circuit is increased, while no noticeable impact are posed by the PM length. When the main PM width is small, L_{md} drops faster than L_{mq} and rotor saliency is enhanced. But both L_{md} and L_{mq} drop severely with large PM width, resulting deterioration in saliency.

As a unique design of the multi-layer configuration, the secondary PM layers play a very important role in regulating the flux between the two core areas. Since the magnetic paths of flux can be altered by the secondary layers, both the d- and q-axis inductances are greatly affected. As shown in Figure 4-10, the influences imposed by the secondary layers are different on the d- and q-axis inductances. Hence, with elaborate design of the secondary poles, the rotor saliency can be improved to boost the reluctance torque.

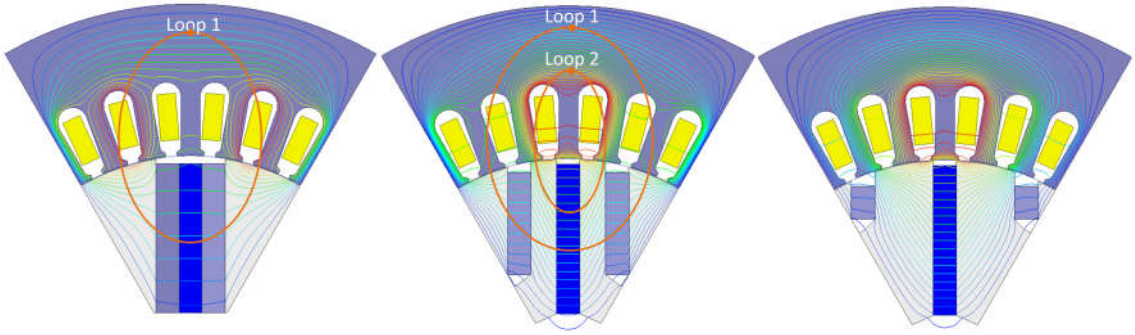

(a) L_2 =32mm; (b) L_2 =22mm; (c) L_2 =7mm;

Figure 4-11 D-axis reactive field distribution and loops with different L_2.

The impact of the secondary PM length is easy to understand. Because the PM slot area is increased, both L_{md} and L_{mq} decrease with wider PM slots. Besides, since part of the d-axis flux travels through the PM slot, L_{md} is more seriously influenced by the PM width. On the other hand, the influence of the location (length) of secondary PMs is more complicated. As shown in Figure 4-11,

profound changes occur in the machine flux distribution due to the variation of the location of secondary PM layers. The maximum length for the secondary PMs is obtained when they touch the main PM, and the model becomes a conventional spoke-type configuration. The main and secondary slots merge together and only one flux loop for d-axis reactive field is formed. All the flux has to cross the large main PM slot, and the reluctance of the magnetic circuit reaches its maximum. As the secondary poles move away from the main pole, Loop 2 emerges and part of the reactive flux goes through only the main PM slot through core area ①. As a result, the overall reluctance is reduced, and the reactive field and L_{md} increases accordingly. With the secondary poles moving further away, more flux goes by Loop 2 due to the much lower reluctance and L_{md} rises dramatically. When the secondary poles moves too far away from the main PM, flux in Loop1 is negligible, and maximum value of L_{md} is reached, as shown in Figure 4-11(c).

As for the q-axis reactive field, since the flux doesn't go through the PM slots, the PM slots only cause the change of equivalent airgap length in the slot area and thus less effect is expected. By ignoring the flux in the PM slot area and higher order space harmonics, roughly estimation of L_{mq} can be obtained with further simplification from Equation (3-72):

$$L_{mq} \approx \frac{8\mu_0 m {N_a}^2 R_{ro} l_{ef} {k_{w1}}^2}{\pi p^2 g_c} \left[\begin{array}{l} 1 - \dfrac{p(\beta_1+\beta_2)}{\pi} - \dfrac{\sin(p\beta_1)}{\pi} \\ - \dfrac{2\sin p(\beta_2/2)\cos p(\alpha_1+\beta_1+\beta_2/2)}{\pi} \end{array} \right] \quad \textbf{(4-8)}$$

If the size of main PMs and the width of secondary PMs are fixed, the radian of area ① (α_1) becomes the only variable in Equation (4-8) and the effect of the location of secondary PMs can be revealed. As they move away from the main PM, L_{mq} rises with the increase of α_1. However, due to the impact of the spatial harmonics from the armature MMF and large PM slots, the value of L_{mq} fluctuates while going up, as illustrated in Figure 4-10 (b). By taking advantages of the different influences on the d- and q-axis flux distribution, the rotor saliency can be further enhanced by the secondary layers, as depicted in Figure 4-10(c).

4.4.3 Torque

The parameters of the PM poles have quite different impacts on the open-circuit flux distribution and rotor saliency. Thus, optimal design process is necessary to achieve better performance. The two-layer structure is more complicated, and more sizing parameters are related for optimization. As the parameters are all interdependent due to geometrical restrains, the variables should be carefully chosen to make the optimization easier and more understandable. The length of the main PMs is set to the maximum value, as it can boost the open-circuit PM flux field effectively while having little impact on rotor saliency. Practically, people are more concerned about the amount of magnet material consumed. With the amount of PM fixed, only two variables can determine the rotor geometry. For a more intuitional view of how the machine performance is affected by the rotor design, the width of the main PM W_1 and location of the secondary pole D_m are chosen as the major parameters for the investigation.

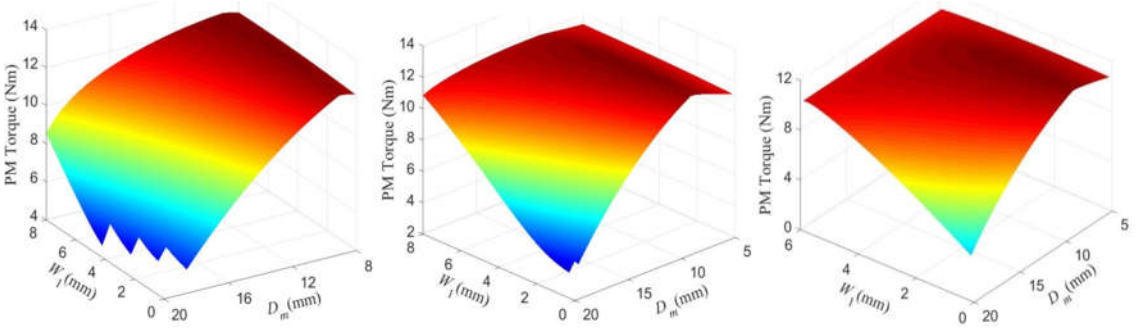

(a) 200 cm^3; (b) 150 cm^3; (c) 100 cm^3;

Figure 4-12 Maximum PM torque against W_1 and D_m with different PM amount.

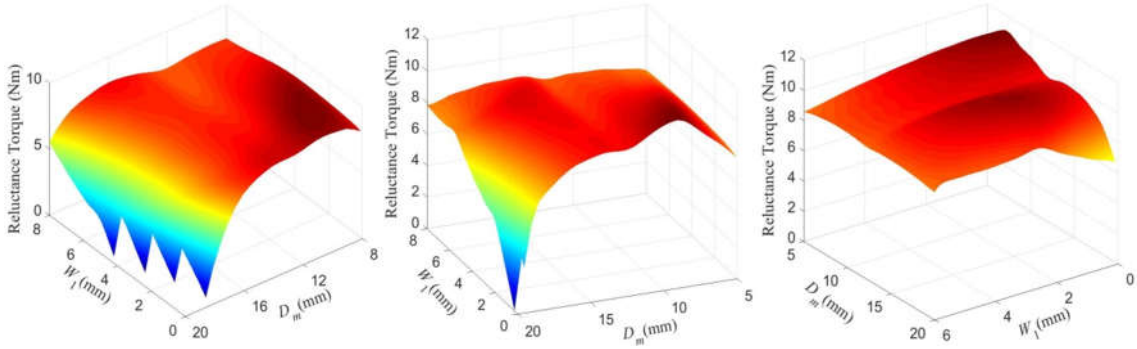

(a) 200 cm^3; (b) 150 cm^3; (c) 100 cm^3;

Figure 4-13 Maximum reluctance torque against W_1 and D_m with different amount of ferrite materials.

With the amount of magnet material fixed, maximum PM torque is achieved when the distance between the main and secondary PM poles are minimum, as depicted in Figure 4-12. In other words, the one-layer configurations offer better flux focusing effect and thus higher PM torque, as expected. And with larger amount of PMs, higher PM torque can be generated, though the increment becomes smaller and smaller. On the other hand, the maximum reluctance torque decreases with the PM amount as shown in Figure 4-13. That's because the larger PM slots occupy more space with less lamination core left, and both the d- and q-axis armature fields are weakened. Actually, only very low amount of PMs are required to achieve the maximum saliency. It is also noteworthy that the reluctance torque tends to increase with thinner main PM slots, which indicates V-shaped structures have higher salient ratio than the two-layer configurations.

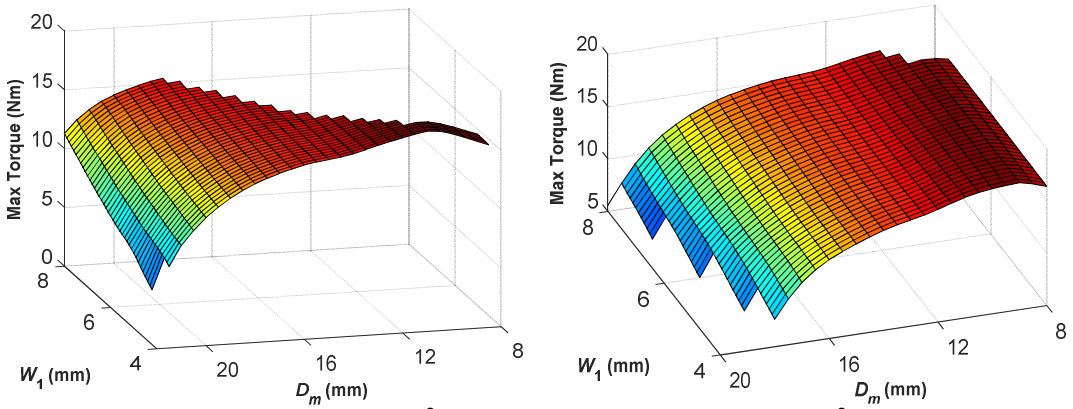

(a) 200 cm^3; (b) 250 cm^3;

Figure 4-14 Maximum torque against W_1 and D_m at different amount of ferrite.

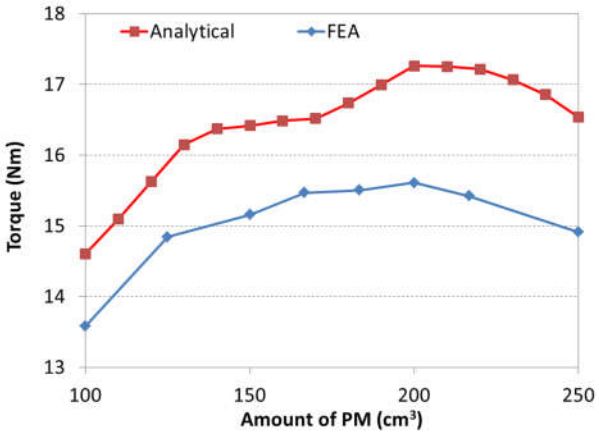

Figure 4-15 Maximum torque achieved against the amount of ferrite.

To achieve an optimal torque density, a compromise is necessary between the two torque components. Figure 4-14 depicts the maximum overall torque that can be delivered by different machine models. Owing to the fragile nature of ferrite PM, the designs with PM poles thinner than 4mm are considered as invalid. The results indicate that the width of PMs has much lower impact on the torque output, and the torque capability is mainly influenced by the location of the secondary poles when the total amount of magnets is fixed. The maximum value increases slowly with D_m at first because of increased rotor salient ratio, and then decreases dramatically as the secondary poles moving further away because both PM and reluctance torque drop greatly. Since the amount of PM material has inverse effects on the PM and reluctance torque components, larger amount of magnet doesn't always mean higher overall torque. More PM can increase PM torque, but it may also deteriorate the rotor saliency. There would be a trade-off between them to achieved maximum value. The overall torque capability against PM volume is illustrated in Figure 4-15. The analytical method shows that the torque increases fast when the PM volume is low, because higher increment in the PM torque is obtained. With the increase of PM volume, it becomes less effective to enhance PM torque by using more magnets, and the negative effect on rotor saliency worsens more seriously. Thus, the torque declines after reaching the maximum value, and the maximum point is the goal of optimization. The influence of PM volume is verified by FEA simulations and the variation trend is well predicted by the analytical method despite of the difference caused by saturation.

Similar to the one-layer structures, the number of poles also has huge impact on the performance of the two-layer configurations. As the descendant of the one-layer structure, the flux focusing effect can also be enhanced by larger number of poles. Meanwhile, the winding inductances decrease greatly causing severely degraded reluctance torque. As reluctance torque plays an important role in the overall torque, the two-layer configuration is not very suitable for machines with very high number of poles. With very low number of poles, the advantage of flux focusing effect would also disappear. To maximize the torque density, compromises should be made between the two torque components.

Table 4-3 Maximum torque with different number of poles

Number of Poles	4	6	8
Max. Torque by Analytical (Nm)	18.70	17.26	16.74
Max. Torque by FEA (Nm)	14.31	15.57	15.63
Core Loss by FEA (W)	36.27	43.32	57.82

Table 4-4 Optimal parameters for two-layer model by analytical and FEA methods

Parameters	**Ana.**	**FEA**	**Unit**
Number of Poles (p)	6	6	
Length of Main PMs (L_1)	31	31	mm
Width of Main PMs (W_1)	4.5	5	mm
Length of Secondary PMs (L_2)	25	21.5	mm
Width of Secondary PMs (W_2)	4.5	5	mm
Location of Secondary Pole (D_m)	11.5	13	mm
Volume of Ferrite	197	200	cm^3

Without considering the saturation, the result from analytical methods implies that the dramatic decrease in reluctance torque diminishes the overall torque as the number of poles increases. But higher saturation occurs in the stator yoke with lower pole number, resulting in much lower actual torque than the ideal models, as shown in Table 4-3. Although the FEA result indicates slightly higher torque for the 8-pole model, the core loss is increased by 33% comparing to the 6-pole design.

4.4.4 Preliminary Design for Two-Layer Structure

To confirm the performance of the analytical design, FEA optimizations are also carried out for final verification. For the ease of manufacture, all the PMs are set to have same width. Due to the influence of the saturation, both the actual PM and reluctance torques will be lower than the analytical model. According to Equation (4-6), maximum PM torque is achieved at zero current angle, while the reluctance reaches peak at 45 electric degrees. The maximum electromagnetic torque is obtained between 0-45 degrees, and negative d-axis current will be

injected to the windings, which will also provide flux weakening field and alleviate the saturation. Hence in practical, PM torque is more affected by saturation, and the optimal design will have higher reluctance torque than the analytical design. The optimal parameters achieved by the analytical and FEA methods are listed in Table 4-4.

4.5 Three-Layer Configuration

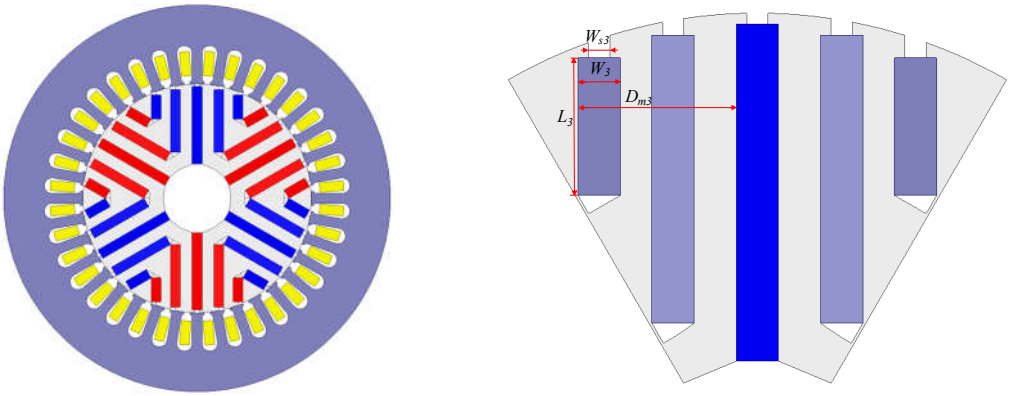

(a) Whole model; (b) Rotor;

Figure 4-16 Demonstration of three-layer spoke-type configuration.

Table 4-5 Optimal parameters for the three-layer configuration

Parameters	Value	Unit
Number of Poles (p)	6	
Length of Main PMs (L_1)	31	mm
Width of Main PMs (W_1)	4	mm
Length of Secondary PMs (L_2)	25	mm
Width of Secondary PMs (W_2)	4	mm
Location of Secondary Pole (D_m)	11	mm
Length of Third PMs (L_3)	9	mm
Width of Third PMs (W_3)	4	mm
Location of Third Pole (D_{m3})	15	mm
Volume of Ferrite	215	cm^3

To further increase the rotor saliency, another layer is affiliated to form the three-layer spoke-type configuration, as shown in Figure 4-16. The width of

PMs (W_1, W_2, W_3) and the distance between the PMs (D_m, D_{m3}) are the design variables to be optimized for the three-layer configurations. Similar procedures are carried out for optimization. With the design theory based on the one-layer and two-layer configurations, FEA models are built and optimized. The optimal design parameters to obtain the maximum torque density are listed in Table 4-5.

4.6 Comparison

4.6.1 Open-Circuit Condition

The PM flux distribution, armature winding inductance and cogging torque have great influence on the performances of the machines. Although all these parameters are strongly affected by the loading conditions, preliminary prediction can still be made based on the open-circuit results. The PM torque component is largely decided by the airgap flux density and back EMF. The harmonics in flux distribution and back EMF would contribute the torque ripple.

Magnetostatic FEA models are first built and the airgap flux distribution is derived and compared in Figure 4-17. Because of the higher number of poles and better flux focusing factor, the one-layer model has the highest open-circuit flux density, and the fundamental is over 25% higher than the other two. But there are higher harmonic contents for the one-layer model, especially the third order. The airgap flux distribution waveform of the two-layer configuration is significantly improved because of the flux regulating effect of the secondary layer. The third and fifth order harmonics are almost eliminated with the two-layer configuration, more sinusoidal waveform is obtained. Despite of the largest amount of magnet used for the three-layer structure, there is little improvement in the flux distribution waveform. Due to the constraint of the rotor geometry, the third PM layer is much shorter than the other two layers, and thus the flux regulating effect is very limited. Though the third to seventh order harmonics are reduced, the ninth order is greatly increased. There is slight decrease in the fundamental flux since more PM layers weaken the flux focusing effect. Figure 4-18 depicts the corresponding back EMF waveforms and spectra. Similar to the airgap flux density, the one-layer configuration has the highest fundamental back EMF component, which indicates the potential of

delivering the highest PM torque. The two-layer one exhibits lowest harmonic contents, which implies smaller cogging torque and core loss. As demonstrated in Figure 4-19, the three-layer model appears to have the highest cogging torque, while that of the two-layer one are much smaller than the other two.

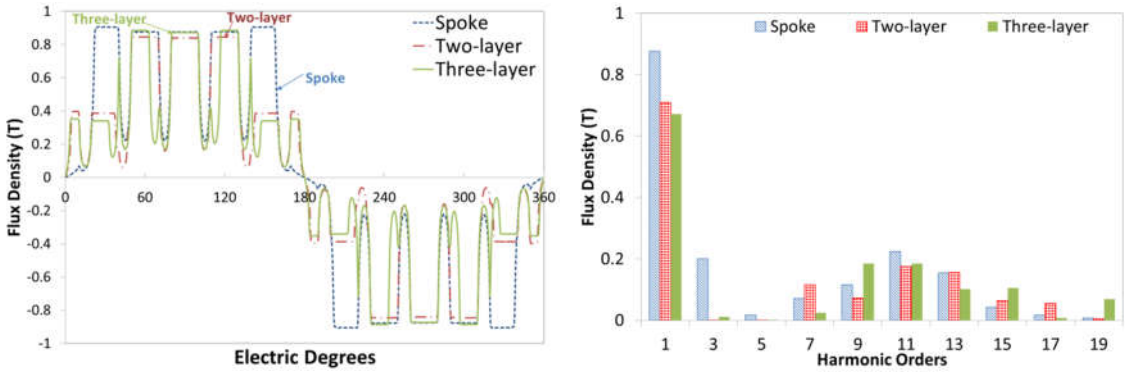

(a) Airgap flux distribution waveform; (b) Spectra of flux distribution;

Figure 4-17 Open-circuit airgap flux distribution waveform and spectra.

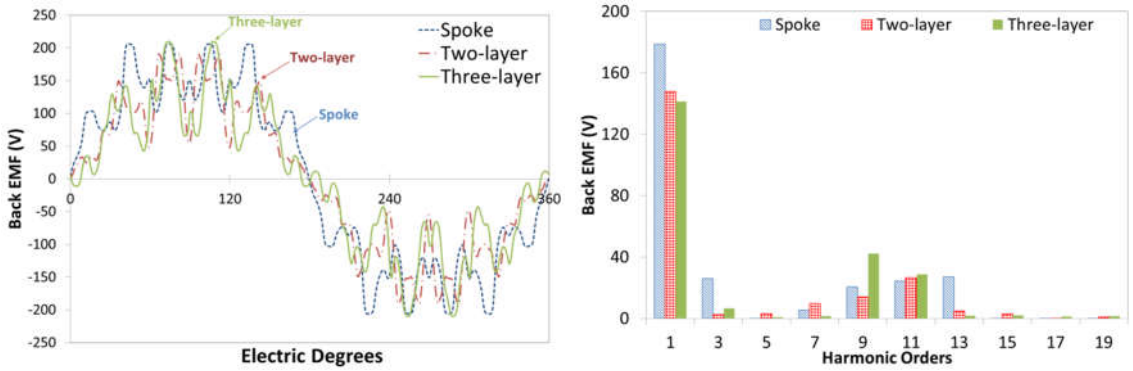

(a) Back EMF waveform; (b) Spectra of Back EMF;

Figure 4-18 Open-circuit back EMF and cogging torque.

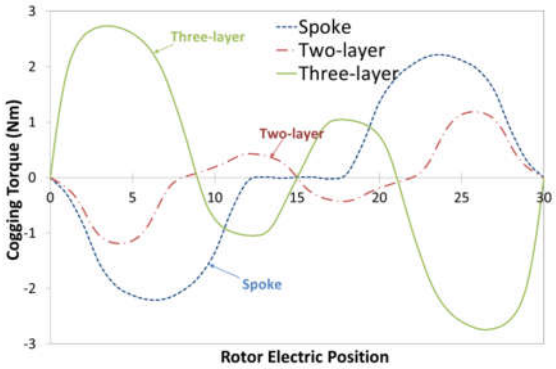

Figure 4-19 Comparison of cogging torque.

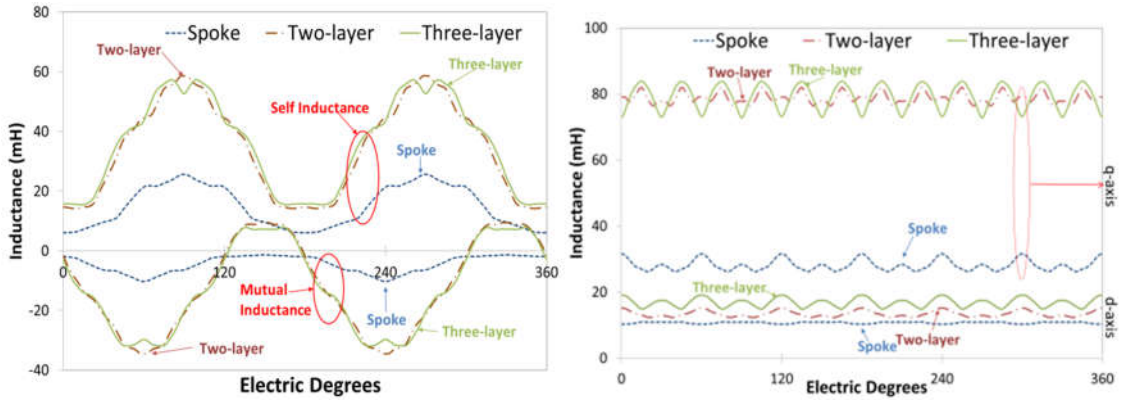

(a) Self and mutual inductances; (b) dq-axis inductance;

Figure 4-20 Armature self and mutual inductance.

The inductance of armature windings indicates the rotor saliency for PMSMs, which plays an important role especially for ferrite machines as reluctance torque is crucial to the overall torque output. The armature self and mutual inductances under open-circuit condition are depicted in Figure 4-20(a). The absolute value of self and mutual inductances for the one-layer structure are much lower than the multi-layer configurations, which indicated very low salient ration and reluctance torque. On the other hand, the two- and three-layer configurations have similar inductance profiles. What's more, the inductance waveforms of two- and three-layer ones exhibit large variations with rotor position. In order to manifest impacts of those differences, the d- and q-axis inductances are derived accordingly by Park Transformation based on self and mutual inductances, as illustrated in Figure 4-20(b). The average values of d- and q-axis inductance for the two- and three-layer configurations are close, thought the three-layer one shows marginally higher value. Although the d-axis inductance of the one-layer model is only slightly lower, its q-axis inductance is less than half of the multi-layer machines, which leads to much lower salient ratio L_q/L_d. Therefore, much higher reluctance torque can be expected for two- and three-layer configurations, while the one-layer machine will be majorly dependent on PM torque. The three-layer structure has the higher L_d, which indicated the flux weakening ability increases with the number of PM layers. It is also noteworthy that the lowest ripple of L_d and L_q waveforms is observed for the two-layer configuration, which reflects lowest torque ripple.

4.6.2 On-Load Conditions

Under various loading conditions, the induced voltage, inductance and even the cogging torque could change dramatically due to the armature reaction and saturation. The machines under study will become nonlinear and the two main torque components will be heavily coupled with each other. Firstly, the overall electromagnetic torque performances of the different machines are investigated for comparisons. The torque profiles are analysed under various current and advanced phase angle using FEA 2D nonlinear transient models. The armature current angle is the armature phase current leading the corresponding phase back EMF, and flux weakening can be achieved with positive current angles.

The average electromagnetic torque characteristics of the three configurations under different armature currents and advanced angle driving conditions are illustrated in Figure 4-21. The results reveal that the torque capabilities of the machines increase with the number of layers, especially under heavy load and overload conditions. Considerable improvement can be observed from one-layer to two-layer structure, while the improvement is not as conspicuous from two-layer to three-layer. When phase current angle equals zero, the one-layer configuration has the highest average torque, which indicates highest PM torque. But as the increase of current angle, the average torque increases much faster for two- and three-layer ones, which implies higher reluctance torque component for the multi-layer configurations. Thus, the optimal current angle to achieve the highest torque is much larger for multi-layer models owing to the greater contribution from reluctance torque. Compared with the two-layer structure, the salient ratio and reluctance torque is further improved for the three-layer one, and larger optimal current angle is observed, as shown in Figure 4-22. According to Equation (4-6), the PM torque is proportional to current, and reluctance torque is proportional to current square. So with the increase of armature current, the reluctance torque will grow more quickly than PM torque. Consequently, the contribution of the two torque components could be quite different under different loading conditions. To further investigate the torque productions of the three models, PM torque and reluctance torque are segregated using frozen permeability techniques.

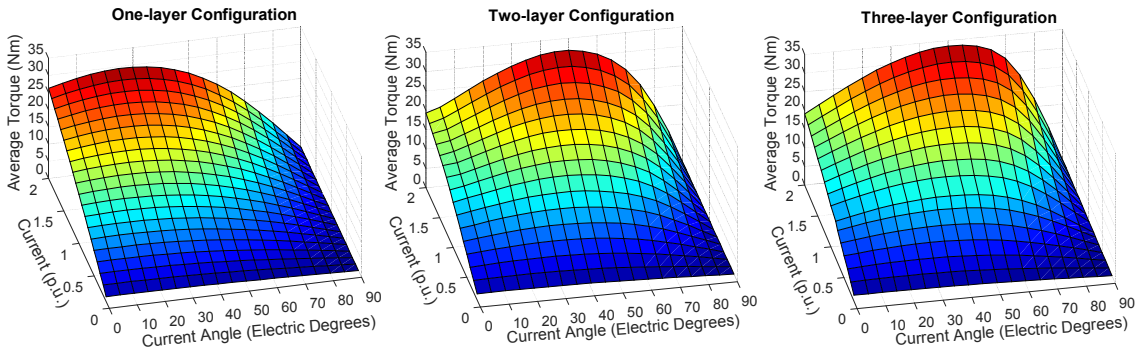

(a) One-layer; (b) Two-layer; (c) Three-layer;

Figure 4-21 Comparison of average torque characteristics.

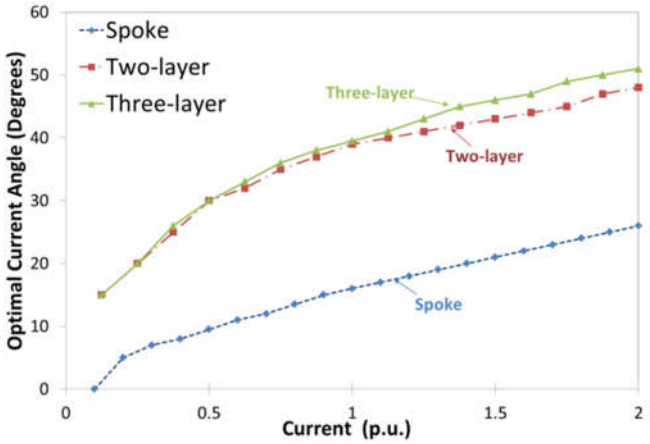

Figure 4-22 Comparison of Optimal current angle.

The torque components of the machines under four typical loading conditions are derived and demonstrated in Figure 4-23. At the rated current excitation as shown in Figure 4-23(a), there are significant improvements in the maximum torque output by adding more PM layers to the conventional spoke-type machine. Reluctance torque contributes larger part of the overall torque output for multi-layer configurations, while PM torque is the major contribution for one-layer design. Although the one-layer design has the highest PM torque, its reluctance torque is only half of the multi-layer machines due to the poor rotor saliency. The three-layer design has the highest average torque at rated current owing to the highest reluctance torque. The two-layer design has slightly lower maximum torque but the difference is less than 1%. In contrast, the one-layer machine relies heavily on the PM torque and the reluctance torque only comprises 25% of the overall torque due to the poor saliency ratio. In spite of

much higher PM torque, maximum torque capability of the one-layer machine is 8% lower than the other two. Since the reluctance torque increases more significantly than PM component, it plays an even more important role in the overall torque output with armature current increased to overloading. On the other hand, the increment of PM torque will be further reduced by larger demagnetizing d-axis current as a result of higher current angle. Therefore, the one-layer configuration is at an even greater disadvantage under overload conditions. The multi-layer configurations, on the contrary, shows even better torque characteristics due to its high rotor saliency even at highly saturated situation, as illustrated in Figure 4-23(b). Under double rated current, the two- and three-layer configurations exhibits 10% and 12% higher torque density than the one-layer design respectively.

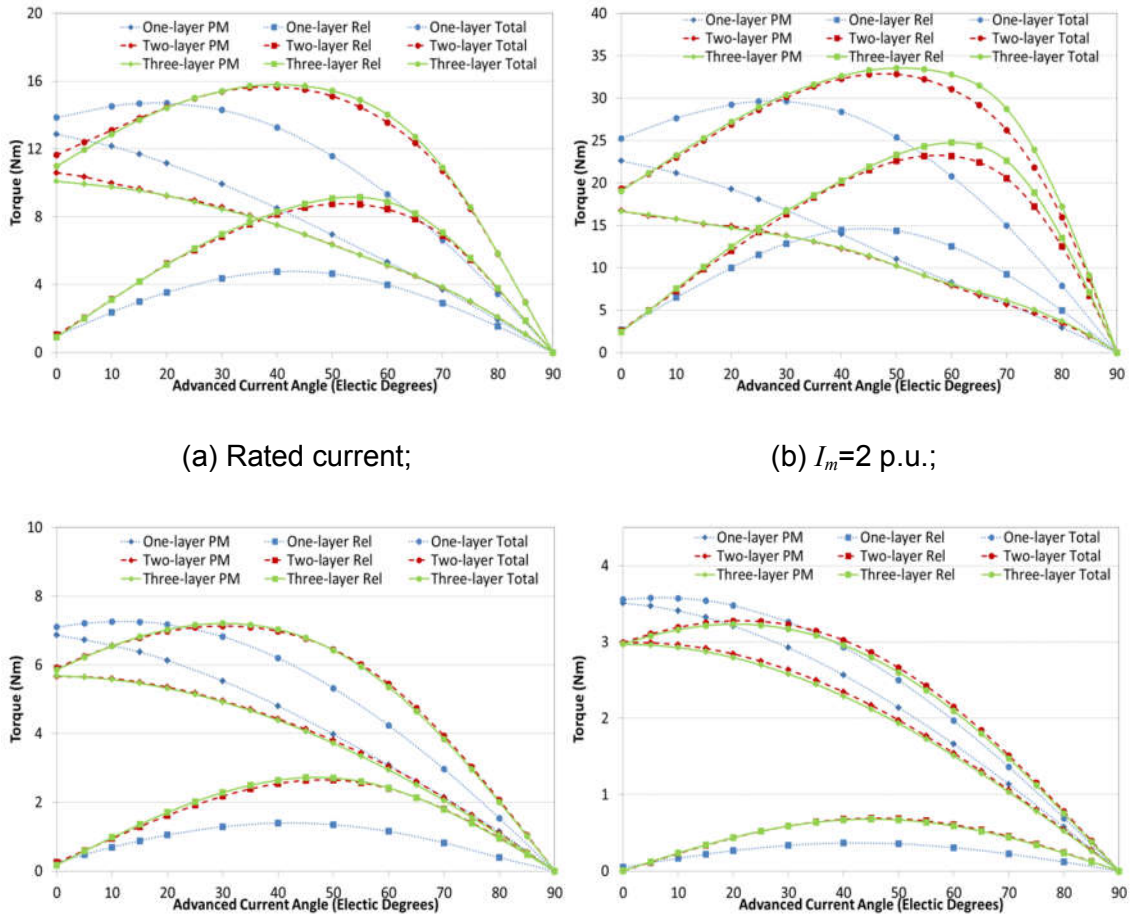

(a) Rated current;

(b) I_m=2 p.u.;

(c) I_m=0.5 p.u.;

(d) I_m=0.25 p.u;

Figure 4-23 Comparison of torque components under different loading current.

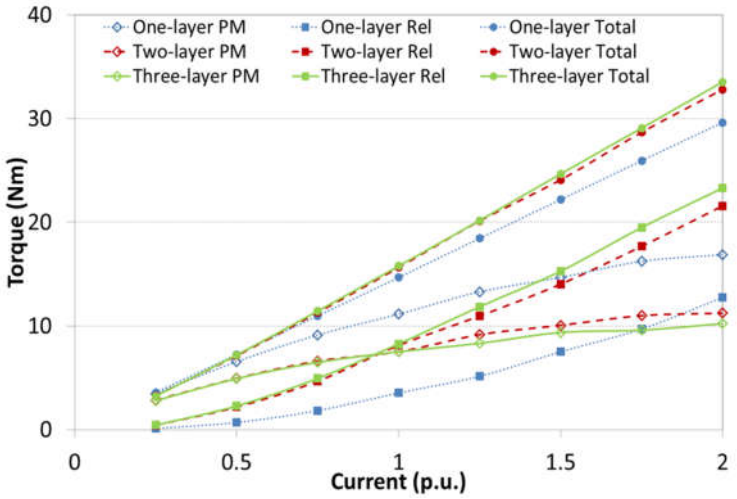

Figure 4-24 Torque segregations under maximum torque per ampere operations.

However, the situation reverses under medium and light load conditions. With the current reduced to half of the rated, reluctance torque of the machines declines dramatically. Since PM torque becomes the main part of the overall torque, the one-layer model can deliver slightly higher torque with better PM component. The two- and three-layer models have very similar torque profiles in terms of average torque output. But when the armature current drops down to light loading, the one-layer design starts to show its advantages because the overall torque output is basically contributed by the PM component. Under one fourth of the rated current, 9% higher torque can be delivered by the one-layer machine, and the two-layer structure exhibits slightly better torque than the three-layer one on account of its better flux focusing effect.

The overall torque characteristics of the three designs under maximum-torque-per-ampere operations are summarized in Figure 4-24. The one-layer design is able to achieve excellent flux focusing factor and maintains large portion of PM torque over most of the operational range. However, it is very difficult to deliver similar torque density as the rare-earth machines owing to the low strength of ferrite magnets. Besides, the PM torque is more prone to the adverse impact of demagnetizing armature current, and the PM torque increment of the one-layer machine is apparently slowed down under over-current conditions. This disadvantage will further affect the performance under heavy loading, limit the overload ability, and even cause demagnetization.

As for the multi-layer configurations, the torque density is prominently increased because of the significant improvement in rotor saliency. As machines are usually running under medium to rated load conditions, the designs with multi-layer configurations exhibit better overall performance than the conventional spoke-type machines. Comparing to two-layer design, the rotor saliency can be further enhanced by applying three or more PM layers. But the PM torque component reduces with more PM layers. Apparently, the improvement in torque is quite exiguous when the number of PM layers is increased from two to three. Furthermore, the machines with high number of PM layers are the more complicated and less rigid, which will inevitably increase the cost in manufacturing and rotor assembly.

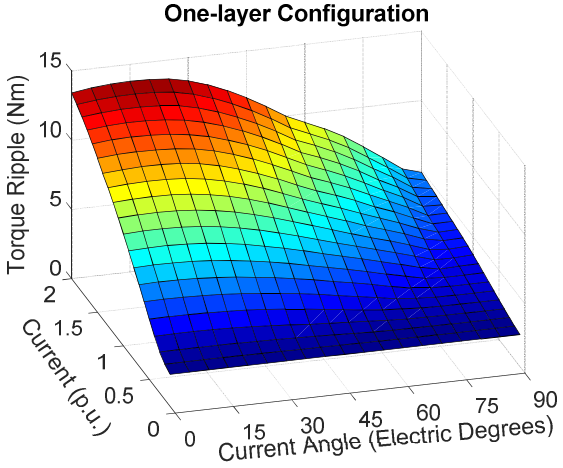

(a) Torque ripple of one-layer;

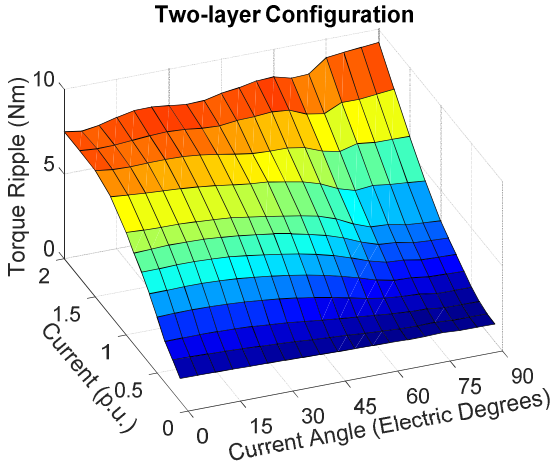

(b) Torque ripple of two-layer;

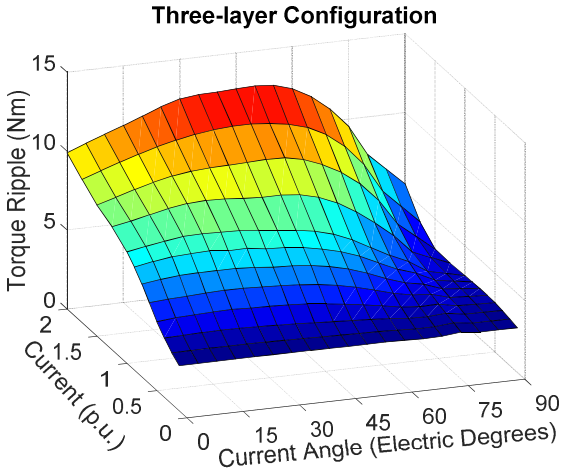

(c) Torque ripple of three-layer;

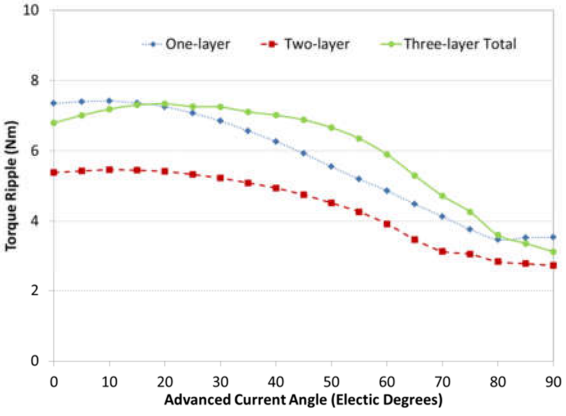

(d) Torque ripple comparison at rated current;

Figure 4-25 Comparison of peak-peak torque ripple of the three configurations.

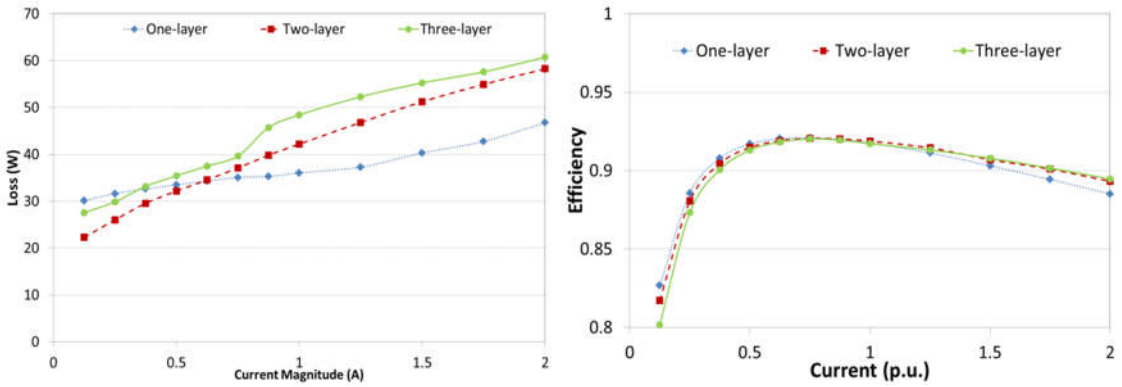

(a) Core loss; (b) Efficiency;

Figure 4-26 Core loss against current magnitude at rated speed.

The torque ripple profile under different exciting current amplitudes and phases is depicted in Figure 4-25. Since there is high content of harmonics in the PM excited field, the spoke-type model shows high torque ripple. And the three-layer design also exhibit high torque ripple because of high spatial harmonics caused by large number of PM slot openings and considerable cogging torque. On the other hand, the torque ripple of the two-layer one is the smallest among the three due to the more sinusoidal flux distribution and well-designed secondary PM layer. But the ripple grows dramatically with the increase of current amplitude and advanced angle.

As ferrite magnet materials are not conductive to electricity, the eddy current loss can be completely eliminated from the PMs. Figure 4-26(a) illustrates the core loss of the three designs under various current loading at rated speed. The core loss increases with current magnitude due to the influence of stronger winding reactive field. The one-layer design exhibits highest core loss at light load because of higher PM excited field. But its core loss is less affected by armature current due to the low inductance of the one-layer machine. Thus, the one-layer design shows lowest core loss under medium to heavy loading. On the other hand, the loss in the multi-layer cores increases much fast with the current as a result of much higher winding inductances and stronger armature reaction. Owing to higher open-circuit harmonic flux contents, the three-layer configuration has slightly higher iron loss than the two-layer one.

The one-layer design can achieve higher efficiency under light to medium load conditions because of higher torque output. However, since its torque capability becomes much smaller than the multi-layer ones under heavy and overload conditions, the efficiency drops much faster because of lower power density. On the other hand, the two-layer machine shows the best average efficiency within rated operating range and achieves the efficiency of 92% at rated operating point, striking the right balance between torque capability and loss, as demonstrated in Figure 4-26(b). The efficiency of the three-layer design only exceeds the two-layer one during overloading operations, which is beyond the nominal requirements and rarely occurs.

4.6.3 Performance at Higher Working Temperature

Due to the power losses in electric machines such as copper loss and iron loss, considerate temperature rise is inevitable under continuous heavy load conditions. The magnetic properties of PMs are sensitive to the temperature and the residual flux density usually decreases with the temperature rise. For ferrite magnets, the temperature coefficient is -0.2% for residual flux density. As a result, PM machines could suffer noticeable decrease in torque output owing to lower PM torque. According to [139], the residual flux density at certain temperature is given by

$$B_{rT} = B_{r20}\left[1 + k_{br}\left(T_c - 20\right)\right] \quad \textbf{(4-9)}$$

where B_{rT} and B_{r20} are the residual flux density under T_c and 20°C respectively, k_{br} is the temperature coefficient. According to Equation (4-9), the residual flux density is 11% lower under a working temperature of 75°C, which will definitely impose considerable effect on the PM torque and thus the torque profiles for PM machines.

The influence of temperature on torque production under different load is demonstrated in Figure 4-27 for all the three configurations. It is obvious that higher temperature decreases torque performance more severely because of lower PM flux field and thus lower PM torque. Since the composition of torque components changes with current amplitude, the influence of temperature rise

on torque output varies under different load conditions. At light loading, torque output is more severely affected. The torque decrease is about 10% at 75°C and 14% at 100°C for all three designs under 1/4 rated current. As the increase of loading current, the influence of temperature decreases, and the multi-layer configurations show more advantageous performance over the one-layer structure. Under rated loading, the one-layer machine suffers 8.7% decrease in torque at 75°C, but the torque declines of the two- and three-layer structures are 4.5% and 4.2% respectively. Under double rated current loading at 75°C, the torque decrement is 5.8% for one-layer, while it is only 3.0% for two-layer and 2.9% for three-layer configurations. Because PM torque contributes the major part of the overall torque at light load, the overall torque will be more severely affected by the temperature rise due to the adverse impact on PM magnetization. However, the increase in temperature has little influence on reluctance component, and the overall torque is less influenced when the reluctance torque component dominates under high current loading.

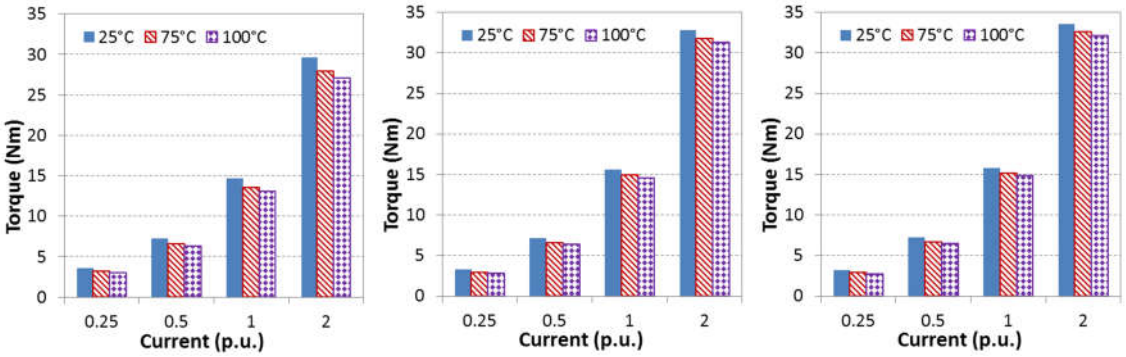

(a) One-layer; (b) Two-layer; (b) Three-layer;

Figure 4-27 Influence of temperature on torque under different load conditions.

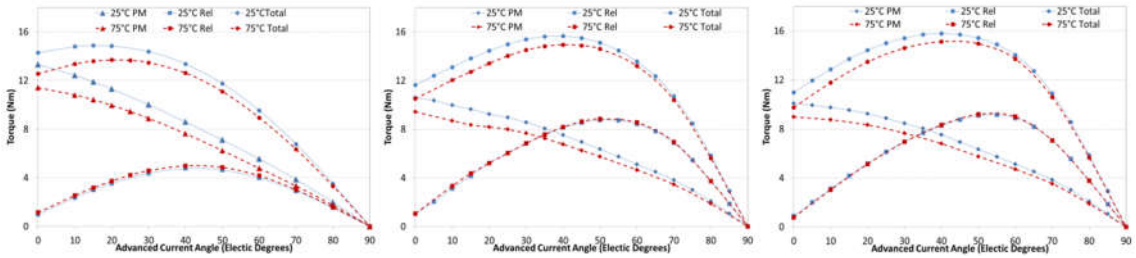

(a) One-layer; (b) Two-layer; (b) Three-layer;

Figure 4-28 Influence of temperature on torque components at rated load.

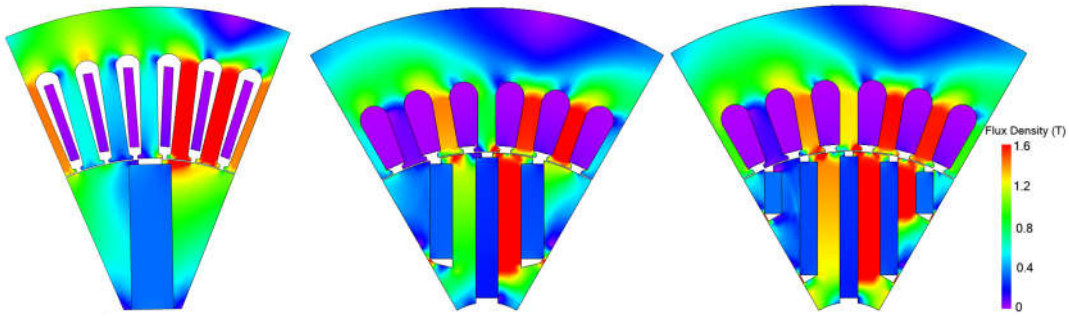

(a) One-layer; (b) Two-layer; (b) Three-layer;

Figure 4-29 Flux distribution at rated current with optimal current angle.

Figure 4-28 depicts the torque profiles of the three configurations under 25°C and 75°C with rated current, and indicates more detailed explanations for the different effect on the performances of the three designs. Because the one-layer machine has highest portion of PM torque, it suffers the worst influence of temperature rise, with 12.5% decrease in PM torque and 8.7% in overall torque. Due to the significant weakened PM field, the saturation is alleviated and slightly higher reluctance torque is observed for the one-layer model under 75°C. On the other hand, the multi-layer configurations show better performance than one-layer design against temperature rise, and the torque decrease at 75°C is 4.5% and 4.3% for two- and three-layer respectively, which makes the rated torque output of multi-layer designs 12% higher than that of spoke-type. The temperature rise only affects the PM torque for multi-layer configurations, while their reluctance torque profiles are almost the same under different temperature. As shown in Figure 4-29, heavy saturation appears in the rotor core between different PM layers for the multi-layer configurations due to the q-axis reactive field, and no such phenomenon occurs for the spoke-type. Thus, weakened PM field can alleviate the saturation for one-layer structure, while it is ineffectual for multi-layer designs as the highly saturated area in the rotor cores is caused by armature reactive field.

4.7 Conclusion

This chapter discussed the design of the one-layer and the proposed multi-layer spoke-type ferrite IPMs based on the analytical models derived, and the final designs of each configuration are verified by FEA methods. Then the

electromagnetic performances of the optimal designs with one to three PM layers are comprehensively investigated and compared to reveal the advantages and disadvantages of among the multi-layer designs and the conventional spoke-type structures. The one-layer machine shows better flux focusing effect and higher PM torque component, and thus higher efficiency can be achieved under light load conditions. The multi-layer structures are able to increase the rotor saliency and enhance the reluctance torque. Hence they can deliver higher torque at high current loading and exhibits good efficiency. What's more, the multi-layer designs show more advantageous performance at higher working temperatures due to larger reluctance torque component. Larger PM layer number can increase the saliency and torque density at heavy load, but it would inevitably lead to complex rotor structure and higher manufacturing cost, while the improvement in torque is not as significant. Thus the two-layer design is the most cost-effective solution for ferrite IPMs, which exhibits much higher torque than one-layer one yet much simpler rotor structure than three-layer design.

5 DEMAGNETIZATION STUDY

5.1 Background Introduction

Permanent magnet synchronous machines are considered to be the most attractive candidates for traction applications owing to the merits of high power density, excellent efficiency and good controllability. However, because the PM poles are pre-magnetized, there is a risk of irreversible demagnetizations for PM machines when facing strong armature reactive field or high temperature or both. If PMs are locally demagnetized, both remanence and coercivity are reduced, which will cause distortion of magnetic field and decrease in torque output. Moreover, the demagnetization might spread to the nearby areas because the degraded magnets could not withstand further demagnetizing magnetomotive force [148,149].

The demagnetization of PMSMs has been investigated in literatures by both analytical and numerical methods. J. Wang et al. in [150] and M. Galea et al. in [151] developed mathematical models for surface-mounted PM machines based on Maxwell's Equations. The open-circuit flux distribution and armature reaction are first calculated separately and then superposed together. In mathematical models, the flux density of any point can be obtained, and thus partial demagnetization is possible to be evaluated. But the derivative process of such pure mathematical model is sophisticated, and the complexity of the analytical models depend on the machine geometries. For IPM machines with more complicated structures, it could be much difficult to obtain accurate equations or even unsolvable. On the other hand, magnetic geometries equivalent circuit models are easier to realize a solution according to the flux loops inside the machine by applying of Gauss's Low and Ampere's Law [152–156]. But magnetic equivalent circuit models usually consider the reluctance of one PM pole as a whole, and thus they provide conceptual explanation and mechanism rather than detailed partial demagnetization calculation. From analytical models, quick calculation and direct relations among different parameters can be achieved. However, the machine geometries are sometimes simplified and saturation is usually neglected in analytical models. As a result, the accuracy is

often not sufficient because intensive saturation occurs during irreversible demagnetization and the machines become highly non-linear systems. To achieve better accuracy, FEA approaches are used for fully investigating the demagnetization phenomenon and verifying analytical results [88,155–158].

Since the discovery of the high-energy rare-earth magnets, they have been dominated in high performance PM machine applications. Since the PM excited field is crucial to rare-earth PM machines, the demagnetizations have been investigated in many past works concerning rare-earth magnets. To minimize the risk of demagnetization, some were focused on the shape of magnet poles and the number of PM layers [152,159], some concentrated on the optimizations of flux barrier shape and position [160,161], and some considered the amount of magnet [162,163]. To reduce the material cost, Dy-free NdFeB motors were studied because of much lower coercive force [164]. Other structures such as dual-cage configurations were proposed for the line-start permanent magnet synchronous motors to lower risk of demagnetisation [148]. According to the temperature property of rare-earth PM material, the rise of temperature will reduce both the residual flux density and coercive force, and thus the risk of irreversible demagnetization is increased [149,165,166]. Moreover, the rare-earth materials are electricity conductive, and eddy current will be induced when exposed to the alternating armature reactive field. Therefore, the reliability of rare-earth PM machines may be seriously deteriorated by the heat generated from eddy current loss.

Recently, due to the soaring price and unstable supply of rare-earth magnets, ferrites PMs are considered to be a most attractive substitution considering the distinctive advantages of its own. Unlike rare-earth magnet, ferrite materials are more stable under higher temperature because the reversible temperature coefficient for the intrinsic coercivity is positive. In other words, the ferrite magnet is able to withstand stronger demagnetizing field under higher working temperature. Besides, ferrite magnets have higher Curie temperature, and can work at much higher temperature than rare-earth PMs. Ferrite magnets also have excellent corrosion resistance as they are essentially made from oxides of

iron, Strontium and Barium. Thus, ferrite magnets have is inherently suitable for applications in harsh environment such as heat and damp.

However, the biggest weakness of ferrite magnets has been the low magnetic strength. Compared with rare-earth PMs, ferrite PM materials have much lower residual flux density and coercive force, and are more vulnerable to the armature reactive field in terms of demagnetization. So it is of great importance to investigate the capability of ferrite PM machine against demagnetization. An analytical model was proposed based on magnetic equivalent circuit in [154] for PMASynRMs, focusing on the influence of flux barrier and machine dimension on demagnetization. But detailed partial demagnetization prediction was not possible by the analytical model, and FEA models were built for final verification. To protect the ferrite magnet poles from armature reactive field, many approaches are investigated for the reduction of demagnetization. Noticeable decrease in demagnetization was achieved by using fillet smoothing the magnet edge [81], tapered flux barriers [82], segmented PM poles [74,83], and re-arrangement of the thickness of multi-layer barriers [84]. Compared with PMASynRM, spoke-type suffers higher risks of irreversible demagnetization [33]. Although demagnetization occurred in [87,105,106], no solution was presented. A few approaches were proposed to reduce demagnetization for spoke-type machines, such as cutting the edge end with chamfered-style [102], deeper PM insertion [107] and magnet overhang [93]. However, no systematic research has been proposed to investigate the robustness toward demagnetization for the spoke-type ferrite machines.

In the literature, the only criterion for demagnetization is whether the flux density of the PM is above or below the knee point, and the demagnetization is only evaluated by adding demagnetized area (or volume) of magnets without considering the level of degradation. When partial demagnetization occurs in the magnets, they do not necessarily lose all the magnetism. In most situations, partially demagnetized PM poles can still provide a fraction of their original magnetic strength. Thus, the estimation is not of enough accuracy by merely counting area (or volume).

In this chapter, the mechanism of the demagnetization of conventional spoke-type and the two-layer configuration are comprehensively investigated. The key factors such as current, material, temperature are all taken into consideration. Effective approaches are also proposed to reduce the risk of demagnetization. For accurate assessment, the term of demagnetization ratio is used to describe the level of degradation in the demagnetized part of magnets. And together with the demagnetized area, the overall quantitative demagnetization ratio can be addressed properly.

5.2 Demagnetization Mechanism

Permanent magnets are also known as hard magnetic materials, because they have very wide hysteresis loop. After being magnetized, PMs can produce and maintain magnetic field in the airgap without excitation windings or power consumption. That is the reason why PM machines are able to achieve higher efficiency and power density.

The characteristics of PM materials are usually described using the upper left part of the magnetic hysteresis loop (usually in the second quadrant), which is called BH demagnetization curve or simply BH curve, as depicted in Figure 5-1. There are several key parameters of the demagnetization curve to characterize the property of a PM. Remanent magnetic flux density (B_r), also called remanence or residual flux density, is the magnetic flux density corresponding to zero magnetic field intensity. High remanence can provide the airgap with higher flux density. Coercive field strength (H_c), or coercivity, is the demagnetization field intensity required to make the flux density to zero in a pre-magnetized PM material. Higher coercivity means better ability to withstand demagnetizing field.

As shown in Figure 5-1, when pre-magnetized, the flux density of the PM is B_r under zero field intensity at point a; if applied to a magnetic circuit, the working point drops down to b; when the opposing magnetic field is removed, the flux density returns to c along a minor hysteresis line at the value of B_{rl}; applying the flux field again, a complete minor hysteresis loop will be formed and the PM

stays at a stable state; if a stronger demagnetization field is applied to the PM, the flux density goes further down to point d, and a new recoil loop will be established with an lower remanence B_{r2}. This is the process of partially demagnetization. And each time this happens, the PM is degraded with a reduced remanent flux density. It is very important to note that the minor hysteresis curves are very close to straight lines [167]. Thus the minor loops are usually replaced by straight recoil lines to simplify the PM model, as indicated by dash lines in Figure 5-1. For each recoil line, irreversible demagnetization happens when the operating point of the PM falls below a threshold value. The inflection point is called knee point and the flux density at this point is used as the judging criterion for whether demagnetization has happened.

For conventional study of demagnetizations, the property of the whole PMs is set to be the same in terms of remanence and coercivity. But such investigation might not be adequate if any local demagnetization happens, because in that case, part of the PMs could be degraded with lower remanence and coercivity. As a result, more accurate result requires real-time update of the BH curve of the relegated PM during the transient calculation.

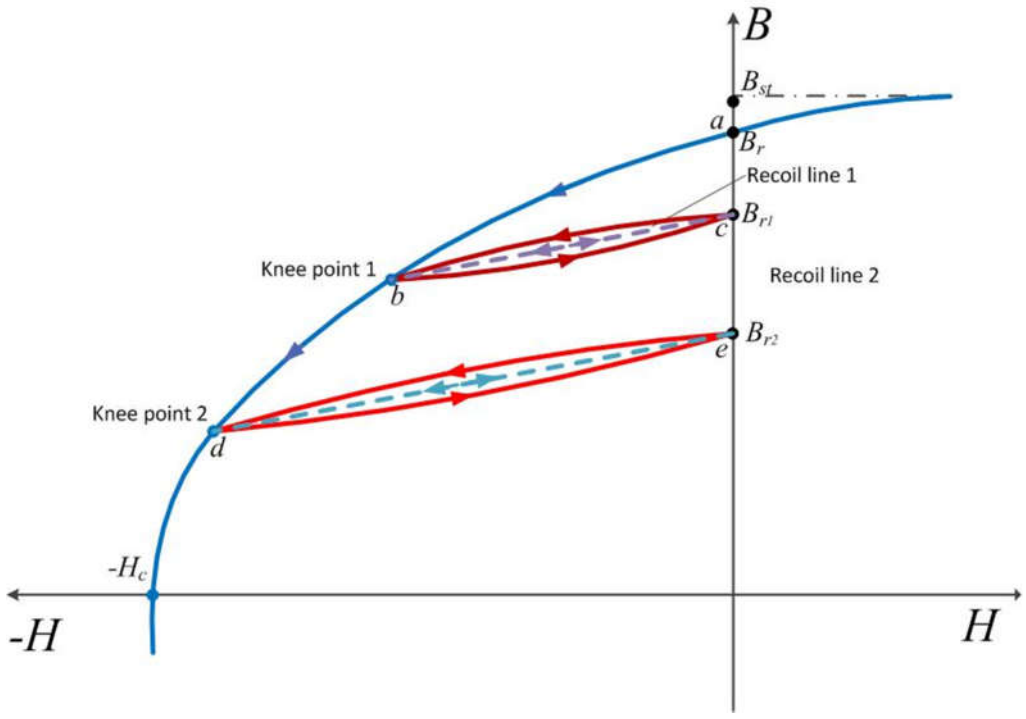

Figure 5-1 Demagnetization curve and recoil lines of a typical PM material

In literature, the severity of demagnetization is usually evaluated by the demagnetized area in the PMs [151,157,158,168]. Although the area can be regarded as an indicator to represent the degree of demagnetization, the severity of the overall demagnetization cannot be described precisely by the area alone. So long as the PM is not fully demagnetized, it is still able to establish a lower remanence. Thus, the degraded level of remanence is also an important parameter to describe the demagnetization.

To evaluate the overall PM demagnetization quantitatively, two parameters are necessary for description of the degradation of the PMs in a machine, namely demagnetized area (volume for 3D models) and demagnetization ratio. The demagnetization ratio describes the level of degradation of the PM. For a certain point or element in the mesh, the demagnetization ratio is defined as ratio of decreased remanence after demagnetization:

$$\xi = 1 - \frac{B_{rn}'}{B_r} \tag{5-1}$$

Together with the area of each element in the mesh, the overall demagnetization of the PMs can be described by demagnetization index:

$$\lambda_d = 1 - \frac{\sum B_{rn}' S_{en}}{B_r S_{PM}} = \frac{\sum \xi S_{en}}{S_{PM}} \tag{5-2}$$

where B_{rn}' is the degraded remanence after partial demagnetization, B_r is the original remanence, S_{en} is the area of element n, and S_{PM} is the total area of all the PMs.

Intrinsic magnetization B_i is also often used to describe the inherent property of a PM material, indicating the flux density contributed by ferromagnetic core. The relationships among the intrinsic magnetization, flux density and field intensity of a ferromagnetic material can be express as [139]:

$$B = \mu_0 H + B_i = \mu_0 \left(H + M \right) \tag{5-3}$$

where M is the magnetization.

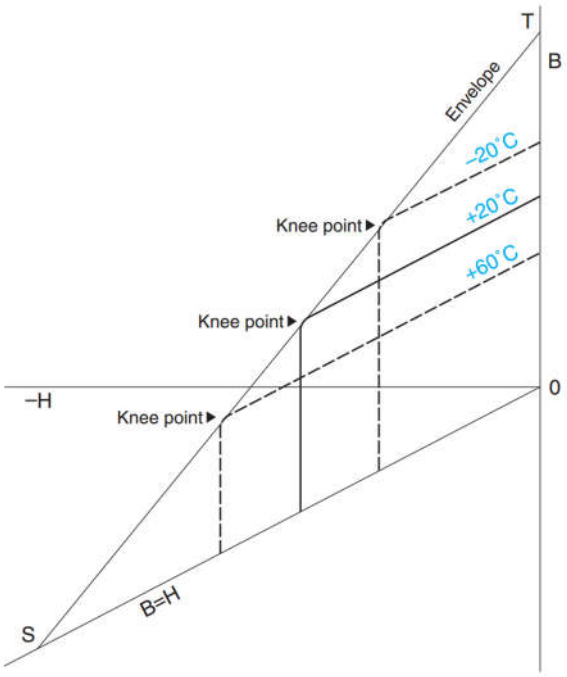

Figure 5-2 Change of BH curves and knee points of ferrite material with different working temperature.

For most of the PM materials, their characteristics are quite sensitive to temperature. As the temperature increases, the remanence decreases and so does the flux density in the airgap. What's more, a pre-magnetized PM can be demagnetized completely if the temperature exceeds its Curie temperature. When investigating the demagnetization, temperature is an important factor because both the BH curve and knee point are changing depending on the operating temperature, as shown in Figure 5-2. Thus, accurate predictions of demagnetization should consider the influence of both opposing magnetic field and the operating temperature. For ferrite PMs, the absolute value of the magnetic flux intensity of the knee point increases with the rise of temperature. Under continuous driving conditions, the operating temperature is relatively high due to the heat generated by various losses in the system, and ferrite materials are able to withstand stronger demagnetizing field. This means ferrite PM machines are more reliable for long term operations. On the other hand, since ferrite magnets are more prone to demagnetization in very cold environments, special attentions should be paid to the protection of ferrite magnets from strong the demagnetizing armature field during cold starting.

5.3 Demagnetization Prediction by Analytical Models

In an ideal d-q frame model, the demagnetizing field over the PMs is attributed to the negative d-axis current. As demonstrated in Figure 3-30 and Figure 3-35, d-axis reactive field goes through the PM slots while q-axis only travels along the lamination core in the rotor. Thus, q-axis is considered irrelevant to demagnetization in the idealized analytical model. Although q-axis current has a cross-coupled effect on the demagnetization due to the saturation in the rotor laminations [169], the influence is insignificant.

The analytical models developed in Chapter 3 are very convenient for preliminary design and performance prediction. But since one piece of the PM is considered to have the properties in the analytical equivalent magnetic circuit in the model, It would very difficult to calculate detailed quantitative partially demagnetization in some specific part of the PMs. However, for large scale demagnetization, the critical d-axis current can be predicted when the reactive field reaches the flux intensity of the knee point in the BH curve to cause the degradation of the PMs. According to Equation (3-49), the flux intensity of the working points of the main and secondary PMs under open-circuit condition can be express as:

$$H_{m1} = -\frac{2g_c}{W_1} H_{g1} = -\frac{2g_c}{W_1} \frac{B_{g1}}{\mu_0} \tag{5-4}$$

$$H_{m2} = \frac{g_c}{W_2}\left(H_{g1} - H_{g2}\right) = \frac{g_c}{W_2} \frac{B_{g1} - B_{g2}}{\mu_0} \tag{5-5}$$

And the demagnetizing flux intensity in the main and secondary PM slots induced by negative d-axis current can be calculated by Equation (3-62) and (3-63) respectively. For better understanding of the investigation, the magnitude of the rated stator current (I_{rated}) is set as the per unit (p.u.) reference value. And i_d=I_{rated} is applied to Equation (3-62) and (3-63) for the calculation of H_{m1d} and H_{m2d} under per unit d-axis current. Thus, for a ferrite material with knee point flux intensity of H_d, the per unit critical current for the main and secondary PMs are obtained:

$$i_{cd1} = \frac{H_d + H_{m1}}{H_{m1d}} \tag{5-6}$$

$$i_{cd2} = \frac{H_d + H_{m2}}{H_{m2d}} \tag{5-7}$$

For the design achieved in the previous chapter and ferrite material Y25 (B_r=0.41T, H_d=155kA), the critical i_d for the main PMs is 2.2 p.u., and is 3.1 p.u. for secondary poles. For more accurate results, FEA model is usually used to verify the results, as shown in Figure 5-3. The prediction from analytical models shows good agreement with FEA. Because the average value is used for the calculation of airgap length, the actual maximum demagnetizing field would be slightly stronger. Hence the actual critical i_d is slightly smaller than the result derived from the analytical models. Since all the d-axis reactive flux goes through the main PMs, the main PMs are more vulnerable than secondary PMs. Large scale demagnetization emerges in the main PMs at -2 p.u., while it spreads to the secondary PM at -3 p.u. of d-axis current. Under this circumstance, nearly all PMs are degraded to some extent. The critical current represents the ability of the PM machine to withstand demagnetizing field during large fault current conditions. To prevent serious demagnetization, the d-axis current should be kept below i_{d1} at all times.

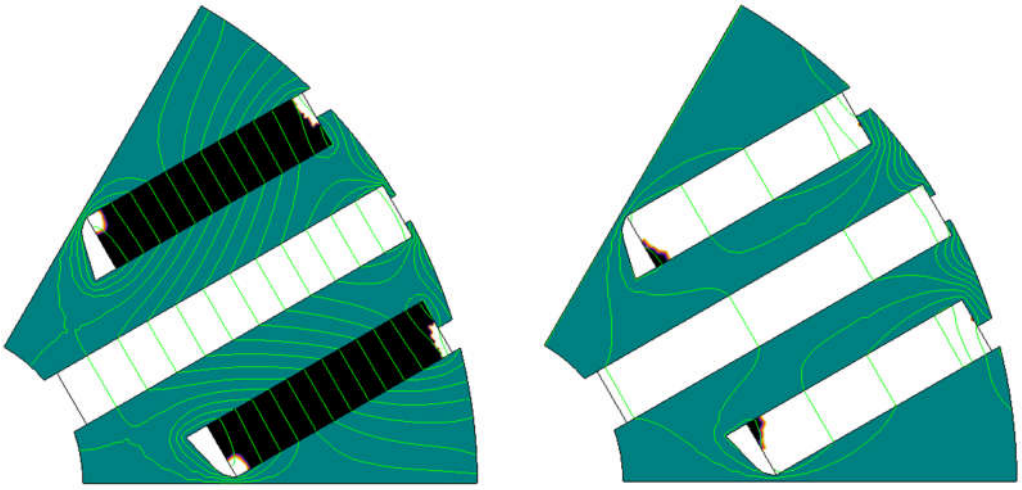

(a) i_d =-2 p.u., i_q=0; (b) i_d=-3 p.u., i_q=0;

Figure 5-3 Demagnetization and flux at different critical *d*-axis current

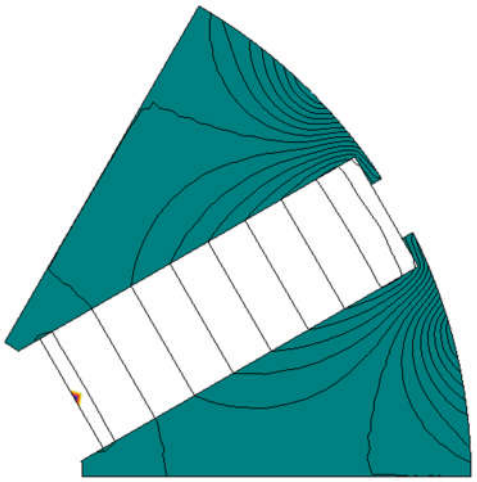

Figure 5-4 Demagnetization and flux at different critical *d*-axis current -2.3 p.u.

Similarly, the critical d-axis current can be predicted by analytical method for the one-layer structure. As there is only one magnet in one pole pitch, the model is much simpler. According to Equation (3-10), the flux intensity of the PM at open-circuit condition can be obtained

$$H_m = -\frac{2g_c}{W_1} H_g = -\frac{2g_c}{W_1}\frac{B_g}{\mu_0} \tag{5-8}$$

Thus, the critical d-axis current for the spoke-type is derived by

$$i_{cd} = \frac{H_d + H_m}{H_{md}} \tag{5-9}$$

The critical d-axis current calculated from analytical model is -2.5 p.u. for the model with Y25 ferrite PMs. As demonstrated in Figure 5-4, the large scale demagnetization occurs at -2.3 p.u. d-axis current by FEA simulations, which verifies the developed analytical models.

5.4 Investigation of Demagnetization by FEA

Large scale demagnetization usually happens under fault conditions such as short circuit current, and there will be serious degradation in the machine performance. Usually local partial demagnetization may occur in certain part of the PMs under heavy loading conditions because of severe saturation and highly distorted reactive MMF distribution in certain part of the rotor. Local

demagnetization can also cause degradation in machine performance. What's more, local demagnetization area might spread as the partial relegated magnets fail to withstand armature demagnetizing field, and deteriorate the performance even further. The analytical method is not adequate to provide detailed answers for local demagnetization because of the ignorance of saturation and simplification of machine geometry. To obtain accurate evaluation, FEA models are necessary to ensure the reliability of the machine models concerning the PMs under required working conditions.

There are many causes of irreversible demagnetization, such as aging, heat, shock and demagnetizing MMF. For permanent magnet machines, armature reactive MMF is the first cause of demagnetization, especially for the low strength ferrite magnets. The intrinsic property of ferrite, more specifically the coercivity, indicates the ability to endure demagnetizing field and is the internal factor of demagnetization. Higher intrinsic coercivity of the material means better anti-demagnetizing capability and higher electric loading is possible. On the other hand, heat is less a concern for ferrite PMs, since the maximum working temperature is usually over 300ºC and the ability to withstand demagnetizing MMF increases with temperature rise. However, the intrinsic coercivity of ferrite magnets decreases with the drop of operational temperature, which makes ferrite PMs more vulnerable in cold environments. In all, the key factors for demagnetization are demagnetizing MMF, intrinsic coercivity of the material, and operating temperature.

5.4.1 Demagnetization of Two-Layer Configurations

5.4.1.1 Influence of Armature Current

5.4.1.1.1 D-axis Current

The reactive field induced by negative i_d is directly opposing PM excitation, and is the main reason of demagnetization. With only d-axis current, the working points along the main PM in the radial direction are shown in Figure 5-5. And Figure 5-6 depicts the demagnetization ratio distributions in the PMs. The demagnetization ratio is indicated by different colours. The colour purple indicates no demagnetization at all, while the colour red means complete

demagnetization with remanence decreased to zero. Obviously, the working points of the PMs decrease with the increase of i_d. Under low i_d condition, the working points in one piece of PM pole are almost the same. As the increase of i_d, the flux density in the outer part of the PMs drops more dramatically, because the magnetizing field is stronger near the airgap close to the stator armature. As a result, irreversible demagnetization occurs in the outer part first and then spreads gradually with further increase of i_d, but refined in only the outer edge area as shown in Figure 5-6 (a) and (b). It is noteworthy that the outer edge of the PMs close to the airgap is more prone to be demagnetized because of stronger reactive field and lack of protection from the lamination core. When the current is reaching critical i_d, the working point of inner part of the main PM drops faster, and large scale of demagnetization starts from the inner part and spreads to the rest of the main pole, as illustrated in Figure 5-6 (c).

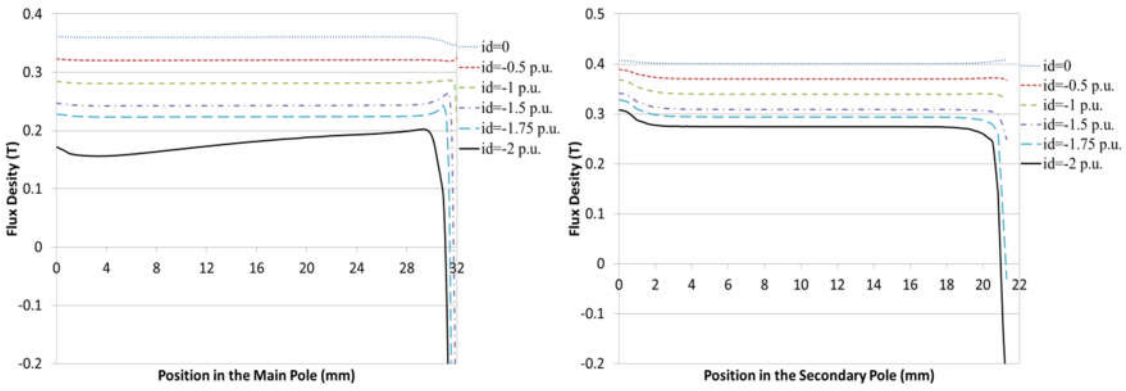

(a) Main PMs; (b) Secondary PMs;

Figure 5-5 Working points of the PMs under different d-axis current.

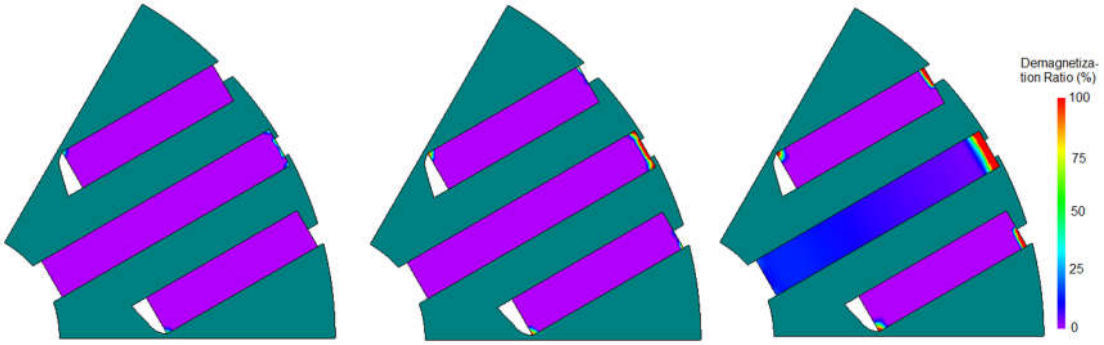

(a) i_d =-1 p.u.; (b) i_d =-1.5 p.u.; (c) i_d =-2 p.u.;

Figure 5-6 Demagnetization ratio distributions under different d-axis current.

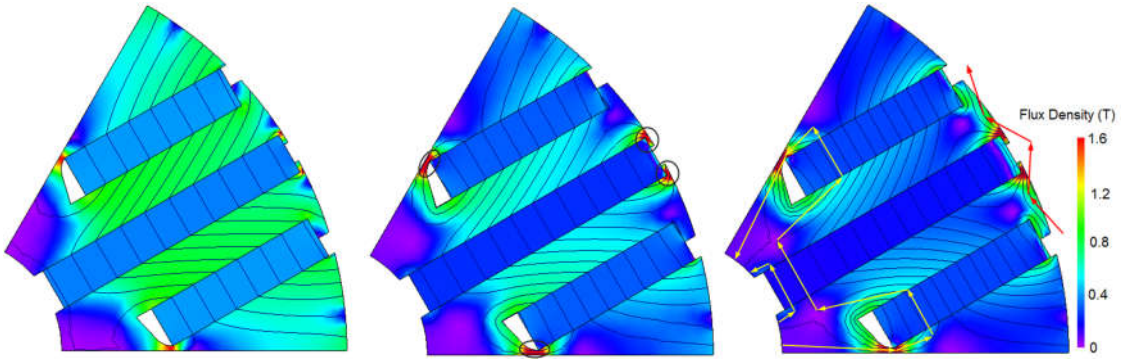

(a) i_d =0; (b) i_d =-1.5 p.u.; (c) i_d =-2 p.u.;

Figure 5-7 Flux distribution in the rotor under different d-axis current.

To explain the pattern of demagnetization due to the d-axis current, the flux distribution under different i_d is demonstrated in Figure 5-7, which provides a deeper insight into how the demagnetization is influenced by d-axis current. Under open-circuit condition, no saturation appears except the surface near the slot opening. With the increase of i_d, the bridge areas become more saturated because the bridges provide a path for the inverse d-axis flux. As the increase of saturation, the demagnetizing flux is forced into the edge of the PMs near the heavily saturated lamination in the bridge areas, as shown in Figure 5-7 (b). Although the flux density in large part of the rotor lamination decreases due to the opposing flux weakening field, the saturation in the rotor surface aggravates because the demagnetizing flux and PM leakage flux share the same path. With further increase of i_d, considerable part of the flux induced by armature windings goes in a zig-zag path from the rotor surface through the airgap to stator teeth and then back to the rotor again, rather than crossing the PM slot, as demonstrated in red arrows in Figure 5-7 (c). That is the major reason why the outer edge of the PM poles suffers much higher risk of demagnetization. On the other hand, the flux lines excited from the inner part of the PMs are pushed inside the non-magnetic shaft area or going through severely saturated bridges, which is depicted with the yellow arrows in Figure 5-7 (c). Hence, the reluctance of the flux loops increased more significantly for the inner part of magnets, and the flux density of this part of the PMs drops more dramatically, resulting in lower working point and causing the emergence of large scale demagnetization from the inner side to the outer.

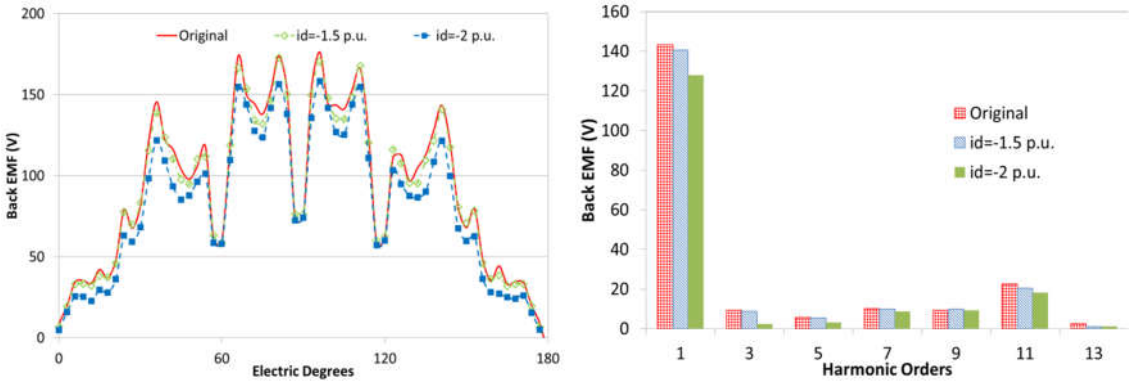

(a) Back EMF; (b) Spectra;

Figure 5-8 Back EMF and spectra comparison after different i_d.

Although local demagnetization appears with i_d smaller than critical d-axis current, the degradation in the PMs is not significant. The demagnetized area is quite small and appears only in the edge. The overall demagnetization index is only 1.3% even under the d-axis current of -1.5 p.u. When the critical i_d for the main PMs is reached, the demagnetization index increases to 8.2%, and noticeable degradation can be observed in the motor performance. The degradation of the PMs can cause the reduction in open-circuit flux density and thus the flux linkage, which is revealed in the back EMF directly. As shown in Figure 5-8, the back EMF of the machine is reduced by 1.6% under 1.5 p.u. demagnetizing current, while the decline in the fundamental grows to 10.9% with 2 p.u. negative i_d.

5.4.1.1.2 *Q*-axis Current

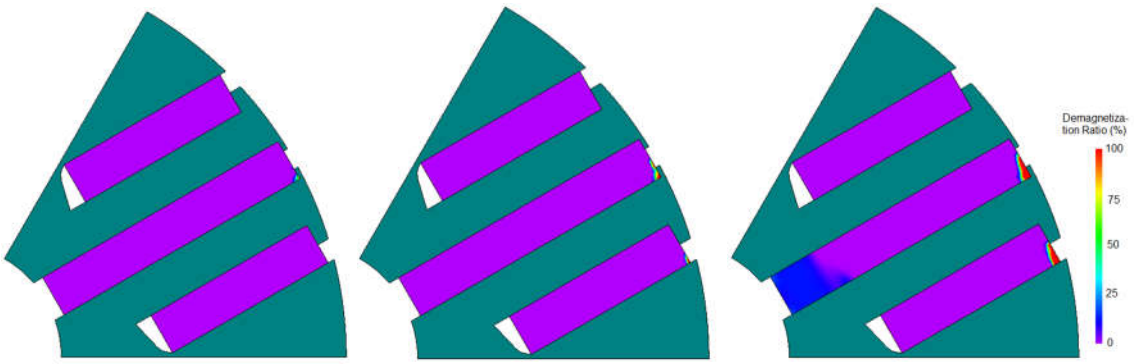

(a) i_q =0.5 p.u.; (b) i_q =1 p.u.; (c) i_q =2 p.u.;

Figure 5-9 Demagnetization ratio distribution under different q-axis current.

The q-axis reactive field is paid little attention to as it is decoupled with exciting field in theory and usually considered irrelevant in ideal circumstances. Instead of opposing the PM magnetization directly, the q-axis current can give rise to saturation in the lamination, aggravate the level of nonlinearity, and influence the overall flux distribution of the machine. Therefore, q-axis current will affect the PM working point and might cause local demagnetization indirectly.

As shown in Figure 5-9, demagnetization begins to appear at the upper corner of the main PM under 0.5 p.u. i_q and the secondary PMs under 1 p.u., and the area expands with the current magnitude. But the overall demagnetization stays insignificant. As i_q increases to 2 p.u., considerable area is demagnetized with mild demagnetization ratio at the inner part of the main PMs. However, the overall situation is not serious with the overall demagnetization index of 2.6%, as depicted in Figure 5-9(c). It should be noted that the demagnetization distribution is not symmetrical to the midline of the main PM, and one side of the PMs are more prone to be demagnetized. That's because of the cross-coupled effect of the d- and q-axis field by the PM and q-axis current. As demonstrated in Figure 5-10(a) in one pole pitch, both the PM excited flux and q-axis reactive flux are going inside in the radially at the right side of the rotor where the flux density is enhanced, while they are going in opposite directions at the other side resulting weaker flux density. Therefore, one side of the rotor is always more saturated than the other, as shown in Figure 5-10 (b) and (c). When the rotor lamination is heavily saturated, the permeance decreases significantly, and cannot be ignored. As there is no i_d involved, the d-axis equivalent circuit equation and working point of the main PM can be written as follows:

$$H_{m1} \cdot W_1 + 2H_{g2} \cdot g_c + H_{lam} \cdot L_{lam} = 0 \quad \textbf{(5-10)}$$

$$B_{m1} = B_r + \mu_0 \mu_m H_{m1} = B_r - \mu_0 \mu_m (2H_{g2} \cdot g_c) - \mu_0 \mu_m H_{lam} \cdot L_{lam} \quad \textbf{(5-11)}$$

where H_{lam} is the flux intensity in the lamination cores and L_{lam} is the length of lamination core in the flux loop. As the saturation in the lamination cores becomes more severe, higher magnetic potential drop ($H_{lam} \cdot L_{lam}$) appears on the lamination core. Accordingly, the working point of the magnets decreases due

to saturation. Apparently, the inner part of the main PM has much longer route through the heavily saturated area than the outer part to close the flux loop, which results in higher reluctance in the lamination and lower PM working point for the inner part, as shown in Figure 5-11. That is the reason why the inner part of the main PMs suffers relatively higher risk of demagnetization under large q-axis current. On the other hand, the flux loops for the secondary PM in the right side shows the outer part has a longer route in the saturated area than the inner part, and thus suffers higher risk of demagnetization.

The result shown in Figure 5-9 only considers the situation that the machine rotates in one direction. If the machine should rotate in both directions, both sides will be demagnetized equally. Thus, the demagnetization index rises to 4.2% at i_q of 2 p.u. after rotating in both directions, as shown in Figure 5-12 (a).

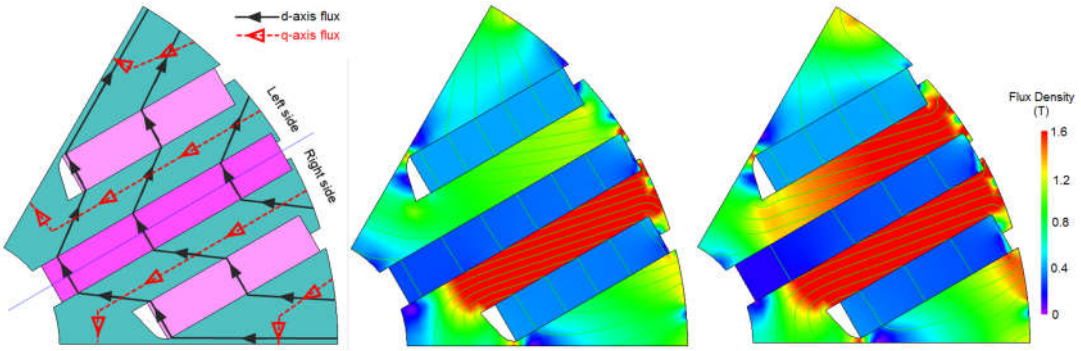

(a) flux path demonstration; (b) i_q =1 p.u.; (c) i_q =2 p.u.;

Figure 5-10 Flux lines and distribution under different q-axis current.

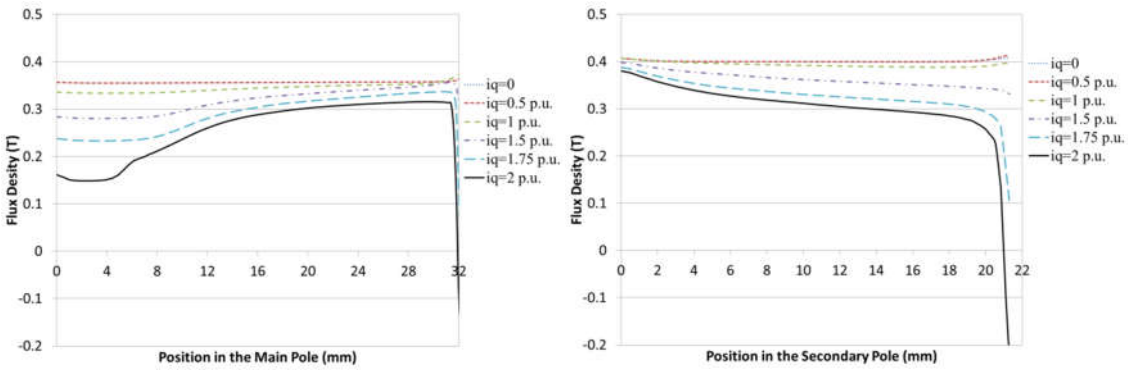

(a) Main PMs; (b) Secondary PMs;

Figure 5-11 Working points of the PMs from inner to outer part under different q-axis current.

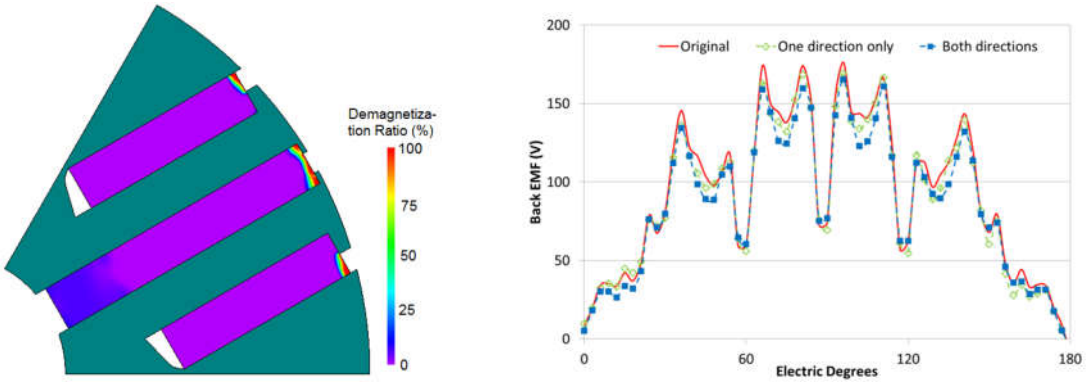

(a) Demagnetization distribution; (b) Back EMF comparison;

Figure 5-12 Demagnetization and back EMF under q-axis current of 2 p.u.

Comparing to the original back EMF, decrease of 3.4% is observed at 2 p.u. of i_q if the machine is rotating in one direction only, and 6.2% by both directions. In all, the demagnetizing effect of q-axis reactive field is not as significant as d-axis MMF. However, it can aggravate the saturation level, decrease the PM working point, and make the PMs more vulnerable to withstand demagnetizing reactive field. Furthermore, serious degradation of magnets is possible under extremely high q-axis current.

5.4.1.1.3 Cross influence of d- and q-axis currents

During practical operations for IPM machines, the PMs are facing the armature reactive field with both d- and q-axis components. The d- and q-axis currents have different impacts on the demagnetization characteristics of the machines, and their interactions make the situation even more complicated. The PM working points under different advanced current angles at 2 p.u. is shown in Figure 5-13. The risk of demagnetization for the outer part of the main PMs rises gradually with the increase of current angle as the outer part is more sensitive to d-axis MMF. Under both the demagnetizing effect of d-axis current and saturation effect of q-axis current, the inner part of the main PMs becomes much more vulnerable than that with only one current component. The worst situation is achieved with 55 degree current angle. The cross coupled effect worsens the situation for the secondary poles as well. Since the outer edge has lower PM working point due to the saturation effect, the outer part of the secondary PMs suffers higher risk of demagnetization.

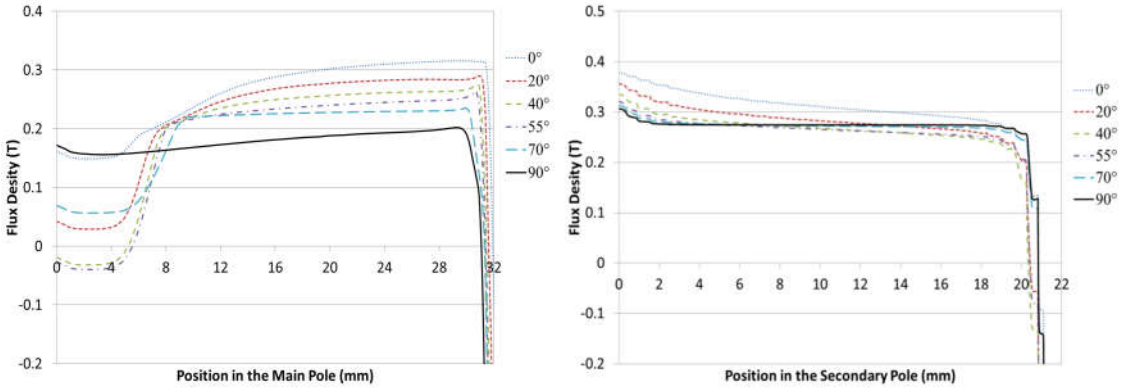

(a) Main PMs; (b) Secondary PMs;

Figure 5-13 Working points of the PMs under different current angle at 2 p.u. armature current.

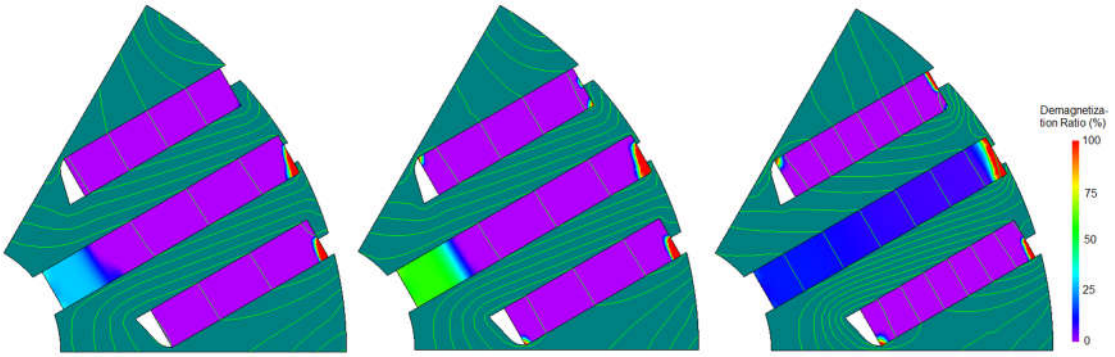

(a) 10 degrees; (b) 55 degrees; (c) 80 degrees;

Figure 5-14 Demagnetization ratio distribution under current angle at 2 p.u. armature current.

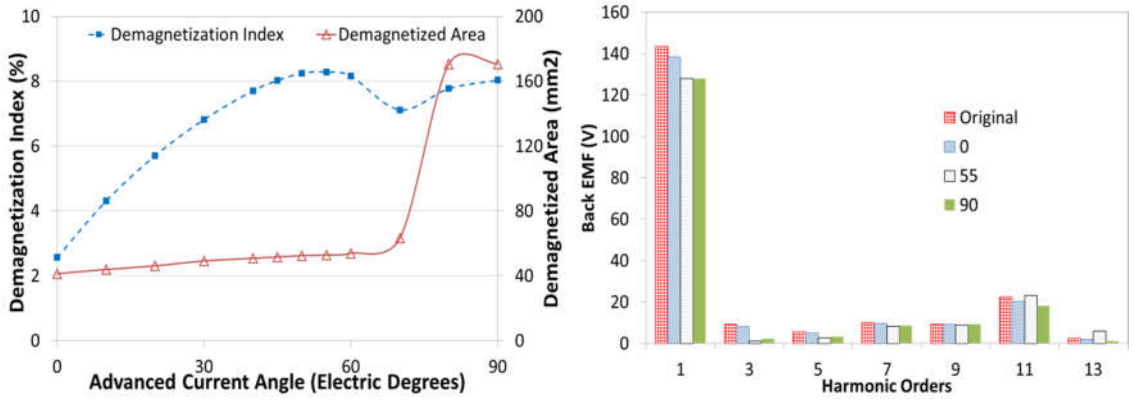

(a) Demagnetization index; (b) Back EMF comparison;

Figure 5-15 Demagnetization after cross coupled effect of d- and q-axis currents.

The demagnetization ratio is demonstrated in Figure 5-14, and the result indicates that the overall demagnetized area increases with current angle. Large scale demagnetization starts from the inner part of the main PMs at zero current angle and spreads out as the increase of current angle, because the d-axis current is the major cause. When critical i_d is reached, sudden increase in demagnetized area occurs and demagnetization spreads to the whole main PM. However, the demagnetization ratio is very low for most of the demagnetized area under pure i_d conditions. Thus, demagnetization index actually peaks at the current angle of 55 electric degrees and then decrease due to the reduced demagnetization ratio in the inner part of the main PMs. The demagnetization index rises again as d-axis current is approaching critical value. As shown in Figure 5-15, the decrease in back EMF after operating at 2 p.u. current of 55 degree is 10.7%, almost the same to that under pure d-axis current.

5.4.1.2 Influence of Ferrite Materials on Demagnetization

The flux intensity of the knee point in the BH curve indicates the ability of withstanding an external magnetic field without becoming demagnetized. As shown in Figure 5-2, the flux density drops dramatically below knee point, which indicates degradation of the magnet. The intrinsic coercivity is approximately equal to the flux intensity at knee point and thus characterizes the anti-demagnetization property of magnet materials. Some of the commonly used commercial ferrite materials are listed in Table 5-1. Although the four grades of ferrite PMs have very similar remanence, their coercivities are quite different from one another. Therefore, the demagnetization characteristics vary in terms of the ability to resist armature reactive field. Without the loss of generality, all the structure, size and amount of ferrite PMs are kept the same.

Table 5-1 Property of ferrite materials

	B_r		H_c		$(BH)_{max}$	
	mT	kG	kA/m	kOe	kJ/m^3	MGOe
Y25	360-400	3.6-4.0	135-170	1.70-2.14	22.5-28.0	2.8-3.0
Y30	370-400	3.7-4.0	175-210	2.20-2.64	26.0-30.0	3.3-3.8
Y36	430-450	4.3-4.5	247-271	3.10-3.41	35.1-38.3	4.4-4.8
Y40	440-460	4.4-4.6	330-350	4.15-4.45	37.5-41.8	4.7-5.3

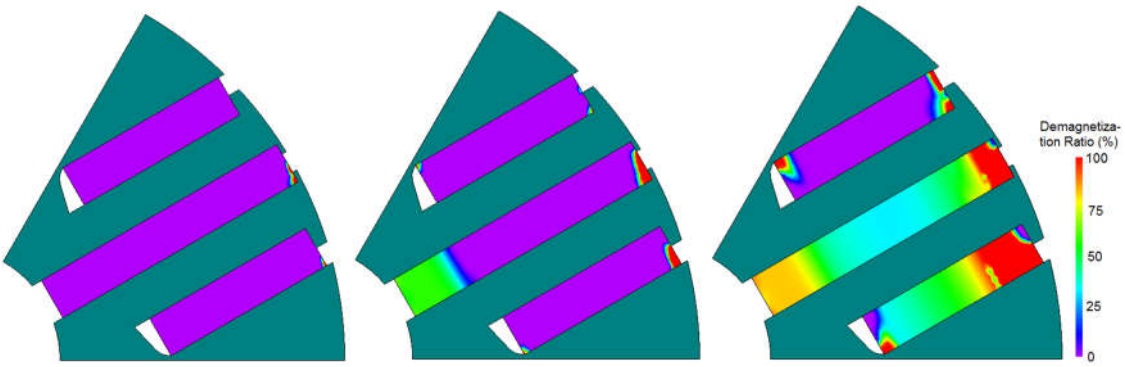

(a) 1 p.u.; (b) 2 p.u.; (c) 4 p.u.;

Figure 5-16 PM demagnetization distribution under rated and overloading armature currents with Y25 ferrite.

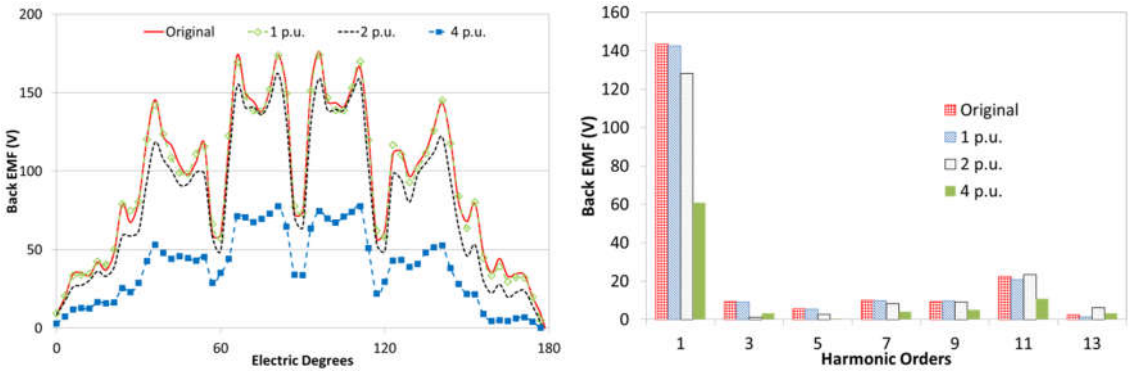

(a) Back EMF; (b) Spectra;

Figure 5-17 Back EMF and spectra after demagnetization of different armature current with Y25 ferrite.

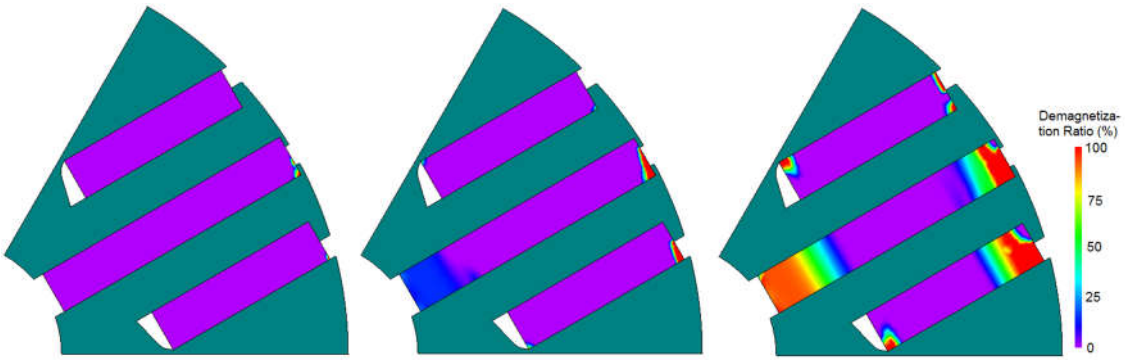

(a) 1 p.u.; (b) 2 p.u.; (c) 4 p.u.;

Figure 5-18 PM demagnetization distribution under rated and overloading armature currents with Y30 ferrite.

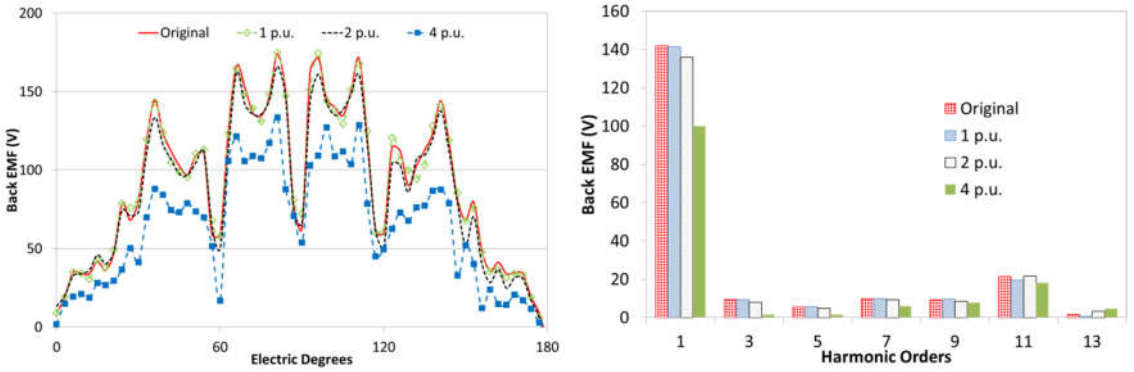

(a) Back EMF; (b) Spectra;

Figure 5-19 Back EMF and spectra after demagnetization of different armature current with Y30 ferrite.

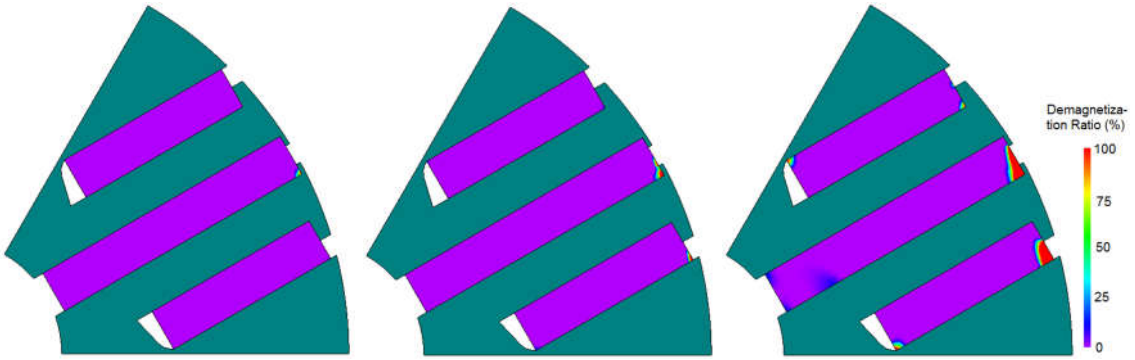

(a) 1 p.u.; (b) 2 p.u.; (c) 4 p.u.;

Figure 5-20 PM demagnetization distribution under rated and overloading armature currents with Y36 ferrite.

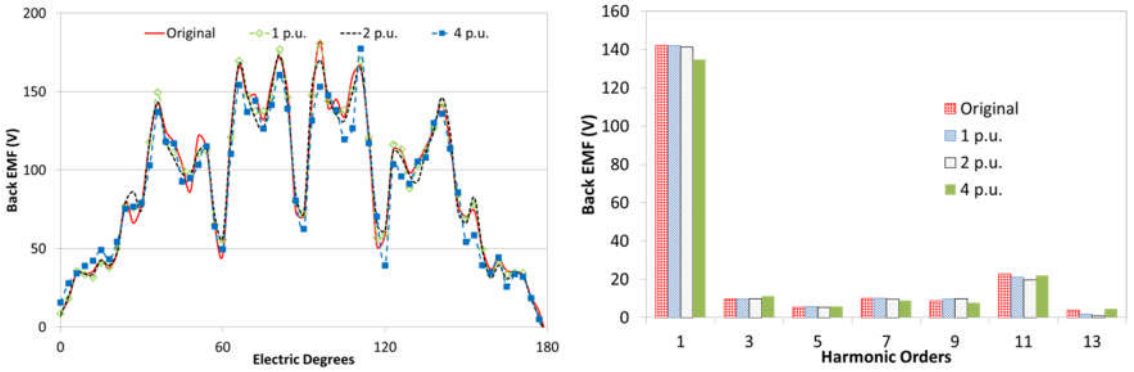

(a) Back EMF; (b) Spectra;

Figure 5-21 Back EMF and spectra after demagnetization of different armature current with Y36 ferrite.

As the one with the lowest coercivity listed in Table 5-1, although Y25 ferrite is able to work under rated current, it suffers much higher risk of demagnetization with overloading current. If operated under double rated current loading, severe demagnetization occurs at the upper edge of the main PMs in small scale, and meanwhile considerable level of demagnetization emerges at the inner part in large scale, as illustrated in Figure 5-16. Over 10% of loss in back EMF is observed after running at double current loading. After possible fault condition of 4 p.u. current, most part of the PMs is severely degraded with the demagnetization index soaring to 50.4%, and nearly 60% of the fundamental back EMF is lost permanently.

Great improvement can be achieved when the material is changed to Y30, as depicted in Figure 5-18 and Figure 5-19. Only a very small part at the upper corner appears to be demagnetized under rated current, and the decrease in the back EMF is only 0.25%, which means the PMs are perfectly safe under rated loading. However, the demagnetization cannot be ignored under double current loading condition. Demagnetized area expands on the upper edge of the main and secondary PMs, and starts to emerge in the inner edge with 4.2% loss in back EMF. The situation could be deteriorated after multiple cycles of overloading. When it comes to 4 times the rated current during fault conditions, there is large area with severe demagnetization on both the main and secondary PMs. As a result, 29.6% decrease is observed in the back EMF with demagnetization index of 24.9%.

Because the coercivity of Y36 ferrite is higher Y30, the risk of demagnetization is further reduced. There is only minor demagnetization in the upper corners of PMs and no visible degradation of back EMF even under the double rated current loading, as shown in Figure 5-20 and Figure 5-21. Despite that demagnetized area expands slightly on the upper edges of the PMs and mild demagnetization occurs in the inner part under 4 p.u. current, the area is quite small and the decrease in back EMF is only 5.2%. Since the reluctance torque is major contribution under heavy load condition, the decrease in the overall torque would be negligible.

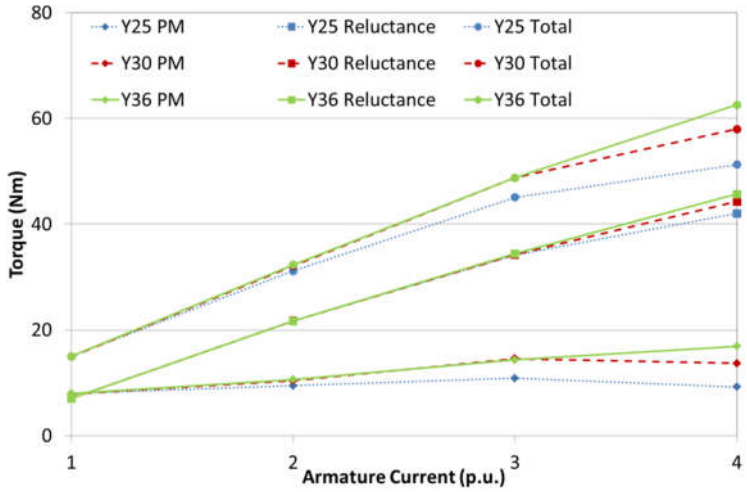

Figure 5-22 Segregation of torque components with different ferrite material under different current.

Surely with higher grades of ferrite PMs such as Y40, the demagnetization performance can be further improved, but the cost of materials should also be taken into consideration. Since the anti-demagnetization ability of Y36 is quite good for the design, the improvement of using Y40 would be very limited.

The loss in back EMF indicates the degradation of PM excited field due to the irreversible demagnetization. And the degeneration of the overall performance is revealed by the decrease in overall torque output. To evaluate the influence of irreversible demagnetization over torque generation, frozen permeability method is applied to segregate the PM and reluctance torque components. The maximum torques of the models with different ferrite materials are compared in Figure 5-22. At rated current, the average value of the overall torque output as well as the PM and reluctance components of all three models are almost the same, despite of different magnets used. That's because the three grades of ferrite have similar remanence and no noticeable demagnetization occurs. But as the increase of armature current, degradation first appears in PM torque of the model with Y25 ferrite at 2 p.u. current loading. Compared with the others, significant decrease of PM torque for the Y25 model can be observed under 3 p.u. current. It is noteworthy that the reluctance torques of the three models are the same despite demagnetization occurs in the PMs to various degrees with less than 3 p.u. armature current. In other words, only the PM torque

component is influenced by demagnetization so long as the PM poles are not severely deteriorated by reactive field. When the current is increased to 4 p.u., the PM torques of both the Y25 and Y30 models decrease, which means severe demagnetization has taken place in the PMs. Under such circumstances, the permeability of the PM poles changes since and the property of the magnets changes significantly or even is reversed. As a result, the saliency of the rotor is changed and degradation of reluctance torque is observed.

5.4.1.3 Influence of Working Temperature

As the absolute value of intrinsic coercivity for ferrite magnets decreases with the drop of temperature, the risk of demagnetization increases in cold operating environment. Since heat will be generated due to the copper and iron losses during continuous operation, the motor will be heated up very quickly. Thus, the most critical scenario is the starting process at cold environmental temperature.

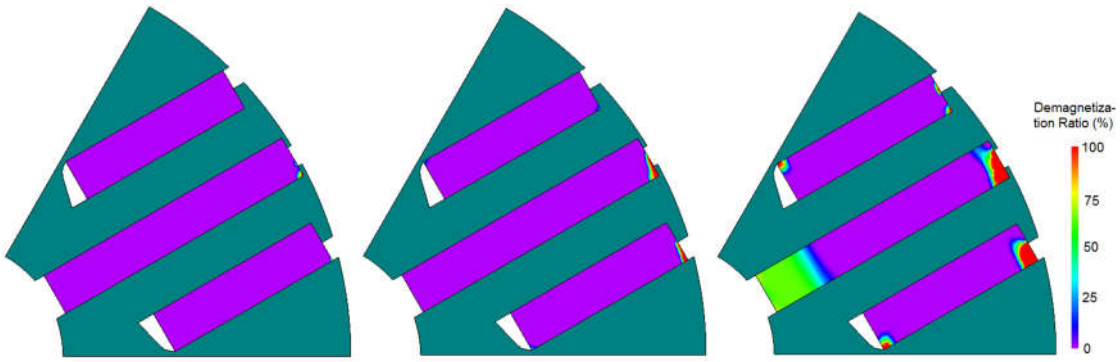

(a) 1 p.u.; (b) 2 p.u.; (c) 4 p.u.;

Figure 5-23 Demagnetization distribution for Y36 under -20 °C.

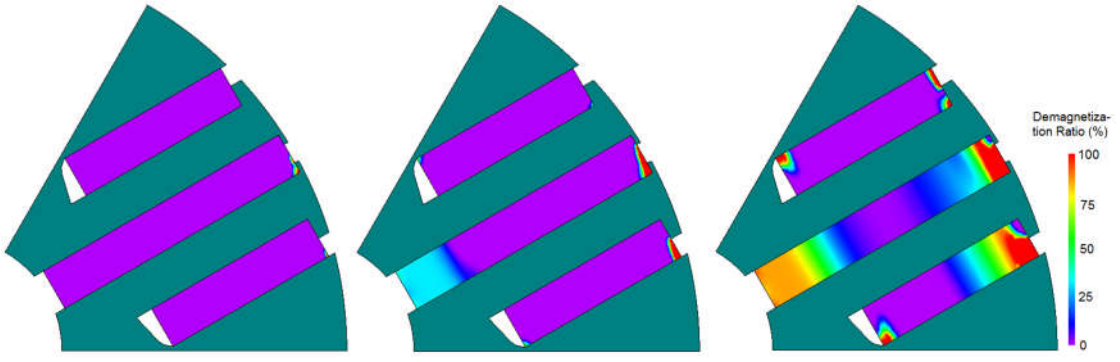

(a) 1 p.u.; (b) 2 p.u.; (c) 4 p.u.;

Figure 5-24 Demagnetization distribution for Y36 under -60 °C.

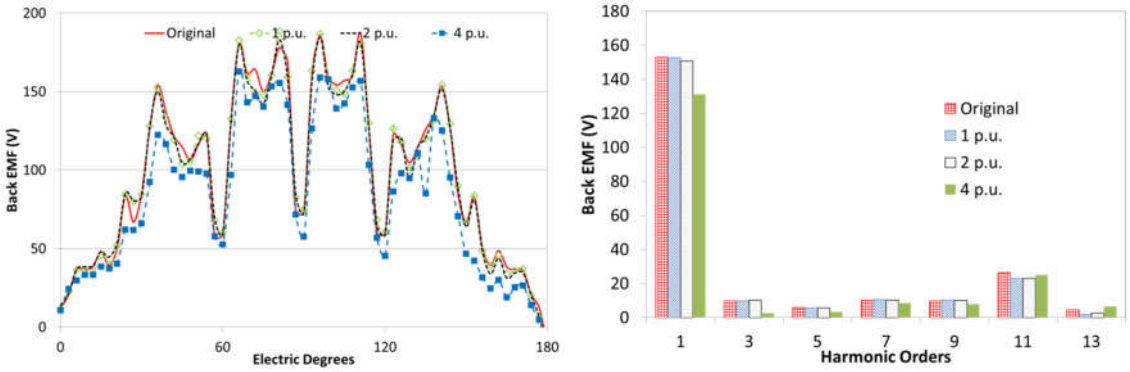

(a) Back EMF; (b) Spectra;

Figure 5-25 Back EMF and spectra after demagnetization of different armature current at -20 °C for Y36 ferrite.

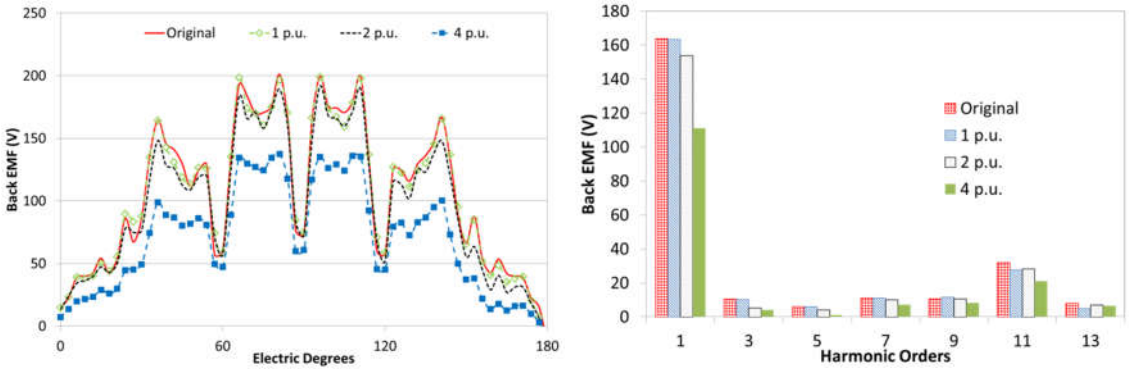

(a) Back EMF; (b) Spectra;

Figure 5-26 Back EMF and spectra after demagnetization of different armature current at -60 °C for Y36 ferrite.

Figure 5-23 and Figure 5-24 demonstrate the demagnetization ratio distributions and back EMF of the model with Y36 ferrite magnet under cold environmental temperature of -20 and -60°C respectively. Under rated loading, the demagnetized area is slightly larger comparing to room temperature, but the demagnetization index is negligible even at -60°C. Thus, no noticeble degradation in the back EMF is shown under rated current, as demonstrated in Figure 5-25 and Figure 5-26. Under 2 p.u. current, the machine can still work perfectly safe at -20 °C, while the moderate demagnetization emerges in the inner part of the main PMs at -60 °C, with 4.8% degraded back EMF. When the loading current is increased to 4 p.u., demagnetization becomes much worse at

low temperature. Demagnetized area spreads at both the upper and inner part of the PMs at -20°C, and 11.2% decrease in back EMF is observed. And when it comes to -60°C, large part of the main and secondary PMs are severely demagnetized, and the back EMF is decreased by 28.5% comparing with only 3.7% at room temperature. Hence, severely deterioration to the performance of the machine is caused by extremely low working temperature.

Due to the inherent feature of ferrite PMs, there is no cost-effective way to prevent the occurrence of demagnetization under extreme low temperature and overloading conditions. Since the machine will be quickly warmed up by the heat generated by the machine losses, the operational temperature will return to that of normal or high conditions after a short period of running. Thus, it is unworthy to replace the PMs with higher grade magnet or re-design the rotor with thicker PMs in practical. The simplest and most effective way is to restrain the armature current below safe value during starting at low temperature by the controling algerithm of the controller.

5.4.2 Demagnetization of One-Layer Configurations

5.4.2.1 Armature Current

5.4.2.1.1 D-axis Current

The demagnetization distributions for the one-layer configuration under different d-axis current are demonstrated in Figure 5-27, and the quantitative results of PM flux density and open-circuit back EMF waveforms after demagnetizing currents are depicted in Figure 5-28. Similarly, the outer edge of the PM pole suffers much higher risk of demagnetization because of stronger reactive armature field. With 1 p.u. demagnetizing current, the working points of the whole PM pole are almost the same, and only negligible area on the upper corner of the PM poles are demagnetized. When the current is increased to 2 p.u., the demagnetization occurs on the upper edge as the working points in the outer part decreases dramatically. Since this is mainly caused by stator tooth leakage flux field, only the rotor surface area is affected and the scale is relatively small, and the demagnetization index is only 3.1% with back EMF loss of 3.5%. While the critical d-axis current is reached, the flux field excited by the

inner part of the PMs are pushed to the inner rotor non-magnetic shaft area by the strong armature field, and the working point of the inner part is slightly lower. Thus, large scale demagnetization spreads all over the PM poles from the inner part. Comparing to the situation under 2 p.u. negative d-axis current, the demagnetization index soars to 14.7% with just 0.3 p.u. current increment, and the loss in back EMF increases to 15.3%.

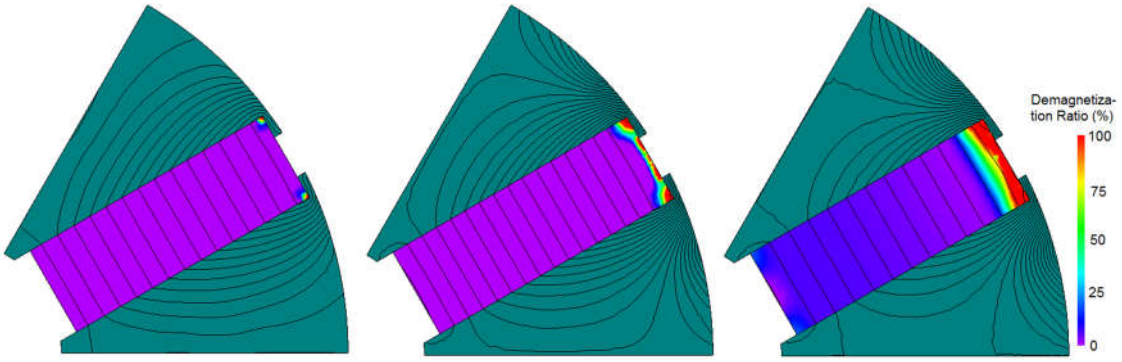

(a) 1 p.u.; (b) 2 p.u.; (c) 2.3 p.u.;

Figure 5-27 Demagnetization distribution and flux lines for Y25 under different d-axis current.

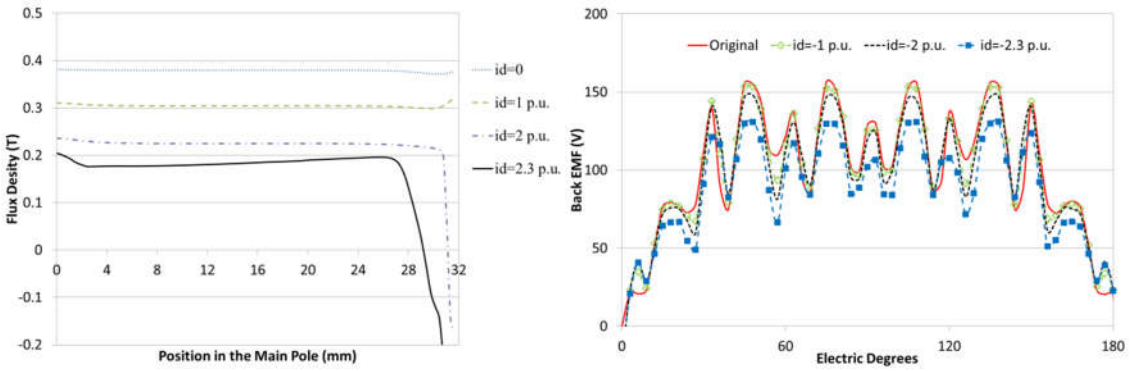

(a) PM working point flux density; (b) Back EMF

Figure 5-28 Comparisons of working points of the PM in the radial direction and back EMF after d-axis current demagnetization.

5.4.2.1.2 Q-axis Current

Figure 5-29 depicts the demagnetization distribution under different q-axis current. Result shows that demagnetization occurs only in the upper corner of the PM poles even under 4 p.u. i_q. Although the demagnetized area in the upper

corner increase with i_q, there is no large scale demagnetization appears in the other part of the PMs. As shown in Figure 5-30(a), the flux density of the whole PM piece is almost the same under certain i_q except the outer part, and the working points of the PMs decrease with the increase of i_q. Therefore, it can be predicted that large scale demagnetization will eventually happen under an extremely high q-axis current due to the severely saturation in the lamination cores and highly distorted q-axis armature field. However, the impact of q-axis current on demagnetization is much weaker than that of d-axis currents. Figure 5-30(b) shows there is no significant degradation in the back EMF, and only 6.1% loss in the fundamental is observed even under 4 p.u. q-axis current.

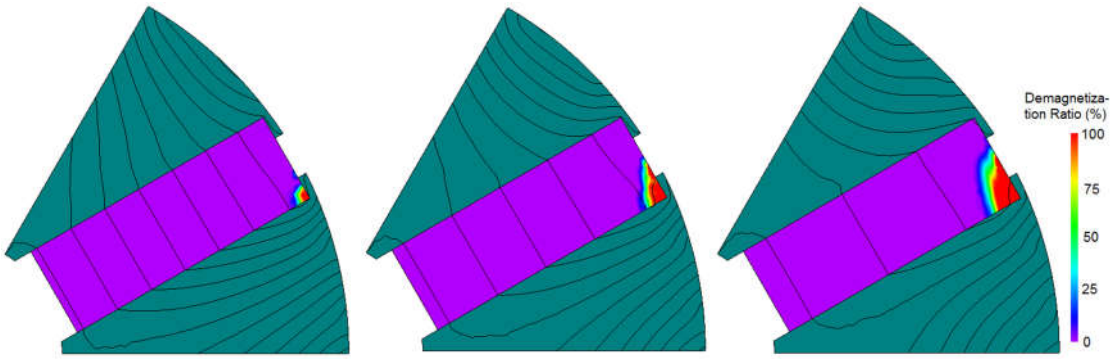

(a) 1 p.u.; (b) 2 p.u.; (c) 4 p.u.;

Figure 5-29 Demagnetization distribution and flux lines for Y25 under different q-axis current.

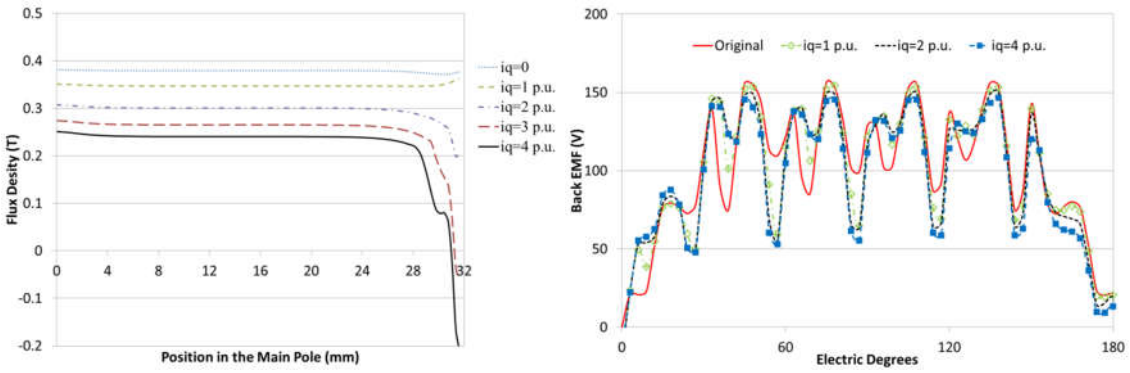

(a) PM working point flux density; (b) Back EMF

Figure 5-30 Comparisons of working points of the PM in the radial direction and back EMF after q-axis current demagnetization.

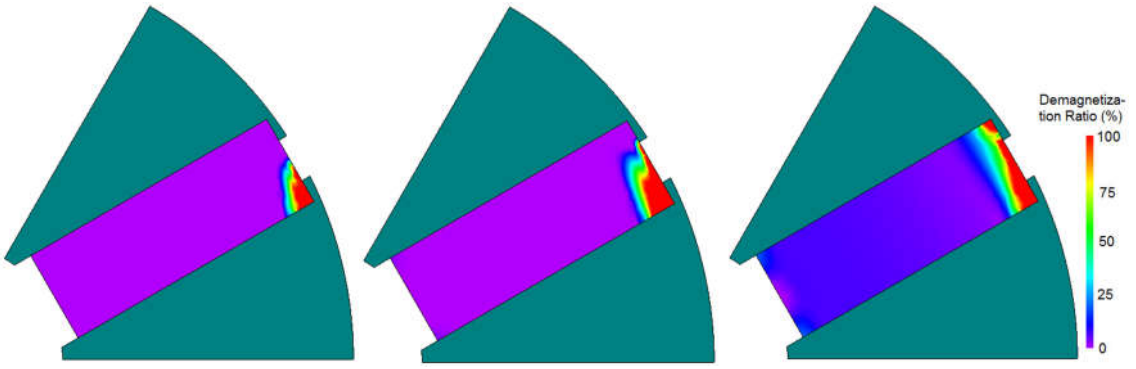

(a) 10 degrees; (b) 40 degrees; (c) 80 degrees;

Figure 5-31 Demagnetization distributions of one-layer model at 2.3 p.u. current with different current angles

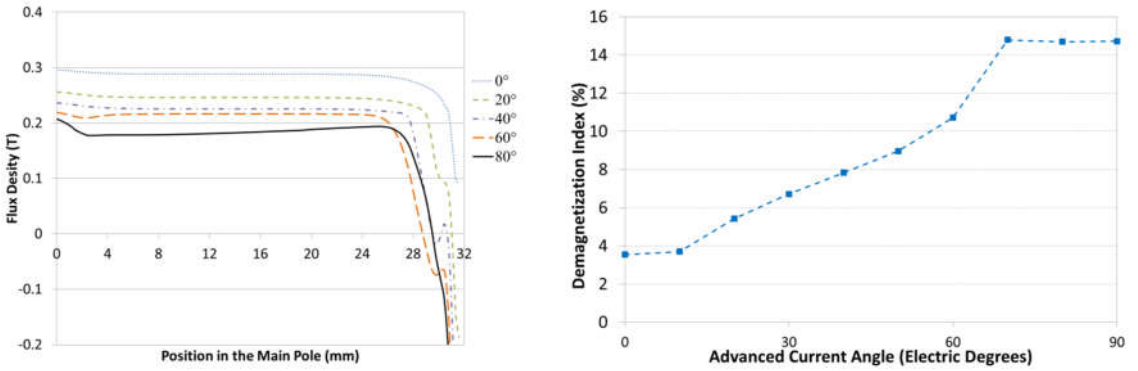

(a) Working points; (b) Demagnetization index

Figure 5-32 Working points and demagnetization index of the PMs under 2.3 p.u. current with different current angles

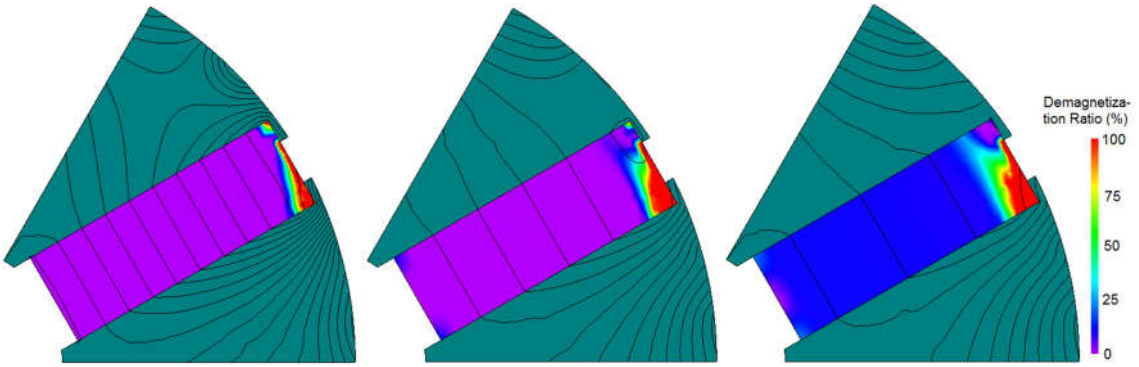

(a) i_d =2 p.u., i_q =0.5 p.u.; (b) i_d =2 p.u., i_q =1 p.u.; (c) i_d =2 p.u., i_q =1.35 p.u.;

Figure 5-33 Demagnetization distribution under different d- and q-axis current combinations.

5.4.2.1.3 Cross influence of d- and q-axis current

The demagnetization distribution under armature current amplitude of 2.3 p.u. with different current angles are illustrated in Figure 5-31. Larger demagnetized area is observed with higher current angle for the one-layer configurations. When the current angle is close to 90 degrees, large scale demagnetization begins to emerge from inner part of the PM. As shown in Figure 5-32, the average working points the PMs decrease with the current angle, and thus the risk of demagnetization increases. The results indicate that d-axis current is the major cause for demagnetization, while q-axis current only has minor influence. Nevertheless, as indicated in Figure 5-30(a), the q-axis armature field does diminish the working point of the PMs and make them more prone to demagnetization. As a result, lower d-axis current is able to cause large scale demagnetization with the existence of q-axis current, though the effect is insignificant. As shown in Figure 5-33, demagnetization aggravates with the increase of q-axis current when the d-axis current is fixed to 2 p.u. With 1.35 p.u. q-axis current, large scale demagnetization spreads out to the entire PM pole at 2 p.u. d-axis current, while the critical d-axis current is 2.3 p.u. for the exactly same model.

5.4.2.2 Ferrite Material

The results of demagnetization index and loss in back EMF for the one-layer configuration with different ferrite magnets are listed in Table 5-2. With higher grades of ferrite materials, the demagnetization can be significantly suppressed, and large scale demagnetization can be prevented even under 4 times rated current by using Y36 ferrite magnet. Demagnetization index can be reduced to a negligible level of 0.86% under 2 p.u. current for Y36, in contrast to 4.66% for Y25. What's more, the Y36 model can endure 4 p.u. over current with only 4.24% degradation of original magnetism, while over 60% of magnetization and back EMF of the Y25 one and over 35% for Y30 are lost. The loss in back EMF indicates the degradation of PM torque. Since the one-layer configuration has a higher portion of PM torque, the overall torque suffers higher decrease caused by irreversible demagnetization.

Table 5-2 Influence of ferrite materials on demagnetization and back EMF

Ferrite Material	Current	Demagnetization Index	Loss in Fundamental back EMF	Overall Torque (Nm)
Y25	1 p.u.	0.79%	0.93%	14.44
	2 p.u.	4.66%	4.72%	29.46
	4 p.u.	60.02%	64.95%	37.35
Y30	1 p.u.	0.55%	0.77%	14.44
	2 p.u.	2.79%	2.86%	29.57
	4 p.u.	35.31%	35.99%	46.27
Y36	1 p.u.	0.29%	0.54%	14.44
	2 p.u.	0.86%	1.05%	29.67
	4 p.u.	4.24%	4.25%	55.34

Table 5-3 Influence of working temperature on demagnetization and back EMF

Working Temperature	Current	Demagnetization Index	Loss in Fundamental back EMF
20°C	1 p.u.	0.29%	0.54%
	2 p.u.	0.86%	1.05%
	4 p.u.	4.24%	4.25%
-20°C	1 p.u.	0.38%	0.71%
	2 p.u.	1.49%	1.69%
	4 p.u.	9.75%	9.79%
-60°C	1 p.u.	0.57%	0.92%
	2 p.u.	2.84%	3.06%
	4 p.u.	42.33%	43.20%

5.4.2.3 Working Temperature

Low temperature apparently increases the risk of demagnetization owing to the lower knee point in the BH curve. With over current of 2 p.u., demagnetization index increases from 0.86% at 20°C to 1.49% at -20°C, and to 2.84% at -60°C. When the current is increased to 4 p.u., mild demagnetization appears on the inner corner of the PM poles at -20°C, but severe degradation is observed in large scale with the demagnetization index of 42.33% and loss in back EMF of 43.2% at the operational temperature of -60°C. Compared with the two-layer configuraiton, the one-layer structure exhibits worse anti-demagnetization performances especially under extremely low temperature. The detailed result of the models with different ferrite magnets under low operational temperature is listed in Table 5-3.

5.5 Rotor Design for Demagnetization Reduction

The demagnetization performance of ferrite machines can always be improved by using higher grades of ferrite materials with higher coercivity. However, the cost of the material will be increased if mass production is considered. Because the risk of local demagnetization is much higher in the area where saturation becomes substantial, it is possible to make minor modifications to the rotor so as to alleviate the saturation or provide additional path for demagnetizing flux to improve the anti-demagnetization ability.

5.5.1 Normal Deeper PM Insertion

The deeper PM insertion method is demonstrated in Figure 5-34. As concluded from the previous sections, the outer edges of the PM poles suffer higher risk of demagnetization due to much stronger armature stator tooth leakage flux field and severe saturation in the bridges. To avoid confronting armature field directly, the PMs are inserted deeper inside the rotor lamination. In such way, thicker slot openings are formed, which can provide an alternative path for the demagnetizing flux field and effectively relieve the saturation level in the rotor surface area. Therefore, more demagnetizing flux would go through the thick PM slot opening rather than the PMs, and it is possible to reduce the risk of the local demagnetization in the outer part of the PMs. Firstly the deeper insertions for the main and secondary PM poles are investigated separately for an easy understanding of their individual influences on demagnetization.

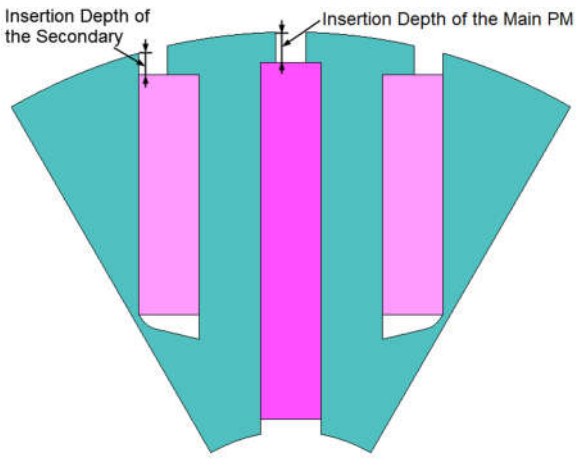

Figure 5-34 Model demonstration for deeper insertion method.

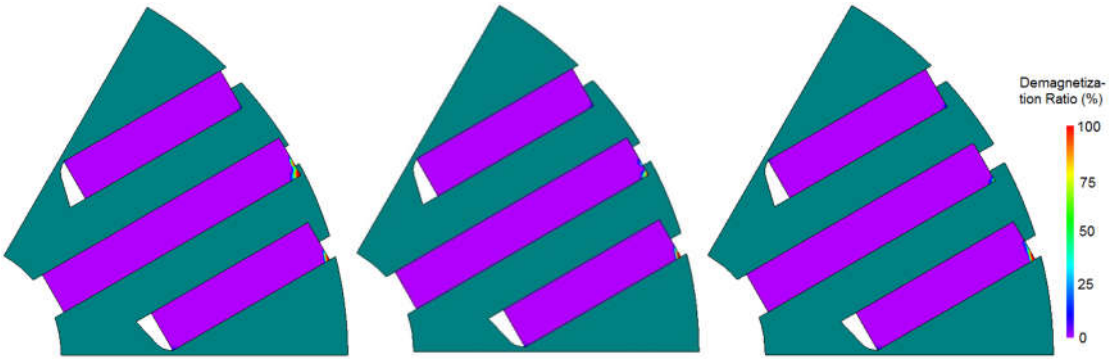

(a) 0.5mm (original); (b) 1mm; (c) 2mm;

Figure 5-35 Demagnetization distribution with different PM insertion depth of the main poles under 2 p.u. current.

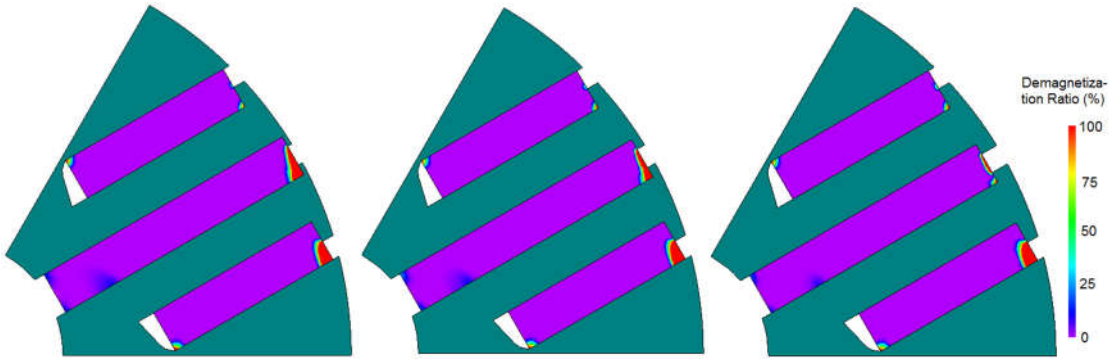

(a) 0.5mm (original); (b) 1mm; (c) 2mm;

Figure 5-36 Demagnetization distribution with different PM insertion depth of the main poles under 4 p.u. current.

Figure 5-35 and Figure 5-36 depict the demagnetization distribution with different main PM insertion depths under 2 p.u. and 4 p.u. armature currents respectively. It is obvious that deeper insertion of the main pole can reduce the demagnetized area effectively on the outer part for the main PMs. With 2mm of insertion, demagnetization on the main PMs can be almost eliminated with the demagnetization index of 0.05% under 2 p.u. current, while the demagnetization index of the main PMs is reduced from originally 4.23% to 1.26% under 4 p.u. current. Moreover, since more demagnetizing flux goes through the thicker bridges, the situation in the inner part of the main PM poles is also improved. As a result, the overall demagnetization index decreases from 0.43% to 0.24% at 2 p.u. current and from 3.73% to 2.76% at 4 p.u. current when the main PM

insertion depth is 2mm. The detailed result for different main pole insertions under various current loadings is listed in Table 5-4.

However, there are minor negative effects as the demagnetization of the secondary poles aggravates with deeper main PM insertions. Since the main PMs avoid facing the strong armature reactive field with deeper insertion, the demagnetizing field strengthens by traveling through thicker slot openings of lower reluctance. Thus, the secondary magnet poles would suffer stronger armature field and have higher risk of demagnetization. But the deterioration is subtle, and it is still beneficial to use deeper insertion for the main PMs. Besides, since radially space of the rotor is limited by the inner rotor diameter, deeper insertion results in shorter PM length. Consequently, the flux focusing effect and thus the PM torque output will be reduced. As a large part of the overall torque comes from rotor saliency for two-layer configurations, reduction is insignificant, as shown in Table 5-5. But the risk of demagnetization can be greatly reduced especially under overloading or fault current conditions.

Table 5-4 Influence of main pole insertion depth on demagnetization

Current	Insertion Depth	Demagnetization Index			
		Main PM	Secondary		Overall
1 p.u.	0.5mm	0.17%	0.01%	0.00%	0.07%
	1mm	0.04%	0.01%	0.00%	0.02%
	1.5mm	0.00%	0.01%	0.00%	0.00%
	2mm	0.00%	0.01%	0.00%	0.00%
2 p.u.	0.5mm	0.70%	0.44%	0.02%	0.43%
	1mm	0.25%	0.49%	0.02%	0.25%
	1.5mm	0.08%	0.57%	0.02%	0.21%
	2mm	0.05%	0.71%	0.03%	0.24%
4 p.u.	0.5mm	4.23%	5.98%	0.71%	3.73%
	1mm	3.00%	6.20%	0.76%	3.27%
	1.5mm	1.73%	6.47%	0.76%	2.82%
	2mm	1.26%	6.96%	0.82%	2.76%

Table 5-5 Influence of main pole insertion depth on torque reduction

Insertion Depth		1mm	1.5mm	2mm
Torque Reduction	1 p.u.	0.01%	1.05%	1.88%
	2 p.u.	0.10%	0.60%	1.12%

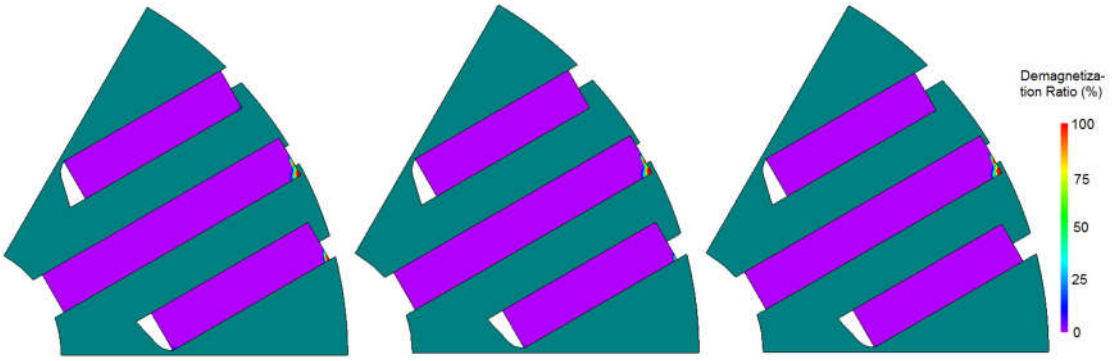

(a) 0.5mm (original); (b) 1mm; (c) 2mm;

Figure 5-37 Demagnetization distribution with different PM insertion depth of the secondary poles under 2 p.u. current.

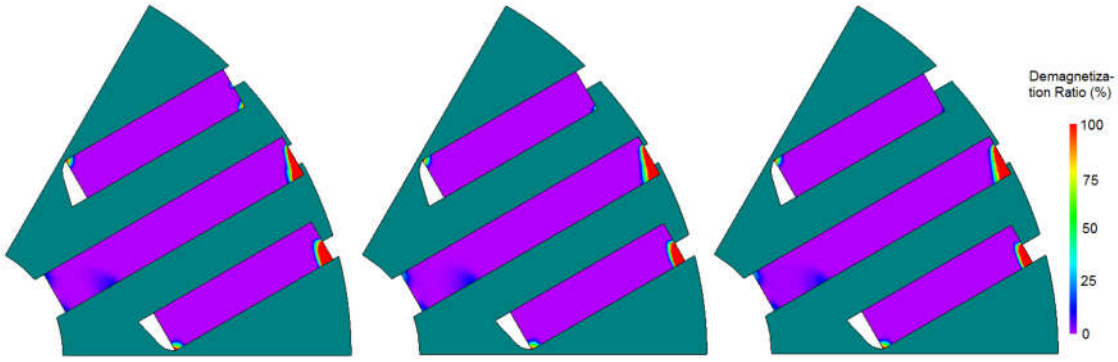

(a) 0.5mm (original); (b) 1mm; (c) 1.5mm;

Figure 5-38 Demagnetization distribution with different PM insertion depth of secondary poles under 4 p.u. current.

The influence of secondary poles insertion depth is demonstrated in Figure 5-37 and Figure 5-38 with the main poles fixed. Demagnetization in the secondary pole can be reduced by inserting the secondary PMs deeper, but the effect is actually quite limited. Only marginal reduction in demagnetization index of the secondary poles is achieved, while demagnetized area in the main PMs is enlarged. And thus the overall demagnetization performance is actually deteriorated by the deeper secondary pole insertion, as shown in Table 5-6. The overall demagnetization index increases from 3.73% to 3.95% with secondary insertion depth of 2mm. On the other hand, since the secondary layer has great influence over the saliency of the rotor, the deeper insertion causes larger decrease in the overall torque, as shown in Table 5-7.

Table 5-6 Influence of secondary pole insertion depth on demagnetization

Current	Insertion Depth	Demagnetization Index			
		Main PM	Secondary		Overall
1 p.u.	1mm	0.18%	0.00%	0.00%	0.08%
	1.5mm	0.19%	0.00%	0.00%	0.09%
	2mm	0.21%	0.00%	0.00%	0.09%
2 p.u.	1mm	0.77%	0.09%	0.02%	0.38%
	1.5mm	0.83%	0.00%	0.02%	0.37%
	2mm	0.89%	0.00%	0.02%	0.40%
4 p.u.	1mm	4.86%	5.57%	0.45%	3.82%
	1.5mm	5.26%	5.28%	0.38%	3.90%
	2mm	5.50%	5.03%	0.34%	3.95%

Table 5-7 Influence of secondary pole insertion depth on torque reduction

Insertion Depth		1mm	1.5mm	2mm
Torque Reduction	1 p.u.	0.64%	1.28%	1.87%
	2 p.u.	0.81%	1.35%	1.82%

Table 5-8 Demagnetization performance with the chosen PM insertion depth

Current	Demagnetization Index			
	Main PM	Secondary		Overall
1 p.u.	0.00%	0.00%	0.00%	0.00%
2 p.u.	0.06%	0.19%	0.00%	0.08%
4 p.u.	1.55%	6.32%	0.49%	2.62%

Since there is interaction between the main and secondary poles, deeper insertion method is applied on both of them to achieve a better result. Because the torque output could be reduced with deeper PM insertion method, the insertion depth should be carefully chosen to maintain relatively high torque density. Considering the nominal operating and required overloading conditions, the insertion depth of 2mm is chosen for the main PM and 1mm for the secondary PMs. The demagnetization performance is shown in Table 5-8 and Figure 5-39. No demagnetization occurs within rated operation range, and the overall demagnetization is only 0.08% at double overloading current. Even under possible 4 p.u. fault current, a very low demagnetization level of 2.62% can be achieved, and the reduction in torque is 2.3%.

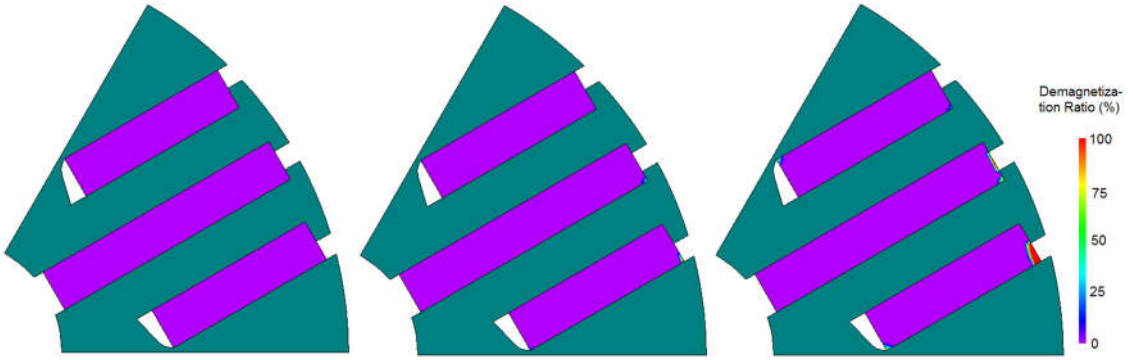

(a) 1 p.u.; (b) 2 p.u.; (c) 4 p.u.

Figure 5-39 Demagnetization distribution with insertion depth of 2mm for the main pole and 1mm for secondary poles.

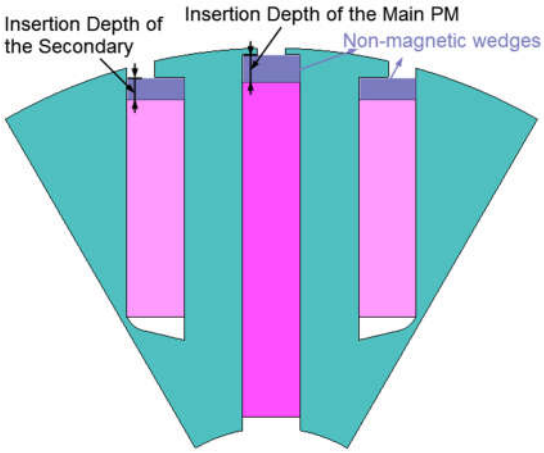

Figure 5-40 Model demonstration for deeper PM insertion with non-magnetic wedges.

5.5.2 Deeper PM Insertion with Non-Magnetic Wedges

Since the laminations are ferromagnetic, the outer part of the PMs are still facing restively strong armature reactive field with normal deeper PM insertion method. Also, thicker lamination bridges reduce the reluctance for the armature flux loop, and thus put the other PMs in the situation of facing stronger reactive field. By using non-magnetic wedges, Deeper PM insertion method is able to keep the PMs further away from strong reactive field without reducing the reluctance of the reactive flux loop. Therefore, it could provide better protection for the PMs. The demonstration model is shown in Figure 5-40, and the influences over the main and secondary PMs are investigated separately first.

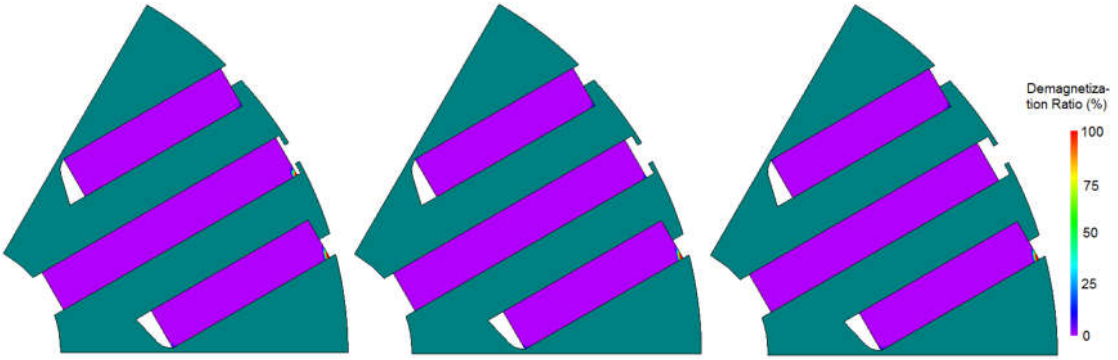

(a) 1mm; (b) 1.5mm; (c) 2mm;

Figure 5-41 Demagnetization distribution with different PM insertion depth of the main poles under 2 p.u. current.

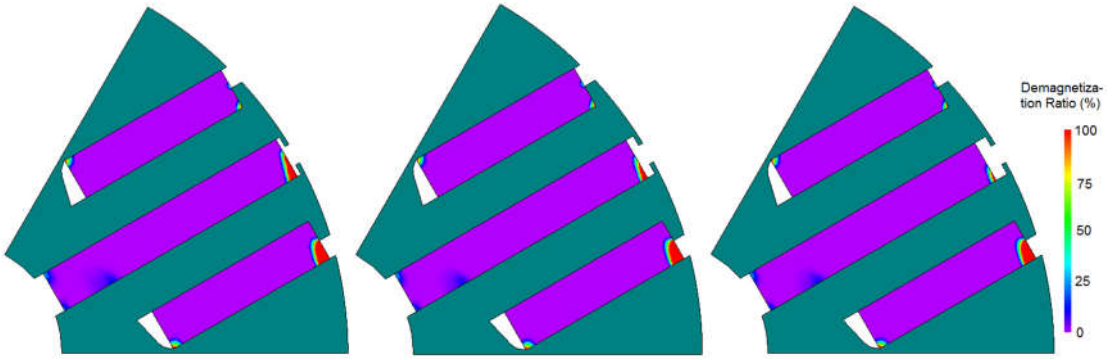

(a) 1mm; (b) 1.5mm; (c) 2mm;

Figure 5-42 Demagnetization distribution with different PM insertion depth of the main poles under 4 p.u. current.

The demagnetization distribution with different main PM insertion depth under 2 and 4 p.u. current is illustrated in Figure 5-41 and Figure 5-42. Results show that the demagnetization in the main PMs is reduced significantly, yet no noticeable negative effect is observed for the secondary PMs. With insertion depth of 2mm, demagnetization is completely eliminated in the main PMs under 2 p.u. current, and is reduced to 0.77% at 4 p.u. current. Since there is no negative influence over the secondary PMs, the overall demagnetization index is reduced to 0.15% at 2 p.u. and 2.30% at 4 p.u. current, comparing to 0.24% at 2 p.u. and 2.76% at 4 p.u. for normal deeper PM insertion method. Only subtle torque reduction is caused owing to the decrease of PM length. The detailed results of demagnetization and torque performances are listed in Table 5-9 and Table 5-10.

Table 5-9 Demagnetization index with main pole insertion depth and current

Current	Insertion Depth	Demagnetization Index			
		Main PM	Secondary		Overall
1 p.u.	original	0.17%	0.01%	0.00%	0.07%
	1mm	0.00%	0.01%	0.00%	0.00%
	1.5mm	0.00%	0.01%	0.00%	0.00%
	2mm	0.00%	0.01%	0.00%	0.00%
2 p.u.	original	0.70%	0.44%	0.02%	0.43%
	1mm	0.19%	0.44%	0.02%	0.21%
	1.5mm	0.01%	0.46%	0.02%	0.14%
	2mm	0.00%	0.48%	0.03%	0.14%
4 p.u.	original	4.23%	5.98%	0.71%	3.73%
	1mm	2.71%	5.98%	0.70%	3.06%
	1.5mm	1.53%	6.00%	0.70%	2.58%
	2mm	0.77%	6.06%	0.72%	2.30%

Table 5-10 Torque reduction with main pole insertion depth and current

Insertion Depth		1mm	1.5mm	2mm
Torque Reduction	1 p.u.	0.36%	0.83%	1.33%
	2 p.u.	0.40%	0.65%	1.03%

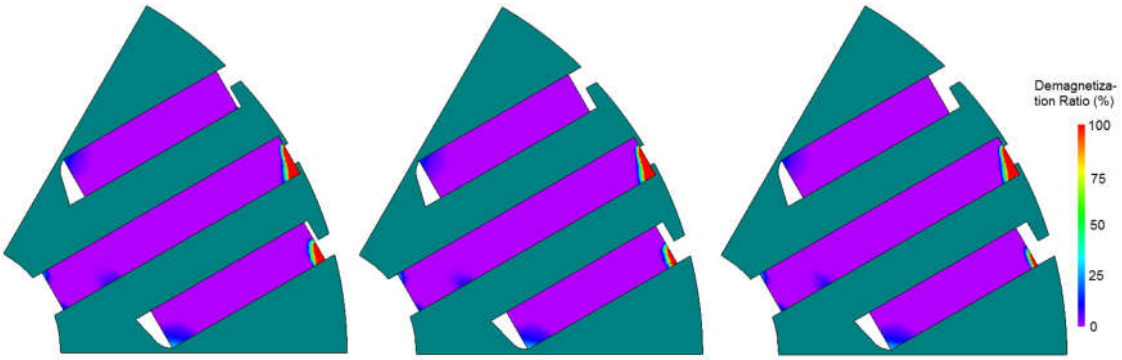

(a) 1mm; (b) 1.5mm; (c) 2mm;

Figure 5-43 Demagnetization distribution with different PM insertion depth of the secondary poles under 4 p.u. current.

Figure 5-43 depicts the demagnetization with different secondary PM insertion depth at 4 p.u. current. The demagnetization index of the secondary PMs is greatly reduced to 2.83% with 1.5mm insertion and 1.81% with 2mm insertion, comparing to the original 5.98%, while the torque reduction is less than 1.5%. The detailed results are shown in Table 5-11 and Table 5-12.

Table 5-11 Influence of secondary pole insertion depth on demagnetization

Current	Insertion Depth	Demagnetization Index			
		Main PM	Secondary		Overall
2 p.u.	original	0.70%	0.44%	0.02%	0.43%
	1mm	0.70%	0.05%	0.00%	0.31%
	1.5mm	0.72%	0.00%	0.00%	0.32%
	2mm	0.76%	0.00%	0.00%	0.34%
4 p.u.	original	4.23%	5.98%	0.71%	3.73%
	1mm	4.27%	4.21%	0.00%	3.13%
	1.5mm	4.39%	2.83%	0.00%	2.80%
	2mm	4.52%	1.81%	0.00%	2.60%

Table 5-12 Influence of secondary pole insertion depth on torque reduction

Insertion Depth		1mm	1.5mm	2mm
Torque Reduction	1 p.u.	0.41%	0.98%	1.49%
	2 p.u.	0.13%	0.57%	0.95%

Since the interaction between the main and secondary poles is negligible with deeper insertion by non-magnetic wedges, the insertion depths for the PMs can be chosen from Table 5-9 and Table 5-11 separately based on the required demagnetization performance. For example, with insertion depth of 2mm for the main PMs and 1mm for the secondary PMs, the demagnetization is 0.76% in the main PMs and 4.21% in the secondary PMs under 4 p.u. current, which makes the overall demagnetization index of 1.61% comparing to 2.62% with normal insertion method. Obviously, deeper PM insertion with non-magnetic wedges is much better in terms of anti-demagnetization capability for the PMs. Besides, because the reluctance of the machine in both d- and q- axis models remains unchanged with non-magnetic wedges, the rotor saliency stays the same as the original and no impact is imposed on the reluctance torque. Thus, the reduction in torque is only caused by shorter PMs, and the overall torque will be higher than that with normal PM insertions. However, the rotor structure becomes more complicated with extra non-magnetic wedges. Furthermore, thinner lamination bridges are applied since non-magnetic wedges have taken some space in the area, which will reduce the mechanical reliability during high speed operation due to the high centrifugal force.

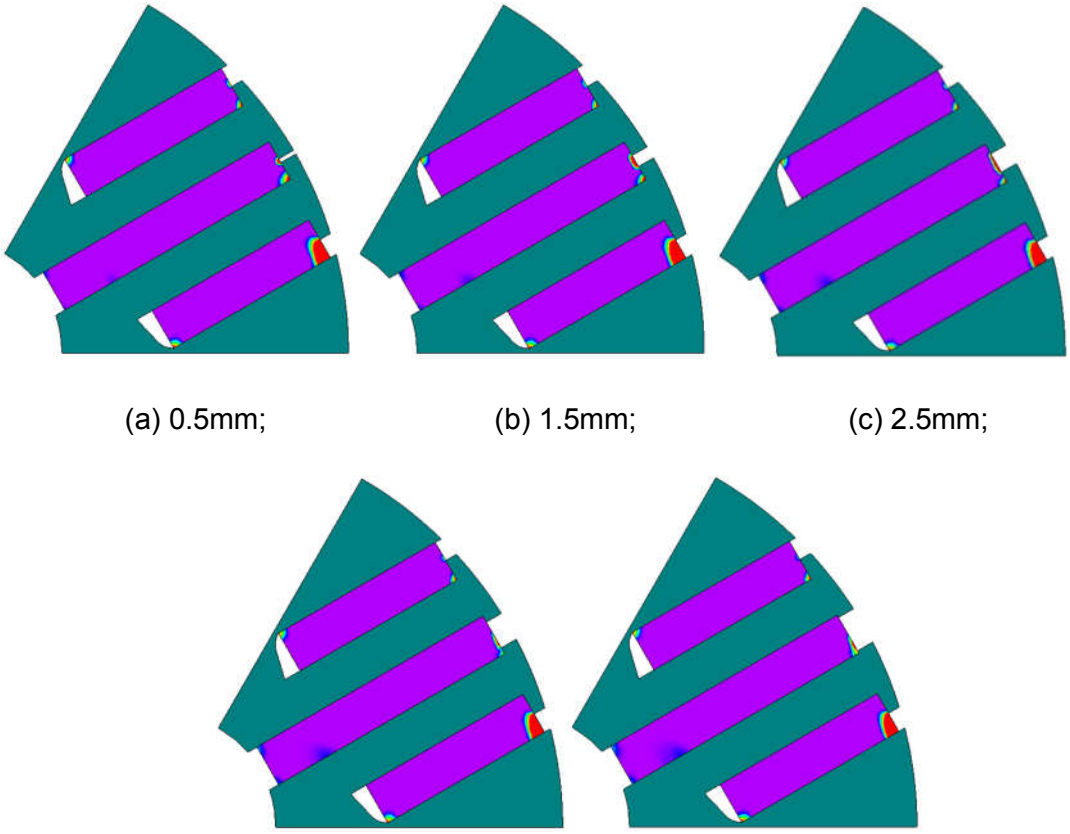

(a) 0.5mm; (b) 1.5mm; (c) 2.5mm;

(d) 3.5mm; (e) 4.5mm;

Figure 5-44 Demagnetization distribution with different PM slot opening of the main poles under 4 p.u. current.

5.5.3 PM Slot Opening

The width of the magnet slot openings can affect the flux path for both the PM excited and armature reactive field, and thus flux distribution and saturation are all influenced especially in the areas near the rotor surface. Therefore, the opening width is considered for the optimization of anti-demagnetization design.

Figure 5-44 demonstrates the demagnetization distribution with different main PM slot openings. Narrow slot openings will reduce the reluctance of the PM and stator tooth leakage flux field, and allow more demagnetization flux to go through the openings instead of opposing the magnetization through the PMs. Thus protection is provided to keep main PMs away from the strong armature field. But this also enhances the reactive field imposing the secondary PMs. Moreover, the flux leakage for both the PM and armature excited field are

greatly increased by narrow slot openings, which not only reduces the utilization ratio of PMs and the PM torque, but also changes the salient ratio of the rotor and thus the torque output. On the other hand, wide slot openings increase the reluctance of the flux loop through the outer part of the PM slots, and thus weaken the reactive flux field. Although the demagnetization in the outer part of the PMs is alleviated, the situation deteriorates in the inner part as part of the demagnetizing flux is forced to go through the magnet poles. Similar influence of the secondary PM slot opening can be observed. As a result of the adverse effects on each other, the overall demagnetization index hardly changes with different PM slot openings despite of noticeable impact on each individual. In all, the models with wider slot openings exhibits slightly better performance concerning demagnetization and torque. But sufficient length for bridges is necessary to hold the large pieces of PM especially at high speed.

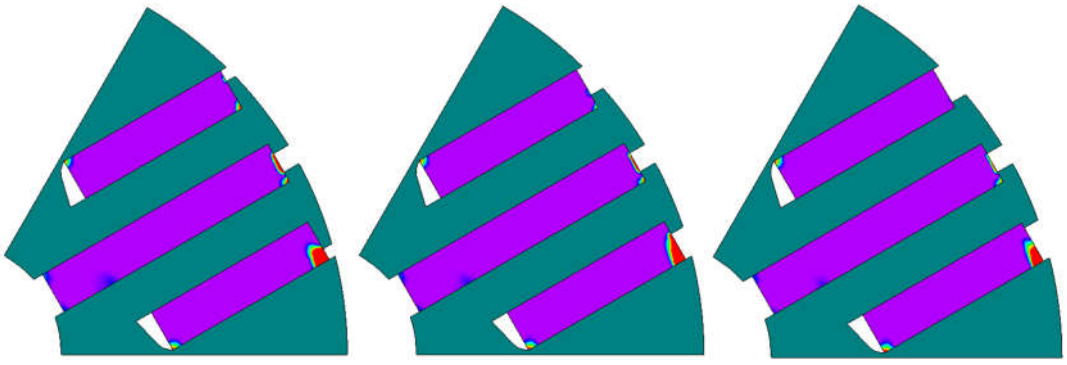

(a) 0.5mm; (b) 1.5mm; (c) 2.5mm;

Figure 5-45 Demagnetization distribution with different PM slot opening of the secondary main poles under 4 p.u. current.

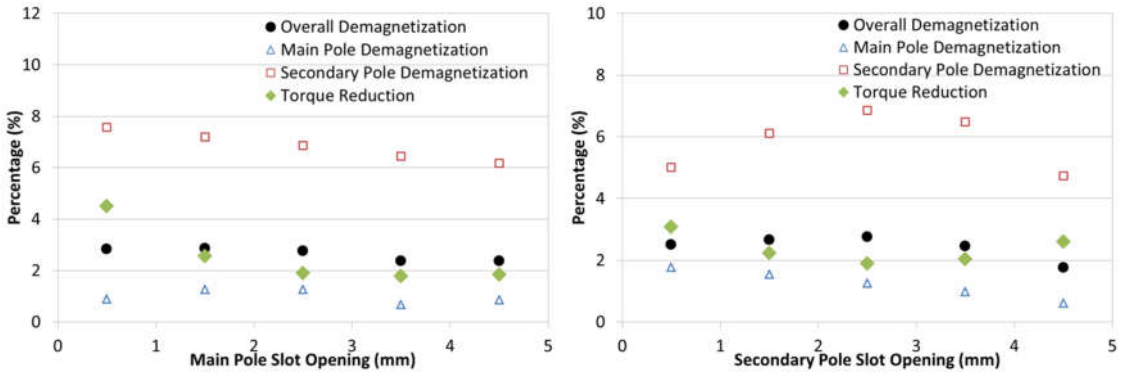

(a) Main PM slot opening; (b) Secondary PM slot opening;

Figure 5-46 Influence of slot opening on torque output and demagnetization.

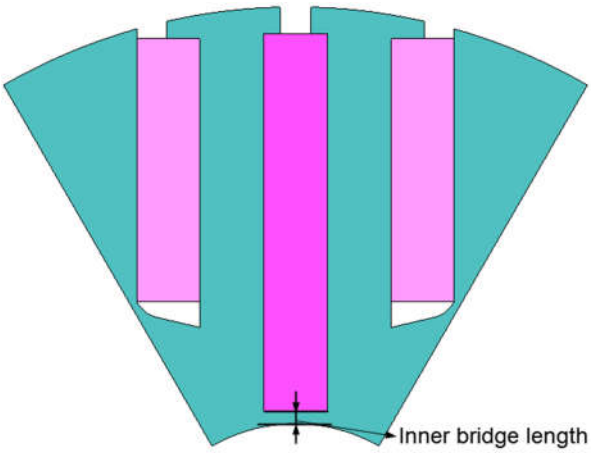

Figure 5-47 Demonstration of proposing inner PM bridges.

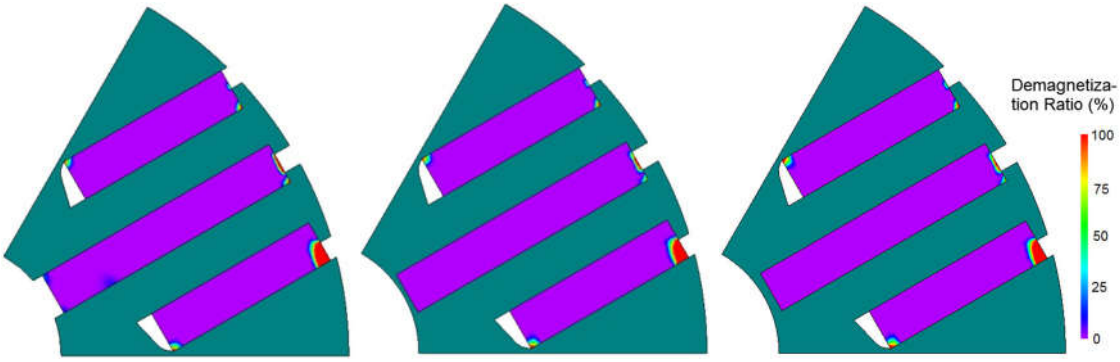

(a) Without inner bridge; (b) 0.5mm inner bridge; (c) 1mm inner bridge;

Figure 5-48 Demagnetization distribution with different inner bridge length under 4 p.u. current at room temperature.

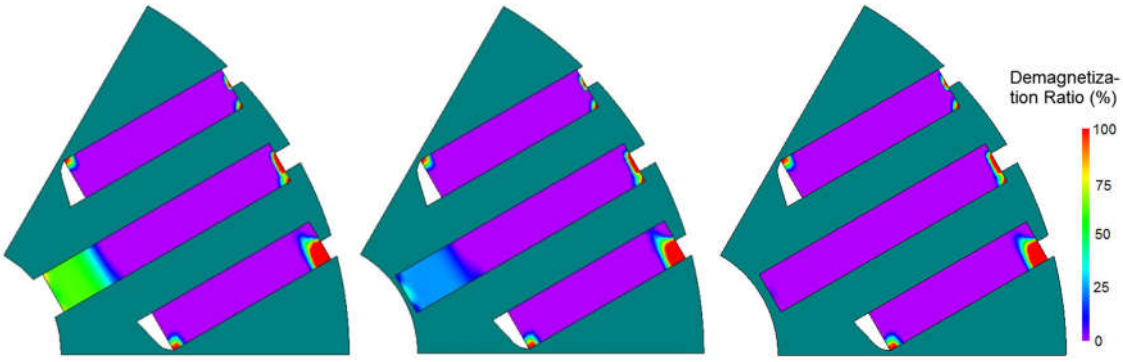

(a) Without inner bridge; (b) 0.5mm inner bridge; (c) 1mm inner bridge;

Figure 5-49 Demagnetization distribution with different inner bridge length under 4 p.u. current at -20°C.

5.5.4 Inner Bridges

The inner part of the PMs has higher risk of large scale demagnetization during overloading or fault current conditions. And some of the methods to reduce local demagnetization in the outer part of the PMs may aggravate the situation in the inner part. To reduce the demagnetizing flux going through the PM poles, inner PM bridges are proposed to provide a path for the opposing reactive field. Meanwhile the inner bridges connect all the rotor parts together, the mechanical robustness of the rotor can be greatly improved, and the cost of assembly can be reduced, as illustrated in Figure 5-47.

Figure 5-48 depicts the demagnetization distribution of models with and without inner bridge under 4 p.u. current and room temperature condition. With 0.5mm of inner bridge, the demagnetization risk is completely eliminated in the inner part of the main PMs. Besides, reduction in demagnetization is also achieved for the out part, with demagnetization index reduced from 1.26% to 0.73%. The effect is more remarkable under low temperature environment. Large scale of demagnetization can be prevented for the inner part of the main PMs, as illustrated in Figure 5-49. The demagnetization index in the main PMs is reduced from 14.6% to 7.85% with 0.5mm of inner bridge, and to only 2.12% with 1mm inner bridge. More importantly, no negative effect on the secondary poles is observed. Apparently, the inner bridge will increase the PM flux leakage and reduce flux density in the airgap and back EMF at open-circuit condition. Noticeable reduction in torque occurs under light load conditions. But the situation is different under medium to heavy loadings. Due to the large portion of reluctance torque, advanced current angle is applied for maximum torque-per-ampere (MTPA) control. Hence, the thin inner bridges will be saturated by the relatively strong armature d-axis field, and the loss of PM flux is actually negligible under such circumstances. As shown in Table 5-13, no degradation in the PM torque despite of considerable loss in open-circuit back EMF by using inner bridges. On the contrary, there is slight improvement for the overall torque when 1mm inner bridges are applied. Because the saturation in the rotor core is alleviated due to the inner bridges, there could be potentially higher reluctance torque as a result of the increased d- and q-axis inductances.

Table 5-13 Influence of inner bridge on torque production and back EMF

Inner Bridge Thickness	Overall Torque (Nm)	PM Torque (Nm)	Reluctance Torque (Nm)	Back EMF Fundamental (V)
None	14.79	7.83	6.96	146.56
0.5mm	14.79	7.85	6.94	136.19
1mm	14.85	7.83	7.02	125.83

5.5.5 Rotor Design for One-Layer Configuration

5.5.5.1 Normal Deeper Insertion

Local demagnetization caused by winding slot leakage flux can be effectively reduced by deeper PM insertion method. As illustrated in Figure 5-50, both the demagnetized area and severity are greatly reduced with 2mm PM insertion, and demagnetization index decreases 5.71% to 2.21% under 4 p.u. current. However, there is a drawback of deeper insertion method, which results in decrease in PM torque owing to reduced PM length. But the increased PM slot bridge thickness can potentially enhance the reluctance torque as the saturation in the rotor surface is alleviated and the average reluctance for both d- and q-axis field is reduced. Hence the influence on the overall torque output is not serious when the insertion depth is relatively small. Comparing to that of 0.5mm insertion depth, only 1.3% torque reduction for the 1.5mm one and 2.2% for the 2mm one are observed. In all, the normal deeper insertion method is quite an effective way to reduce local demagnetization in the outer part of the PMs, yet there is no serious degradation in the torque output, as shown in Table 5-14.

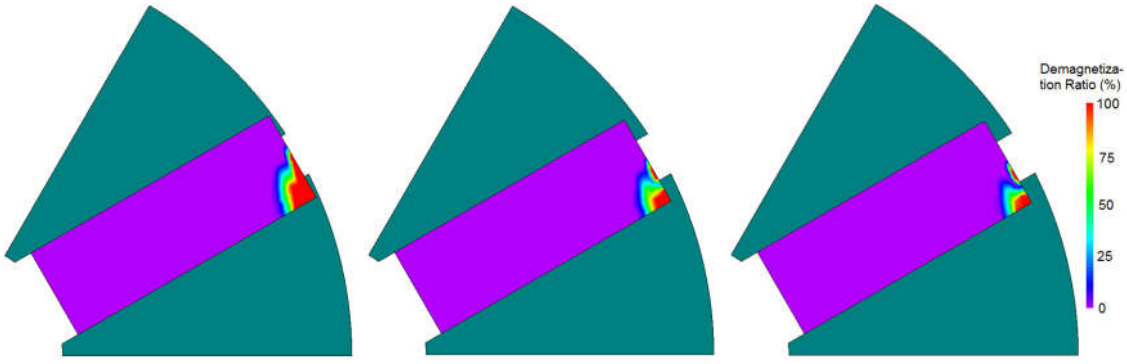

(a) 0.5mm; (b) 1.5mm; (c) 2mm;

Figure 5-50 Demagnetization distribution of different PM insertion depth under 4 p.u. current.

Table 5-14 Influence of PM deeper insertion on demagnetization and torque

Insertion Depth / Current	1 p.u.	2 p.u.	4 p.u.	Decrease in Torque
0.5mm	0.38%	1.48%	5.71%	-
1mm	0.29%	0.85%	4.24%	0.16%
1.5mm	0.21%	0.61%	3.01%	1.33%
2mm	0.11%	0.45%	2.21%	2.19%

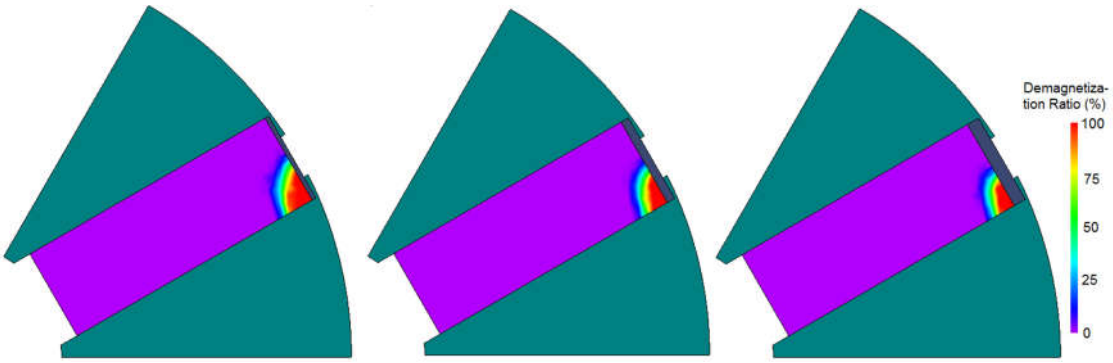

(a) 0.5mm; (b) 1mm; (c) 1.5mm;

Figure 5-51 Demagnetization distribution of PM deeper insertion with different non-magnetic wedges thickness under 4 p.u. current.

Table 5-15 Influence of deeper insertion with non-magnetic wedges on demagnetization and torque

Thickness of Wedges / Current	Demagnetization Index			Decrease in Torque
	1 p.u.	2 p.u.	4 p.u.	
0.5mm	0.29%	0.93%	4.61%	0.69%
1mm	0.01%	0.51%	3.74%	1.91%
1.5mm	0.00%	0.16%	3.14%	2.87%
2mm	0.00%	0.03%	2.53%	3.92%

5.5.5.2 Deeper Insertion with Non-Magnetic Wedges

The non-magnetic wedge is placed in between the PM and slot bridges. The thickness of the PM slot bridges are set to be 0.5mm to hold the PMs and non-magnetic wedges. This alternative PM deeper insertion method is not as effective as the normal insertion method to reduce local demagnetization, as shown in Figure 5-51. Under 4 p.u. current, the demagnetization index drops from originally 5.71% to 2.53% with 2mm wedges. Since the PM slot opening is much wider than the stator tooth, there is no way of forming a zig-zag flux path

for the stator demagnetizing field. Thicker bridges are obtained with normal PM insertion method, which provides a low reluctance path for the demagnetization field. In contrast, most of the opposing flux of the model with non-magnetic wedges will have to travel through the PM slot as there is no other options. Thus, the reduction in demagnetization is not as effective. Moreover, the non-magnetic wedge insertion method have stronger negative impact on torque output because there is no improvement in the rotor saliency. By using 2mm wedges, the torque is decreased by almost 4%. In all, deeper insertion with non-magnetic wedges is not as useful as the normal insertion method for anti-demagnetization design. Additionally, it has larger adverse impacts on the torque ouput. Besides, extra wedges require more work and material cost in manufacturing and assembling the parts.

5.5.5.3 PM Slot Opening

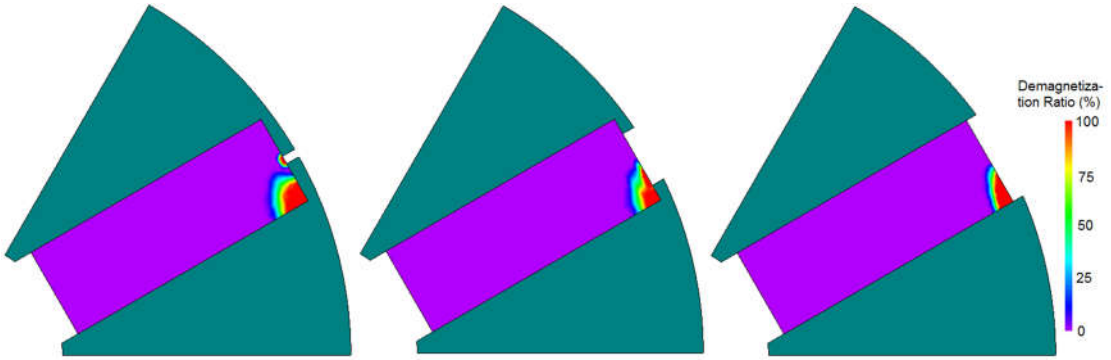

(a) 1mm; (b) 7mm; (c) 11mm;

Figure 5-52 Demagnetization distributions with different PM slot openings under 4 p.u. current.

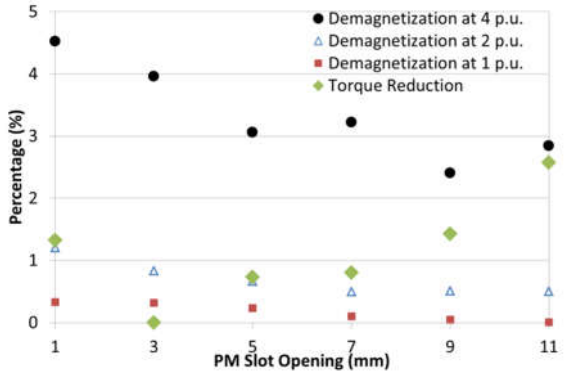

Figure 5-53 Demagnetization and torque reduction of different PM slot openings.

As demonstrated in Figure 5-52, only minor impact of the PM slot opening appears on the demagnetization. With smaller PM slot opening, the average reluctance for the demagnetizing field is reduced, and more flux will go through the slot opening area because of the higher permeance in this flux loop, causing more severe saturation the in bridge area. Part of the d-axis reactive field will travel through the upper corner of the PM pole and then into the iron bridge. And local demagnetization occurs in the upper part adjacent to the highly saturated bridge. As the widening the slot opening, demagnetized area reduces because the reluctance of the flux path through the openings rises and the demagnetizing field declines. Meanwhile, larger slot opening increases the equivalent reluctance for both the main PM and armature excited field, which leads to lower PM and reluctance torque. It should be noted that decrease in torque with very small PM slot opening is also observed as a result of severe flux leakage. The detailed result is shown in Figure 5-53.

5.5.5.4 Inner Bridges

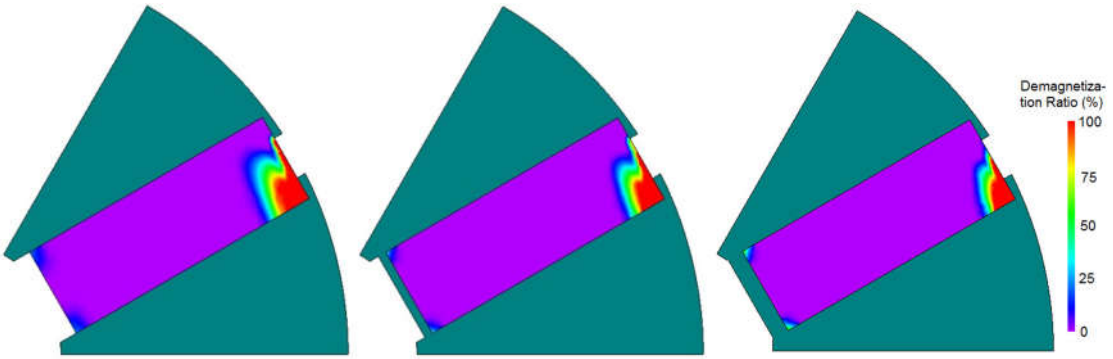

(a) None; (b) 1mm; (c) 2mm;

Figure 5-54 Demagnetization distributions with different inner bridge thickness under 4 p.u. current and -20°C.

Table 5-16 Influence of inner bridge on demagnetization and torque

Inner Bridge Thickness / Current	Demagnetization Index			Decrease in Torque
	1 p.u.	2 p.u.	4 p.u.	
None	0.38%	1.49%	9.75%	-
0.5mm	0.37%	1.45%	8.53%	3.43%
1mm	0.37%	1.38%	7.44%	6.99%
2mm	0.33%	1.30%	5.76%	14.47%

As demonstrated in Figure 5-54, improvement is achieved with the increase of the thickness of inner bridges because a path for the demagnetizing d-axis reactive field is provided by applying the inner bridges. However, the improvement is quite limited while the drawback of torque reduction is significant. By applying 2mm inner bridge to the rotor design, the demagnetization index is decreased from 9.75% to 5.76% under 4 p.u. current, while the rated torque is reduced by 14.47%, as listed in Table 5-16. Since the inner bridge provides a lower reluctance flux path for d-axis flux and yet has little effect on q-axis field, the d-axis inductance is increased significantly. As a result, there will be considerate decrease in reluctance torque component because of decreased rotor saliency. Additionally, PM flux leakage is increased due to the inner bridge, which leads to loss in open-circuit back EMF and PM torque. As shown in Table 5-17, significant decrease in fundamental back EMF is observed with the increase of inner bridge thickness, but the decline in the PM torque component is much smaller at rated load. That's because the highly saturated bridges is caused by both the PM flux leakage and armature d-axis flux field under loading conditions. And under heavy loading, the strong armature reactive becomes the main reason for the saturation. On the other hand, the d-axis inductance increases dramatically with the thickness of the bridges, while the actual loss in the PM torque is not as significant. Although there is 14.47% decline in the overall torque with 2mm inner bridges at rated current, only 4.3% comes from PM torque, and the rest 10.2% is due to the reduced reluctance torque. In all, the inner PM bridge method is not very suitable for the one-layer configurations to reduce the risk of demagnetization, because the effect on the anti-demagnetization ability is not appealing, not to mention the severe degradation in the torque capability.

Table 5-17 Influence of inner bridge on torque production and back EMF

Inner Bridge Thickness	Overall Torque (Nm)	PM Torque (Nm)	Reluctance Torque (Nm)	Back EMF Fundamental (V)
None	13.99	8.37	5.62	138.65
0.5mm	13.51	8.22	5.28	128.79
1mm	13.01	8.08	4.93	119.22
2mm	11.96	7.76	4.20	99.78

5.6 Final Anti-Demagnetization Designs

5.6.1 The Two-Layer Structure

Table 5-18 Final anti-demagnetization design for the two-layer structure

Ferrite Material	Ferrite Y36
Normal PM Deeper Insertion	2mm for the main pole, and 1mm for the secondary pole.
Deeper PM Insertion with Non-Magnetic Wedges	Not Applied. The non-magnetic wedges require extra cost for the manufacture and assembly.
PM Slot Opening	2.5mm for both the main and secondary poles
Inner bridges	1mm for the main PM.
Torque Output	**98.1% of original design.**
Demagnetisation Index	Reduced from **3.73%** to **0.73%** under 4 p.u. current at 20°C; from **11.23%** to **4.12%** at -20°C.

The final anti-demagnetization designs and the improvement of the two-layer configurations are listed in Table 5-18. With the compromise of good intrinsic coercivity and lower price, ferrite Y36 magnet is chosen for the PM poles. Although deeper PM insertion method with non-magnetic wedges shows better potential to reduce demagnetization, extra material is required for the non-magnetic wedges. Moreover, there will be thinner outer PM slot bridges to hold the wedges and PM poles, and the mechanical robustness would be deteriorated, especially under high speed operations. For the ease of mass production and more rigid structure, normal deeper insertion with 2mm for the main pole and 1mm for the secondary poles. The PM slot openings for the main and secondary poles are all 2.5mm. Despite of the negligible impact on demagnetization index, the torque can be slightly improved. To reduce the risk of demagnetization in the inner part of the main PM, inner bridge of 1mm is adopted and significant improvement is achieved. Together with normal PM insertion, optimal slot openings and inner bridges, the demagnetization index is

reduced from 3.73% to 0.73% under 4 p.u. at room temperature, and from 11.23% to 4.12 at -20°C. Since the PM poles are shorter than the original design due to PM deeper insertion, the torque output is reduced by 1.9% owing to decreased PM torque.

5.6.2 The One-Layer Structure

Table 5-19 listed the detailed anti-demagnetization designs and improvement for the one-layer structure. As the normal PM deeper insertion exhibits better effect than deeper PM insertion with non-magnetic wedges method, 2mm normal insert is applied. The PM slot opening is 7mm for the balance between demagnetization index and torque output. Inner bridges show no noticeable impact of on demagnetization reduction, yet cause dramatic decrease in machine performance in terms of back EMF and torque output. For the one-layer structure, only normal PM deeper insertion is effective to supress the risk of demagnetization. Thus, the anti-demagnetization design is not as effective as the two-layer structure. The demagnetization index reduced from 5.71% to 2.21% at room temperature, and from 9.75% to 7.33% at -20°C, while the torque output is reduced by 2.19% compared with the original design.

Table 5-19 Final anti-demagnetization design for the one-layer structure

Ferrite Material	Ferrite Y36
Normal PM Deeper Insertion	2mm for the PM poles
Deeper PM Insertion with Non-Magnetic Wedges	Not Applied. Not as effective as normal deeper insertion method.
PM Slot Opening	7mm for the PM poles
Inner bridges	Not Applied. No noticeable impact but significant decrease in torque.
Torque Output	**97.81% of original design.**
Demagnetisation Index	Reduced from **5.71%** to **2.21%** under 4 p.u. current at 20°C; from **9.75%** to **7.33%** at -20°C.

5.7 Comparison of Demagnetization Performances

Since the main poles of the two-layer structure is thinner than those of one-layer one, there is higher risk of large scale demagnetization for the main poles when facing over-current reactive field. But the secondary poles can endure much higher demagnetizing field since not all the d-axis main flux goes through them. In this sense, the two-layer structure has better redundancy as the PMs are more difficult to be completely demagnetized. Moreover, the q-axis current has more serious influence on the demagnetization of two-layer configurations than the one-layer ones. For the two-layer structure, q-axis current alone can cause demagnetization to occur in the inner part of the main PM. With the cross-coupling effect of both d- and q-current, the inner part of the main PMs are more prone to large scale demagnetization. As for the one-layer design, it is clear that q-axis current increases the local demagnetization on the outer corner of the PMs, but its effect on large scale demagnetization is quite limited. As shown in Figure 5-55 (a), the saturation in the rotor core in between the main and secondary poles becomes prominent at rated current for the two-layer motor, which will have considerable impact on the flux distribution of the d-axis flux field. Thus, the high cross-coupling effect of d- and q-axis flux field is expected. On the other hand, saturation is only observed on the edge of the one-layer rotor near the outer PM slot bridge in small scale even at twice rated current, as shown in Figure 5-55 (b) and (c). Accordingly, the d- and q-axis components are less coupled together for the one-layer structures.

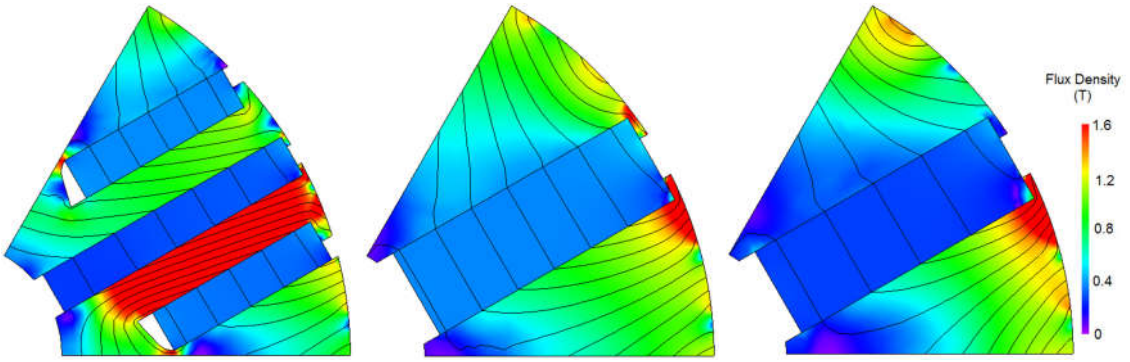

(a) Two-layer at 1 p.u.; (b) One-layer at 1 p.u.; (c) One-layer at 2 p.u.;

Figure 5-55 Flux distributions of the two- and one-layer models.

To reduce the risk of demagnetization, the normal deeper PM insertion methods work effectively for both one- and two-layer configurations, with only subtle decrease in the torque performance. The non-magnetic wedge insertion method works better for the two-layer structure because zig-zag flux leakage path in between the rotor and stator tooth is much easier to form with much smaller PM slot openings.

The inner PM bridge method only shows palpable effect on the torque of two-layer machine, while it causes severe reduction in the torque output for one-layer design with insignificant improvement for demagnetization. That's because the different flux distribution in the rotor. For the two-layer model, since part of the lamination core in between the main and secondary PMs are easily saturated by the d-axis PM and q-axis armature flux, the inner bridge is able to provide a path for the d-axis field and alleviate the saturation in the rotor core at the same time. Therefore, both d-axis and q-axis inductance will be increased to maintain similar reluctance torque. As for its one-layer counterpart, there is no severe saturation occurs in large scale, and thus the inner bridge has little impact on the q-axis flux field. But the inner bridges can increase the d-axis inductance dramatically, which leads to the decrease of saliency and reluctance torque. Furthermore, the one-layer machine has smaller current angle and thus lower d-axis current due to its larger PM torque component. As a result, armature d-axis flux field is weaker with smaller amount of flux contributed to the saturation for the inner bridge. As a result, more PM leakage flux goes through the inner bridge, causing higher loss in the PM torque.

In all, the two-layer configurations proposed in this project have distinctive flux distributions in the rotor side, and thus a number of modifications can be applied to reduce the risk of irreversible demagnetizations. But many of these methods are not applicable for the one-layer structures.

5.8 Conclusion

Irreversible demagnetization can cause performance degradation of PM machines permanently and it is of great important to avoid it. Three key factors for demagnetization are comprehensively investigated to evaluate the

demagnetization performances. Armature MMF is the main reason of demagnetization of PM machines. The property of a PM material represents its intrinsic ability of withstanding reactive field. Thus, the ferrite material needs to be elaborately selected from commonly used commercial products to control the cost and more importantly, to ensure safe operation under required conditions. Due to the inherent property of ferrite materials, the risk of demagnetization increases significantly at low operational temperature. The anti-demagnetization performances of the conventional spoke-type machines are also studied and comparisons are carried out between the one- and two-layer configurations for better understanding of the demagnetization mechanism.

Based on the knowledge derived from the investigations, some rotor design methods are proposed and studied to reduce the risk of demagnetization by minor modifications on the rotor lamination, such as the applications of deeper PM insertion, optimal PM slot opening and inner bridges. Without increasing the cost of material or manufacture, these methods are quite effective to improve the anti-demagnetization capability for the two-layer configurations.

6 FINAL PROTOTYPE MACHINE AND EXPERIMENTAL VALIDATION

6.1 Introduction

The electromagnetic design of the novel multi-layer ferrite IPM configurations is carried out in the previous chapters. However, the final prototype machine may be slightly different since mechanical robustness, assembling feasibility and manufacture should be taken into consideration. Thus, a few compromises have to be made based on the electromagnetic design to obtain lower cost for mass production. For the performance evaluation of the proposed machine design, a benchmark is necessary to reveal its advantages.

Induction machines, especially the cage ones, are the most widely machine type in industry due to its low cost and rigid rotor structure. Since one aim of the project is to replace the low efficiency IMs in the vast industrial and domestic market, it is perfect to benchmark a commercial IM with the same housing and stator dimensions. As the high-price rare-earth materials are excluded from the design, the cost of the ferrite PM motors is comparable with IMs. On the other hand, by using PM excitation and salient rotor structure, higher efficiency, torque density and power factor can be achieved for the proposed ferrite IPM motor. Furthermore, due to the increasing mandatory efficiency standards to be implemented, the proposed ferrite machine will become more and more competitive in near future.

Due to the instinctive structure of two-layer configurations and ferrite materials, practical issues about rotor assembly are then discussed for improvement of mechanical design. Finally, the performance of the prototype machine is tested and validated under various operating conditions.

6.2 Final Design of the Prototype Machine

Owing to the distinguished rotor structure, spoke-type IPM machines have long PM poles and it is ideal to eliminate the iron bridges so as to reduce PM flux leakage and maximize the torque capability, as shown in Figure 6-1(a). In this way, the rotor would be divided into a number of rotor modules by the main

PMs, and smaller segments would also be cut out by secondary PM slots. In [88,107] non-magnetic dovetail joint structures were proposed to fix rotor modules to the shaft for conventional spoke-type machine. But this joint part needs to take up some space within the rotor area, potentially reduces the limited space for the installation of longer magnet poles, and causes decrease in the PM torque. Moreover, the extra joint parts complicate the motor structures and increases manufacture cost. In this case, two-layer configurations will be far more complex than the conventional spoke-type rotor, since the number of segments is doubled due to the secondary PM slots. Thus, it is more practical to retain iron bridge structures to connect the rotor pole modules as a whole considering the mechanical robustness and manufacturing cost, especially for small-scale machines. As a result, saturation bridges are used in the inner main PM slots and in between the two adjacent V-shaped PM slots, as depicted in Figure 6-1(b). From anti-demagnetization ability perspective, the application of iron bridges in the inner side of the main PM slots can effectively increase the resistance of PM poles against armature reactive field. Meanwhile, although the PM flux leakage is increased under very light loadings, there is no noticeable effect under medium to heavy loading conditions. With the rated current, the inner iron bridges of main PM slots can alleviate the saturation of the highly saturated area in between the main and secondary poles, and could potentially increase the main flux linkage. Accordingly, rated torque output can be improved slightly. As for use of the iron bridges in between the V-shaped secondary PM slots, decrease in torque is caused due to the higher flux leakage of the secondary poles. But they are necessary for the rotor integrity and lower assembly cost.

(a) Ideal rotor design; (b) with iron bridges; (c) with holes;

Figure 6-1 Rotor models with and without iron bridges.

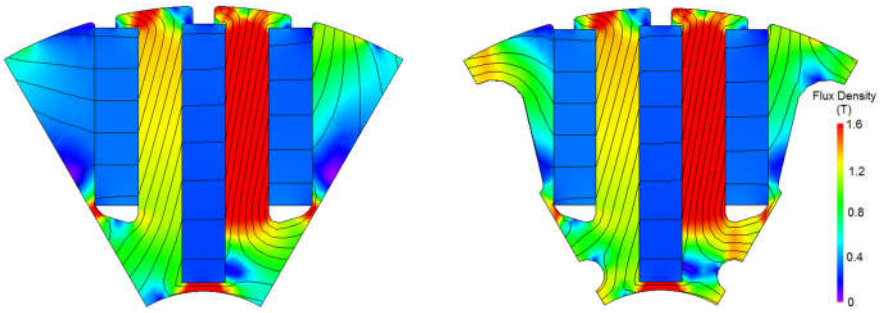

(a) without cut-outs; (b) with cut-outs;

Figure 6-2 Rotor flux distribution with and without cut-outs under rated load.

In order to reduce the overall mass of the machine, it is of interest to cut out some part of the rotor lamination which affects little of the flux distribution. As illustrated in Figure 6-2(a), the flux distribution of the rotor area in between the secondary PMs is quite low even under rated loading, mostly under 0.5T. That means the permeability in these areas is relatively high, and even with a considerable part removed, no noticeable influence will be imposed on the overall flux distribution. The flux distribution of the rotor under rated load with large cut-outs is demonstrated in Figure 6-2(b). The result shows that no saturation is caused by the cut-outs, and the FEA simulation confirms that torque output is not affected at all. Since the inner rotor areas in between two adjacent main PMs are also far from saturation, holes are cut out for the ease of lamination stacking process and final rotor assembly. With all these factors taken into considerations, the final rotor lamination design is demonstrated in Figure 6-1(c).

6.3 Performance Comparison with Induction Machine

The cross sections of the proposed two-layer ferrite IPM and a commercial IM models are demonstrated in Figure 6-3, and the detailed dimensional specifications are listed in Table 6-1. The size and geometry of the stator lamination are exactly identical, and the stacking length, inner and outer diameters of the rotor are also of the same size. Both machines are facilitated by short-pitched single-layer distributed windings. The IPM has 36 slots in the stator and 6 poles in the rotor with two slots per pole per phase, while the IM

has 36 slots in the stator and 44 slots in the rotor with 4-pole armature windings. Since the number of poles is not the same for the two machines, the windings distributions are different from each other. The ferrite IPM is equipped with single-layer chain windings, and the IM is facilitated by single-layer cross windings. Not to lose generality, the maximum electrical loads of the stators are kept the same.

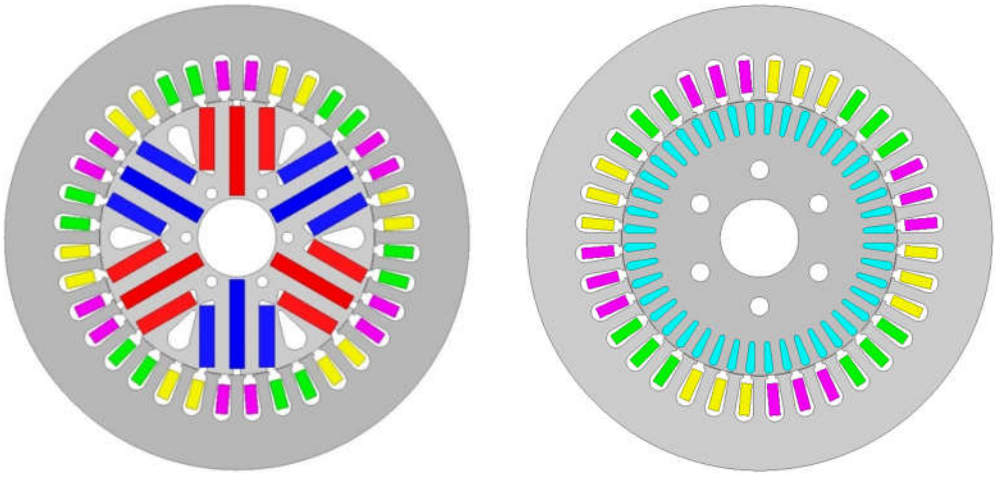

Figure 6-3 2D Models of the ferrite IPM and IM.

Table 6-1 Dimensional specifications of the ferrite IPM and IM

Parameters	**PM**	**IM**	**Unit**
Stator Outer Diameter	160	160	mm
Stator Inner Diameter	95	95	mm
Rotor Outer Diameter	94.5	94.5	mm
Rotor Inner Diameter	27	27	mm
Airgap Length	0.25	0.25	mm
Stacking Length	90	90	mm
Number of Stator Slots	36	36	
Number of Poles	6	4	
Number of Rotor Slots	-	44	
Number of Conductors per Slot	108	100	
Material of Rotor PM/Cage	Ferrite	Aluminum	
Material of Lamination	50W470	50W470	

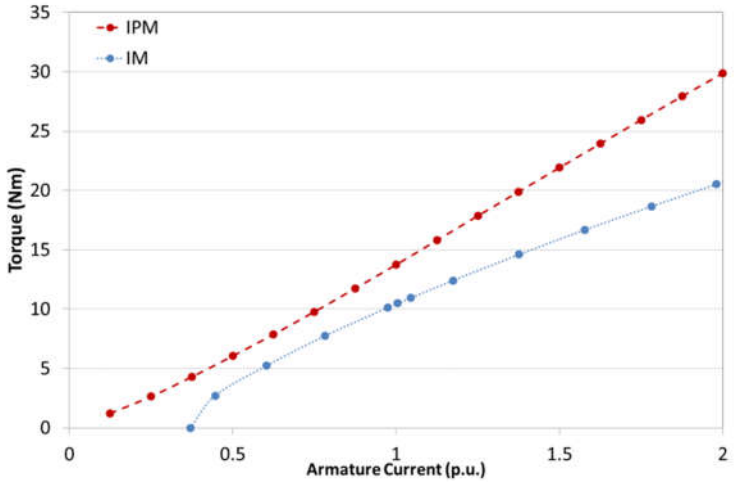

Figure 6-4 Comparison of average electromagnetic torque with armature current.

6.3.1 Torque Capability

The torque profiles against armature current are illustrated in Figure 6-4 for both the IPM and IM with MTPA control scheme. The ferrite IPM exhibits much better torque capability than its IM counterpart. Since the excitation field of the IM is generated by armature current, the current is 0.36 p.u. under no-load condition. For the IPM, the excitation field is mostly produced by the PMs under light and medium loadings, which improves the utilization of the armature current for torque production purpose. Thus, the no-load current of the IPM is very low, ideally only to overcome the no-load losses. With the increase of armature current, the increment in torque against current is close for the two machines. As the current grow higher, though the PM excited field abates owing to the saturation, the reluctance torque increases and dominates under heavy and over load conditions, which would help to further increase the torque ability of the IPM. On the other hand, the current in the squirrel cage increases dramatically with the load for the IM due to larger rotor slip, which consumes part of the input power and places a negative influence on the torque increment under overload conditions. Thus, the ferrite IPM has a much better torque profile. At rated current, the torque output of the IPM is 1.27 times that of the IM, which means 27% higher torque and power density is achieved with the same electric loading. And the IPM exhibits even more remarkable advantages over the IM under overload conditions.

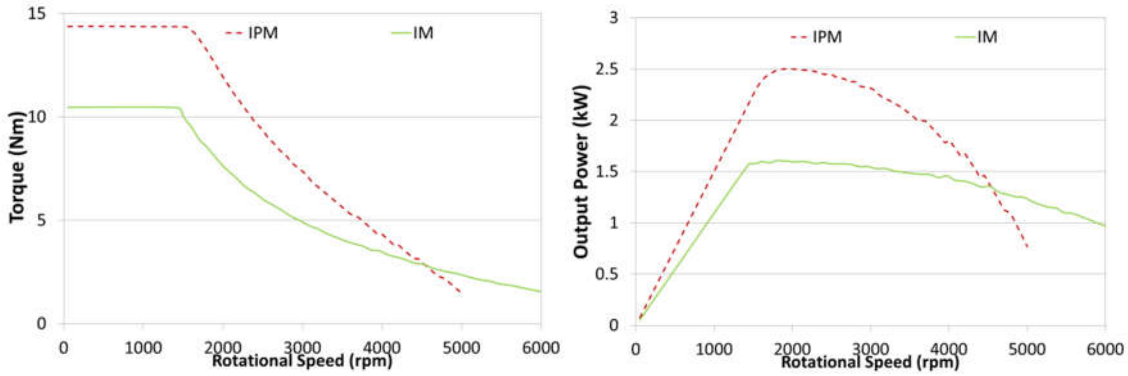

(a) Torque-speed curves; (b) Power-speed curves;

Figure 6-5 Torque-speed and Power-speed characteristics of the IPM and IM

6.3.2 Torque-Speed and Torque-Power Curve

Figure 6-5(a) depicts the torque-speed characteristics of the IPM and IM at rated current under MTPA control strategy. Since the torque capability of the ferrite PM has been improved greatly, much higher torque can be delivered within the rated base speed range comparing to the IM. But under flux weakening operation, the torque output of the IPM reduces faster with speed. Hence, the torque difference between the two machines becomes smaller and the torque delivered by the IM eventually exceeds that of ferrite PM when the speed is over 4800rpm. What's more, the IM has a wider operational speed range of over 6000rpm, while the induced voltage of the ferrite PM exceeds that of power supply at the speed of 5400rpm.

The power-speed curves of the ferrite PM and IM are illustrated in Figure 6-5(b). With rated current, the ferrite PM machine is able to deliver 2.1kW at rated speed and 2.3kW at 2000rpm. Then the output power reduces with speed, and drops below 2.1kW when the speed exceeds 3100rpm. The IM achieves 1.5kW at rated speed and 1.6kW at 1600rpm, and its constant power speed range (CPSR) of the IM reaches 3500rpm. Due to the better flux weakening performance, the power of the IM drops much slower than the IPM. The IM delivers 1.1kW power at 5400rpm and nearly 1kW at the speed of 6000rpm.

Because the excitation field of IMs is generated by armature current, it can be directly adjusted by controlling the reactive current. Thus better flux weakening

performances and wider operational speed range can be achieved for the IM. For PM machines, the exciting field is mainly provided by PMs, which is not adjustable since the PMs are pre-magnetized. To operate over the rated base speed, flux weakening control strategy is applied to generate armature reactive field opposing the PM magnetization for weakened excitation. The flux weakening performance depends on the ratio of the product of current amplitude I_m and d-axis inductance L_d over PM flux linkage Ψ_f. According to d-axis magnetizing inductance derivation in subsection 3.2.3.2, L_d is greatly influenced by the width of PMs and reduces with PM width. Besides, wider PMs will enhance PM flux field and thus Ψ_f. Hence, the flux weakening performance deteriorates dramatically with the increase of PM width. However, the design of spoke-type machines requires certain PM width for sufficient PM excitation and rotor saliency to achieved high torque density, which inevitably leads to relatively small L_d and inferior flux weakening ability.

6.3.3 Losses

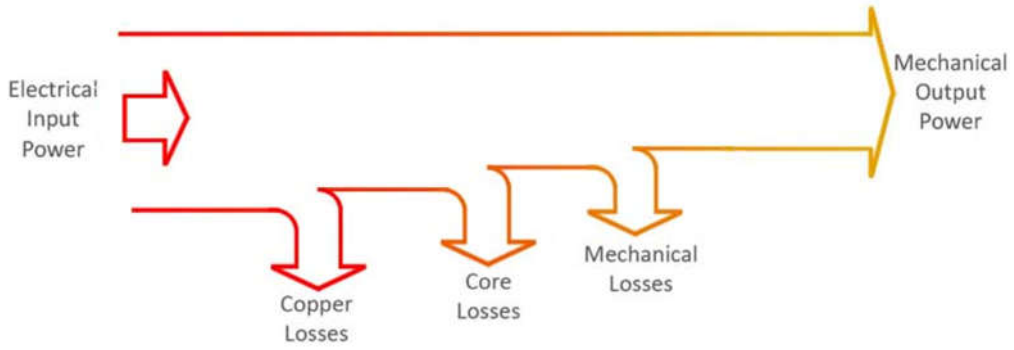

Figure 6-6 Power and loss flow diagram of the ferrite and induction motors.

In electric machines, the estimation of the losses is of great importance concerning the thermal limitation and energy conversion efficiency. Because the losses would eventually be transferred into heat and result in temperature rise of the machines, the maximum continuous loading abilities and lifespan of the machines are significantly influenced. The losses in electric machines can be usually divided into four categories: copper loss in stator and rotor windings, core loss in stator and rotor lamination cores, eddy current loss in back iron and PMs, and mechanical losses. The power and loss flow diagram is depicted in

Figure 6-6 for the ferrite IPM and IM. Since eddy current loss is completely eliminated from the ferrite PMs and does not exist in the IM, it is not included in the flow diagram and this section.

The mechanical loss due to the bearing friction and windage is dependent upon rotational speed but independent on the load. It is difficult to estimate by direct calculation since the core loss is also dependent on rotational speed and coupled together with mechanical loss. But according to the datasheet of the IM, mechanical loss can be approximated empirically as 2% that of rated power under full load condition, and proportional to the rotating speed square [170]. In this study, the total loss is dominated by electrical and electromagnetic losses. As a result, only copper loss and core loss are investigated and compared in detail for the ferrite PM and IM.

6.3.3.1 Copper Loss

The copper loss usually takes up a large part of the total loss. The copper loss can be derived from the current flowing in the armature winding and the estimated winding resistance, and hence is also called resistive loss and I^2R loss. According to Ohm's law, the DC resistance of a conductor is dependent on its resistivity, length and cross-section area, and can be easily estimated [171]. But in alternating current (AC) systems, the situation is more complicated. Due to the skin and proximity effects, the AC resistance of a conductor increases with the frequency.

Skin effect is the tendency of AC current becoming distributed so that the current density decreases greatly with the depth inside a conductor. In other words, the current tends to flow at the skin of the conductor and the skin depth is usually used to describe the severity level of skin effect [172]:

$$\delta = \sqrt{\frac{\rho_c}{\pi f \mu_0 \mu_r}} \qquad \textbf{(6-1)}$$

where δ is the skin depth, f is the operating frequency, ρ_c and μ_r are the the resistivity and relative permeability of the conductor. In this case, copper wires with diameter of 0.6mm are used, and the skin depth at rated speed is 8.23mm.

Apparently, the skin depth is much larger than the diameter of the copper wires, and thus the skin effect can be neglected.

In multi-stranded coil systems, the current density distribution in one conductor becomes non-uniform because of the alternating magnetic field associated to the AC current in adjacent conductors. This phenomenon is termed the proximity effect. According to [173], the increment factor caused by proximity effect can be represented by

$$k_{rpac} = \frac{R_a - R_{dc}}{R_{dc}} = \frac{\zeta}{2} \frac{\sinh\zeta + \sin\zeta}{\cosh\zeta - \cos\zeta} - 1 \quad \textbf{(6-2)}$$

$$\zeta = \frac{d_c \sqrt{\pi}}{2\delta} \quad \textbf{(6-3)}$$

where R_a and R_{dc} are AC and DC resistances of the winding respectively, d_c is the diameter of the copper wire in the stator slots. In this case, k_{rpac} is less than 10^{-7}, and proximity effect is also ignored for the copper loss estimation.

Therefore, only DC resistance is necessary for the estimation of copper losses for the IPM and IM. As a basic condition for the performance comparisons between the ferrite PM and IM, the stator copper losses are set to be equal at rated operational condition, so that the electrical loading and thermal condition of the stators are the same. Since torque can be approximately regarded as proportional to current below rated speed, copper loss of stator windings increases with torque and is independent on the speed for both the IPM and IM, as shown in Figure 6-7. Although the two machines under comparison have the same maximum copper loss in the stator, their copper loss features are quite different under various operational conditions because of the different operating principles due to different machine types. When below the rated speed and torque, the ferrite PM machine achieves lower copper loss level because of the advantage of PM excitation, while high copper loss is observed for the IM as excitation current is required to establish the flux field. The difference is more obvious at light or no-load conditions when copper loss is close to zero for the ferrite PM and over 15W for the IM.

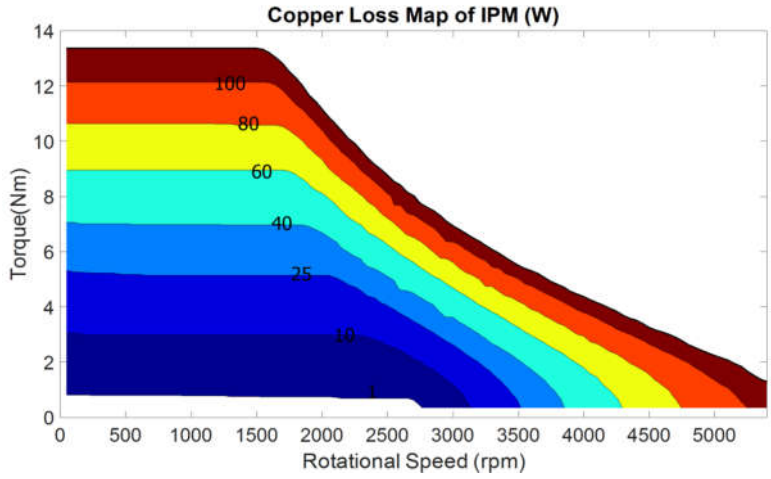

(a) Ferrite IPM;

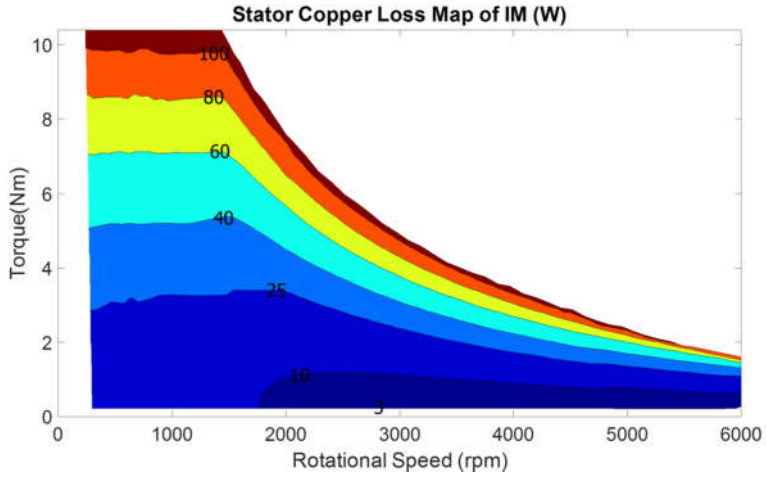

(b) IM;

Figure 6-7 Stator copper loss maps of IPM and IM.

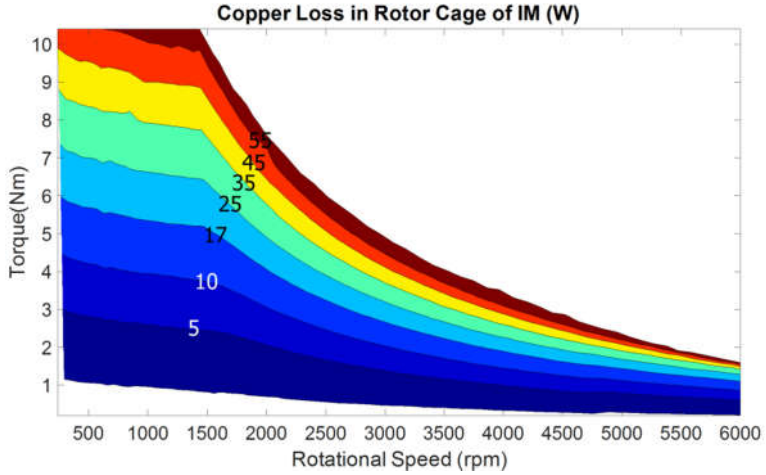

Figure 6-8 Copper loss map in the rotor cage of the IM.

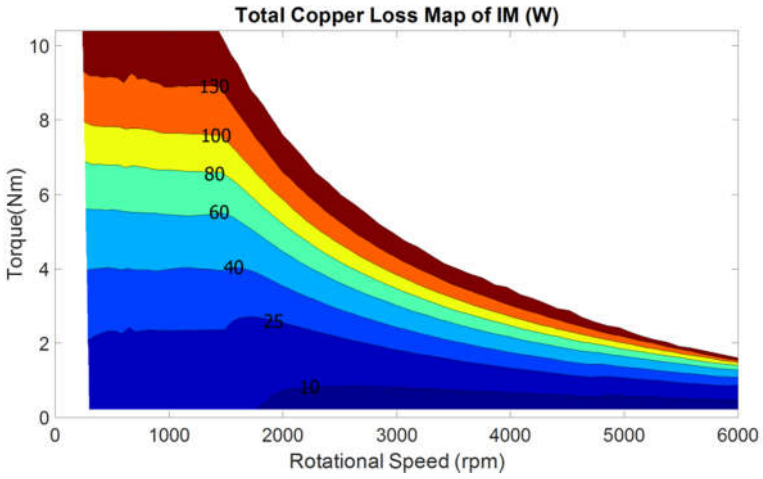

Figure 6-9 Total copper loss map of the IM.

However, the result is completely different when it comes to high speed range. Decrease in copper loss for the IM is observed with speed under no-load condition since the excitation current is reduced during flux weakening control. But under loaded condition, torque generating current increases to maintain the same torque, and thus copper loss still increases with speed. On the other hand, much higher stator copper loss is observed for the IPM as larger d-axis current is necessary for to achieve flux weakening operation. Accordingly, the copper loss increases dramatically with speed.

For the IM, there is considerable amount of copper loss in the rotor side due to the existence of squirrel cage. Since the current in the rotor cage is induced from stator reactive field, the copper loss increases with stator current and rotating speed, as depicted in Figure 6-8. The rotor copper loss of the IM can reach up to half of stator copper loss at rated torque output, which means 50% higher overall copper loss for the IM compared with the ferrite IPM. Considering only the stator copper loss, those of the IM and IPM are comparable below rated speed. But with the rotor copper loss taken into consideration, the overall copper loss of the IM is much higher than that of ferrite PM when the speed is lower than 3000rpm. Nevertheless, under very high speed operations, the copper loss of the ferrite PM machine is still higher because extremely large d-axis current is required for the deep flux weakening control, as demonstrated in Figure 6-9.

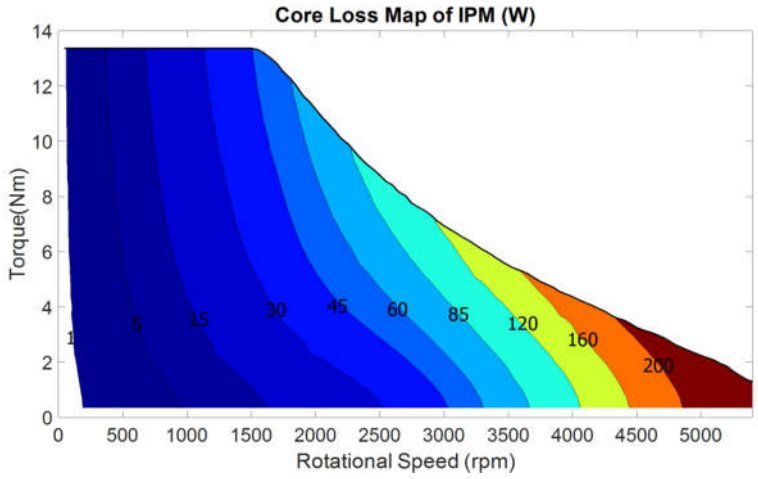

Figure 6-10 Core loss map of the IPM.

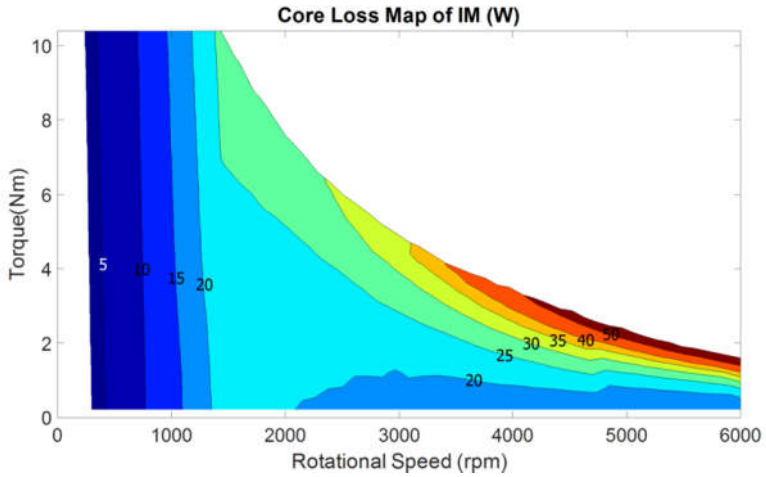

Figure 6-11 Core loss map of the IM.

6.3.3.2 Core Loss

Core loss, which consists of hysteresis loss, eddy current loss and excessive loss in the lamination cores, is another major source of heat especially at high speed operations. Core loss is significantly influenced by the operating frequency, and hence the losses increase with rotational speed exponentially for both the ferrite PM and IM, as demonstrated in Figure 6-10 and Figure 6-11. Moreover, the flux density also has considerate impact, so the core loss could be aggrandized by the armature current. Since the excitation field is largely decided by the PMs for the IPM, the rotational speed has a major influence on the core loss over the whole operational range. Minor effect is shown by the armature current, and core loss rises as the increase of loading due to the

stronger armature reaction. As for the IM, the flux field is almost constant when below the rated speed, because excitation is controlled by armature current. As a result, core loss can be approximately regarded as only dependent on rotational speed. But under flux weakening operations, the excitation current decreases and lower core loss can be observed under no-load condition. But as the increase of output, core loss increases significantly due to the influence of reactive field at high speed.

The core losses of both machines are quite small under rated speed. Compared with the IM, core loss of the IPM is slightly higher because of higher flux density owing to the PM excitation and higher electrical frequency due to higher number of poles. The core loss of ferrite PM becomes much higher than IM when the speed is over nominal value. As a result of better flux weakening ability for the IM, much lower flux density can be achieved as the speed grows, which results in much slower rise in core loss. On the other hand, the flux density of the ferrite PM stays at a relative high level owing to the fixed PM excitation and inferior flux weakening ability, which leads to exponential increase in core loss with speed. This is certainly one of the factors that deteriorate the performance of the IPM at high speed range.

6.3.4 Efficiency

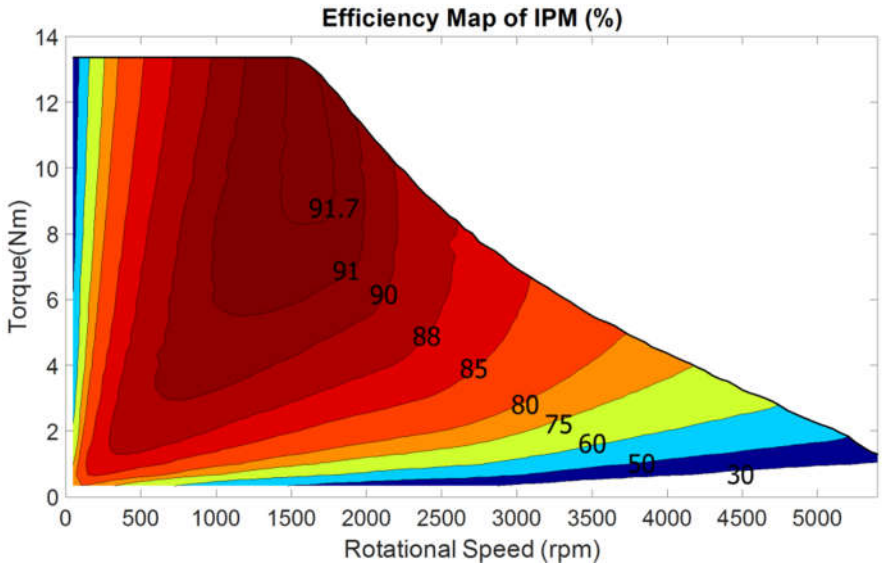

Figure 6-12 Efficiency map of the IPM.

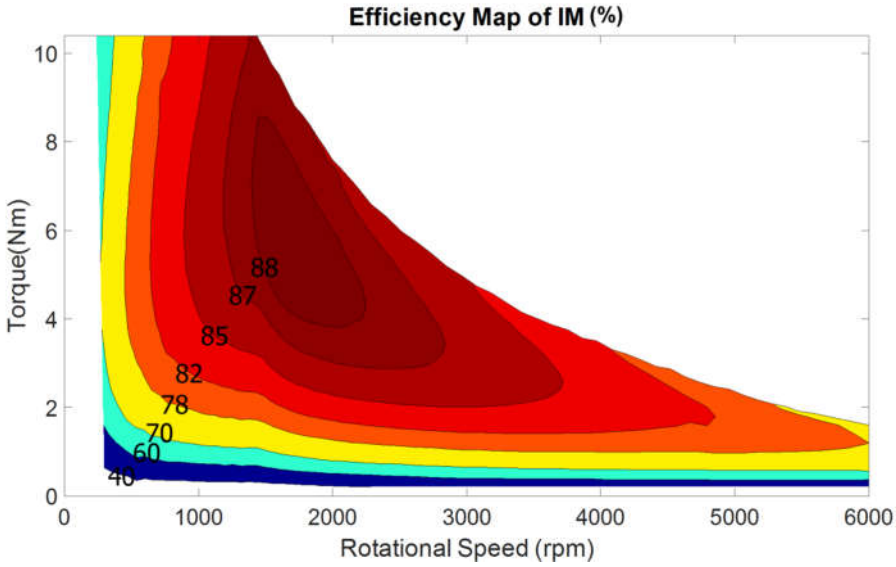

Figure 6-13 Efficiency map of the IM.

By compiling the losses calculated in the previous sections, efficiency maps of the proposed ferrite PM and the commercial IM are derived, as shown in Figure 6-12 and Figure 6-13. Due to the different loss features under different torque and speed conditions, the whole speed-torque operation region is divided into four sub-regions for detailed comparisons and discussions.

- Sub-Region I: Low Speed and Low Torque

In this sub-region the load torque is less than 40% of rated and the rotating speed is lower than 1000rpm. As the speed is relatively low, the core loss for the two machines is similar. The difference in behaviour mainly lies in copper loss. The main flux field of the IPM is established by PMs and thus the armature current is much lower, while a large part of the armature current is for the build-up of field excitation. As a result, the efficiency of the IPM is much better than the IM for lower copper loss in the region.

- Sub-Region II: Low Speed and High Torque

Since the current is high under these circumstances, copper loss dominates the overall loss. Although the maximum stator electric loadings are kept the same for both the machines, extra copper loss in the rotor bar can add up to 25% of the total loss for the IM. What's more, higher torque per ampere can be

achieved for the IPM, which means higher power output. Combining the two factors, much higher efficiency is expected for the IPM in this sub-region.

- Sub-Region III: Medium Speed and Medium to High Torque

Normally the most frequent operational ranges for a motor lie in this region, and both of the motors are designed to exhibit the highest efficiency under the torque-speed range of 1000 to 2000rpm speed and half to full load torque. Apparently, the ferrite IPM shows better performance in efficiency against its IM counterpart. At rated working points, the proposed IPM machine operates with efficiency of over 91.7%, against that of 87.8% for the IM. Within this sub-region, the IPM maintains the efficiency over 90% with the highest achieving 91.9%, while the IM obtains over 85% with the highest efficiency of 88.7%. About 2-4% higher efficiency can be attained compared with the IM, which makes big difference for the energy saving because the motors work in this region for most of the time in operation.

- Sub-Region IV: High Speed

The motors enter deep flux weakening operation in this sub-region. For the IPM, negative d-axis current is necessary to weaken the PM excited field so as to reduce the induced voltage during high speed operations. The increased demagnetizing current will not only increase the copper loss but also intensify the spatial harmonic of the armature MMF resulting in higher core loss. Thus, the efficiency of the IPM decreases significantly with speed. On the other hand, the excitation current of the IM can be reduced for weaker flux field, and both copper loss and core loss are much lower than the IPM. Therefore, the efficiency of the IM exceeds that of IPM when the speed is over 3000rpm, and becomes far more superior over 4000rpm.

To conclude, the IPM achieves higher efficiency in most of the operational region, and most importantly in the most frequently operating sub-region III. Although the IM obtains higher efficiency during high speed range, it is not the main working region for most of the small-scale industrial applications. On this basis, the IPM exhibits much higher overall efficiency.

6.3.5 Power Factor

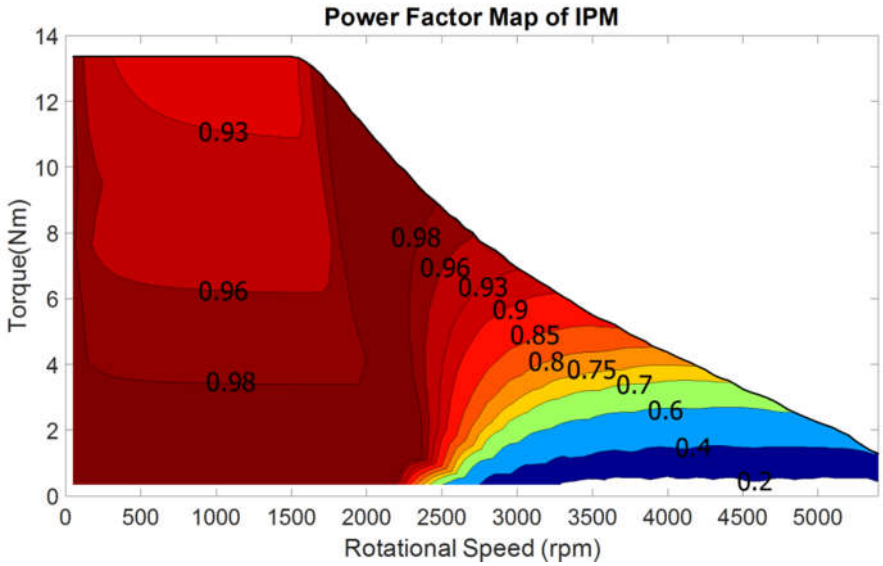

Figure 6-14 Power factor of the IPM.

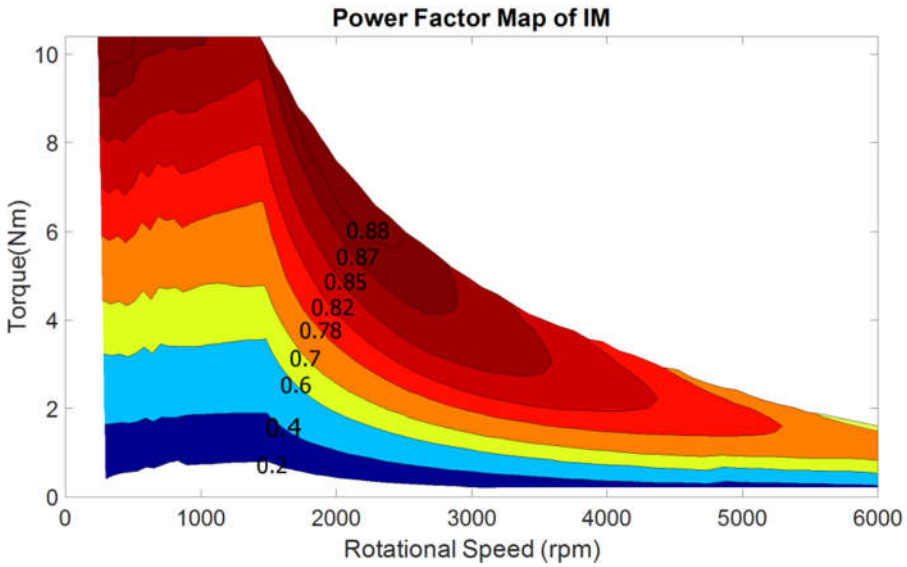

Figure 6-15 Power factor of the IM.

Power factor is an important index for electric machines especially in inverter-fed variable speed systems. High power factor can reduce the power rating of the inverter and thus reduces the cost for power electronics since lower apparent power and current can be achieved.

The IPM achieves relatively high power factor from low to medium speed range owing to PM excitation, as illustrated in Figure 6-14. Its power factor decreases slightly with the increase of torque load when below rated speed, because

higher current generates higher armature reactive field which increases the leading phase angle of the armature voltage vector. When the speed is over the rated, larger advanced current angle is required for flux weakening, and the power factor increases as the phase angle difference between winding voltage and current reduces. When entering the high speed sub-region, even larger current angle is necessary. This makes power factor change from lagging to leading, and decreases dramatically with speed.

The power factor map of the IM is depicted in Figure 6-15. Due to the inherent disadvantage of the IM, it has a much lower power factor when below rated speed. The power factor is extremely low under no-load or light load because of its indispensable magnetizing current, even though the active power is very low. With the increase of loading, the active power rises and so does the power factor. The IM only shows its advantage over the IPM during high speed range, when the excitation current is reduced.

6.3.6 Material Costs

The economical performance and weight of the motor is also very important from the market perspective. The main materials of electric machines include silicon steel lamination, copper wires, ferrite PMs, and aluminum. The weight and material cost of the ferrite PM and IM are listed in Table 6-2. The total weight of the two motors is approximately the same since the same stator lamination, shaft, rotor dimension and housing assembly are used. The IM has slightly heavier rotor lamination as the IPM motor uses large amount of ferrite material in the rotor. And since the mass density of ferrite is lower than silicon steel, the overall weight of the IPM is marginally smaller. The material cost estimation is based on the UK market price in [174]. The costs of motor cores and stator windings are almost the same due to the similar material usage. The difference is reflected in the rotor. The IM rotor contains only die-casted aluminum bars besides lamination core, making IM rotor one of the cheapest structures in electric machines. Although highly expensive rare-earth PM materials are excluded for the IPM, the considerable amount ferrite used still costs more than the IM rotor. Therefore, the overall cost of the PM motor is 15%

higher. However, the ferrite IPM machine can obviously deliver much higher torque density. If the power output is taken into consideration, the cost per kilowatt of the IPM is about 18% lower than the IM, which makes the two-layer ferrite IPM much more attractive for various applications.

Table 6-2 Material costs of the ferrite PM and IM

	IPM	IM
Lamination Mass (Kg)	10.0	10.7
Copper Mass (Kg)	2.1	2.1
PM/Aluminum Mass (Kg)	1.0	0.5
Total Mass (Kg)	13.1	13.2
Lamination Cost (£)	20.0	21.4
Copper Cost (£)	14.7	14.7
PM/Aluminum Cost (£)	8.0	2.0
Total Cost (£)	42.7	37.1
Cost per Kilowatt (£/kW)	20.3	24.7

6.4 Prototype Machine Manufacture

The stator, rotor and PMs of the two-layer ferrite IPM prototype machine are demonstrated in Figure 6-16 depicts, and the dimensional specification is listed in Table 6-1. The housing and stator lamination is directly adopted from a commercial IM. To adapt the design of ferrite IPM machine, the stator coils are re-winded with four strands of 0.6mm diameter copper wires. The winding pitch is five stator slots, and thus the windings are short-pitched by 30 electric degrees. Because thinner copper wires and chain coil configuration with shorter end-winding are employed for the IPM, there are eight more conductors per stator slot than the original IM.

The assembly of the rotor is more complicated. Firstly, the rotor laminations are stacked axially in an assembly fixture, and then pressed together as a whole. As ferrite materials have very brittle physical nature, there is a risk of chipping and breaking the magnets when stress is exerted on them. For the convenience of rotor assembly, clearance fit is applied to avoid imposing strong force when inserting magnets, and the PM poles will be glued to the rotor core afterward for fixation. To further reduce the risk of breaking the long ferrite magnets, each of

the PM pole is divided into two parts in axial direction and then asserted inside the rotor from different end of the rotor lamination. Two pieces of aluminum end-plates are used in each end of the rotor to hold the whole rotor together with screws and increase the robustness of the rotor.

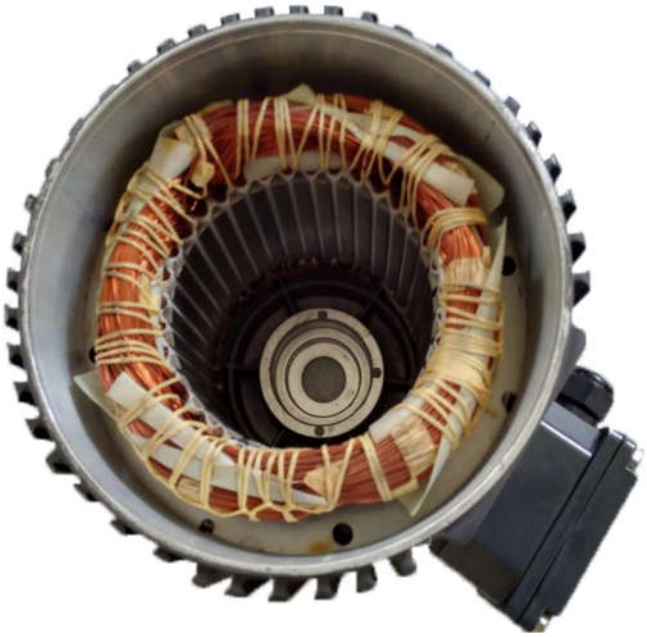

(a) Stator with housing;

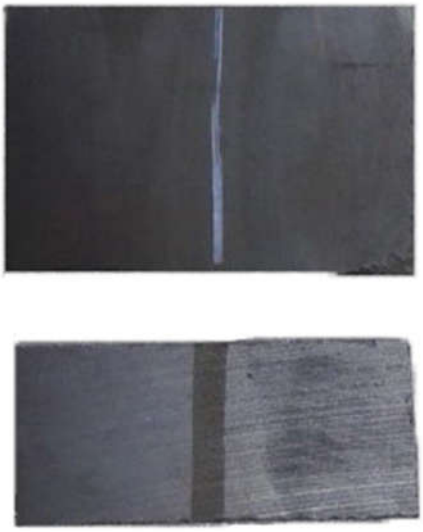

(b) The main and secondary PMs;

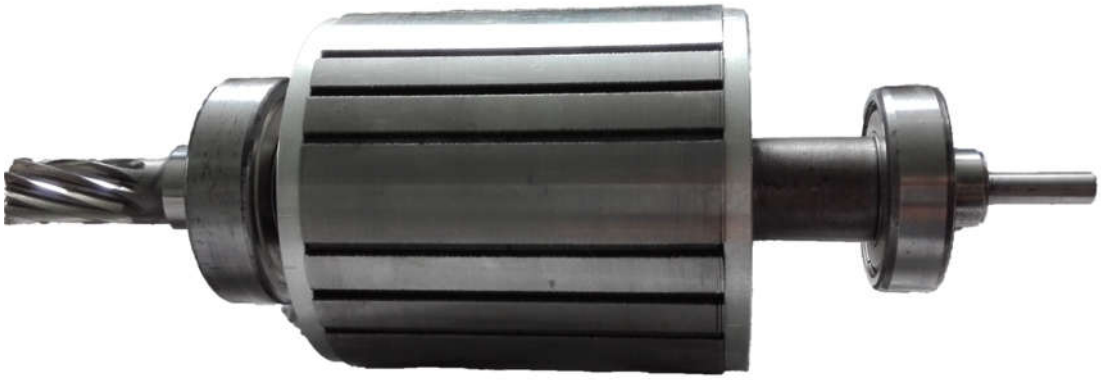

(c) Rotor with bearings.

Figure 6-16 Stator, rotor and PMs of the prototype machine.

6.4.1 Influence of the Machining Tolerance and Deviation of Ferrite Magnets

The most economical way for the mass production of ferrite magnet is by molding with tooling. Owing to the variation in shrinkage rate during the

manufacturing process, grinding is usually necessary to achieve a better tolerance. The dimensional tolerance can be controlled within ±2% before machining for most of the providers. And after simple grinding, the tolerances can be attained at ±0.2mm in the length and width dimensions, and ±0.1mm in the thickness dimension. Even tighter tolerance can be achieved at ±0.015mm, but at the expense of much higher cost. The machining process is better conducted prior to magnetization in case of adhesive loss caused by the heat during machining.

Due to the brittleness and high electric resistivity, standard drilling and wire-electrode cutting are not appropriate for ferrite materials. However, they can be cut or machined by diamond tooling. Hence it is more practical to slice big block into the required dimensions to save tooling cost with low quantity orders, especially at prototype phase. Since the aim of this project is to achieve a low-cost design for IPM machines, ferrite PMs after simple grinding are used for manufacture to reduce cost. The tolerance grade of ferrite PMs is lower than that of rare-earth materials, and thus the influence on electromagnetic performances should be considered for the prototype machine.

For easy assembly of the rotor and avoiding breaking of the PMs, clearance fit between the rotor lamination and the ferrite magnets is applied for the design. Then the PMs are glued to the PM slot. To realize the loose fit, the actual dimensions would be slightly smaller than that in electromagnetic design. With the consideration of the tolerance of rotor lamination, the dimensional deviation limits for the magnets are -0.2~0mm in the thickness direction and -0.4~0mm in the radial length direction. As the axial length of the magnets is not critical for the assembly, no tolerance limits are assigned.

Since the nominal size of the PM should be slightly smaller than the theoretical design to ensure that the PMs fit into the PM slot, degradation of the PM excitation will be caused by the smaller PMs, and decrease in the torque output will be expected accordingly. It is better to assess the impact with theoretical analysis prior to the experimental tests, so that the models built are more close to the practical situations.

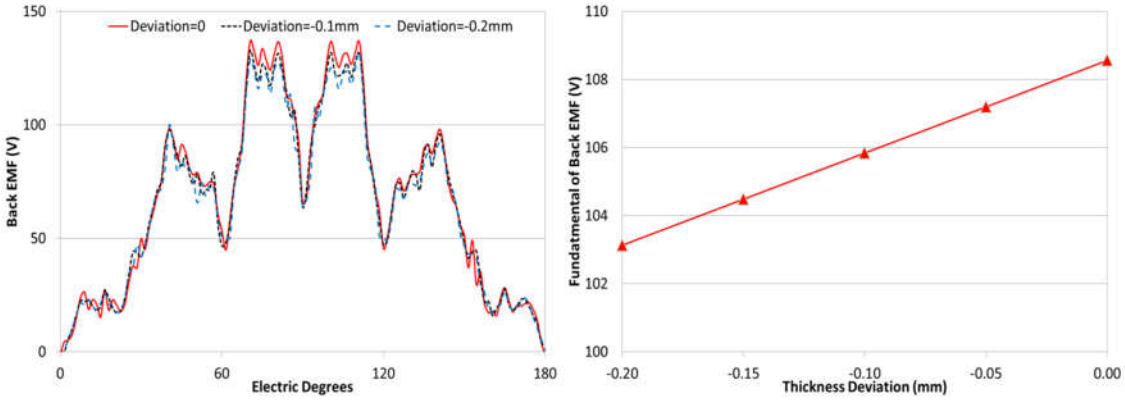

(a) Back EMF waveforms; (b) Fundamental magnitudes;

Figure 6-17 Back EMF waveforms and fundamental magnitudes against thickness deviation of the PMs.

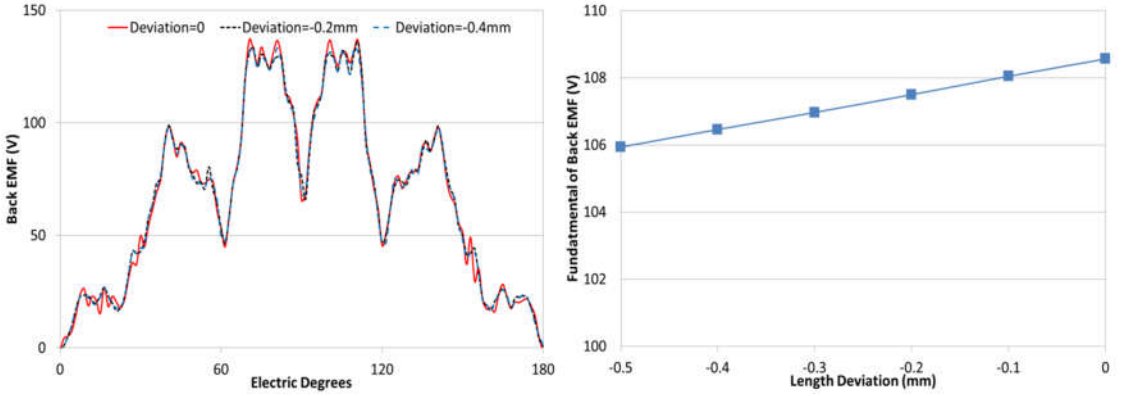

(a) Back EMF waveforms; (b) Fundamental magnitudes;

Figure 6-18 Back EMF waveforms and fundamental magnitudes against length deviation of the PMs.

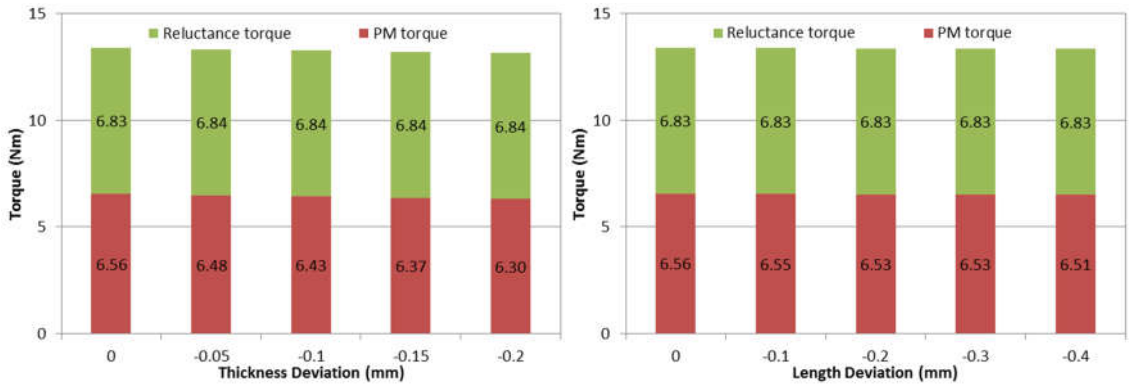

(a) Impact of thickness deviation; (b) Impact of length deviation;

Figure 6-19 Impact of dimensional deviations on torque production.

Figure 6-17 depicts the back EMF waveforms and fundamentals with different thickness deviations. The decrease in back EMF is proportional to the deviations. If the deviation of PM thickness is at the maximum limit of -0.2mm, the fundamental of back EMF will be reduced by 5%. On the other hand, since the length of the PMs is much larger than their thickness, the deviation percentage in length is much smaller and the influence is less sensitive. Even with maximum deviation of -0.4mm, there is only less than 2% of difference in the fundamental component of back EMF, as illustrated in Figure 6-18.

However, the influence over the torque production is much small since a considerable portion of the total torque comes from the rotor reluctance difference between d- and q-axis. As demonstrated in Figure 6-19, the reluctance torque portion keeps almost constant at difference deviations, which means no impact is imposed upon it. Negative effect over PM torque component can be observed in Figure 6-19 due to the weakened PM excitation. As expected, the deviation in thickness causes larger decline in torque. Up to 4% of decrease could occur to the PM torque because of the thickness deviation, which causes less than 2% drop in the overall torque. While in the length direction, the influence is negligible.

6.4.2 Influence of Grinding after Magnetization

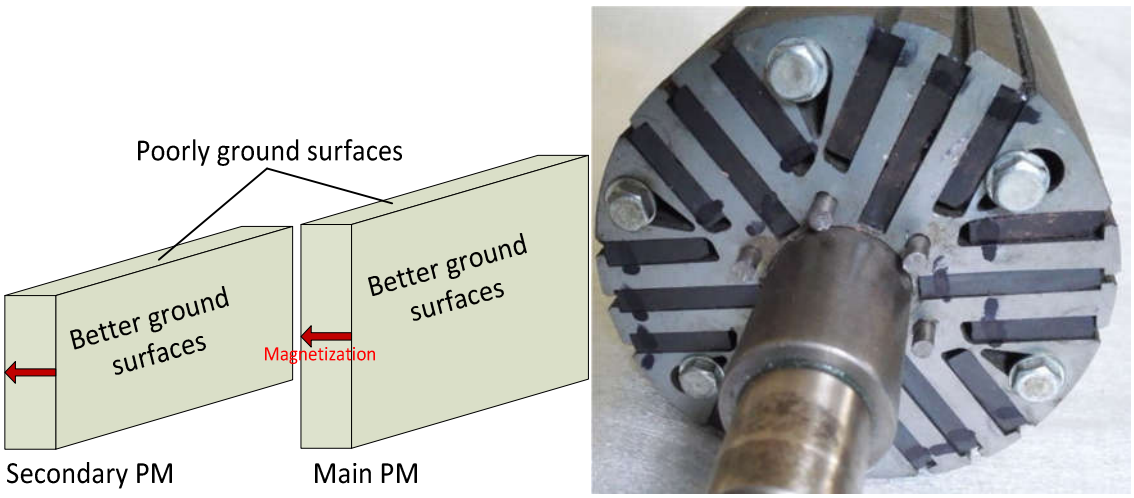

(a) Demonstrations of the ferrite magnets; (b) Rotor with PMs inserted;

Figure 6-20 Demonstration of the magnets and the rotor after insertion of PMs.

Because the quantity of the ferrite magnets ordered is too small for the prototype machine, the some dimensional deviations are beyond the required tolerance limits as claimed. Since the thickness of all the magnets is the same, better grinding is performed on the surfaces perpendicular to the magnetization direction and good precision is achieved. However, the other dimensional deviations are not as well controlled as it is more difficult to grind small surfaces especially in small quantity. Imperfections in magnet edges can be observed in Figure 6-16 (b), and the poorly grounded magnet surfaces are demonstrated in Figure 6-20 (a). The dimension precision in the radial direction is quite critical for assembly, which did cause trouble in this case.

Because there is gap left for the saturation bridge in between the V-shaped magnets, the PM slots for the secondary magnets are actually longer than PMs. Thus it is less critical for the secondary poles and they can fit in the slots. But for the main PMs, the mechanical allowance is still too tight in the radial direction and it is too difficult to press the magnets inside the slots. If the pressing force is increased, there is high chance of breaking the PMs for their low tensile strength. Without any other feasible option, extra grinding work was carried out on the two ends of the magnets in the radial length direction even though the PMs were already magnetized. The rotor with magnets assembled is depicted in Figure 6-20(b), and gaps are visible between the PMs and rotor lamination indicating that very loose clearance fit is applied. As discussed in the previous section, slight deviations for this ferrite IPM have very little effect on the overall loaded performance, particularly in the radial length direction. To ensure the ease of rotor PM assembly, larger allowance should be assigned to the sizes of the PMs and lamination during design process.

Due to the limitation of equipment available in the workshop, part of the main PMs near the ground ends may suffer complete or partial demagnetization because of the heat generated during grinding. This may result in more negative influence over the machine performance, such as loss in back EMF, torque output and harmonics. It is necessary to foresee the possible impact by simulation, and then compare the results with experiments for further analysis. It

is difficult to measure the area and ratio of demagnetization on the PMs, and it is impossible to build a model exactly the same as the actual situation without measure results. However, the effect of the partially demagnetized main PMs can be equivalent to shorter PMs with original magnetization. The major impact caused by the demagnetization is the reduced main PM flux due to the PM degradation, while the airgap flux distribution is decided by the rotor lamination shape and PM slot openings if the total flux is kept the same. Since the total PM flux is approximately proportional to the length of the main PMs, reduced PM length can represent the same impact for simulation.

The influence of the demagnetization caused by extra machining on the open-circuit performances is predicted by FEA and shown in Figure 6-21. The maximum flux density in the air gap keeps almost the same because the flux in this area is decided by the secondary pole length. But the flux density drops with equivalent reduced length in the areas in between the main and secondary poles due to the decreased PM flux. Since the flux distribution waveform is changed, the harmonic contents are different and unwanted harmonics may be incurred. As indicated in Figure 6-21(b), the negative impacts include not only reduced fundamental back EMF but also much higher 3rd order harmonic content. If the equivalent length of the demagnetized area goes up to 2mm each side, the back EMF suffers 7.2% decline in fundamental and over 3 times 3rd harmonic component. Although star connection of the windings can eliminate the 3rd order back EMF, the harmonic flux would increase the core loss.

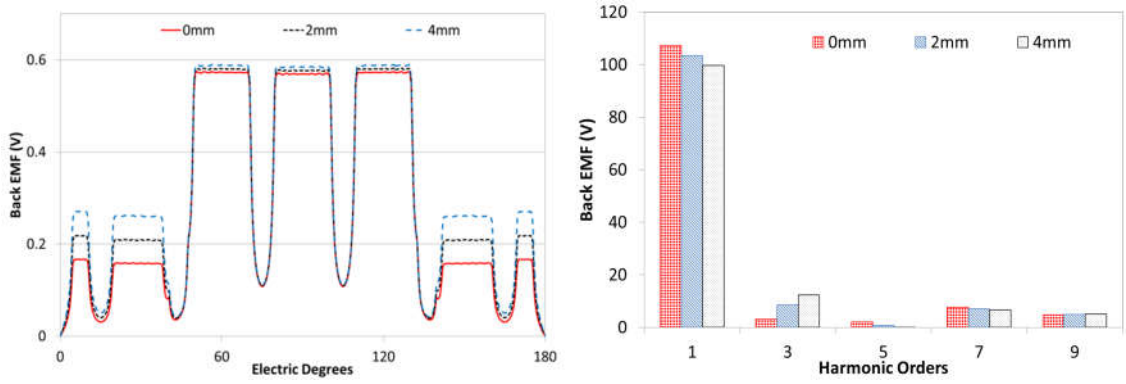

(a) Influence on airgap flux distribution; (b) Influence on back EMF;

Figure 6-21 Influence of reduced main PM length on open-circuit performances.

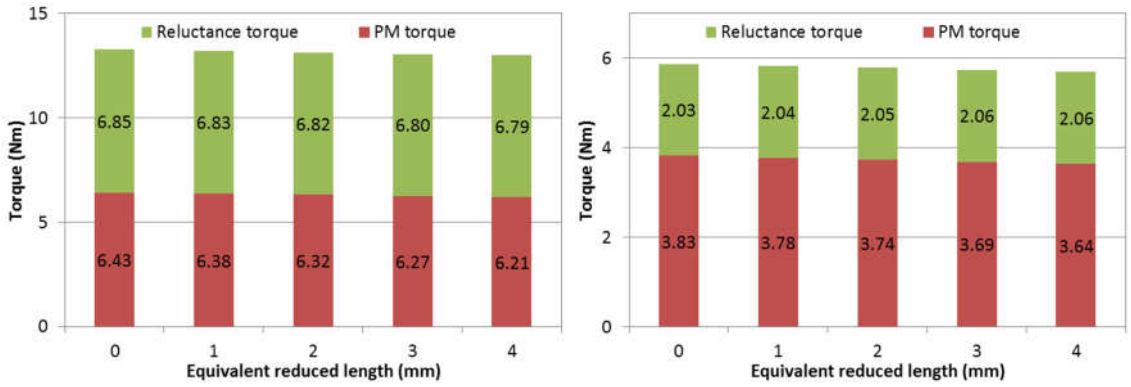

(a) Full load; (b) Half load;

Figure 6-22 Influence of demagnetized main PMs on loaded performances.

Although noticeable influence is observed for the open-circuit performances of the machine, the situation is not as bad under loaded conditions. Because of the saturation, the decrease of the PM excitation is less severe when operating with load. Additionally, the considerable portion of reluctance torque will not be affected, which attenuates the impact on the overall output characteristics. As illustrated in Figure 6-22(a), the overall torque is only decreased by 2% under rated load even with 4mm equivalent demagnetized length. And the torque drops by 2.7% at half rated current, when the major output comes from PM torque. This also reveals an advantage of the proposed ferrite IPM design, and the output can sustain approximately the same level even when minor demagnetization occurs in the PMs.

However, such situation is merely a minor accident during the manufacturing process, and can be completely avoided under mass production by assigning larger mechanical allowance for the design.

6.5 Experimental Validation

6.5.1 Open-Circuit Test

The rig for the back EMF test is illustrated in Figure 6-23. A converter controlled induction machine works as a primary motor, and connects the prototype machine through a coupling. Since the primary machine is for low speed applications, only 300rpm can be achieved for the back EMF testing. The phase

back EMF waveforms and spectra are depicted in Figure 6-24. According to the prediction in the previous section, noticeable third order harmonic is caused by partial demagnetization due to the grinding. To assess the level of demagnetization, the back EMF data from experiment is compared with FEA simulation results. As illustrated in Figure 6-25, good agreement is achieved with equivalent FEA model assuming a length of 5mm in the main PMs has been completely demagnetized. As a result, the fundamental back EMF is 10% lower comparing to ideal machine model, and 3.3 times higher 3rd harmonic appears. Result from analytical method is also compared the tested back EMF, and good agreement is achieved for the fundamental and the harmonics of relatively lower orders, which validated the analytical model of open-circuit.

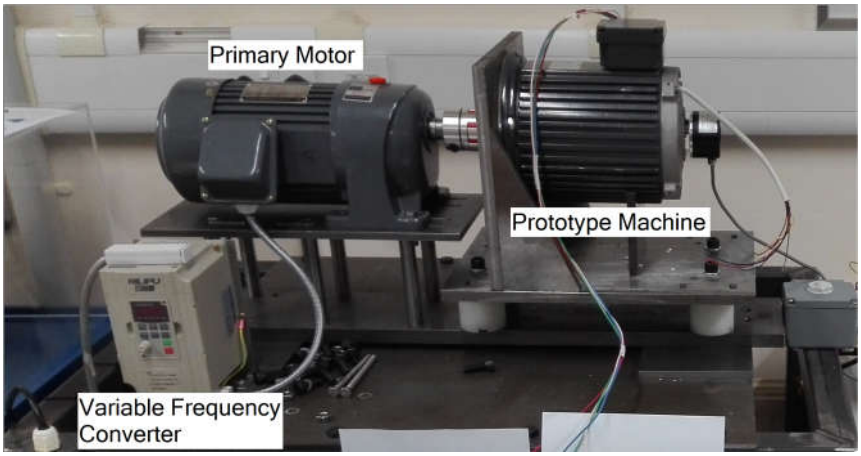

Figure 6-23 Testing rig for back EMF.

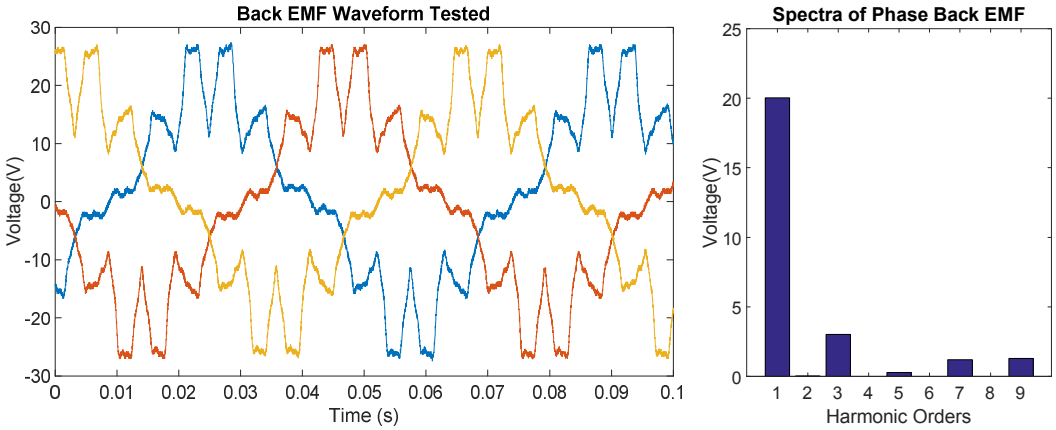

(a) Three phase back EMF waveforms; (b) Spectra;

Figure 6-24 Phase back EMF waveforms and the spectra of the prototype machine at 300rpm.

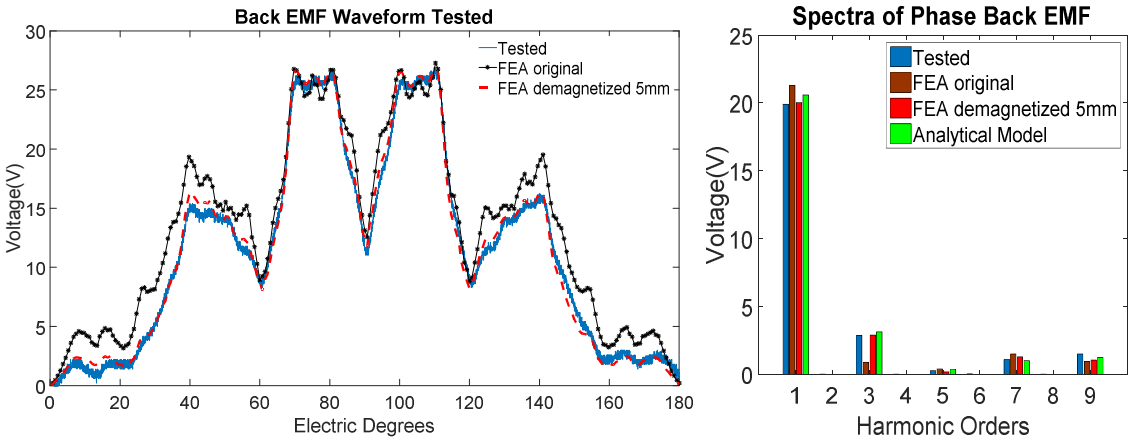

(a) Back EMF waveform comparison; (b) Spectra;

Figure 6-25 Comparisons of phase back EMF waveforms and spectra among tested, FEA and analytical method.

6.5.2 No-Load Test

The prototype machine is firstly tested without connecting any loading to the shaft for the no-load current measurement, and the phase voltage and current are shown in Figure 6-26. The fundamental amplitude of no-load current is only 0.206A, and the no-load loss is 4.6W running at 200rpm. As the fundamental current is very small, the magnitude of spatial harmonics appears to have the similar level with the fundamental, especially 11^{th} and 13^{th} tooth harmonics.

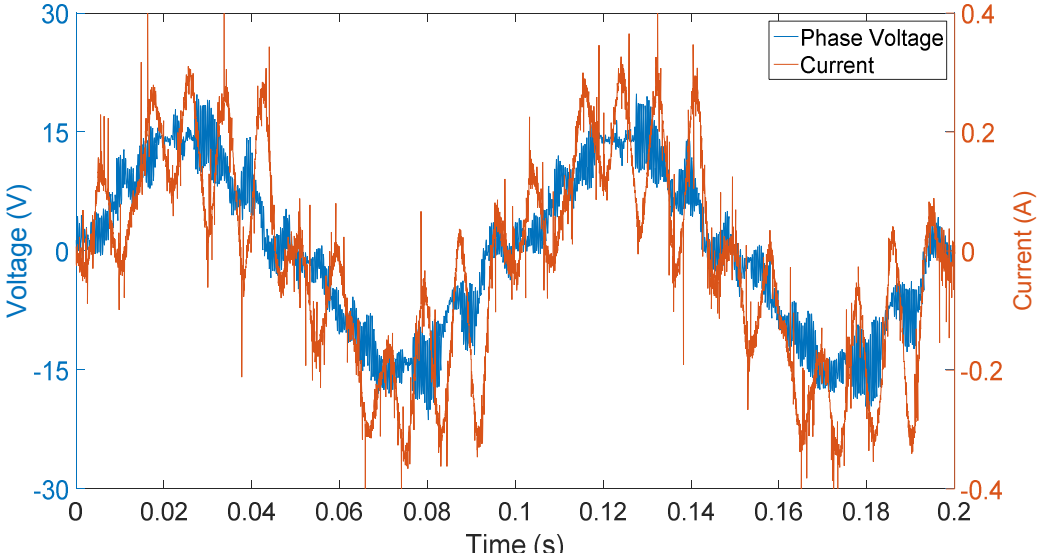

Figure 6-26 No-load phase voltage and current waveforms at 200rpm.

6.5.3 Loaded Test

The setup of the testing rig for loaded experiments is depicted in Figure 6-27. The prototype machine is powered by TI HVDMC Kit. Torque sensor is connected directly to the motor shaft to measure the output torque. Programmable dynamometer is connected to the other side of the torque sensor to provide required loading.

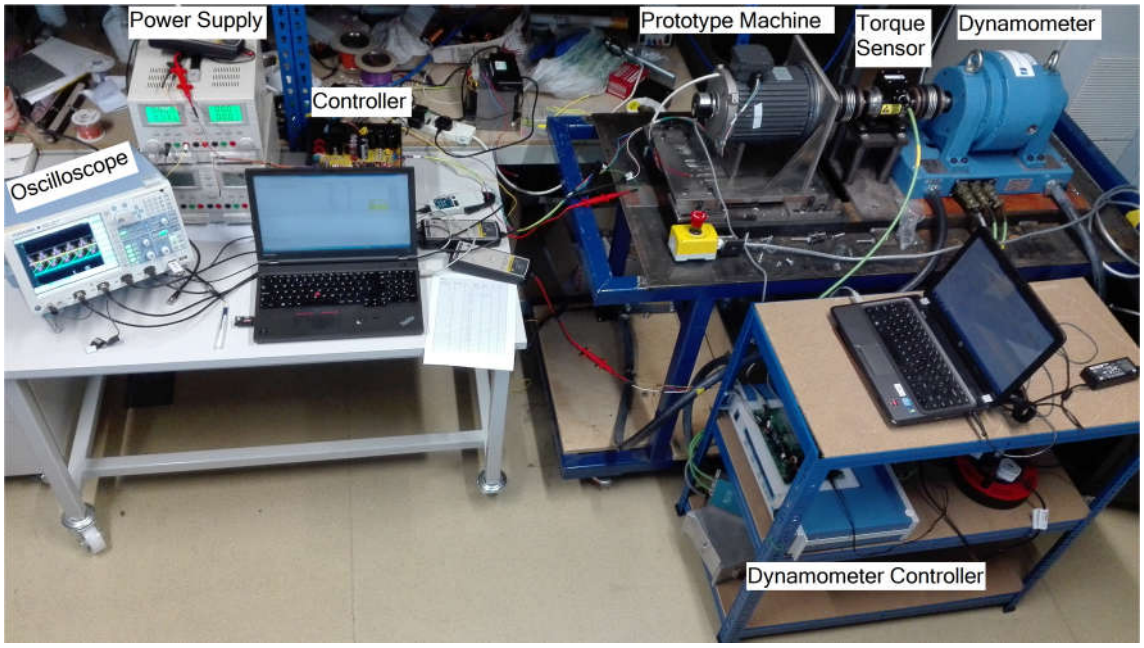

Figure 6-27 Setup of the testing rig.

6.5.3.1 Torque Characteristics

The performance of an electric motor is mainly revealed by its torque characteristics. The generated torque in an IPM motor depends on both the magnitude and phase of the current according to Equation (4-6). Since the prototype machine is designed with large saliency ratio and flux focusing structure, similar portions of reluctance and PM torque will be achieved to for torque enhancement. Thus, relatively large advanced current angle should be expected under loaded operations for harnessing considerable reluctance torque component. To validate the torque curve, the prototype machine is tested with different d-axis current under various loading torque. Lower speed is preferred for the torque tests so as to minimize the influence of core loss and mechanical loss, as they all increase significantly with speed and difficult to

measure directly. On the other hand, the stability of the system reduces at very low speed. As a balance from both sides, rotational speed of 200rpm is chosen for the torque tests, and the impact of mechanical loss and core loss will later be considered based on the no-load test under this speed.

By giving different d-axis current commands to the controller while keeping the amplitude of armature current constant, torque curves against advanced current angle are measured, and the attained results are compared with FEA and analytical models. As illustrated in Figure 6-28 (a) and (b), the amplitudes of the armature current are 5A and 6.2A respectively. Since saturation is ignored in the analytical models, the torque calculated is much higher than the other two as expected. The higher the current is, the larger the difference appears to be. Since the decrease in torque caused by saturation would be proportional to both the two torque components, the analytical models are able to follow the changing trend and approximately predict the optimal current angle. On the other side, the FEA models exhibit good agreement with experiments, with the imperfection in manufacturing and on-load current taken into consideration. It can be noticed that the tested torque is slightly smaller than FEA under lower current angle, and coincides with FEA when negative d-axis current is very high. That may be caused by slightly lower coercivity of the magnet material or slightly lower knee point in the BH curve of the lamination.

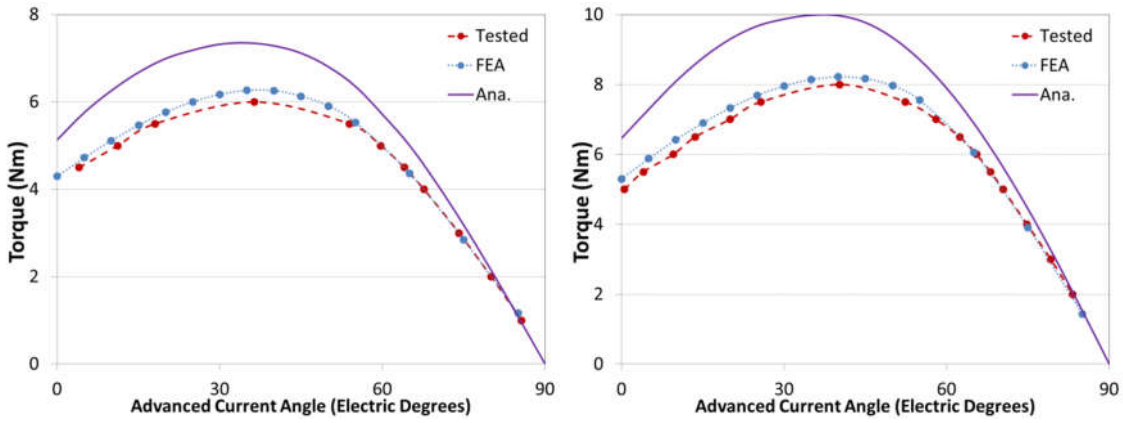

(a) Armature current amplitude of 5A; (b) Armature current amplitude of 6.2A;

Figure 6-28 Torque curve against current angle.

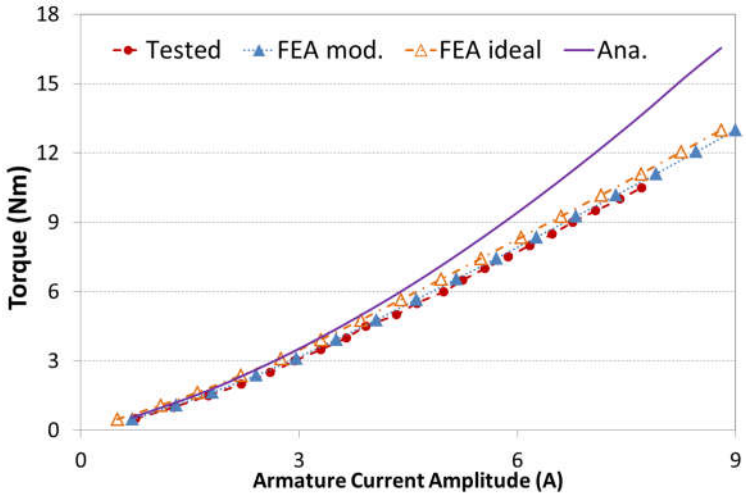

Figure 6-29 Torque output versus current amplitude

Efficiency is also a key indicator for machine performance. It is of special meaning for the prototype machine in the aim of replacing the widely used induction machines in industry. Several control principles have been developed for the motor operations to reduce the loss and improve the performance. Among them the maximum torque-per-ampere current control is one of the most widely used control strategies as the copper loss can be minimized with minimum current. The MTPA algorithm is adopted based on the loss analysis result that copper loss contributes the largest part to the total loss from medium to full loading operation range, will be more effective for efficiency improvement.

The torque-current curve is obtained under MTPA control strategy, and the results from experiment, FEA and analytical models are compared in Figure 6-29. With no saturation taken into account, the torque derived from analytical models becomes much higher than the others under higher loadings, but good accuracy can be achieved at light loading. Since the ideal FEA model is set up in ideal mechanical condition without any frictional torque, the output torque predicted is slightly higher than experiment, and the difference stays approximately constant despite of the increase of the current. By considering the current under no-load in FEA model to compensate the frictional loss, the modified results shows great agreement with the torque tested, which validates the torque capability of the proposed two-layer ferrite design.

Figure 6-30 depicts the phase voltage and current under 3 and 6Nm at 200rpm with MTPA method. As the fundamental current component increases with the load, the current waveforms are much more sinusoidal than no-load, which indicates low harmonic current content. Because the motor is fed by PWM controller inverter, 8k Hz filter is applied to the phase voltage for a clear view. As shown in Figure 6-30(a), the phase angles of voltage and current are almost aligned, indicating high power factor under low load condition. With the increase of output, slightly larger phase shift between voltage and current can be observed in Figure 6-30(b), owing to higher armature reaction and larger reluctance torque component.

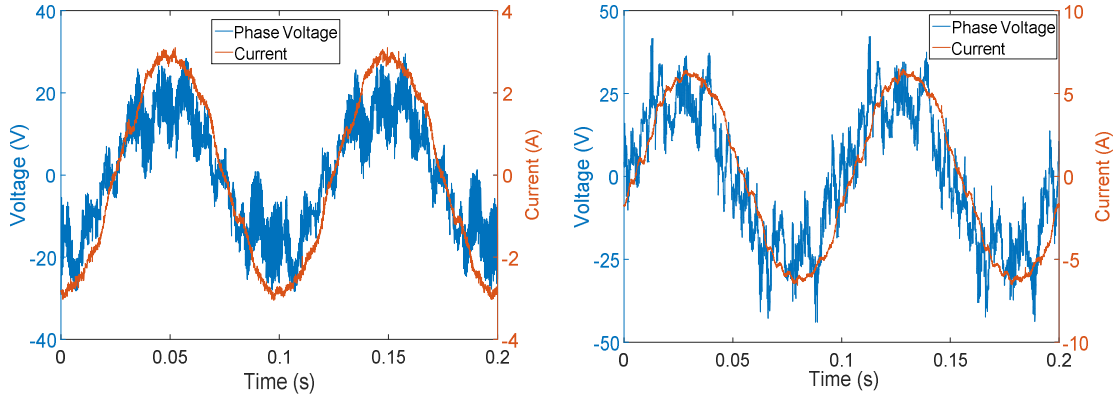

(a) With 3Nm load at 200rpm; (b) With 6Nm load at 200rpm;

Figure 6-30 Phase voltage and current under loaded conditions.

6.5.3.2 Efficiency

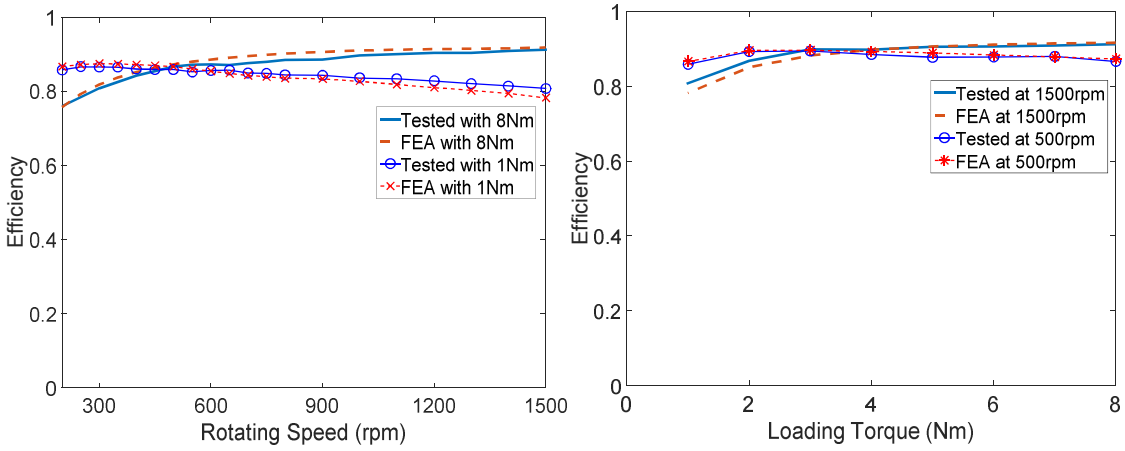

(a) Against rotational speed; (b) Against torque output;

Figure 6-31 Efficiency comparisons between the tested and FEA results.

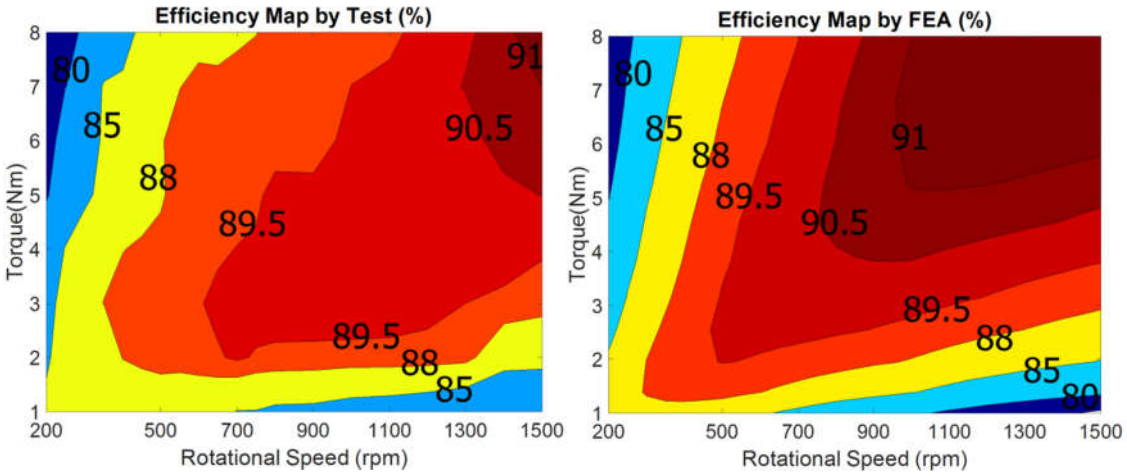

(a) Experimental; (b) FEA simulation;

Figure 6-32 Efficiency maps of experimental and FEA results.

Due to the power limitation of the controller available, the prototype machine is tested from 1-8Nm with maximum speed of 1500rpm for power and efficiency validation. The efficiency of the prototype machine is obtained and compared with FEA model, and good agreement is achieved as illustrated in Figure 6-31 and Figure 6-32.

Figure 6-31(a) depicts the efficiency of experimental and FEA results against rotational speed. Efficiency increases with speed at higher torque loading while decreases during light load. Because copper loss contributes more to the overall losses at high load and can be regarded as constant under such constant torque conditions, the efficiency increases at higher speed when power is increased. On the other hand, core loss dominates at light load and is aggrandized more significantly with speed, resulting decrease of efficiency.

Under constant speed conditions, core loss is far less sensitive to armature current comparing to copper loss, and the mechanical loss is constant. On the other hand, copper is proportional to current square and increase exponentially with load. Thus, at low speed when copper loss takes up contributes to most the overall losses, the motor efficiency decrease with load due to the higher loss increment. However, the efficiency increases with load at rated speed when core loss and mechanical loss take up considerable portion of the total loss whose increment is less significant.

As demonstrated in Figure 6-32, the efficiency of the prototype machine is 0.5-1.5% lower than FEA at relatively high speed and torque operating conditions, and slightly high efficiency is obtained for experiment when the loading torque is small. There are two possible reasons that would contribute to the difference. To simplify the FEA simulation, the armature resistance is calculated at 70°C and set as a constant. But under light load conditions, the temperature rise is very low. Thus, the resistance for simulation is actually higher than actual value, resulting higher copper loss and lower efficiency for the FEA. What's more, since it is too time-consuming to consider PWM signal in FEA simulation, pure sinusoidal current is injected to the windings instead. As a result, the core loss in practical should be higher and the efficiency is lower since the harmonics caused by PWM control is ignored in simulation. Under high speed high torque operation when core loss is serious, larger differences is seen in efficiency.

The fact that the efficiency by test and FEA agrees with each other better under low speed high torque conditions can also be explained based on the theory. Because the core loss is very low and the armature temperature in simulation is closer to that in actual situation within this operational range, the working conditions are quite close to the actual testing environment, and good accuracy is achieved.

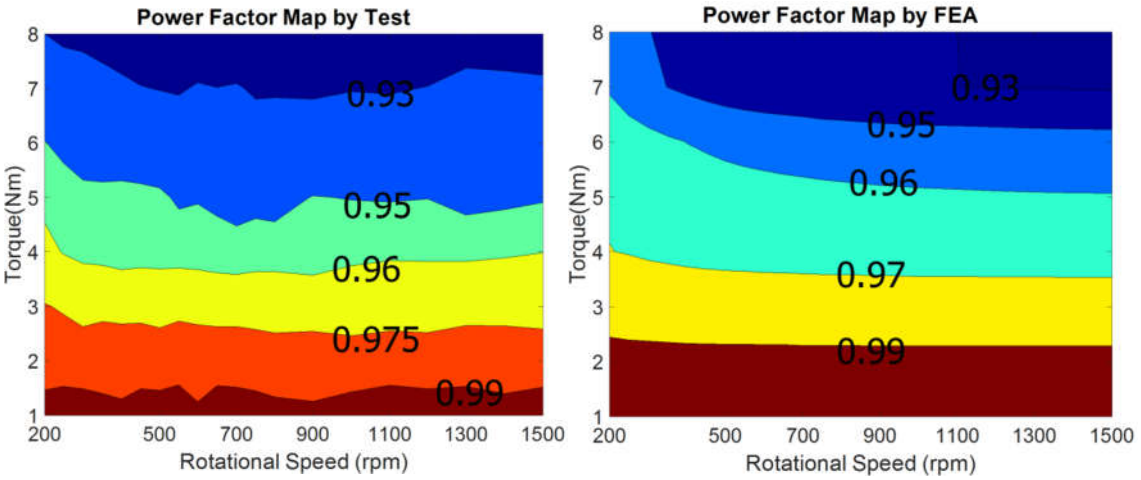

(a) Experimental; (b) FEA simulation;

Figure 6-33 Power factor maps of experimental and FEA results.

6.5.3.3 Power Factor

The power factor maps of tested and FEA result of the prototype machine are illustrated in Figure 6-33. In all, relatively high power factor is achieved by the proposed design. The experimental validation confirms the prediction obtained from FEA simulation, though minor difference exists due to the inevitable errors caused by imperfection in testing environment and measurement equip precisions. In all, the prototype achieves very high power factor because of the high PM excitation. The power factor decreases gradually with the increase of loading torque as predicted, owing to the increased armature reaction.

6.6 Conclusion

Comprehensive comparisons of the performances between the proposed ferrite PM machine and a commercial IM are carried out at first. The same stator lamination geometry and housing assembly are used for both of the two machines. Despite the winding arrangements are different, the amount of copper wires and stator copper loss at rated condition are kept the same to set the basis for performance comparisons. The proposed ferrite PM machine exhibits great superiority to the IM in terms of torque capability, power density, efficiency and power factor below the rated speed. It's noteworthy that ferrite PM achieves 38% higher torque density, 3-4% higher efficiency as well as much higher power factor. Even when the operational speed reaches twice the rated at 3000rpm, the ferrite PM still holds some advantages over the IM in the overall performances. The only disadvantage of the proposed ferrite PM to the IM is the poorer flux weakening ability owing to the large amount of PM materials used. The cost of materials is estimated based on the market price, and the cost of the ferrite machine can be regarded as similar to that of IMs since no expensive material is used. A prototype machine is built and tested under various working conditions. The testing results validate the design by both the analytical and FEA methods, confirm superior overall performances over the commercial IM, and reveal great potential market for various applications for both industrial and domestic use.

7 CONCLUSION AND FUTURE WORK

The work done in this research project is summarized with the outcomes and findings outlined. The overall conclusions and possible future works are presented in this chapter.

7.1 Conclusions

The thesis proposed a multi-layer spoke-type IPM configuration with ferrite magnets. The investigations were mainly focused on the systematic design, optimization and demagnetization of the proposed ferrite machine. Furthermore, performance comparisons were carried out with a commercial induction machine, and confirmed the advantages of the multi-layer spoke-type ferrite design as a potential and practical solution to meet the requirements of low cost and high performance with the merits of high torque density, outstanding power factor and excellent efficiency. Finally, a prototype machine is built and tested, and the performance of the proposed design is comprehensively validated under various operating conditions.

7.1.1 Multi-Layer Configurations

Spoke-type configurations and PMASynRMs appeared to be the most potential candidates for low-cost high-performance ferrite PM machines in the literature [77,80,88,93,114,175,176]. Spoke-type IPMs used flux focusing structure, and were able to achieved similar PM flux field with rare-earth machines and high PM torque. PMASynRMs obtained high saliency ratio and harness high reluctance torque. By introducing multiple flux barrier concept of PMASynRM into the flux-focusing spoke-type machine, better trade-off between PM torque and reluctance torque can be met, and a most promising multi-layer spoke-type structure was possible to achieve better torque density due to high PM flux density and excellent rotor saliency.

7.1.2 Analytical Models

Analytical models were developed based on equivalent magnetic circuit theory for simpler modelling and good accuracy. The derived models showed good

accuracy comparing with FEA models under light load condition with errors within 2% as shown in Figure 3-23 and Figure 3-43. Since the saturation was not considered in analytical model, considerate difference existed in the value of torque output between analytical and FEA models. But the influence of the key design parameters and trend of torque profiles against current angle can be well predicted, which can provide helpful insight into the design and optimization of multi-layer machines.

As for the one-layer configuration, longer PMs were always preferable because of higher PM flux distribution and little impact on saliency. Wider PM can surely increase the PM torque, but too wide PMs would deteriorate saliency ratio. Since the one-layer structure has high PM torque, wider PMs could still increase torque density.

The flux distribution of two-layer models was much more complicated because of the introduction of secondary layers. The main poles of the two-layer structure showed similar function with PMs in the one-layer one, concentrating PM flux. The secondary layers could modify the flux distribution in different area of rotor surface with more sinusoidal airgap flux distribution. Furthermore, the rotor saliency was also greatly affected by the location of the secondary poles, and the torque density can be enhanced by optimal design of the secondary PM layers.

7.1.3 Design of Multi-Layer Ferrite Machine

The influence of key design parameters on the machine performance is comprehensively investigated based on the analytical models derived in Chapter 3. The individual parameter as well as their interactions is also discussed to provide insightful guidelines for the design of multi-layer spoke-type machines.

Since the one-layer configuration relies highly on PM torque, large amount of PMs usually can increase the torque output. Though wider PMs deteriorate rotor saliency, higher increment in PM torque is gained. The ratio of PM length over pole pitch reflects the flux focusing effect, which is crucial for the one-layer

structure. Thus designs with higher pole number are able to achieve higher torque output. However, larger pole number also brings about issues of significant increase in iron loss and higher manufacturing requirements.

By introducing secondary magnet layers, the flux distribution waveform can be greatly improved for the two-layer configurations with lower harmonic contents. In the meantime, the rotor saliency is also significantly intensified. Due to the increased contribution of reluctance torque, larger amount of PM doesn't necessarily mean higher overall torque output. Thus, finding the optimal compromise between PM torque and reluctance torque is essential for two-layer structures to achieve higher torque density.

With more magnet layers applied, the reluctance torque of the three-layer configuration can be further improved. But the flux-focusing effect is weakened with more PM layers, and the improvement in overall torque is less than 1%. However, the rotor structure becomes more complicated, which is not practical considering the manufacturing cost.

It should be noted that iron loss increase with the number of PM layers. Thus, the two-layer design is able to achieved better overall efficiency. Despite the loss of the one-layer machine is the lowest, its power density is about 10% lower than the other two. Furthermore, the multi-layer designs show more advantageous performance at higher working temperatures due to larger reluctance torque component. In all, the two-layer design is able to deliver much higher torque than one-layer one with much simpler rotor structure than three-layer structure, appears to be the best solution for low cost high performance ferrite IPMs.

7.1.4 Investigation on Demagnetization

Owing to the disadvantage of much lower magnetic strength, there is higher risk of demagnetization for ferrite magnets facing strong armature reactive field. The influence of the three key factors, namely demagnetizing MMF, coercivity, and operating temperature, are investigated to reveal the demagnetization mechanism for the one- and two-layer configurations.

The d-axis MMF opposes directly the initial PM magnetization, and is main cause of demagnetization. Since the one-layer design has thicker PM poles, it can withstand higher d-axis negative current. Q-axis reactive field gives rise to saturation in the lamination, and reduces the threshold of d-axis current to cause large-scale degradation in the PMs. Because of higher saturation in the rotor, the two-layer design exhibits higher cross-coupling effect.

Ferrite magnets are more fragile to demagnetization under low temperature. Since the motor will be heated up very quickly under continuous load, the most critical scenario is during the starting process at cold environmental temperature. Higher grade ferrite materials can always improve the demagnetization performances, but it is not cost-effective due to the higher price. Based on the understanding of the demagnetization mechanism, modifications of the rotor design is able to improve the performance towards demagnetizing field with on extra costs. Deeper PM insertion method is proved to be an effective way to reduce the risk of demagnetization for both one- and two-layer designs. The proposal of inner PM slot bridge can increase the anti-demagnetization ability greatly with no adverse impact for the two-layer design because of its distinctive flux distribution in the rotor, but is not applicable to one-layer design as PM flux leakage is increased significantly.

7.1.5 Validation of the Proposed Two-layer Configuration

The main aim of this research work is to provide practical solutions for low-cost high-performance designs to replace the widely installed IMs in industry. The performance of a commercial induction machine is compared with the proposal two-layer spoke-type ferrite IPM machine. Despite of slightly poorer flux weakening ability, the proposed ferrite design exhibits great superiority to the IM in performance under nominal operating conditions, with 27% higher torque density, 3-4% higher efficiency and much higher power factor. Although the estimated overall cost for the ferrite machine is 15% higher, the per kilowatt cost is actually 18% lower than the IM, which indicates comparable price with better performance for various domestic and industrial applications. And with thorough

experimental validation of the prototype machine carried out, the advantageous performance is confirmed.

7.2 Future Work

1. Since there is still noticeable difference between the analytical methods and actual machine performances under heavy loading conditions, improvements can be made by using empirical coefficients for the influences of saturations and flux leakage based on extensive FEA simulation and experimental results. Hence, the accuracy and complexity can be further improved for the complete design of multi-layer ferrite IPM machines.
2. Since there is large amount of ferrite materials inserted inside the machine rotor with very long PM poles, only very thin connection in the rotor is left to hold the whole rotor together. And sometimes even modular rotor designs are used with rotor part completely disconnected. Thus, it is of great importance to investigate the mechanical design of the rotor especially under high speed applications.
3. Due to the high saliency ratio, the torque ripple of the multi-layer configurations is relatively high. In order to extend the usage of ferrite PM machines to the applications with higher torque requirements, it is of great importance to improve the design to reduce the torque ripple.
4. To reduce the cost of overall drive system for ferrite IPM machines, low cost controller should also be developed accordingly, for example using single resistor current sampling and sensorless control to further reduce the cost of the whole system. Since the harmonic contents under light load conditions are relatively high, improvements should be made to extract useful information from the current feedback.
5. Owing to the inherent demagnetization property of ferrite materials, the load capacity would be strictly limited concerning the high risk of demagnetization under very low working temperature. Although the temperature will rise eventually because of the machine losses, it will of interest to deliberately increase the core loss by control strategy or apply

heating accessory to quicken the temperature rise during cold starting process.

6. To ensure the safe operation of the ferrite IPM, it is important to monitor the temperature of the ferrite magnets to avoid large current under cold or overheating working conditions. Since the magnets are in the spinning rotor, the difficulties lie in the applications of contactless temperature sensing and data transmission in the high electromagnetic interference environment.

REFERENCES

[1] P. Waide and C.U. Brunner, *Energy efficiency policy opportunities for electric motor-driven systems*, 2011.

[2] A.T. de Almeida, F.J.T.E. Ferreira, and G. Baoming, “Beyond Induction Motors—Technology Trends to Move Up Efficiency,” *IEEE Transactions on Industry Applications* , vol. 50, pp. 2103–2114, 2014.

[3] A. Boglietti, A. Cavagnino, and S. Vaschetto, “Induction motor EU standards for efficiency evaluation: The scenario after IEC 60034-2-1,” *37th Annual Conference on IEEE Industrial Electronics Society (IECON)*, pp. 2786–2791, 2011.

[4] Y. Guan, Z.Q. Zhu, I.A.A. Afinowi, J.C. Mipo, and P. Farah, “Comparison between induction machine and interior permanent magnet machine for electric vehicle application,” *17th International Conference on Electrical Machines and Systems (ICEMS)*, pp. 144–150*,* 2014.

[5] V.T. Buyukdegirmenci, A.M. Bazzi, and P.T. Krein, “Evaluation of Induction and Permanent-Magnet Synchronous Machines Using Drive-Cycle Energy and Loss Minimization in Traction Applications,” *IEEE Transactions on Industry Applications*, vol. 50, pp. 395–403, 2014.

[6] D.T. Peters, J.G. Cowie, E.F. Brush, and D.J. Van Son, “Copper in the squirrel cage for improved motor performance,” *IEEE International Electric Machines and Drives Conference (IEMDC’03),* vol. 2, pp. 1265–1271 , 2003.

[7] Y. Liu, P. Han, and A.M. Bazzi, “A comparison of rotor bar material of squirrel-cage induction machines for efficiency enhancement purposes,” *17th European Conference on Power Electronics and Applications (EPE’15 ECCE-Europe)*, 2015, pp. 1–7*, 2015*.

[8] B. Fahimi and S. Pekarek, “Design and control of electric machines utilizing a field reconstruction method,” *36th Annual Conference on IEEE Industrial Electronics Society (IECON)*, pp. 1–2, 2010.

[9] D.G. Dorrell, “The challenges of meeting IE4 efficiency standards for induction and other machines,” *IEEE International Conference on Industrial Technology (ICIT)*, pp. 213–218*,* 2014.

[10] E.B. Agamloh and A. Cavagnino, “High efficiency design of induction machines for industrial applications,” *IEEE Workshop on Electrical Machines Design Control and Diagnosis (WEMDCD)*, pp. 33–46*, 2013*.

[11] G. Bramerdorfer, S. Silber, G. Weidenholzer, and W. Amrhein, “Comprehensive cost optimization study of high-efficiency brushless synchronous machines,” *IEEE International Electric Machines & Drives Conference (IEMDC)*, pp. 1126–1131*,* 2013.

[12] E. Richter, T.J.E. Miller, T.W. Neumann, and T.L. Hudson, “The Ferrite

Permanent Magnet AC Motor--A Technical and Economical Assessment," *IEEE Transactions on Industry Applications,* vol. IA-21, pp. 644–650, 1985.

[13] K.T. Chau, C.C. Chan, and C. Liu, "Overview of Permanent-Magnet Brushless Drives for Electric and Hybrid Electric Vehicles," *IEEE Transactions on Industrial Electronics*, vol. 55, pp. 2246–2257, 2008.

[14] S. Javadi and M. Mirsalim, "Design and Analysis of 42-V Coreless Axial-Flux Permanent-Magnet Generators for Automotive Applications," *IEEE Transactions on Magnetics,* vol. 46, pp. 1015–1023, 2010.

[15] E. Sulaiman, T. Kosaka, and N. Matsui, "High Power Density Design of 6-Slot-8-Pole Hybrid Excitation Flux Switching Machine for Hybrid Electric Vehicles," *IEEE Transactions on Magnetics,* vol. 47, pp. 4453–4456, 2011.

[16] Z.Q. Zhu and D. Howe, "Electrical Machines and Drives for Electric, Hybrid, and Fuel Cell Vehicles," *Proceedings of the IEEE*, vol. 95, pp. 746–765, 2007.

[17] N. Hashemnia and B. Asaei, "Comparative study of using different electric motors in the electric vehicles," *18th International Conference on Electrical Machines (ICEM 2008)*, pp. 1–5, 2008.

[18] I. Boldea, L.N. Tutelea, L. Parsa, and D. Dorrell, "Automotive Electric Propulsion Systems With Reduced or No Permanent Magnets: An Overview," *IEEE Transactions on Industrial Electronics,* vol. 61, pp. 5696–5711, 2014.

[19] D. Dorrell, L. Parsa, and I. Boldea, "Automotive Electric Motors, Generators, and Actuator Drive Systems With Reduced or No Permanent Magnets and Innovative Design Concepts," *IEEE Transactions on Industrial Electronics,* vol. 61, pp. 5693–5695, 2014.

[20] S. Morimoto, Y. Asano, T. Kosaka, and Y. Enomoto, "Recent technical trends in PMSM," *2014 International Power Electronics Conference (IPEC-Hiroshima 2014 - ECCE-ASIA),* pp. 1997–2003, 2014.

[21] C.U. Brunner, P. Waide, and M. Jakob., "Harmonized Standards for Motors and Systems Global progress report and outlook," *7th International Conference EEMODS*, 2011.

[22] C.C. Chan, "An overview of electric vehicle technology," *Proceedings of the IEEE*, vol. 81, pp. 1202–1213, 1993.

[23] J.E. Gould, "Permanent magnets," *Proceedings of the Institution of Electrical Engineers,* vol. 125, pp. 1137–1151, 1978.

[24] U.S. Deshpande, "Recent advances in materials for use in permanent magnet machines-a review," *IEEE International Electric Machines and Drives Conference (IEMDC'03),* vol. 1, pp. 509–515, 2003.

[25] S. Zhang, J. Xu, J. Junak, D. Fiederling, G. Sawczuk, M. Koch, A. Schalja, M. Podack, and J. Baumgartner, “Permanent magnet technology for electric motors in automotive applications,” *2012 2nd International Electric Drives Production Conference (EDPC),* pp. 1–11, 2012.

[26] E. Grant and L.M. Roszyk, “Design Consideration for Permanent Magnet Motors in Appliance Applications,” vol. I, 1968.

[27] T.W. Nehl, F.A. Fouad, and N.A. Demerdash, “Digital simulation of power conditioner-machine interaction for electronically commutated DC permanent magnet machines,” *IEEE Transactions on Magnetics,* vol. 17, pp. 3284–3286, 1981.

[28] F.A. Fouad, T.W. Nehl, and N.A. Demerdash, “Permanent magnet modeling for use in vector potential finite element field analysis in electrical machinery,” *IEEE Transactions on Magnetics,* vol. 17, pp. 3002–3004, 1981.

[29] E. Richter, T.J.E. Miller, T.W. Neumann, and T.L. Hudson, “The Ferrite Permanent Magnet AC Motor---A Technical and Economical Assessment,” *IEEE Transactions on Industry Applications,* vol. IA-21, pp. 644–650, 1985.

[30] H.R. Bolton, Y.D. Liu, and N.M. Mallinson, “Investigation into a class of brushless DC motor with quasisquare voltages and currents,” *IEE Proceedings Electric Power Applications,* vol. 133, pp. 103–111, 1986.

[31] E. Richter and T. Neumann, “Line start permanent magnet motors with different materials,” *IEEE Transactions on Magnetics,* vol. 20, pp. 1762–1764, 1984.

[32] A. Fasolo, L. Alberti, and N. Bianchi, “Performance Comparison Between Switching-Flux and IPM Machines With Rare-Earth and Ferrite PMs,” *IEEE Transactions on Industry Applications,* vol. 50, pp. 3708–3716, 2014.

[33] E.E. Montalvo-Ortiz, S.N. Foster, J.G. Cintron-Rivera, and E.G. Strangas, “Comparison between a spoke-type PMSM and a PMASynRM using ferrite magnets,” *2013 IEEE International Electric Machines & Drives Conference (IEMDC)*, pp. 1080–1087*,* 2013.

[34] E. Carraro, M. Degano, M. Morandin, and N. Bianchi, “PM synchronous machine comparison for light electric vehicles,” *2014 IEEE International Electric Vehicle Conference (IEVC),* pp. 1–8, 2014.

[35] S.B. Bhat, S.P. Nikam, and B.G. Fernandes, “Design and analysis of ferrite based permanent magnet motor for electric assist bicycle,” *2014 International Conference on Electrical Machines (ICEM)*, pp. 106–111*,* 2014.

[36] S.-J. Lee, S.-I. Kim, J.-P. Hong, B.-Y. Song, and J.-W. Park, “Characteristic analysis of the water pump motor considering polar

anisotropie ferrite bonded magnet," *2010 International Conference on Electrical Machines and Systems (ICEMS),* pp. 1242–1245, 2010.

[37] R.K. Gupta and N. Mohan, "A Three-Phase Permanent Magnet Brushless DC Motor for Low-Power Low-Speed Fan Applications - Optimizing Cost and Efficiency," *Conference Record of the 2007 IEEE Industry Applications Conference Annual Meeting*, pp. 846–852, 2007.

[38] S.K. Pal, "Comparative study of the design and manufacturing processes of electrical motors with low and high energy permanent magnets," *Sixth International Conference on Electrical Machines and Drives,* pp. 339–346*, 1993*.

[39] P. Sekerak, V. Hrabovcova, J. Pyrhonen, S. Kalamen, P. Rafajdus, and M. Onufer, "Comparison of Synchronous Motors With Different Permanent Magnet and Winding Types," *IEEE Transactions on Magnetics,* vol. 49, pp. 1256–1263, 2013.

[40] A.M. Mihai, S. Benelghali, L. Livadaru, A. Simion, and R. Outbib, "FEM analysis upon significance of different permanent magnet types used in a five-phase PM generator for gearless small-scale wind," *Electrical Machines (ICEM), 2012 XXth International Conference on*, pp. 267–273, 2012.

[41] S. Laurit, A. Kallaste, T. Vaimann, and A. Belahcen, "Cost efficiency analysis of slow-speed slotless permanent magnet synchronous generator using different magnetic materials," *Electric Power Quality and Supply Reliability Conference (PQ)*, pp. 221–224*,* 2014.

[42] G.-C. Lee and T.-U. Jung, "Design comparisons of BLDC motors for electric water pump," *IEEE Vehicle Power and Propulsion Conference (VPPC),* pp. 48–50, 2012.

[43] J.A. Krizan and S.D. Sudhoff, "Theoretical performance boundaries for permanent magnet machines as a function of magnet type," *2012 IEEE Power and Energy Society General Meeting,* pp. 1–6, 2012.

[44] K.H. Kim, H.I. Park, S.M. Jang, D.J. You, and J.Y. Choi, "Comparative Study of Electromagnetic Performance of High-Speed Synchronous Motors with Rare-Earth and Ferrite Permanent Magnets," *IEEE Transactions on Magnetics*, pp. 1, 2016.

[45] S.-M. Jang, H.-J. Seo, Y.-S. Park, H.-I. Park, and J.-Y. Choi, "Design and Electromagnetic Field Characteristic Analysis of 1.5 kW Small Scale Wind Power Generator for Substitution of Nd-Fe-B to Ferrite Permanent Magnet," *IEEE Transactions on Magnetics,* vol. 48, pp. 2933–2936, 2012.

[46] P. Sekerak, V. Hrabovcova, M. Onufer, L. Kaiamen, and P. Rafajdus, "Synchronous motors with different PM materials," *ELEKTRO,* pp. 241–246, 2012.

[47] D.-K. Woo, D.-K. Lim, H.-K. Yeo, J.-S. Ro, and H.-K. Jung, "A 2-D Finite-

Element Analysis for a Permanent Magnet Synchronous Motor Taking an Overhang Effect Into Consideration," *IEEE Transactions on Magnetics,* vol. 49, pp. 4894–4899, 2013.

[48] H.-C. Kim and T.-U. Jung, "Analysis of rotor overhang effect considering load torque variance in automobile BLDC fan motor," *IEEE Vehicle Power and Propulsion Conference (VPPC),* pp. 68–71, 2012.

[49] H.-S. Chang and S.-H. Baek, "Finite element analysis of an anisotropic ferrite bonded magnet for BLDC motor design," *Proceedings of the Fifth International Conference on Electrical Machines and Systems (ICEMS)*, vol. 2, pp. 1170–1173 vol.2, 2001.

[50] S.-J. Lee, J.-J. Lee, J.-P. Hong, B.-Y. Song, and J.-W. Park, "Magnetic field analysis of polar anisotropic ferrite bonded magnet to outer rotor type brushless dc motor considering magnetizing process," *14th Biennial IEEE Conference on Electromagnetic Field Computation (CEFC)*, pp. 1*,* 2010.

[51] I.-S. Jung, H.-G. Sung, Y.-D. Chun, and J.-H. Borm, "Magnetization modeling of a bonded magnet for performance calculation of inner-rotor type BLDC motor," *IEEE Transactions on Magnetics, v*ol. 37, pp. 2810–2813, 2001.

[52] I. Petrov and J. Pyrhonen, "Performance of Low-Cost Permanent Magnet Material in PM Synchronous Machines," *IEEE Transactions on Industrial Electronics,* vol. 60, pp. 2131–2138, 2013.

[53] I. Petrov, M. Polikarpova, and J. Pyrhonen, "Rotor surface ferrite magnet synchronous machine for generator use in a hybrid application — Electro-magnetic and thermal analysis," *39th Annual Conference of the IEEE Industrial Electronics Society (IECON)*, pp. 3090–3095, 2013.

[54] R. Qu and T.A. Lipo, "Dual-rotor, radial-flux, toroidally wound, permanent-magnet machines," *IEEE Transactions on Industry Applications,* vol. 39, pp. 1665–1673, 2003.

[55] S. Zeze, T. Todaka, and M. Enokizono, "Improvement of rotor structure of concentrated surface permanent magnet synchronous motor," *International Conference on Electrical Machines and Systems, (ICEMS)*, pp. 1–6, 2009.

[56] Y. Shen and Z.Q. Zhu, "Analysis of Electromagnetic Performance of Halbach PM Brushless Machines Having Mixed Grade and Unequal Height of Magnets," *IEEE Transactions on Magnetics,* vol. 49, pp. 1461–1469, 2013.

[57] H. Kim, Y.-M. You, and B. Kwon, "Rotor Shape Optimization of Interior Permanent Magnet BLDC Motor According to Magnetization Direction," *IEEE Transactions on Magnetics,* vol. 49, pp. 2193–2196, 2013.

[58] Y.-H. Im, S.-I. Hwang, S.-M. Jang, J.-Y. Choi, and J.-H. Choi, "Analysis of Torque Pulsation Considering Interior Permanent Magnet Rotor Rib

Shape Using Response Surface Methodology," *IEEE Transactions on Magnetics,* vol. 48, pp. 979–982, 2012.

[59] B.K. Chaudhari, B.G. Fernandes, and S.K. Pillai, "A new hybrid rotor geometry for permanent magnet synchronous motor," *Proceedings of International Conference on Power Electronic Drives and Energy Systems for Industrial Growth,* vol. 1, pp. 260–263 *1998.*

[60] B.N. Chaudhari and B.G. Fernandes, "Permanent magnet synchronous motor for general purpose energy efficient drive," *IEEE Power Engineering Society Winter Meeting,* vol. 1, pp. 213–218 vol.1 *2000.*

[61] E. Richter and T. Neumann, "Line start permanent magnet motors with different materials," *IEEE Transactions on Magnetics,* vol. 20, pp. 1762–1764, 1984.

[62] L. Fang, B.H. Lee, J.J. Lee, H.J. Kim, and J.-P. Hong, "Study on high-efficiency characteristics of interior permanent magnet synchronous motor with different magnet material," *International Conference on Electrical Machines and Systems (ICEMS)*, pp. 1–4, 2009.

[63] R. Vartanian, H.A. Toliyat, B. Akin, and R. Poley, "Power factor improvement of synchronous reluctance motors (SynRM) using permanent magnets for drive size reduction," *Twenty-Seventh Annual IEEE Applied Power Electronics Conference and Exposition (APEC),* pp. 628–633, *2012*.

[64] J.X. Shen, S. Cai, H. Shao, and H. Hao, "Evaluation of low-cost high-performance synchronous motors for ventilation application," *2015 International Conference on Sustainable Mobility Applications, Renewables and Technology (SMART)*, 2015, pp. 1–6.

[65] Y. Wang, D.M. Ionel, M. Jiang, and S.J. Stretz, "Establishing the Relative Merits of Synchronous Reluctance and PM Assisted Technology Through Systematic Design Optimization," *IEEE Transactions on Industry Applications*, vol. PP, p. 1, 2016.

[66] E. Armando, P. Guglielmi, M. Pastorelli, G. Pellegrino, and A. Vagati, "Performance of IPM-PMASR Motors with Ferrite Injection for Home Appliance Washing Machine," *IEEE Industry Applications Society Annual Meeting (IAS)* pp. 1–6, 2008.

[67] R. Vartanian, Y. Deshpande, and H.A. Toliyat, "Performance analysis of a ferrite based fractional horsepower permanent magnet assisted SynRM for fan and pump applications," *IEEE International Electric Machines & Drives Conference (IEMDC)*, pp. 1405–1410*,* 2013.

[68] R. Vartanian, Y. Deshpande, and H.A. Toliyat, "Performance analysis of a rare earth magnet based NEMA frame Permanent Magnet assisted Synchronous Reluctance Machine with different magnet type and quantity," *IEEE International Electric Machines & Drives Conference (IEMDC)*, pp. 476–483*,* 2013.

[69] D. Prieto, B. Daguse, P. Dessante, and J.-C. Vannier, “Performance comparison of the permanent magnet assisted synchronous reluctance motor and the double magnet synchronous motor,” *15th European Conference on Power Electronics and Applications (EPE)*, pp. 1–7*,* 2013.

[70] M. Barcaro and N. Bianchi, “Interior PM Machines using Ferrite to Replace Rare-Earth Surface PM Machines,” *IEEE Transactions on Industry Applications,* vol. PP, p. 1, 2013.

[71] S. Musuroi, C. Sorandaru, M. Greconici, V.N. Olarescu, and M. Weinman, “Low-cost ferrite permanent magnet assisted synchronous reluctance rotor an alternative solution for rare earth permanent magnet synchronous motors,” *39th Annual Conference of the IEEE Industrial Electronics Society (IECON)*, pp. 2966–2970, 2013.

[72] K. Hayakawa, M. Sanada, S. Morimoto, and Y. Inoue, “Evaluation of IPMSMs with concentrated windings using powder magnets for high torque,” *IEEE 10th International Conference on Power Electronics and Drive Systems (PEDS)*, pp. 735–740*,* 2013.

[73] Y. Matsumoto, I. Miki, and K. Morinaga, “Study on IPMSM with ferrite magnets driven at high speeds,” *International Conference on Electrical Machines and Systems (ICEMS)*, pp. 1064–1067*,* 2013.

[74] M. Obata, S. Morimoto, M. Sanada, and Y. Inoue, “Performance of PMASynRM With Ferrite Magnets for EV/HEV Applications Considering Productivity,” *IEEE Transactions on Industry Applications,* vol. 50, pp. 2427–2435, 2014.

[75] M. Sanada, S. Morimoto, and Y. Inoue, “Development of high-power PMASynRM using ferrite magnets for reducing rare-earth material use,” *International Power Electronics Conference (IPEC-Hiroshima ECCE-ASIA)*, pp. 3519–3524, 2014.

[76] N. Bianchi, “Synchronous reluctance and interior permanent magnet motors,” *IEEE Workshop on Electrical Machines Design Control and Diagnosis (WEMDCD)*, pp. 75–84*,* 2013.

[77] W. Zhao, D. Chen, T. Lipo, and B. Kwon, “Performance Improvement of Ferrite-Assisted Synchronous Reluctance Machines Using Asymmetrical Rotor Configurations,” *IEEE Transactions on Magnetics,* vol. PP, p. 1, 2015.

[78] M. Paradkar and J. Boecker, “Design of a high performance ferrite magnet-assisted synchronous reluctance motor for an electric vehicle,” *38th Annual Conference on IEEE Industrial Electronics Society IECON*, pp. 4099–4103, 2012.

[79] Y.-H. Jeong, K. Kim, Y.-J. Kim, B.-S. Park, and S.-Y. Jung, “Design characteristics of PMa-SynRM and performance comparison with IPMSM based on numerical analysis,” *XXth International Conference on Electrical Machines (ICEM)*, pp. 164–170*,* 2012.

[80] H. Cai, B. Guan, and L. Xu, “Low-Cost Ferrite PM-Assisted Synchronous Reluctance Machine for Electric Vehicles,” *IEEE Transactions on Industrial Electronics,* vol. 61, pp. 5741–5748, 2014.

[81] D. Takishima, I. Miki, and M. Nakamura, “Study of torque performance for IPMSM with ferrite magnet,” *International Symposium on Power Electronics, Electrical Drives, Automation and Motion (SPEEDAM),* pp. 83–86, 2012.

[82] M. Sanada, Y. Inoue, and S. Morimoto, “Rotor structure for reducing demagnetization of magnet in a PMASynRM with ferrite permanent magnet and its characteristics,” *IEEE Energy Conversion Congress and Exposition (ECCE)*, pp. 4189–4194*,* 2011.

[83] S. Ooi, S. Morimoto, M. Sanada, and Y. Inoue, “Performance Evaluation of a High-Power-Density PMASynRM With Ferrite Magnets,” *IEEE Transactions on Industry Applications,* vol. 49, pp. 1308–1315, 2013.

[84] T. Tokuda, M. Sanada, and S. Morimoto, “Influence of rotor structure on performance of permanent magnet assisted synchronous reluctance motor,” *International Conference on Electrical Machines and Systems, (ICEMS)*, pp. 1–6, 2009.

[85] A.-S. Isfanuti, M. Baba, L. Tutelea, A. Moldovan, and I. Boldea, “Surface NdFeB versus Ferrite IPM motor drive for low power (100W to 2000W) applications: FEM embedded optimal design with full step torque response validation in sensorless vector control,” *Annual Conference of the IEEE Industrial Electronics Society (IECON)*, pp. 3177–3182, 2013.

[86] S. Eriksson and H. Bernhoff, “Rotor design for PM generators reflecting the unstable neodymium price,” *XXth International Conference on Electrical Machines (ICEM)*, pp. 1419–1423*,* 2012.

[87] D.G. Dorrell, M.-F. Hsieh, and A.M. Knight, “Alternative Rotor Designs for High Performance Brushless Permanent Magnet Machines for Hybrid Electric Vehicles,” *IEEE Transactions on Magnetics,* vol. 48, pp. 835–838. , 2012

[88] S.J. Galioto, P.B. Reddy, A.M. El-Refaie, and J.P. Alexander, “Effect of Magnet Types on Performance of High-Speed Spoke Interior-Permanent-Magnet Machines Designed for Traction Applications,” *IEEE Transactions on Industry Applications,* vol. 51, pp. 2148–2160, 2015.

[89] Q. Chen, G. Liu, W. Zhao, M. Shao, and Z. Liu, “Design and Analysis of the New High-Reliability Motors With Hybrid Permanent Magnet Material,” *IEEE Transactions on Magnetics*, vol. 50, pp. 1–10, 2014.

[90] F. Demmelmayr, B. Weiss, M. Troyer, and M. Schroedl, “Comparison of PM-machines with ferrite and NdFeB magnets in terms of machine performance and sensorless start-up control,” *IEEE International Conference on Industrial Technology (ICIT)*, pp. 272–277, 2013.

[91] K.-C. Kim and J. Lee, “The dynamic analysis of a spoke-type permanent magnet generator with large overhang,” *IEEE Transactions on Magnetics,* vol. 41, pp. 3805–3807, 2005.

[92] I.C. Chabu, V.C. Silva, S.I. Nabeta, M.A.M. Afonso, and J.R. Cardoso, “Axial flux concentration technique applied to the design of permanent magnet motors: theoretical aspects and their numerical and experimental validation,” *IEEE International Conference on Electric Machines and Drives*, pp. 1988–1994, 2005.

[93] W. Kakihara, M. Takemoto, and S. Ogasawara, “Rotor Structure in 50 kW Spoke-Type Interior Permanent Magnet Synchronous Motor with Ferrite Permanent Magnets for Automotive Applications,” *IEEE Energy Conversion Congress and Exposition (ECCE)*, pp. 606–613*,* 2013.

[94] D. Matsuhashi, K. Matsuo, T. Okitsu, T. Ashikaga, and T. Mizuno, “Comparison study of various motors for EVs and the potentiality of a ferrite magnet motor,” *International Power Electronics Conference (IPEC-Hiroshima 2014 - ECCE-ASIA)*, pp. 1886–1891*,* 2014.

[95] S. Ohira, N. Hasegawa, I. Miki, D. Matsuhashi, and T. Okitsu, “Torque characteristics of IPMSM with spoke and axial type magnets,” *International Symposium on Power Electronics, Electrical Drives, Automation and Motion (SPEEDAM)*, pp. 818–821*,* 2012.

[96] I.-M. Seo, H.-K. Kim, and J. Hur, “Design and analysis of modified spoke type BLDC motor using a ferrite permanent-magnet,” *International Conference on Electrical Machines and Systems (ICEMS)*, pp. 1701–1705*,* 2014.

[97] H.-W. Kim, K.-T. Kim, Y.-S. Jo, and J. Hur, “Optimization Methods of Torque Density for Developing the Neodymium Free SPOKE-Type BLDC Motor,” *IEEE Transactions on Magnetics*, vol. 49, pp. 2173–2176, 2013.

[98] K. Chiba, M. Takemoto, S. Ogasawara, and W.G. Yim, “Ferrite-magnet spoke-type IPMSM with W-shaped magnet placement,” *39th Annual Conference of the IEEE Industrial Electronics Society (IECON)*, pp. 2869–2874*,* 2013.

[99] M.M. Rahman, K.-T. Kim, and J. Hur, “Design and Optimization of Neodymium-Free SPOKE-Type Motor With Segmented Wing-Shaped PM,” *IEEE Transactions on Magnetics*, vol. 50, pp. 865–868, 2014.

[100] M.M. Rahman, K.-T. Kim, and J. Hur, “Design and analysis of neodymium free SPOKE-type motor with segmented wing shape permanent-magnet for concentrating flux density,” *IEEE Energy Conversion Congress and Exposition (ECCE)*, pp. 4991–4997*,* 2013.

[101] H.-W. Kim, K.-T. Kim, B.-W. Kim, J. Hur, and Y.-S. Jo, “Design of new spoke type brushless DC motor for neodymium permanent magnet free,” *IEEE Vehicle Power and Propulsion Conference (VPPC)*, pp. 133–137*,* 2012.

[102] K. Kondo, S. Kusase, T. Maekawa, and K. Hanada, “A New PM-Assisted Synchronous Reluctance Motor With Three-Dimensional Trench Air Gap,” *IEEE Transactions on Industry Applications*, vol. 50, pp. 2485–2492, 2014.

[103] S.-I. Kim, J. Cho, S. Park, T. Park, and S. Lim, “Characteristics Comparison of a Conventional and Modified Spoke-Type Ferrite Magnet Motor for Traction Drives of Low-Speed Electric Vehicles,” *IEEE Transactions on Industry Applications,* vol. 49, pp. 2516–2523, 2013.

[104] S.-I. Kim, S. Park, T. Park, J. Cho, W. Kim, and S. Lim, “Investigation and Experimental Verification of a Novel Spoke-Type Ferrite-Magnet Motor for Electric-Vehicle Traction Drive Applications,” *IEEE Transactions on Industrial Electronics,* vol. 61, pp. 5763–5770, 2014.

[105] G.-H. Kang, J. Hur, H.-G. Sung, and J.-P. Hong, “Optimal design of spoke type BLDC motor considering irreversible demagnetization of permanent magnet,” *Sixth International Conference on Electrical Machines and Systems (ICEMS)*, vol. 1, pp. 234–237, 2003.

[106] B. Lee, G.-H. Kang, J. Hur, and D.-W. You, “Design of spoke type BLDC motors with high power density for traction applications,” *Conference Record of IEEE Industry Applications Conference (IAS)*, vol. 2, pp. 1068–1074, 2004.

[107] M. Kimiabeigi, J.D. Widmer, R. Long, Y. Gao, J. Goss, R. Martin, T. Lisle, J.M.S. Vizan, A. Michaelides, and B. Mecrow, “High-Performance Low-Cost Electric Motor for Electric Vehicles Using Ferrite Magnets,” *IEEE Transactions on Industrial Electronics*, vol. 63, pp. 113–122, 2016.

[108] K.-Y. Hwang, S.-B. Rhee, J.-S. Lee, and B.-I. Kwon, “Shape optimization of rotor pole in spoke type permanent magnet motor for reducing partial demagnetization effect and cogging torque,” *International Conference on Electrical Machines and Systems (ICEMS)*, pp. 955–960, 2007.

[109] K.-Y. Hwang, S.-B. Rhee, B.-Y. Yang, and B.-I. Kwon, “Rotor Pole Design in Spoke-Type Brushless DC Motor by Response Surface Method,” *IEEE Transactions on Magnetics,* vol. 43, pp. 1833–1836, 2007.

[110] P. Zhang, G.Y. Sizov, D.M. Ionel, and N.A.O. Demerdash, “Establishing the Relative Merits of Interior and Spoke-Type Permanent-Magnet Machines With Ferrite or NdFeB Through Systematic Design Optimization,” *IEEE Transactions on Industry Applications*, vol. 51, pp. 2940–2948, 2015.

[111] D.M. Ionel, D.C. Jackson, G. Starr, and A.P. Turner, “Permanent magnet brushless motors for industrial variable speed drives,” *International Conference on Power Electronics, Machines and Drives*, pp. 650–654*,* 2002.

[112] S. Hlioui, L. Vido, Y. Amara, M. Gabsi, A. Miraoui, and M. Lecrivain, “Design of a synchronous machine with concentric stator windings and

permanent magnets in focusing configuration," *International Aegean Conference on Electrical Machines and Power Electronics (ACEMP)*, pp. 507–512, 2007.

[113] K. Boughrara, R. Ibtiouen, and N. Takorabet, "Analytic calculation of magnetic field and electromagnetic performances of spoke type IPM topologies with auxiliary magnets," *International Conference on Electrical Machines (ICEM)*, pp. 51–57*,* 2014.

[114] M.R. Mohammad, K.-T. Kim, and J. Hur, "Design and Analysis of a Spoke Type Motor With Segmented Pushing Permanent Magnet for Concentrating Air-Gap Flux Density," *IEEE Transactions on Magnetics,* vol. 49, pp. 2397–2400, 2013.

[115] X. Jannot, J.C. Vannier, J. Saint-Michel, M. Gabsi, C. Marchand, and D. Sadarnac, "An analytical model for interior permanent-magnet synchronous machine with circumferential magnetization design," *8th International Symposium on Advanced Electromechanical Motion Systems and Electric Drives Joint Symposium (ELECTROMOTION)*, pp. 1–3, 2009.

[116] X. Jannot, J.-C. Vannier, C. Marchand, M. Gabsi, J. Saint-Michel, and D. Sadarnac, "Multiphysic Modeling of a High-Speed Interior Permanent-Magnet Synchronous Machine for a Multiobjective Optimal Design," *IEEE Transactions on Energy Conversion,* vol. 26, pp. 457–467, 2011.

[117] E. Hoang, M. Gabsi, M. Lecrivain, and B. Multon, "Influence of magnetic losses on maximum power limits of synchronous permanent magnet drives in flux-weakening mode," *Conference Record of the IEEE Industry Applications Conference,* vol. 1, pp. 299–303 vol.1, 2000.

[118] J. Zhang, M. Cheng, and X. Feng, "Design and comparison of wind power permanent magnet generator with doubly salient structure and full pitched windings," *International Conference on Electric Utility Deregulation and Restructuring and Power Technologies (DRPT)*, pp. 1329–1334*,* 2011.

[119] M.M.J. Al-Ani and Z.Q. Zhu, "Novel switched flux machine with radial and circumferential permanent magnets," *17th International Conference on Electrical Machines and Systems (ICEMS)*, pp. 2903–2909*,* 2014.

[120] D. Kim, H. Hwang, S. Bae, and C. Lee, "Analysis and Design of a Double-Stator Flux-Switching Permanent Magnet Machine Using Ferrite Magnet in Hybrid Electric Vehicles," *IEEE Transactions on Magnetics*, vol. PP, pp. 1, 2016.

[121] F. Leonardi, T. Matsuo, Y. Li, T.A. Lipo, and P. McCleer, "Design considerations and test results for a doubly salient PM motor with flux control," *Conference Record of IEEE Industry Applications Conference, Thirty-First IAS Annual Meeting (IAS),* vol. 1, pp. 458–463 vol.1, 1996.

[122] K. Kurihara, T. Kubota, M. Shimazaki, and T. Nakamura, "EMF and

efficiency measurements of a novel self-excited reluctance generator," *IEEE International Electric Machines & Drives Conference (IEMDC),* pp. 1195–1200, 2011.

[123] C.-C. Hwang, P.-L. Li, and C.-T. Liu, "Design and Analysis of a Novel Hybrid Excited Linear Flux Switching Permanent Magnet Motor," *IEEE Transactions on Magnetics,* vol. 48, pp. 2969–2972, 2012.

[124] W. Hua, G. Zhang, and M. Cheng, "Flux-Regulation Theories and Principles of Hybrid-Excited Flux-Switching Machines," *IEEE Transactions on Industrial Electronics*, vol. 62, pp. 5359–5369, 2015.

[125] E. Muljadi, C.P. Butterfield, and Y.-H. Wan, "Axial-flux modular permanent-magnet generator with a toroidal winding for wind-turbine applications," *IEEE Transactions on Industry Applications,* vol. 35, pp. 831–836, 1999.

[126] W. Zhao, T.A. Lipo, and B. Kwon, "Design and analysis of a novel dual stator axial flux spoke-type ferrite permanent magnet machine," *Annual Conference of the IEEE Industrial Electronics Society (IECON)*, pp. 2714–2719*,* 2013.

[127] M. Chirca, S. Breban, C. Oprea, and M.M. Radulescu, "Comparative design analysis of ferrite-permanent-magnet micro-wind turbine generators," *2015 Intl Aegean Conference on Electrical Machines & Power Electronics (ACEMP), 2015 Intl Conference on Optimization of Electrical & Electronic Equipment (OPTIM) & 2015 Intl Symposium on Advanced Electromechanical Motion Systems (ELECTROMOTION)*, pp. 687–692, 2015.

[128] Z. Wang, R. Masaki, S. Morinaga, Y. Enomoto, H. Itabashi, M. Ito, and S. Tanigawa, "Development of an Axial Gap Motor With Amorphous Metal Cores," *IEEE Transactions on Industry Applications,* vol. 47, pp. 1293–1299, 2011.

[129] K. Chiba, S. Chino, M. Takemoto, and S. Ogasawara, "Fundamental analysis for a ferrite permanent magnet axial gap motor with coreless rotor structure," *International Conference on Electrical Machines and Systems (ICEMS)*, pp. 1–6*,* 2012.

[130] K. Sone, M. Takemoto, S. Ogasawara, K. Takezaki, and W. Hino, "Consideration of 10kW in-wheel type axial-gap motor using ferrite permanent magnets," *International*,*Power Electronics Conference (IPEC-Hiroshima 2014 - ECCE-ASIA)*, pp. 3525–3531*,* 2014.

[131] S. Chino, S. Ogasawara, T. Miura, A. Chiba, M. Takemoto, and N. Hoshi, "Fundamental characteristics of a ferrite permanent magnet axial gap motor with segmented rotor structure for the hybrid electric vehicle," *IEEE Energy Conversion Congress and Exposition (ECCE)*, pp. 2805–2811*,* 2011.

[132] K. Sone, M. Takemoto, S. Ogasawara, K. Takezaki, and H. Akiyama, "A

Ferrite PM In-Wheel Motor Without Rare Earth Materials for Electric City Commuters," *IEEE Transactions on Magnetics,* vol. 48, pp. 2961–2964, 2012.

[133] Y. Kuroda, M. Morita, M. Hazeyama, M. Azuma, and M. Inoue, "Improvement of a claw pole motor using additional ferrite magnets for hybrid electric vehicles," *International Conference on Electrical Machines (ICEM)*, pp. 1–3*,* 2010.

[134] M. Azuma, M. Morita, M. Hazeyama, Y. Kuroda, A. Daikoku, and M. Inoue, "Fundamental characteristics of a claw pole motor using additional ferrite magnets for HEV," *Electric Vehicle Conference (IEVC), 2012 IEEE International*, pp. 1–4, 2012.

[135] K.J. Binns and T.-S. Low, "Performance and application of multistacked imbricated permanent magnet generators," *IEE Proceedings Electric Power Applications,* vol. 130, pp. 407–414, 1983.

[136] P. Brockerhoff, Y. Burkhardt, T. Ehlgen, and P. Lucas, "Electrical drivetrain without rare earth magnets and integrated inverter with inherent redundancy," *3rd International Electric Drives Production Conference (EDPC),* pp. 1–7, 2013.

[137] R. Hosoya, H. Shimada, and S. Shimomura, "Design of a ferrite magnet vernier machine for an in-wheel machine," *IEEE Energy Conversion Congress and Exposition (ECCE)*, pp. 2790–2797*,* 2011.

[138] K. Sato, R. Hosoya, and S. Shimomura, "Improved ferrite magnet vernier machine for an in-wheel machine," *IEEE International Conference on Power and Energy (PECon)*, pp. 414–419*,* 2012.

[139] J.F. Gieras and M. Wing, *Permanent Magnet Motor Technology: Design and Applications*, Marcel Dekker, 2002.

[140] Z.Q. Zhu, D. Howe, E. Bolte, and B. Ackermann, "Instantaneous magnetic field distribution in brushless permanent magnet DC motors. I. Open-circuit field," *IEEE Transactions on Magnetics,* vol. 29, pp. 124–135, 1993.

[141] A. Bellara, Y. Amara, G. Barakat, and B. Dakyo, "Two-Dimensional Exact Analytical Solution of Armature Reaction Field in Slotted Surface Mounted PM Radial Flux Synchronous Machines," *IEEE Transactions on Magnetics,* vol. 45, pp. 4534–4538, 2009.

[142] A. Rahideh, M. Mardaneh, and T. Korakianitis, "Analytical 2-D Calculations of Torque, Inductance, and Back-EMF for Brushless Slotless Machines With Surface Inset Magnets," *IEEE Transactions on Magnetics*, vol. 49, pp. 4873–4884, 2013.

[143] L. Zhu, S.Z. Jiang, Z.Q. Zhu, and C.C. Chan, "Analytical Modeling of Open-Circuit Air-Gap Field Distributions in Multisegment and Multilayer Interior Permanent-Magnet Machines," *IEEE Transactions on Magnetics,*

vol. 45, pp. 3121–3130, 2009.

[144] M. Cheng, K.T. Chau, C.C. Chan, E. Zhou, and X. Huang, “Nonlinear varying-network magnetic circuit analysis for doubly salient permanent-magnet motors,” *IEEE Transactions on Magnetics,* vol. 36, pp. 339–348, 2000.

[145] E.C. Lovelace, T.M. Jahns, and J.H. Lang, “A saturating lumped-parameter model for an interior PM synchronous machine,” *IEEE Transactions on Industry Applications,* vol. 38, pp. 645–650, 2002.

[146] Z.Q. Zhu and D. Howe, “Instantaneous magnetic field distribution in brushless permanent magnet DC motors. III. Effect of stator slotting,” *IEEE Transactions on Magnetics,* vol. 29, pp. 143–151, 1993.

[147] T.A. Lipo, *Analysis of Synchronous Machines*, CRC Press, 2012.

[148] J.-X. Shen, P. Li, M.-J. Jin, and G. Yang, “Investigation and Countermeasures for Demagnetization in Line Start Permanent Magnet Synchronous Motors,” *IEEE Transactions on Magnetics,* vol. 49, pp. 4068–4071, 2013.

[149] S. Ruoho, J. Kolehmainen, J. Ikaheimo, and A. Arkkio, “Interdependence of Demagnetization, Loading, and Temperature Rise in a Permanent-Magnet Synchronous Motor,” *IEEE Transactions on Magnetics,* vol. 46, 2010, pp. 949–953.

[150] J. Wang, W. Wang, K. Atallah, and D. Howe, “Demagnetization Assessment for Three-Phase Tubular Brushless Permanent-Magnet Machines,” *IEEE Transactions on Magnetics,* vol. 44, pp. 2195–2203, 2008.

[151] M. Galea, L. Papini, H. Zhang, C. Gerada, and T. Hamiti, “Demagnetisation Analysis for Halbach Array Configurations in Electrical Machines,” *IEEE Transactions on Magneticsm*, vol. PP, p. 1,2015.

[152] K.-C. Kim, K. Kim, H. Kim, and J. Lee, “Demagnetization Analysis of Permanent Magnets According to Rotor Types of Interior Permanent Magnet Synchronous Motor,” *Magnetics, IEEE Transactions on*, vol. 45, pp. 2799–2802, 2009.

[153] M. Niazazari, M. Mirsalim, and S. Mohammadi, “Analytical framework for analysis and demagnetization study of a slotted solid-rotor line-start permanent-magnet synchronous motor,” *5th Annual International Power Electronics, Drive Systems and Technologies Conference*, pp. 494–499, 2014.

[154] A. Vagati, B. Boazzo, P. Guglielmi, and G. Pellegrino, “Design of Ferrite-Assisted Synchronous Reluctance Machines Robust Toward Demagnetization,” *IEEE Transactions Industry Applications,* vol. 50, pp. 1768–1779, 2014.

[155] S. Li, Y. Li, and B. Sarlioglu, “Partial Irreversible Demagnetization Assessment of Flux Switching Permanent Magnet Machine using Ferrite Permanent Magnet Material,” *IEEE Transactions on Magnetics,* vol. PP, p. 1, 2015.

[156] H. Huang, Y. Hu, Y. Xiao, and H. Lyu, “Research of Parameters and Anti-demagnetization of Rare-earth-less Permanent Magnet assisted Synchronous Reluctance Motor,” *IEEE Transactions on Magnetics,* vol. PP, p. 1, 2015.

[157] H. Chen, R. Qu, J. Li, and D. Li, “Demagnetization Performance of a 7 MW Interior Permanent Magnet Wind Generator with Fractional-slot Concentrated Windings,” *IEEE Transactions on Magnetics,* vol. PP, p. 1, 2015.

[158] M. Fasil, N. Mijatovic, B.B. Jensen, and J. Holboll, “Performance Variation of Ferrite Magnet PMBLDC Motor with Temperature,” *IEEE Transactions on Magnetics,* vol. PP, p. 1, 2015.

[159] K.C. Kim, S.B. Lim, D.H. Koo, and J. Lee, “The Shape Design of Permanent Magnet for Permanent Magnet Synchronous Motor Considering Partial Demagnetization,” *IEEE Transactions on Magnetics*, vol. 42, pp. 3485–3487, 2006.

[160] K.-D. Lee, W.-H. Kim, C.-S. Jin, and J. Lee, “Local demagnetisation analysis of a permanent magnet motor,” *IET Electric Power Applications,* vol. 9, pp. 280–286, 2015.

[161] C.-M. Kim, G.-W. Cho, G.-T. Kim, and H.-G. Shin, “The design of flux barrier for improvement of demagnetization endurance in BLDC Motor,” *International Conference on Electrical Machines and Systems (ICEMS)*, pp. 1198–1201*,* 2013.

[162] P. Sergeant and A.P.M. Van den Bossche, “Influence of the Amount of Permanent-Magnet Material in Fractional-Slot Permanent-Magnet Synchronous Machines,” *IEEE Transactions on Industrial Electronics*, vol. 61, pp. 4979–4989, 2014.

[163] M. Satoh, S. Kaneko, M. Tomita, and S. Doki, “Study to reduce the amount of magnetic materials in IPM motor which focuses on the rare earth magnet usage and demagnetization,” *2015 18th International Conference on Electrical Machines and Systems (ICEMS)*, pp. 195–199, 2015.

[164] K. Imamura, M. Sanada, S. Morimoto, and Y. Inoue, “Improvement of demagnetization by rotor structure of IPMSM with Dy-free rare-earth magnet,” *15th International Conference on Electrical Machines and Systems (ICEMS)*, pp. 1–6*,* 2012.

[165] S. Lim, S. Min, and J.-P. Hong, “Optimal Rotor Design of IPM Motor for Improving Torque Performance Considering Thermal Demagnetization of Magnet,” *IEEE Transactions on Magnetics, v*ol. 51, pp. 1–5, 2015.

[166] P. Zhou, D. Lin, Y. Xiao, N. Lambert, and M.A. Rahman, “Temperature-Dependent Demagnetization Model of Permanent Magnets for Finite Element Analysis,” *IEEE Transactions on Magnetics, v*ol. 48, pp. 1031–1034, 2012.

[167] S. Ruoho, E. Dlala, and A. Arkkio, “Comparison of Demagnetization Models for Finite-Element Analysis of Permanent-Magnet Synchronous Machines,” *IEEE Transactions on Magnetics,* vol. 43, pp. 3964–3968, 2007.

[168] V.I. Patel, J. Wang, and S.S. Nair, “Demagnetization Assessment of Fractional-Slot and Distributed Wound 6-Phase Permanent Magnet Machines,” *IEEE Transactions on Magnetics,* vol. 51, pp. 1–11, 2015.

[169] J.D. McFarland and T.M. Jahns, “Influence of d- and q-axis currents on demagnetization in PM synchronous machines,” *IEEE Energy Conversion Congress and Exposition (ECCE)*, pp. 4380–4387*,*2013.

[170] R.K. Rajput, *A Text Book of Electrical Machines*, Laxmi Publications, 2006.

[171] J. Pyrhonen, T. Jokinen, and V. Hrabovcova, *Design of Rotating Electrical Machines*, John Wiley & Sons, Ltd, 2008.

[172] D.A. Gonzalez and D.M. Saban, “Study of the Copper Losses in a High-Speed Permanent-Magnet Machine With Form-Wound Windings,” *IEEE Transactions on Industrial Electronics*, vol. 61, pp. 3038–3045, 2014.

[173] X. Nan and C.R. Sullivan, “An improved calculation of proximity-effect loss in high-frequency windings of round conductors,” *IEEE 34th Annual Power Electronics Specialist Conference*, vol. 2, pp. 853–860 vol.2, 2003.

[174] I.A.A. Afinowi, Z.Q. Zhu, Y. Guan, J.C. Mipo, and P. Farah, “Performance analysis of switched-flux machines with hybrid NdFeB and ferrite magnets,” *17th International Conference on Electrical Machines and Systems (ICEMS)*, pp. 3110–3116*,* 2014.

[175] D.G. Dorrell, M.-F. Hsieh, and A.M. Knight, “Alternative Rotor Designs for High Performance Brushless Permanent Magnet Machines for Hybrid Electric Vehicles,” *IEEE Transactions on Magnetics,* vol. 48, pp. 835–838, 2012.

[176] S. Morimoto, S. Ooi, Y. Inoue, and M. Sanada, “Experimental Evaluation of a Rare-Earth-Free PMASynRM With Ferrite Magnets for Automotive Applications,” *IEEE Transactions on Industrial Electronics,* vol. 61, pp. 5749–5756, 2014.

APPENDICES

Appendix A Two-layer Analytical Model for Armature Reactive Field with PM Slot Flux Counted

A.1 Open-Circuit Model

The complete Fourier transformation of Equation (3-58) can be expanded as:

$$B_{fgv}=\frac{4}{v\pi}B_{g2}\sin\left(\frac{vp\alpha_2}{2}\right)+\frac{4}{v\pi}B_{g1}\left[\sin\left(v\frac{\pi-p\beta_1}{2}\right)-\sin\left(vp\frac{\alpha_2+\beta_2}{2}\right)\right]+\frac{4pg_c}{\pi^2R_{ro}}\cdot$$
$$\left\{\begin{array}{l}B_{g1}\cos v\left(\frac{\pi}{2}-\frac{pg_c}{\pi R_{ro}}-\frac{p\beta_1}{2}\right)\left\{\mathrm{Ci}\left[v\left(\frac{pg_c}{\pi R_{ro}}+\frac{p\beta_1}{2}\right)\right]-\mathrm{Ci}\left[v\left(\frac{pg_c}{\pi R_{ro}}\right)\right]\right\}\\ -B_{g1}\sin v\left(\frac{\pi}{2}-\frac{pg_c}{\pi R_{ro}}-\frac{p\beta_1}{2}\right)\left\{\mathrm{Si}\left[v\left(\frac{pg_c}{\pi R_{ro}}+\frac{p\beta_1}{2}\right)\right]-\mathrm{Si}\left[v\left(\frac{pg_c}{\pi R_{ro}}\right)\right]\right\}\\ +\left[\begin{array}{l}B_{g1}\cos v\left(\frac{pg_c}{\pi R_{ro}}+\frac{p\alpha_2}{2}+\frac{p\beta_2}{2}\right)\\ +B_{g2}\cos v\left(\frac{p\alpha_2}{2}-\frac{pg_c}{\pi R_{ro}}\right)\end{array}\right]\left\{\mathrm{Ci}\left[v\left(\frac{pg_c}{\pi R_{ro}}+\frac{p\beta_2}{4}\right)\right]-\mathrm{Ci}\left[v\left(\frac{pg_c}{\pi R_{ro}}\right)\right]\right\}\\ +\left[\begin{array}{l}B_{g1}\sin v\left(\frac{pg_c}{\pi R_{ro}}+\frac{p\alpha_2}{2}+\frac{p\beta_2}{2}\right)\\ -B_{g2}\sin v\left(\frac{p\alpha_2}{2}-\frac{pg_c}{\pi R_{ro}}\right)\end{array}\right]\left\{\mathrm{Si}\left[v\left(\frac{pg_c}{\pi R_{ro}}+\frac{p\beta_2}{4}\right)\right]-\mathrm{Si}\left[v\left(\frac{pg_c}{\pi R_{ro}}\right)\right]\right\}\end{array}\right\} \quad \textbf{(A-1)}$$

A.2 D-Axis Model

The complete Fourier transformation of Equation (3-67) can be expanded as:

$$B_{gduv}(\theta)=\frac{4}{\pi}B_{adu}\left[\begin{array}{l}\int_0^{\frac{p\alpha_2}{2}}\cos(u\theta)\cos(v\theta)\,d\theta+\int_{\frac{p\alpha_2}{2}}^{\frac{p\alpha_2}{2}+\frac{p\beta_2}{4}}\frac{\cos(u\theta)\cos(v\theta)}{\frac{\pi R_{ro}}{pg_c}\left(\theta-\frac{p\alpha_2}{2}+\frac{pg_c}{\pi R_{ro}}\right)}d\theta\\ +\int_{\frac{p\alpha_2}{2}+\frac{p\beta_2}{4}}^{\frac{p(\alpha_2+\beta_2)}{2}}\frac{\cos(u\theta)\cos(v\theta)}{\frac{\pi R_{ro}}{pg_c}\left(p\frac{\alpha_2+\beta_2}{2}-\theta+\frac{pg_c}{\pi R_{ro}}\right)}d\theta+\int_{\frac{p(\alpha_2+\beta_2)}{2}}^{\frac{\pi-p\beta_1}{2}}\cos(u\theta)\cos(v\theta)\,d\theta\\ +\int_{\frac{\pi-p\beta_1}{2}}^{\frac{\pi}{2}}\frac{\cos(u\theta)\cos(v\theta)}{\frac{\pi R_{ro}}{pg_c}\left(\theta-\frac{\pi}{2}+\frac{p\beta_1}{2}+\frac{pg_c}{\pi R_{ro}}\right)}d\theta\end{array}\right] \quad \textbf{(A-2)}$$

When $u \neq v$, Equation (A-2) can be calculated by:

$$B_{gduv}(\theta)=\frac{2B_{adu}}{\pi}\left[\begin{array}{l}\dfrac{\sin\dfrac{(u+v)p\alpha_2}{2}+\sin\dfrac{(u+v)(\pi-p\beta_1)}{2}-\sin\dfrac{(u+v)p(\alpha_2+\beta_2)}{2}+}{u+v}\\ +\dfrac{\sin\dfrac{(u-v)p\alpha_2}{2}+\sin\dfrac{(u-v)(\pi-p\beta_1)}{2}-\sin\dfrac{(u-v)p(\alpha_2+\beta_2)}{2}}{u-v}\end{array}\right]+\frac{2pg_cB_{adu}}{\pi^2R_{ro}}$$

$$\cdot\left\{\begin{array}{l}\cos\left[(u+v)\left(\frac{\pi}{2}-\frac{pg_c}{\pi R_{ro}}-\frac{p\beta_1}{2}\right)\right]\left\{\mathrm{Ci}\left[(u+v)\left(\frac{pg_c}{\pi R_{ro}}+\frac{p\beta_1}{2}\right)\right]-\mathrm{Ci}\left[(u+v)\left(\frac{pg_c}{\pi R_{ro}}\right)\right]\right\}\\ -\sin\left[(u+v)\left(\frac{\pi}{2}-\frac{pg_c}{\pi R_{ro}}-\frac{p\beta_1}{2}\right)\right]\left\{\mathrm{Si}\left[(u+v)\left(\frac{pg_c}{\pi R_{ro}}+\frac{p\beta_1}{2}\right)\right]-\mathrm{Si}\left[(u+v)\left(\frac{pg_c}{\pi R_{ro}}\right)\right]\right\}\\ +\cos\left[(u-v)\left(\frac{\pi}{2}-\frac{pg_c}{\pi R_{ro}}-\frac{p\beta_1}{2}\right)\right]\left\{\mathrm{Ci}\left[(u-v)\left(\frac{pg_c}{\pi R_{ro}}+\frac{p\beta_1}{2}\right)\right]-\mathrm{Ci}\left[(u-v)\left(\frac{pg_c}{\pi R_{ro}}\right)\right]\right\}\\ -\sin\left[(u-v)\left(\frac{\pi}{2}-\frac{pg_c}{\pi R_{ro}}-\frac{p\beta_1}{2}\right)\right]\left\{\mathrm{Si}\left[(u-v)\left(\frac{pg_c}{\pi R_{ro}}+\frac{p\beta_1}{2}\right)\right]-\mathrm{Si}\left[(u-v)\left(\frac{pg_c}{\pi R_{ro}}\right)\right]\right\}\\ +2\cos\left[(u+v)\left(\frac{p\alpha_2}{2}+\frac{p\beta_2}{4}\right)\right]\cos\left[(u+v)\left(\frac{p\beta_2}{4}+\frac{pg_c}{\pi R_{ro}}\right)\right]\left\{\begin{array}{l}\mathrm{Ci}\left[(u+v)\left(\frac{pg_c}{\pi R_{ro}}+\frac{p\beta_2}{4}\right)\right]\\ -\mathrm{Ci}\left[(u+v)\frac{pg_c}{\pi R_{ro}}\right]\end{array}\right\}\\ +2\cos\left[(u+v)\left(\frac{p\alpha_2}{2}+\frac{p\beta_2}{4}\right)\right]\sin\left[(u+v)\left(\frac{p\beta_2}{4}+\frac{pg_c}{\pi R_{ro}}\right)\right]\left\{\begin{array}{l}\mathrm{Si}\left[(u+v)\left(\frac{pg_c}{\pi R_{ro}}+\frac{p\beta_2}{4}\right)\right]\\ -\mathrm{Si}\left[(u+v)\frac{pg_c}{\pi R_{ro}}\right]\end{array}\right\}\\ +2\cos\left[(u-v)\left(\frac{p\alpha_2}{2}+\frac{p\beta_2}{4}\right)\right]\cos\left[(u-v)\left(\frac{p\beta_2}{4}+\frac{pg_c}{\pi R_{ro}}\right)\right]\left\{\begin{array}{l}\mathrm{Ci}\left[(u-v)\left(\frac{pg_c}{\pi R_{ro}}+\frac{p\beta_2}{4}\right)\right]\\ -\mathrm{Ci}\left[(u-v)\frac{pg_c}{\pi R_{ro}}\right]\end{array}\right\}\\ +2\cos\left[(u-v)\left(\frac{p\alpha_2}{2}+\frac{p\beta_2}{4}\right)\right]\sin\left[(u-v)\left(\frac{p\beta_2}{4}+\frac{pg_c}{\pi R_{ro}}\right)\right]\left\{\begin{array}{l}\mathrm{Si}\left[(u-v)\left(\frac{pg_c}{\pi R_{ro}}+\frac{p\beta_2}{4}\right)\right]\\ -\mathrm{Si}\left[(u-v)\frac{pg_c}{\pi R_{ro}}\right]\end{array}\right\}\end{array}\right\} \quad \textbf{(A-3)}$$

When $u=v$, Equation (A-2) can be calculated by:

$$
\begin{aligned}
B_{gdvv}(\theta) &= \frac{4B_{adv}}{\pi}\left[\begin{array}{l}
\int_0^{\frac{p\alpha_2}{2}}\cos^2(v\theta)\,d\theta+\int_{\frac{p(\alpha_2+\beta_2)}{2}}^{\frac{\pi-p\beta_1}{2}}\cos^2(v\theta)\,d\theta+\int_{\frac{p\alpha_2}{2}}^{\frac{p\alpha_2}{2}+\frac{p\beta_2}{4}}\dfrac{\cos^2(v\theta)\,d\theta}{\frac{\pi R_{ro}}{pg_c}\left(\theta-\frac{p\alpha_2}{2}+\frac{pg_c}{\pi R_{ro}}\right)} \\
+\int_{\frac{p\alpha_2}{2}+\frac{p\beta_2}{4}}^{\frac{p(\alpha_2+\beta_2)}{2}}\dfrac{\cos^2(v\theta)\,d\theta}{\frac{\pi R_{ro}}{pg_c}\left(p\frac{\alpha_2+\beta_2}{2}-\theta+\frac{pg_c}{\pi R_{ro}}\right)}+\int_{\frac{\pi-p\beta_1}{2}}^{\frac{\pi}{2}}\dfrac{\cos^2(v\theta)\,d\theta}{\frac{\pi R_{ro}}{pg_c}\left(\theta-\frac{\pi}{2}+\frac{p\beta_1}{2}+\frac{pg_c}{\pi R_{ro}}\right)}
\end{array}\right] \\
&= B_{adv}\left[1-\frac{p(\beta_1+\beta_2)}{\pi}+\frac{\sin v(\pi-p\beta_1)-\sin vp(\alpha_2+\beta_2)+\sin vp(\alpha_2)}{v\pi}\right]+\frac{2pg_c}{\pi^2R_{ro}}B_{adv}\cdot \\
&\left\{\begin{array}{l}
\cos\left[2v\left(\frac{\pi}{2}-\frac{pg_c}{\pi R_{ro}}-\frac{p\beta_1}{2}\right)\right]\left\{\mathrm{Ci}\left[2v\left(\frac{pg_c}{\pi R_{ro}}+\frac{p\beta_1}{2}\right)\right]-\mathrm{Ci}\left[2v\left(\frac{pg_c}{\pi R_{ro}}\right)\right]\right\} \\
-\sin\left[2v\left(\frac{\pi}{2}-\frac{pg_c}{\pi R_{ro}}-\frac{p\beta_1}{2}\right)\right]\left\{\mathrm{Si}\left[2v\left(\frac{pg_c}{\pi R_{ro}}+\frac{p\beta_1}{2}\right)\right]-\mathrm{Si}\left[2v\left(\frac{pg_c}{\pi R_{ro}}\right)\right]\right\} \\
+2\cos\left[2v\left(\frac{p\alpha_2}{2}+\frac{p\beta_2}{4}\right)\right]\cos\left[2v\left(\frac{p\beta_2}{4}+\frac{pg_c}{\pi R_{ro}}\right)\right]\left\{\mathrm{Ci}\left[2v\left(\frac{pg_c}{\pi R_{ro}}+\frac{p\beta_2}{4}\right)\right]-\mathrm{Ci}\left[2v\left(\frac{pg_c}{\pi R_{ro}}\right)\right]\right\} \\
+2\cos\left[2v\left(\frac{p\alpha_2}{2}+\frac{p\beta_2}{4}\right)\right]\sin\left[2v\left(\frac{p\beta_2}{4}+\frac{pg_c}{\pi R_{ro}}\right)\right]\left\{\mathrm{Si}\left[2v\left(\frac{pg_c}{\pi R_{ro}}+\frac{p\beta_2}{4}\right)\right]-\mathrm{Si}\left[2v\left(\frac{pg_c}{\pi R_{ro}}\right)\right]\right\} \\
+\ln\left(1+\frac{\pi R_{ro}\beta_1}{2g_c}\right)+2\ln\left(1+\frac{\pi R_{ro}\beta_2}{4g_c}\right)
\end{array}\right\}
\end{aligned}
\tag{A-4}
$$

A.3 Q-Axis Model

By including the flux in the PM slot areas, the complete form of Equation (3-70) can be expanded as:

$$
\begin{aligned}
B_{gquv}(\theta) &= \frac{4}{\pi}B_{aqv}\left[\begin{array}{l}
\int_0^{\frac{p\beta_1}{2}}\dfrac{\cos(u\theta)\cos(v\theta)}{\frac{\pi R_{ro}}{pg_c}\left(\frac{p\beta_1}{2}+\frac{pg_c}{\pi R_{ro}}-\theta\right)}d\theta+\int_{\frac{p\beta_1}{2}}^{p\frac{\alpha_1+\beta_1}{2}}\cos(u\theta)\cos(v\theta)\,d\theta \\
+\int_{\frac{\pi-p\alpha_1}{2}}^{\frac{\pi}{2}}\cos(u\theta)\cos(v\theta)\,d\theta+\int_{\frac{p(\alpha_1+\beta_1)}{2}}^{\frac{p(\alpha_1+\beta_1)}{2}+\frac{p\beta_2}{4}}\dfrac{\cos(u\theta)\cos(v\theta)}{\frac{\pi R_{ro}}{pg_c}\left(\theta-p\frac{\alpha_1+\beta_1}{2}+\frac{pg_c}{\pi R_{ro}}\right)}d\theta \\
+\int_{\frac{p(\alpha_1+\beta_1)}{2}+\frac{p\beta_2}{4}}^{\frac{\pi-p\alpha_1}{2}}\dfrac{\cos(u\theta)\cos(v\theta)}{\frac{\pi R_{ro}}{pg_c}\left(\frac{\pi-p\alpha_1}{2}+\frac{pg_c}{\pi R_{ro}}-\theta\right)}d\theta
\end{array}\right]
\end{aligned}
\tag{A-5}
$$

When $u \neq v$, Equation (A-5) can be expressed by:

$$B_{gquv}=\frac{2B_{aqu}}{\pi}\left[\begin{array}{l}\dfrac{\sin\dfrac{(u+v)\,p(\alpha_1+\beta_1)}{2}-\sin\dfrac{(u+v)\,p\beta_1}{2}-\sin\dfrac{(u+v)(\pi-p\alpha_2)}{2}}{u+v}\\ +\dfrac{\sin\dfrac{(u-v)\,p(\alpha_1+\beta_1)}{2}-\sin\dfrac{(u-v)\,p\beta_1}{2}-\sin\dfrac{(u-v)(\pi-p\alpha_2)}{2}}{u-v}\end{array}\right]+\frac{2pg_cB_{aqu}}{\pi^2R_{ro}}$$

$$\cdot\left\{\begin{array}{l}\cos\left[(u+v)\left(\dfrac{pg_c}{\pi R_{ro}}+\dfrac{p\beta_1}{2}\right)\right]\left\{\mathrm{Ci}\left[(u+v)\left(\dfrac{p\beta_1}{2}+\dfrac{pg_c}{\pi R_{ro}}\right)\right]-\mathrm{Ci}\left[(u+v)\left(\dfrac{pg_c}{\pi R_{ro}}\right)\right]\right\}\\ +\sin\left[(u+v)\left(\dfrac{pg_c}{\pi R_{ro}}+\dfrac{p\beta_1}{2}\right)\right]\left\{\mathrm{Si}\left[(u+v)\left(\dfrac{p\beta_1}{2}+\dfrac{pg_c}{\pi R_{ro}}\right)\right]-\mathrm{Si}\left[(u+v)\left(\dfrac{pg_c}{\pi R_{ro}}\right)\right]\right\}\\ +\cos\left[(u-v)\left(\dfrac{pg_c}{\pi R_{ro}}+\dfrac{p\beta_1}{2}\right)\right]\left\{\mathrm{Ci}\left[(u-v)\left(\dfrac{p\beta_1}{2}+\dfrac{pg_c}{\pi R_{ro}}\right)\right]-\mathrm{Ci}\left[(u-v)\left(\dfrac{pg_c}{\pi R_{ro}}\right)\right]\right\}\\ +\sin\left[(u-v)\left(\dfrac{pg_c}{\pi R_{ro}}+\dfrac{p\beta_1}{2}\right)\right]\left\{\mathrm{Si}\left[(u-v)\left(\dfrac{p\beta_1}{2}+\dfrac{pg_c}{\pi R_{ro}}\right)\right]-\mathrm{Si}\left[(u-v)\left(\dfrac{pg_c}{\pi R_{ro}}\right)\right]\right\}\\ +2\left\{\begin{array}{l}\cos\left[(u+v)\left(p\dfrac{\alpha_1+\beta_1}{2}+\dfrac{p\beta_2}{4}\right)\right]\\ \cdot\cos\left[(u+v)\left(\dfrac{p\beta_2}{4}+\dfrac{pg_c}{\pi R_{ro}}\right)\right]\end{array}\right\}\left\{\begin{array}{l}\mathrm{Ci}\left[(u+v)\left(\dfrac{pg_c}{\pi R_{ro}}+\dfrac{p\beta_2}{4}\right)\right]\\ -\mathrm{Ci}\left[(u+v)\dfrac{pg_c}{\pi R_{ro}}\right]\end{array}\right\}\\ +2\left\{\begin{array}{l}\cos\left[(u+v)\left(p\dfrac{\alpha_1+\beta_1}{2}+\dfrac{p\beta_2}{4}\right)\right]\\ \cdot\sin\left[(u+v)\left(\dfrac{p\beta_2}{4}+\dfrac{pg_c}{\pi R_{ro}}\right)\right]\end{array}\right\}\left\{\begin{array}{l}\mathrm{Si}\left[(u+v)\left(\dfrac{pg_c}{\pi R_{ro}}+\dfrac{p\beta_2}{4}\right)\right]\\ -\mathrm{Si}\left[(u+v)\dfrac{pg_c}{\pi R_{ro}}\right]\end{array}\right\}\\ +2\left\{\begin{array}{l}\cos\left[(u-v)\left(p\dfrac{\alpha_1+\beta_1}{2}+\dfrac{p\beta_2}{4}\right)\right]\\ \cdot\cos\left[(u-v)\left(\dfrac{p\beta_2}{4}+\dfrac{pg_c}{\pi R_{ro}}\right)\right]\end{array}\right\}\left\{\begin{array}{l}\mathrm{Ci}\left[(u-v)\left(\dfrac{pg_c}{\pi R_{ro}}+\dfrac{p\beta_2}{4}\right)\right]\\ -\mathrm{Ci}\left[(u-v)\dfrac{pg_c}{\pi R_{ro}}\right]\end{array}\right\}\\ +2\left\{\begin{array}{l}\cos\left[(u-v)\left(p\dfrac{\alpha_1+\beta_1}{2}+\dfrac{p\beta_2}{4}\right)\right]\\ \cdot\sin\left[(u-v)\left(\dfrac{p\beta_2}{4}+\dfrac{pg_c}{\pi R_{ro}}\right)\right]\end{array}\right\}\left\{\begin{array}{l}\mathrm{Si}\left[(u-v)\left(\dfrac{pg_c}{\pi R_{ro}}+\dfrac{p\beta_2}{4}\right)\right]\\ -\mathrm{Si}\left[(u-v)\dfrac{pg_c}{\pi R_{ro}}\right]\end{array}\right\}\end{array}\right\} \quad \textbf{(A-6)}$$

And when u=v, Equation (A-5) can be calculated by:

$$
\begin{aligned}
B_{gqvv}(\theta) &= \frac{4}{\pi} B_{aqv} \left[\begin{array}{l}
\int_0^{\frac{p\beta_1}{2}} \dfrac{\cos^2(v\theta)}{\dfrac{\pi R_{ro}}{pg_c}\left(\dfrac{p\beta_1}{2}+\dfrac{pg_c}{\pi R_{ro}}-\theta\right)} d\theta + \int_{\frac{p\beta_1}{2}}^{p\frac{\alpha_1+\beta_1}{2}} \cos^2(v\theta)\, d\theta \\
+\int_{\frac{\pi-p\alpha_1}{2}}^{\frac{\pi}{2}} \cos^2(v\theta)\, d\theta + \int_{\frac{p(\alpha_1+\beta_1)}{2}}^{\frac{p(\alpha_1+\beta_1)}{2}+\frac{p\beta_2}{4}} \dfrac{\cos^2(v\theta)}{\dfrac{\pi R_{ro}}{pg_c}\left(\theta - p\dfrac{\alpha_1+\beta_1}{2}+\dfrac{pg_c}{\pi R_{ro}}\right)} d\theta \\
+\int_{\frac{p(\alpha_1+\beta_1)}{2}+\frac{p\beta_2}{4}}^{\frac{\pi-p\alpha_1}{2}} \dfrac{\cos^2(v\theta)}{\dfrac{\pi R_{ro}}{pg_c}\left(\dfrac{\pi-p\alpha_1}{2}+\dfrac{pg_c}{\pi R_{ro}}-\theta\right)} d\theta
\end{array} \right] \\
&= B_{aqv}\left[1-\frac{p(\beta_1+\beta_2)}{\pi}+\frac{\sin vp(\alpha_1+\beta_1)-\sin(vp\beta_1)-\sin v(\pi-p\alpha_2)}{v\pi}\right]+\frac{2pg_c}{\pi^2 R_{ro}} B_{aqv} \cdot \\
&\left\{ \begin{array}{l}
\cos\left[2v\left(\dfrac{pg_c}{\pi R_{ro}}+\dfrac{p\beta_1}{2}\right)\right]\left\{\mathrm{Ci}\left[2v\left(\dfrac{pg_c}{\pi R_{ro}}+\dfrac{p\beta_1}{2}\right)\right]-\mathrm{Ci}\left[2v\left(\dfrac{pg_c}{\pi R_{ro}}\right)\right]\right\}+\ln\left(1+\dfrac{\pi R_{ro}\beta_1}{2g_c}\right) \\
+\sin\left[2v\left(\dfrac{pg_c}{\pi R_{ro}}+\dfrac{p\beta_1}{2}\right)\right]\left\{\mathrm{Si}\left[2v\left(\dfrac{pg_c}{\pi R_{ro}}+\dfrac{p\beta_1}{2}\right)\right]-\mathrm{Si}\left[2v\left(\dfrac{pg_c}{\pi R_{ro}}\right)\right]\right\}+2\ln\left(1+\dfrac{\pi R_{ro}\beta_2}{4g_c}\right) \\
+2\cos\left[2v\left(p\dfrac{\alpha_1+\beta_1}{2}+\dfrac{p\beta_2}{4}\right)\right]\cos\left[2v\left(\dfrac{p\beta_2}{4}+\dfrac{pg_c}{\pi R_{ro}}\right)\right]\left\{\begin{array}{l}\mathrm{Ci}\left[2v\left(\dfrac{pg_c}{\pi R_{ro}}+\dfrac{p\beta_2}{4}\right)\right] \\ -\mathrm{Ci}\left[2v\left(\dfrac{pg_c}{\pi R_{ro}}\right)\right]\end{array}\right\} \\
+2\cos\left[2v\left(p\dfrac{\alpha_1+\beta_1}{2}+\dfrac{p\beta_2}{4}\right)\right]\sin\left[2v\left(\dfrac{p\beta_2}{4}+\dfrac{pg_c}{\pi R_{ro}}\right)\right]\left\{\begin{array}{l}\mathrm{Si}\left[2v\left(\dfrac{pg_c}{\pi R_{ro}}+\dfrac{p\beta_2}{4}\right)\right] \\ -\mathrm{Si}\left[2v\left(\dfrac{pg_c}{\pi R_{ro}}\right)\right]\end{array}\right\}
\end{array} \right\}
\end{aligned}
\tag{A-7}
$$

Appendix B Mechanical Drawing for the Prototype Machine and the Testing Rig

B.1 The Prototype Machine

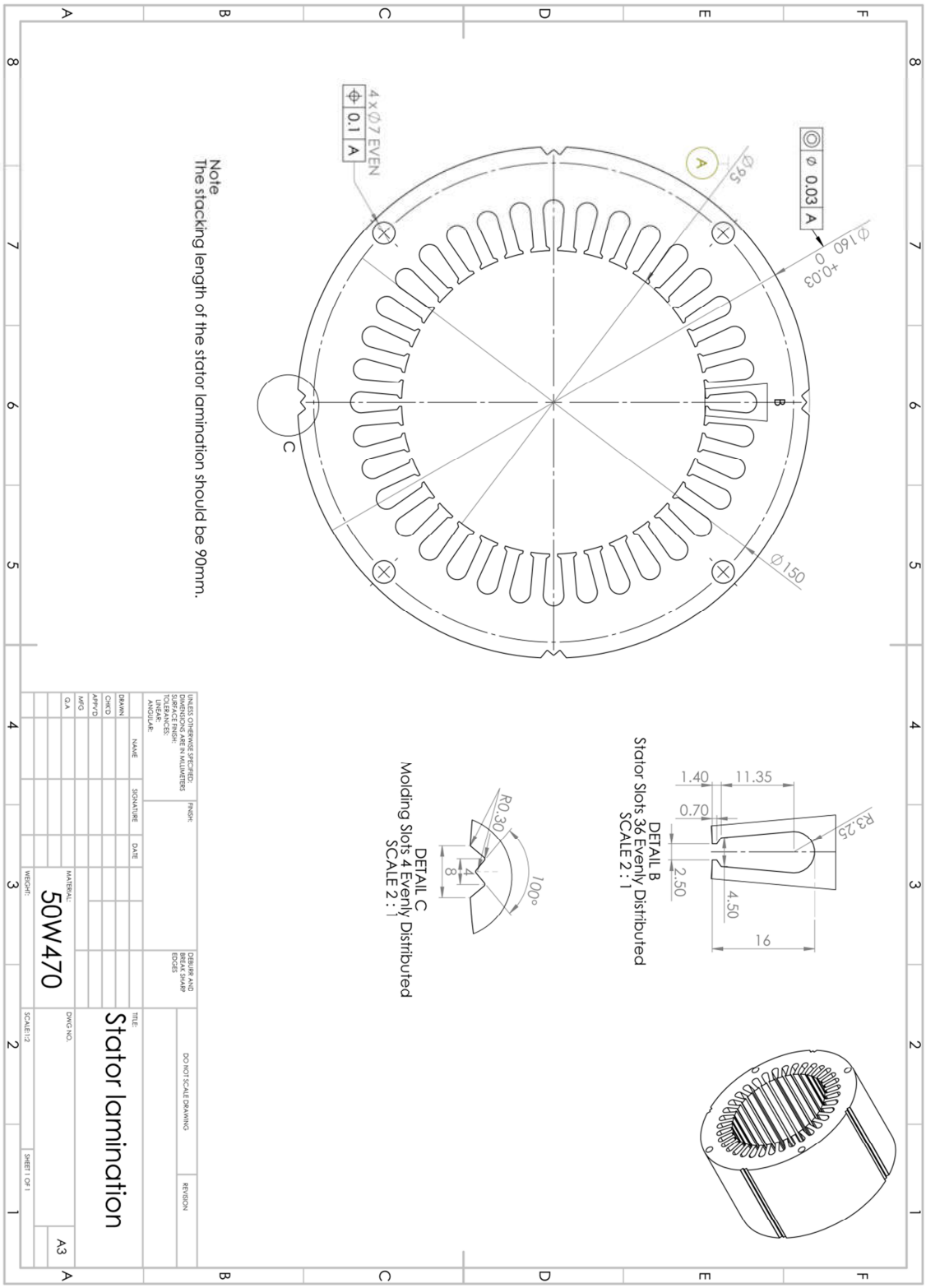

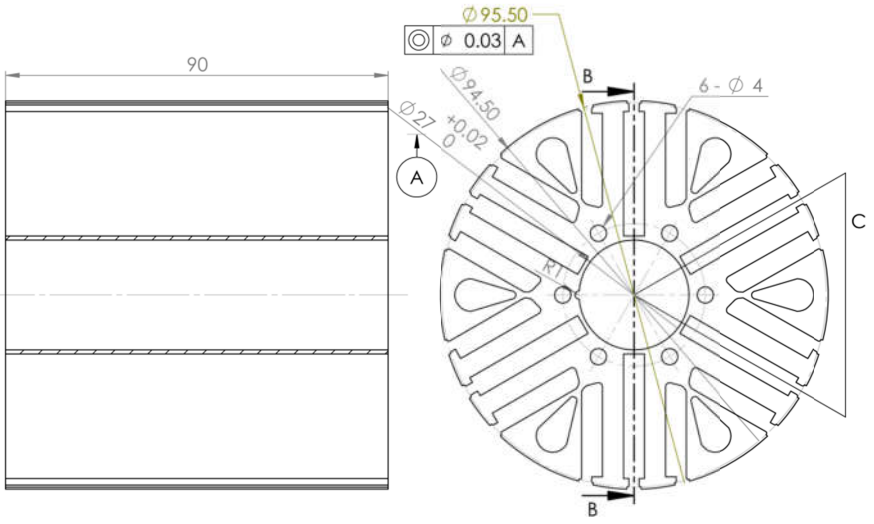

SECTION B-B
SCALE 1 : 1

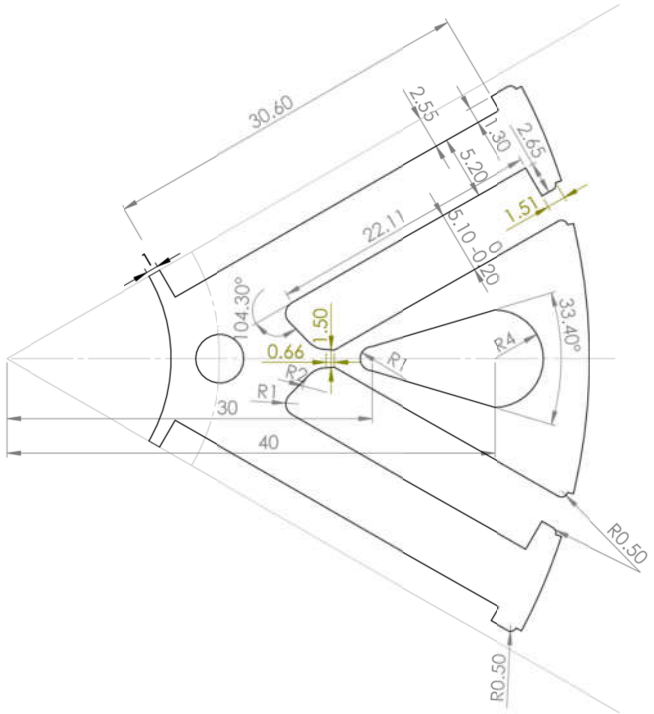

DETAIL C
SCALE 3 : 1

UNLESS OTHERWISE SPECIFIED: DIMENSIONS ARE IN MILLIMETERS SURFACE FINISH: TOLERANCES: LINEAR: ANGULAR:			FINISH:			DEBUR AND BREAK SHARP EDGES	DO NOT SCALE DRAWING	REVISION
	NAME	SIGNATURE	DATE				TITLE: Ferrite1	
DRAWN								
CHK'D								
APPV'D								
MFG								
Q.A				MATERIAL: 50W470			DWG NO.	A3
				WEIGHT:			SCALE:1:2	SHEET 1 OF 1

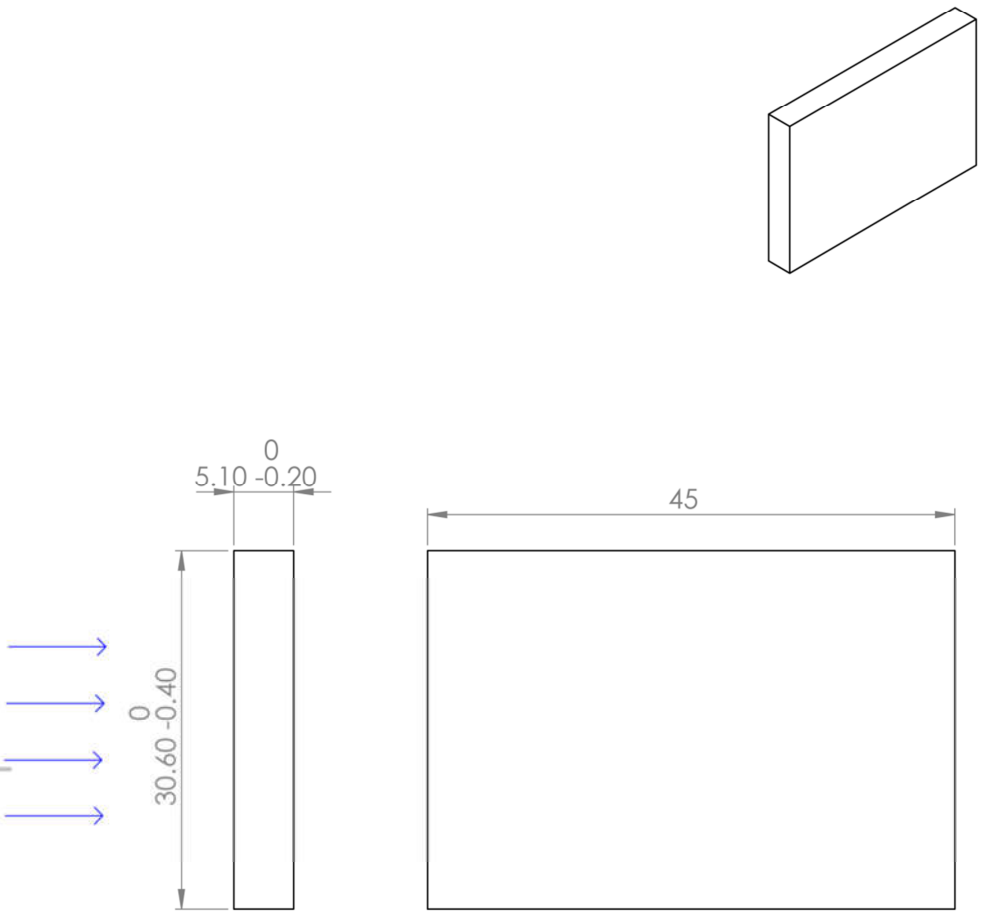

Note
1. Direction of magnetization is indicated as the arrows above.
2. All together 12 pieces are required for one prototype machine.

UNLESS OTHERWISE SPECIFIED: DIMENSIONS ARE IN MILLIMETERS SURFACE FINISH: TOLERANCES: LINEAR: ANGULAR:	FINISH:		DEBURR AND BREAK SHARP EDGES	DO NOT SCALE DRAWING	REVISION	
	NAME	SIGNATURE	DATE	TITLE:		
DRAWN						
CHK'D						
APPV'D						
MFG						
Q.A				MATERIAL:	DWG NO. Main Pole	A4
				WEIGHT:	SCALE:2:1	SHEET 1 OF 1

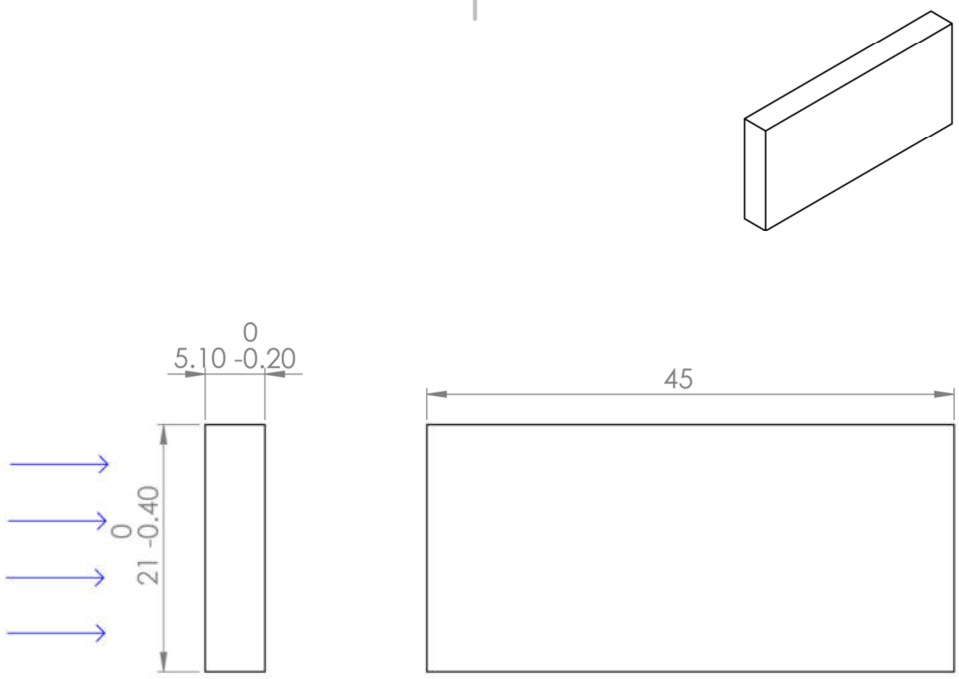

Note
1. Direction of magnetization is indicated as the arrows above.
2. All together 24 pieces are required for one prototype machine.

UNLESS OTHERWISE SPECIFIED: DIMENSIONS ARE IN MILLIMETERS SURFACE FINISH: TOLERANCES: LINEAR: ANGULAR:	FINISH:	DEBURR AND BREAK SHARP EDGES	DO NOT SCALE DRAWING	REVISION	
	NAME	SIGNATURE	DATE	TITLE:	Secondary Pole
DRAWN					
CHK'D					
APPV'D					
MFG					
Q.A				MATERIAL: Y30H	DWG NO. A4
				WEIGHT:	SCALE:2:1 SHEET 1 OF 1

B.2 The Testing Rig

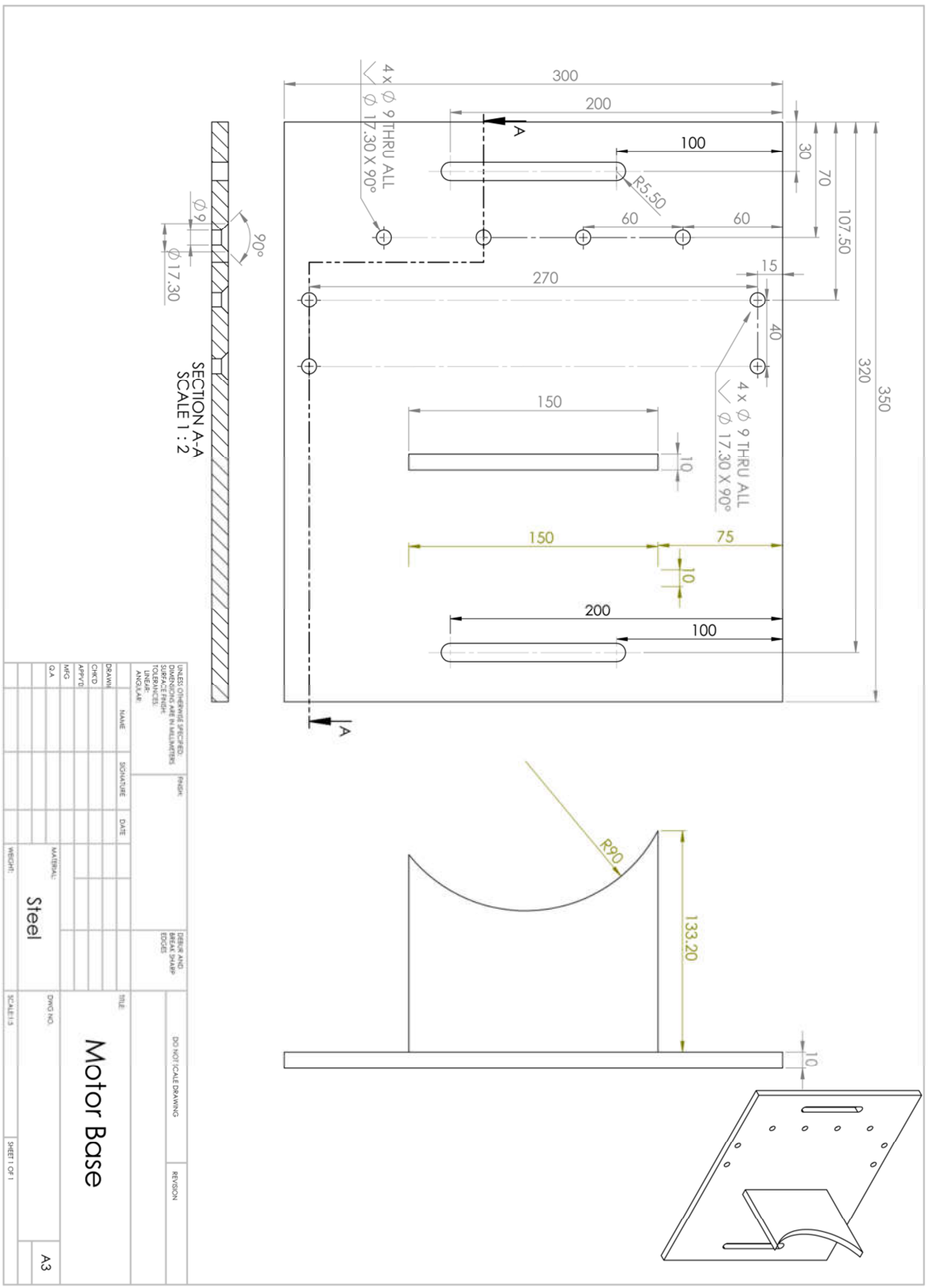

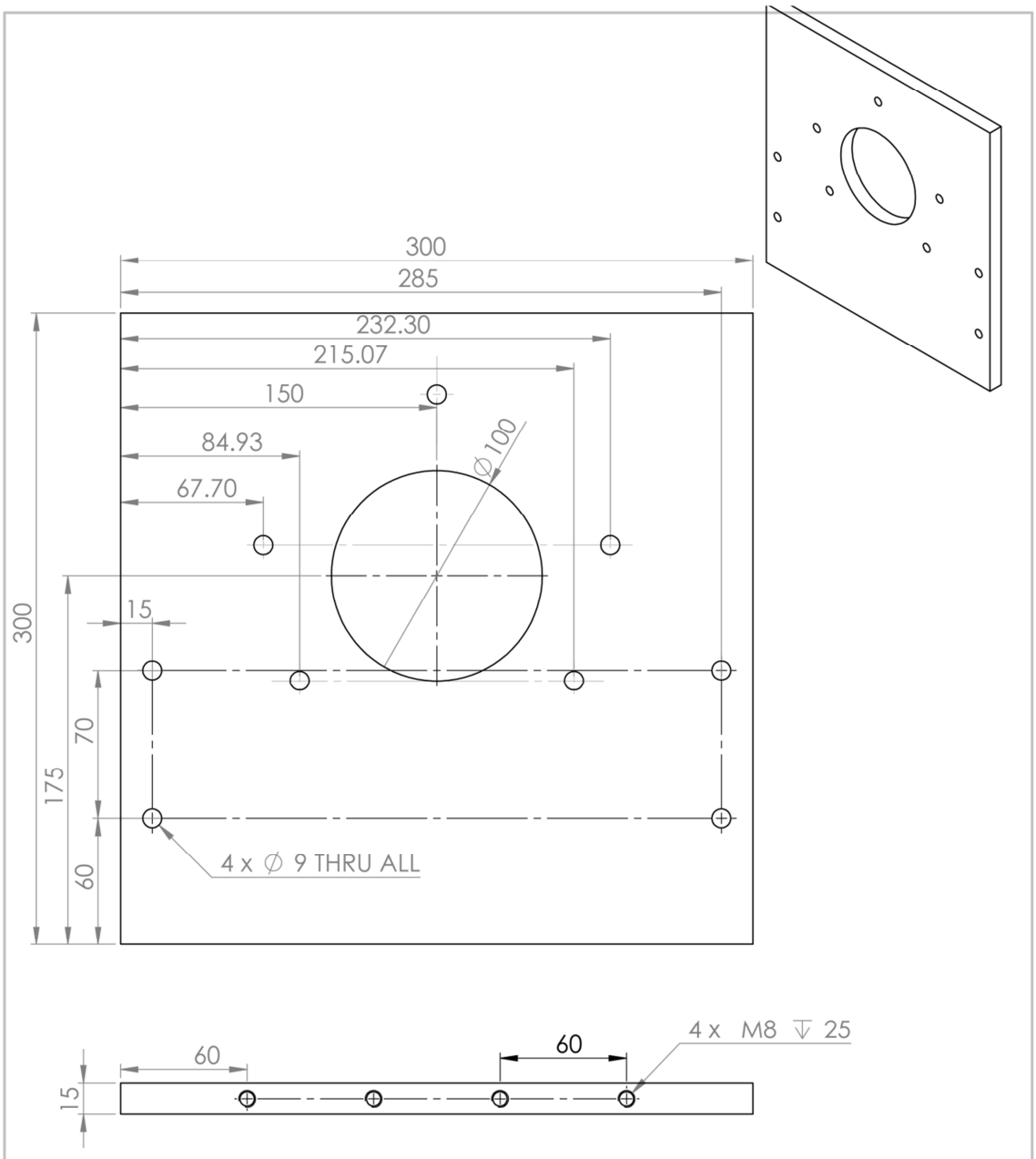

UNLESS OTHERWISE SPECIFIED: DIMENSIONS ARE IN MILLIMETERS SURFACE FINISH: TOLERANCES: LINEAR: ANGULAR:	FINISH:		DEBUR AND BREAK SHARP EDGES			DO NOT SCALE DRAWING	REVISION
	NAME	SIGNATURE	DATE			TITLE:	
DRAWN						Motor Fixture Plate	
CHK'D							
APPV'D							
MFG							
Q.A				MATERIAL:		DWG NO.	A4
				Steel			
				WEIGHT:		SCALE:1:5	SHEET 1 OF 1

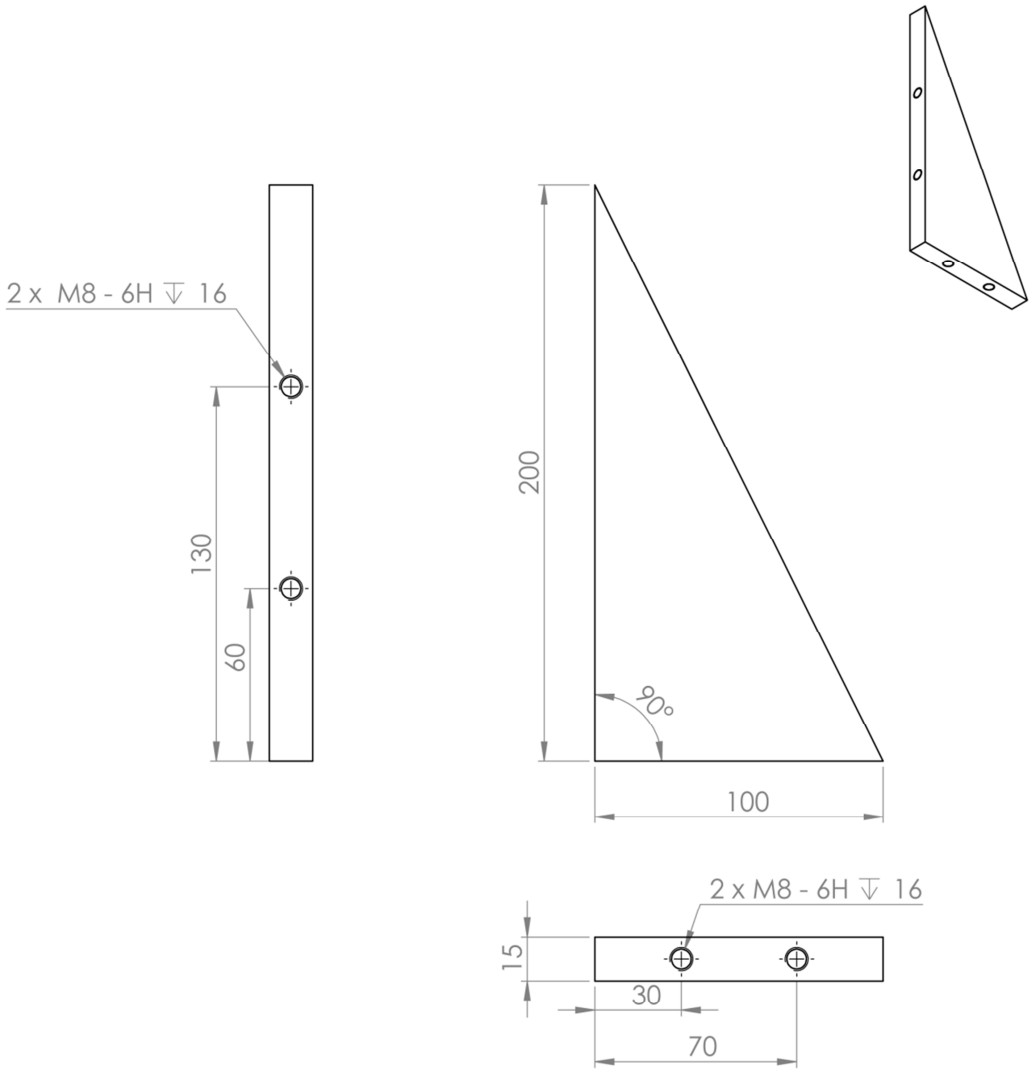

UNLESS OTHERWISE SPECIFIED: DIMENSIONS ARE IN MILLIMETERS SURFACE FINISH: TOLERANCES: LINEAR: ANGULAR:		FINISH:			DEBUR AND BREAK SHARP EDGES	DO NOT SCALE DRAWING	REVISION
	NAME	SIGNATURE	DATE			TITLE:	
DRAWN						Triangle Support	
CHK'D							
APPV'D							
MFG							
Q.A				MATERIAL:		DWG NO.	A4
				Steel			
				WEIGHT:		SCALE:1:2	SHEET 1 OF 1

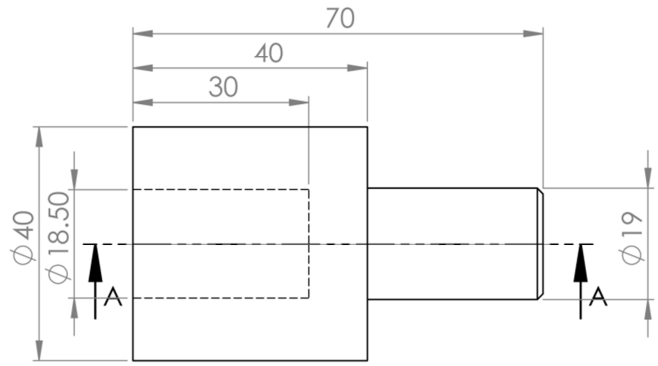

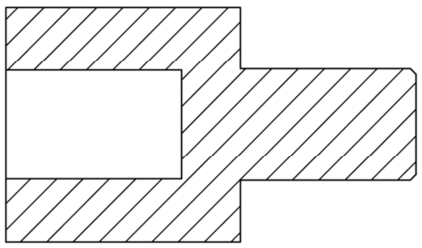

SECTION A-A

UNLESS OTHERWISE SPECIFIED: DIMENSIONS ARE IN MILLIMETERS SURFACE FINISH: TOLERANCES: LINEAR: ANGULAR:		FINISH:		DEBURR AND BREAK SHARP EDGES		DO NOT SCALE DRAWING	REVISION
	NAME	SIGNATURE	DATE			TITLE:	
DRAWN						Coupler for Dyno	
CHK'D							
APPV'D							
MFG							
Q.A				MATERIAL:		DWG NO.	A4
				Aluminum			
				WEIGHT:		SCALE:1:1	SHEET 1 OF 1

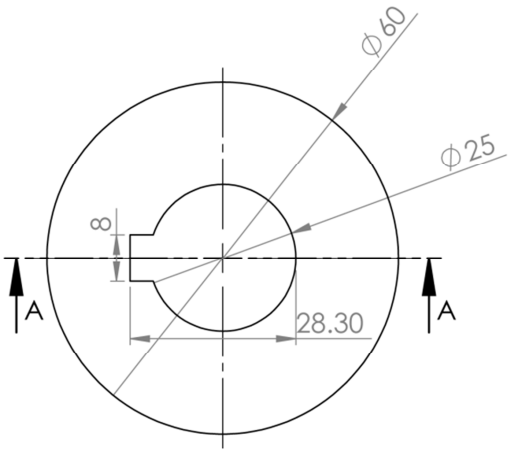

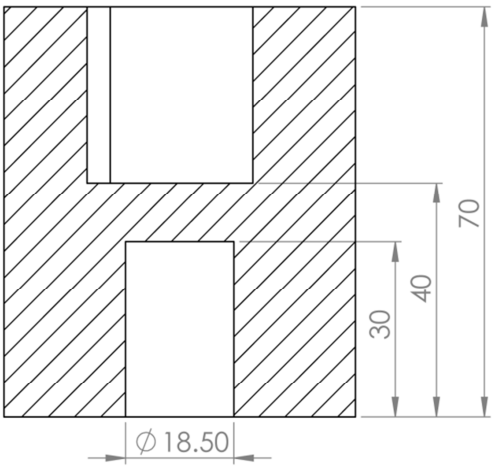

SECTION A-A
SCALE 1 : 1

UNLESS OTHERWISE SPECIFIED: DIMENSIONS ARE IN MILLIMETERS SURFACE FINISH: TOLERANCES: LINEAR: ANGULAR:	FINISH:	DEBURR AND BREAK SHARP EDGES	DO NOT SCALE DRAWING / REVISION

	NAME	SIGNATURE	DATE
DRAWN			
CHK'D			
APPV'D			
MFG			
Q.A			

TITLE: Coupler for the IM

MATERIAL: Aluminum

DWG NO. A4

WEIGHT:

SCALE:1:2

SHEET 1 OF 1

Appendix C TI High Voltage Motor Control and PFC Kit

C.1 Kit Feature

The high voltage motor control and PFC developer's kit is equipped with 32-bit floating-point microcontrollers TMS320F2803x/TMS320F2833x, which enable cost-effective design of intelligent controllers for three phase motors by reducing the system components and increase efficiency, as depicted in Figure_Apx 1. With these great advantages, it is possible to realize far more precise digital vector control algorithms.

- 350V DC max input voltage;
- 1KW/1.5KW maximum load;
- Sensorless and Sensored Field Oriented Control of PMSM Motor;
- QEP and CAP inputs available for speed and position measurement;
- High precision low-side current sensing using the C2000's high-performance ADC, TI OPA2350 high speed op-amps and Texas Instrument REF5025 high precision voltage reference chip.

Figure_Apx 1 The High Voltage Motor Control and PFC Developer's Kit

C.2 Control Kit Diagrams

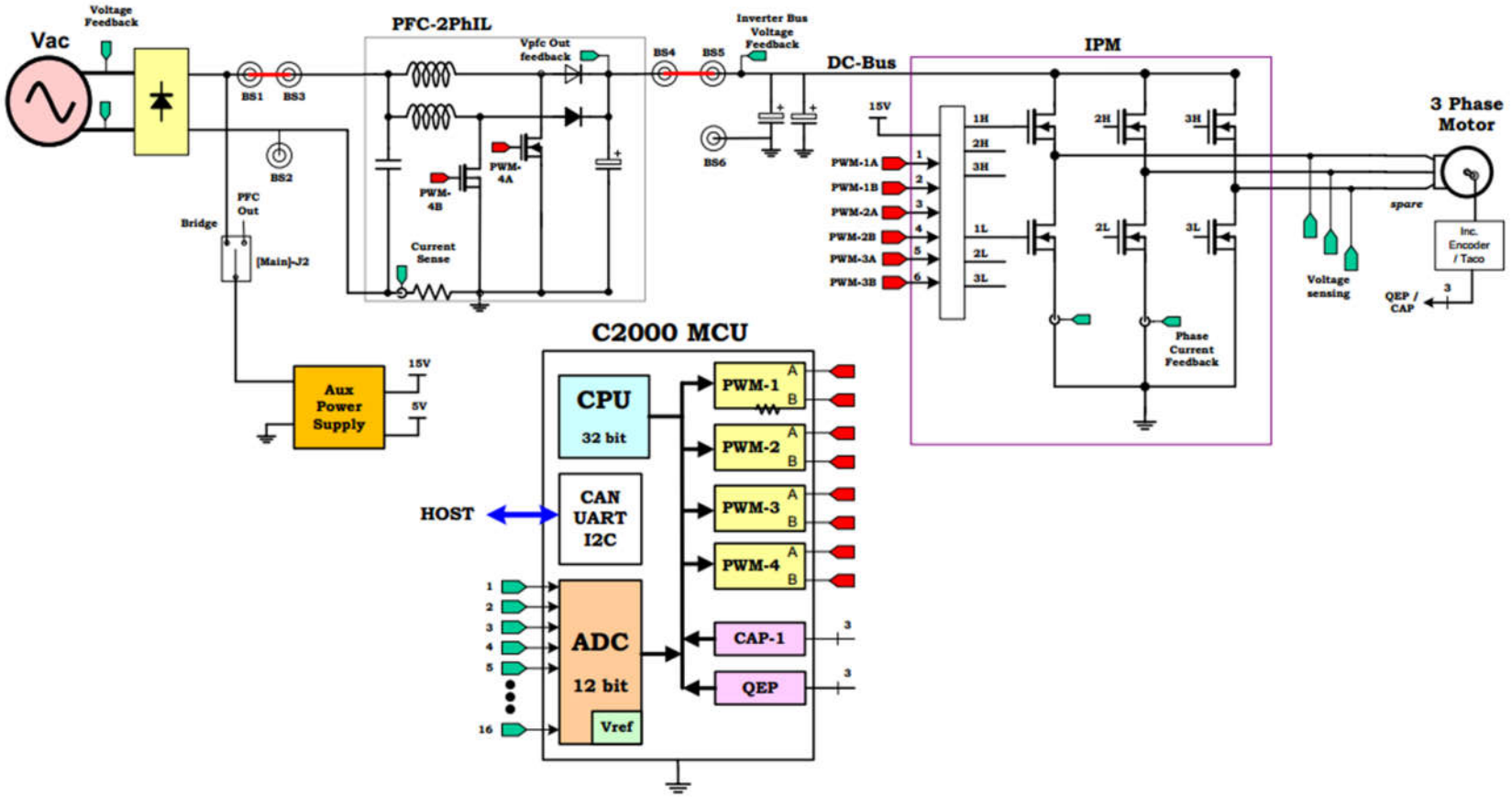

Figure_Apx 2 Control kit hardware diagram

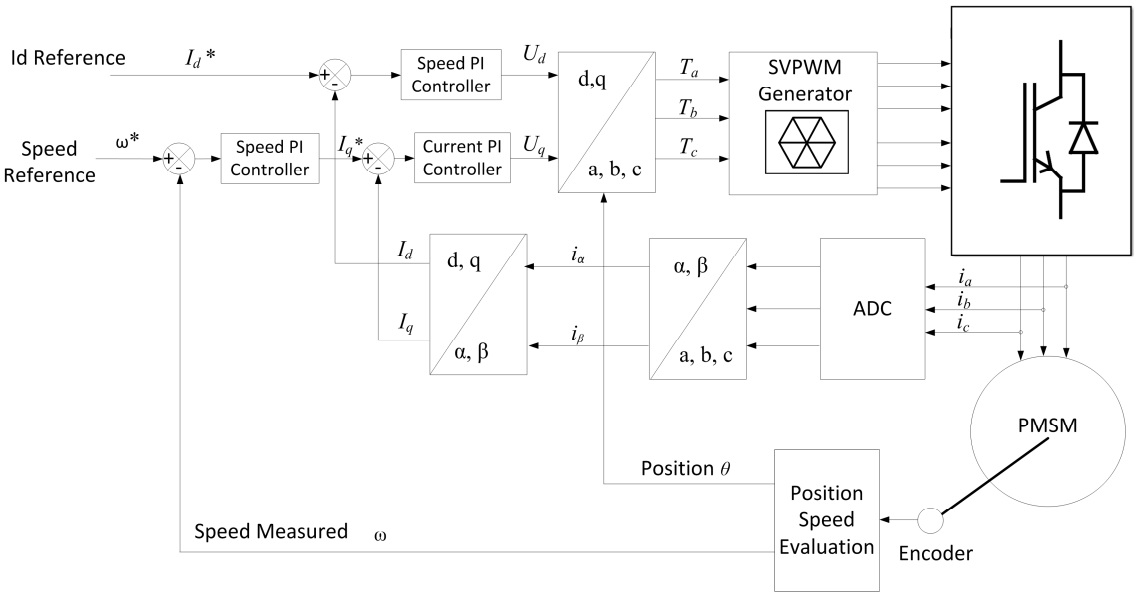

Figure_Apx 3 Control diagram of the applied vector control strategy.

Appendix D The Programmable Dynamometer System

To validate the performances of the prototype machine under various working conditions, the programmable dynamometer system is necessary to provide required torque loadings under different rotational speeds. The whole testing system in the lab consists of the powder brake dynamometer, the controller, brake supply, torque transducer and cooling sub-system.

D.1 The Powder Brake Dynamometer

The Magtrol powder brake dynamometer (PB Series) contains magnetic powders inside. When electrical current is passing through the coils, magnetic field is generated, and the property of the powders changes. Accordingly, smooth braking torque is produced because of the friction between the powders and spinning rotor. Since the braking torque is generated by friction, relatively large torque can be achieved under low speed range, and the powder brake dynamometer is ideal for applications operating in the low to middle speed range or when operating in the middle to high torque range. The powder brake provides full torque at zero speed and requires water-cooling. The PB dynamometer has accuracy ratings of ± 0.3% to 0.5% full scale with integrated optical speed sensor, and is quite suitable for performance tests of electric motors.

D.2 The Programmable Dynamometer Controller

Magtrol programmable dynamometer controller employs state-of-the-art digital signal processing technology to provide superior motor testing capabilities. In the laboratory, the controller's high sample rate provides superior resolution for data acquisition and curve plotting. This allows for capturing more usable motor test data during switching, breakdown and other transitional areas of the motor test curve, with complete PC control via IEEE-488 or RS-232 interface. On the other hand, the controller can display torque, speed and power at all times, which can also be used as a manual standalone unit or part of a PC controlling system.

D.3 The Dynamometer Power Supply

The dynamometer power supplies (DES 311) are suited to the entire range of Magtrol's powder brake dynamometers. The unit supplies the required current to the coils of the brake within the dynamometer to generate torque loadings, and the current can be controlled by analogue and digital set-points coming from an electronic peripheral, in this case, from the Magtrol's programmable dynamometer controller. To avoid any disruption of the surrounding electronic modules, the power supply is fitted in an industrial housing made of extruded cast aluminium.

D.4 The Controller In-Line Torque Transducers

The Magtrol's in-line torque transducer is a standalone measuring chain. The transducer provides extremely accurate torque and speed measurement over a very broad range. The torque transducer is very reliable, providing high overload protection, excellent long term stability and high noise immunity. Non-contact differential transformer torque measuring technology is employed for the transducer, and no electronic components rotate during operation. The transducer consists of a hardened stainless steel shaft with smooth shaft ends, an anodized aluminium housing containing the guide bearings and an electronic measurement conditioner. The integrated electronic circuit, supplied by single DC voltage, provides torque and speed signals without any additional amplifier.

D.5 The Differential Probes

To reduce signal interference from the inverter, differential voltage probes are used to measure terminal voltages of the prototype machine. The model type of the voltage probe is YOKOGAWA 70701921, with maximum voltage range of ±700V and accuracy of ±2%. The probe makes wide-bandwidth differential measurements up to 100MHz.

D.6 The Current sensors

The current sensors used in the experimental tests are PR30 based on Hall Effect technology. The current probe can measure both DC and AC current with

frequency range from DC to 100kHz. The measuring range is ±30A and the accuracy is ±1% of the reading ±2mA. The PR30 may be used in conjunction with oscilloscopes and other suitable recording instruments for accurate non-intrusive current measurement.

D.7 The Overall Diagram of the Testing System

The overall diagram of the testing system is demonstrated in Figure_Apx 4. The connections among the equipment can be divided into three categories, mechanical, electrical and water cooling. The prototype machine is connected to the dynamometer through the torque transducer for mechanical power output testing. The controlling and measuring units are connected to provide the drive for the prototype machine and collect experimental data. To dissipate the heat generated in the power brake, water cooling pipes are necessary for continuous loading tests.

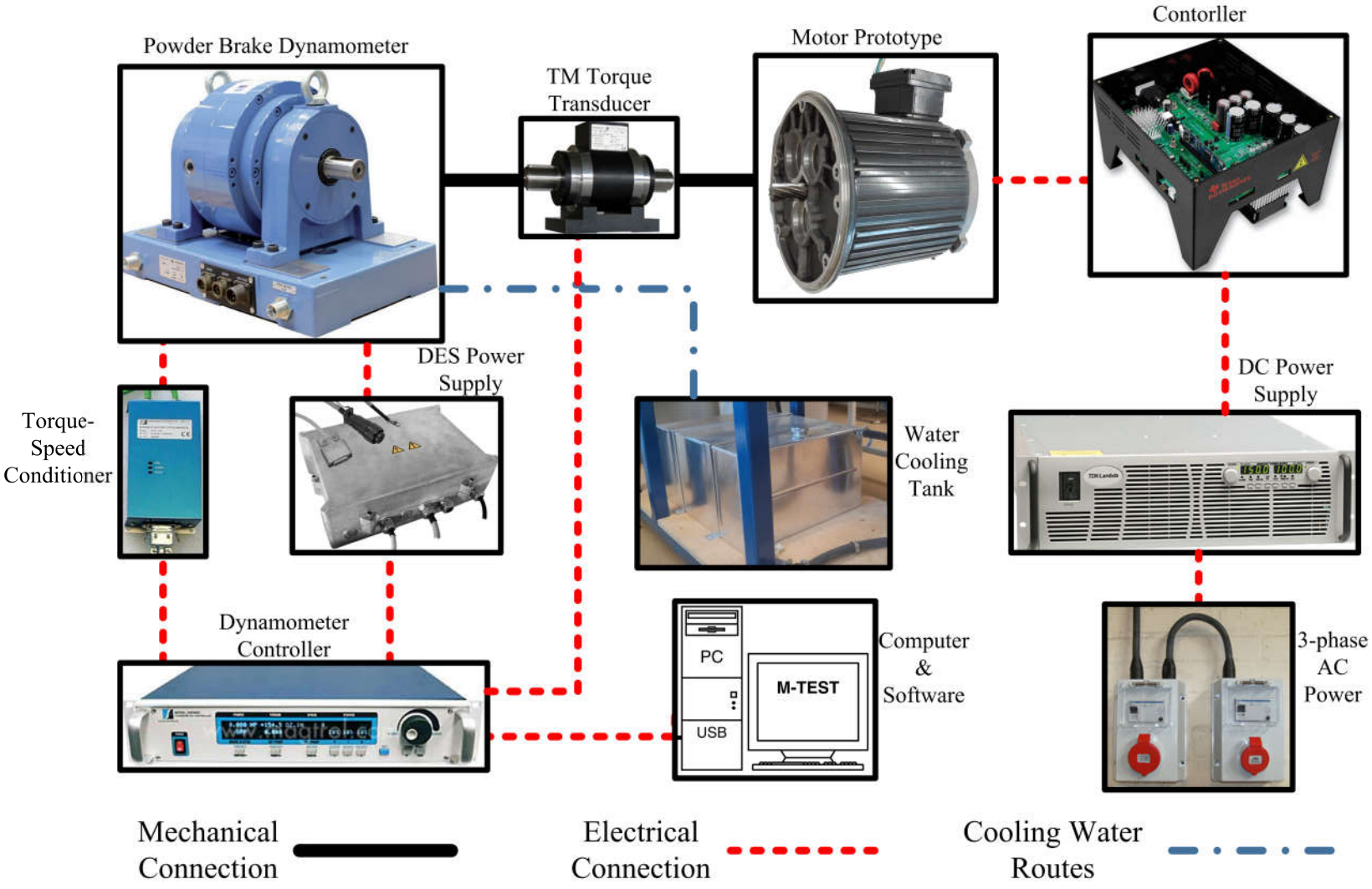

Figure_Apx 4 Control kit hardware diagram